Acute exposure to high-induction electromagnetic field affects activity of model peripheral sensory neurons

Jaroslav Prucha [a, b], Jan Krusek [c], Ivan Dittert [c], Viktor Sinica [c], Anna Kadkova [c], Viktorie Vlachova [c, *] iD

[a] *Department of Information and Communication Technologies in Medicine, Czech Technical University in Prague, Prague, Czech Republic*
[b] *Department of Health Care Disciplines and Population Protection, Faculty of Biomedical Engineering, Czech Technical University in Prague, Prague, Czech Republic*
[c] *Department of Cellular Neurophysiology, Institute of Physiology, Czech Academy of Sciences, Prague, Czech Republic*

Abstract

Exposure to repetitive low-frequency electromagnetic field (LF-EMF) shows promise as a non-invasive approach to treat various sensory and neurological disorders. Despite considerable progress in the development of modern stimulation devices, there is a limited understanding of the mechanisms underlying their biological effects and potential targets at the cellular level. A significant impact of electromagnetic field on voltage-gated calcium channels and downstream signalling pathways has been convincingly demonstrated in many distinct cell types. However, evidence for clear effects on primary sensory neurons that particularly may be responsible for the analgesic actions of LF-EMF is still lacking. Here, we used F11 cells derived from dorsal root ganglia neurons as an *in vitro* model of peripheral sensory neurons and three different protocols of high-induction magnetic stimulation to determine the effects on chemical responsiveness and spontaneous activity. We show that short-term (<180 sec.) exposure of F11 cells to LF-EMF reduces calcium transients in response to bradykinin, a potent pain-producing inflammatory agent formed at sites of injury. Moreover, we characterize an immediate and reversible potentiating effect of LF-EMF on neuronal spontaneous activity. Our results provide new evidence that electromagnetic field may directly modulate the activity of sensory neurons and highlight the potential of sensory neuron-derived cell line as a tool for studying the underlying mechanisms at the cellular and molecular level.

Keywords: electromagnetic field ● primary sensory neuron ● ion channel ● bradykinin receptor ● transient receptor potential channel

Introduction

Diverse cellular and physiological effects induced by exposure to repetitive low-frequency electromagnetic field (LF-EMF, <300 Hz) have a common denominator: calcium homoeostasis. Calcium ions (Ca^{2+}) control processes as critical as cell proliferation, differentiation, neuronal development, muscle contraction, transmitter release, vesicle endocytosis, gene transcription and cell death [1]. All these events have been convincingly shown to be affected by LF-EMF, and there is a large body of literature suggesting that activation of voltage-gated Ca^{2+} channels and downstream intracellular responses produce most of the LF-EMF effects (e.g. Ref. [2–6] and references therein). However, recent evidence suggests that LF-EMF may also primarily act via up-regulation of arachidonic acid and its metabolites, prostaglandin E2 or leukotriene E4. These inflammatory mediators sensitize excitatory (sodium) or inhibitory (γ-aminobutyric acid type A) ion channels and reduce the activity of low-voltage-gated T-type calcium channels [5, 7, 8]. The differential mechanisms of modulation may underlie diverse effects of LF-EMF which could have beneficial or deleterious outcome depending on the cell type and cell environment [2, 9]. It is increasingly understood that cellular processes affected by exposure to high-induction electromagnetic field have to be considered and appropriately characterized in a strictly cellular-specific context to assure a rational and safe usage of electromagnetic stimulators in future clinical practice [10].

High-induction electromagnetic field applied peripherally over a muscle or spinal nerve roots is capable of improving sensorimotor impairments and reducing acute and persistent pain [11–15].

*Correspondence to: Viktorie VLACHOVA
E-mail: Viktorie.Vlachova@fgu.cas.cz*

Proprioceptive as well as superficial cutaneous and nociceptive afferents may be recruited in these processes, although the latter are generally thought to be less involved [15]. Recent advances in single cell transcriptomics enabling to dissect sensory responsive cells into distinct neuronal subtypes [16] together with the ever-increasing information available on the multitude of specific receptors and channels involved in sensory transduction and nociception [17, 18] have opened an exciting opportunity to study the effects of LF-EMF in a manner even more focused on cellular and molecular mechanisms. Particularly, the recent systematic functional and transcriptomic characterization of neuroblastoma cells derived from dorsal root ganglia neurons [19] demonstrated that F11 cell line represents a convenient model to study the cellular mechanisms of sensory transduction and transmission *in vitro*. These cells endogenously express a well-characterized range of receptors and ion channels with potential roles in neuronal signalling and intracellular pathways implicated in various sensory functions, including those for nociceptive sensory neurons [19–22]: voltage-gated K^+ and Na^+ channels (particularly $Na_V1.6$, $Na_V1.7$ and $K_V11.1$), and many other ion channels and receptors with recognized roles in neuronal excitability. Moreover, F11 cells exhibit robust Ca^{2+} transients in response to subnanomolar concentrations of bradykinin [20, 22], a potent algogenic nonapeptide that is known to be released *in vivo* by tissue damage and under inflammatory conditions [23]. These responses are mediated by bradykinin B2 and, to a lesser extent, B1 receptors that belong to a family of G-protein coupled receptors and activate the G_q/phospholipase C pathway, catalysing the hydrolysis of phosphatidylinositol 4,5-bisphosphate and the production of the two second messengers, inositol triphosphate (IP_3) and diacylglycerol (DAG). The former product of hydrolysis activates intracellular Ca^{2+} release via IP_3 receptor channels located on the endoplasmic reticulum, whereas the membrane-bound DAG activates protein kinase C (PKC). Upon tissue trauma, inflammation or nerve injury, the B1 receptors are up-regulated and together with constitutive B2 receptors contribute to the development of pain and hyperalgesia not only in periphery but also in the spinal cord and higher centres [23].

The recent findings on F11 cells providing a well-characterized cellular model of peripheral sensory neurons [19] and the widely accepted important role of bradykinin as a mediator of pain and inflammation [23] prompted us to investigate the impact of LF-EMF on calcium responses induced in naïve and transfected F11 cells. W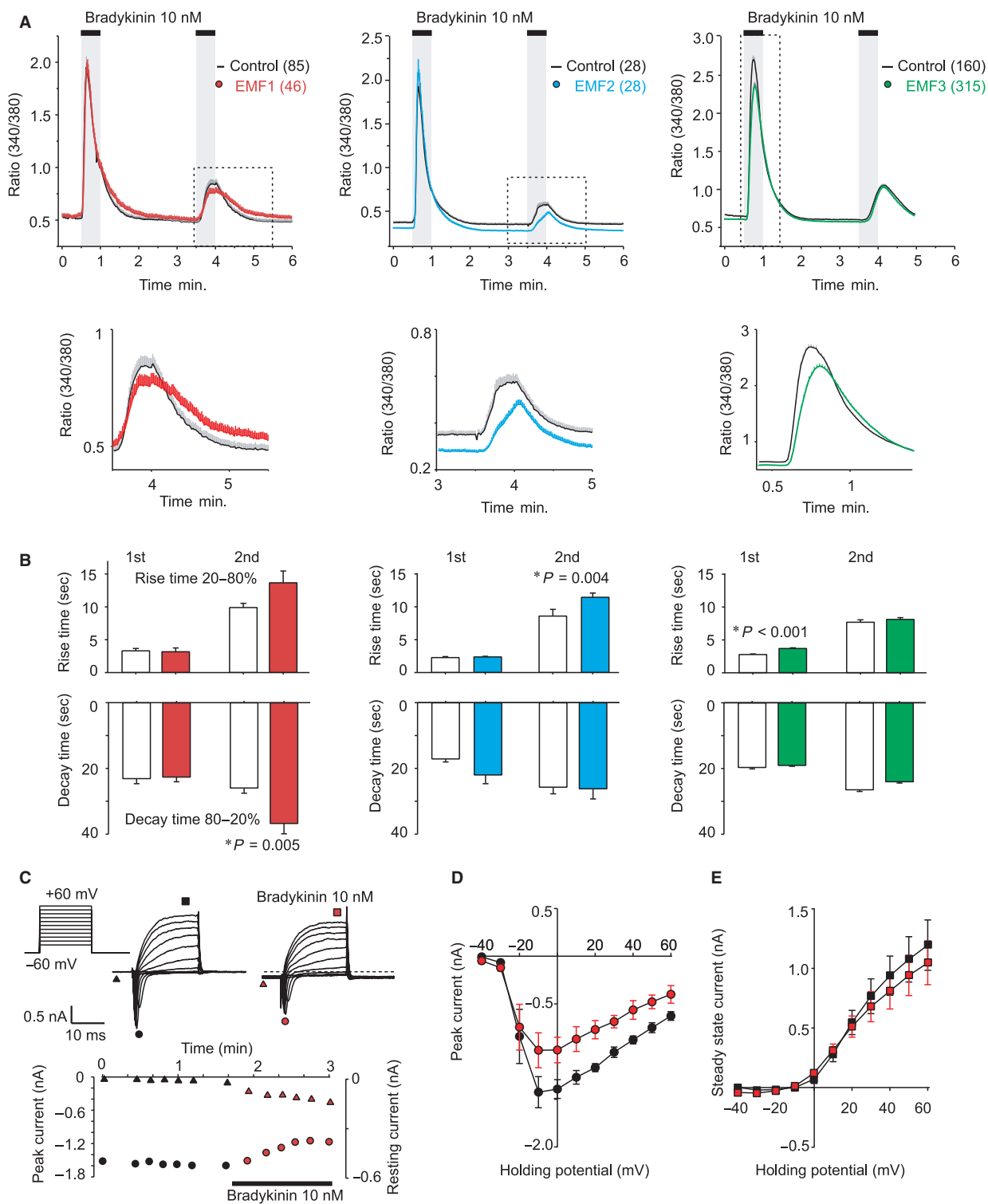e focus on acute changes because their understanding would greatly help our further comprehension of the molecular and cellular mechanisms that initiate the analgesic effects of LF-EMF.

Materials and methods

LF-EMF exposure systems

Three different systems for repetitive electromagnetic stimulation were used: EMF1, in physiotherapy so-called electrodeless electrotherapy, type name VAS-07 STRONG (EMBITRON s.r.o., Plzen, Czech Republic) generated, by means of the ring coil (7 cm middle radius), rectangular bipolar impulses of the induced electrical field of the intensity of 0.2–2 V/m and, consequently, electrical current density between 0.1 and 1 A/m² at the average tissue conductivity of 0.5 S/m. The positive part of the impulses had time duration of 340 μs, and the negative part, with a smaller amplitude, had time duration approximately 4.5 ms (this is the "repetitive single pulse" according to C.A.L. Bassett [24], and Ref. see [25] and references therein). The repetitive frequency was 72 Hz. Carrier magnetic field had an average amplitude of 5 mT. EMF2, in physiotherapy so-called high-induction magnetic stimulation, medical device of type name "SALUTER MOTI" (EMBITRON s.r.o., Plzen, Czech Republic), was produced by an electromagnetic generator system characterized by magnetic induction of amplitude of about 2 T, sinusoidal bipolar pulses with a width of 350 μs. The induced electrical field of the intensity of 20–200 V/m and consequently, electrical current density was between 10 and 100 A/m² at the average tissue conductivity of 0.5 S/m. The stimulator induced a repetitive 10 sec. packet of pulses at a frequency of 25 Hz or 1 Hz with respectively 50 sec. (at 25 Hz) or 2 sec. (at 1 Hz) after-pause. EMF3, in physiotherapy so-called high-induction magnetic stimulation, medical device type name "DIPOL SETA-D, I-100" (NPF Dipol, Vitebsk, Belarus), generated 170 μs rectangular pulses of magnetic field, in the burst of six pulses, with a delay between the pulses about 500 ms, one burst takes approximately 2.5 sec., followed by a 3.5 sec. pause, hence, the frequency of the bursts was 10 per minute. Magnetic induction amplitude was about 1 T, the induced electrical field was roughly 20 V/m and consequently, electrical current density was 10 A/m² at the average tissue conductivity of 0.5 S/m. In all cases, we took care to orient the system so that the surface of the culture dish bottom was as perpendicular as possible to the lines of force of the alternating magnetic field. Changes of temperature around the recording area were measured by a sensitive digital thermometer before and after each recording. If the temperature changed more than ~1°C, the data were discarded.

Fig. 1 Exposure to high-induction electromagnetic field attenuates responses to 10 nM bradykinin in cultured F11 cells. (**A**) Average calcium responses obtained from control cells and from cells continuously exposed to three different types of electromagnetic field (EMF1, EMF2, EMF3, see Materials and Methods). Continuous curves are the mean, colour envelopes the +S.E.M. (*n* indicated in parentheses). Magnified view of average data in dotted box is shown below each graph. The electromagnetic field was switched on 30 sec. before the recording. (**B**) Summary of the effects of LF-EMF on average rise time (20–80%) and average decay time (80–20%) constants of the second (in case of EMF1 and EMF2) and the first Ca^{2+} response (in case of EMF3) to bradykinin. (**C**) Whole-cell patch-clamp recording from a typical naïve F11 cell showing Na^+ and K^+ responses to repeated stimulation by depolarizing steps from −40 mV to +60 mV (holding potential −60 mV) in the absence and in the presence of bradykinin. Graph below shows the effects of bradykinin on the inward peak current (left axis, circles) and the resting membrane current (right axis, triangles). Note that upon bradykinin application, the resting inward membrane current increased from −4 pA to −143 pA. Effects of bradykinin on the average current-voltage relationship of the peak amplitude (**D**, indicated by circles in C), and the steady-state current (**E**, indicated by squares in C). Data are represented as mean ± S.E.M. (*n* = 3).

© 2017 The Authors.

Journal of Cellular and Molecular Medicine published by John Wiley & Sons Ltd and Foundation for Cellular and Molecular Medicine.

1357

Cell cultures and transfection

F11 cells (The European Collection of Authenticated Cell Cultures) cultured in Dulbecco's modified Eagle's medium (DMEM) supplemented with 2 mM glutamine and 10% foetal bovine serum were passaged once a week using trypsin-EDTA (Invitrogen, Carlsbad, CA, USA) and grown under 5% CO_2 at 37°C. For experiments, cells were grown for 7–11 days to properly differentiate. The day before transfection, cells were plated in 24-well plates (2×10^5 cells per well) in 0.5 ml of medium and became confluent on the day of transfection. The cells were transiently cotransfected with 300 ng of cDNA plasmid encoding human TRPA1 (in the pCMV6-XL4 vector, OriGene Technologies, Rockville, MD, USA) and with 200 ng of GFP plasmid (TaKaRa, Japan) with the use of Lipofectamine 2000 (Invitrogen) and then plated on poly-L-lysine-coated glass coverslips.

Measurement of intracellular Ca^{2+} responses

The cells were loaded with 1 μM Fura-2-AM (Invitrogen) dissolved in a bath solution (160 mM NaCl, 2.5 mM KCl, 1 mM $CaCl_2$, 2 mM $MgCl_2$, 10 mM HEPES, 10 mM glucose, adjusted to pH 7.3 with NaOH, 320 mOsm) for 1 hr followed by a 20-min. wash in fresh bath solution. The Cell^R imaging system (Olympus Biosystems, Planegg, Germany) was used to capture the fluorescence images obtained with alternating excitation at 340 and 380 nm (TILL Photonics, Planneg, Germany) and emission at >510 nm. The metal xy positioning microscope stage (Olympus IX81) was replaced by plastic stage to prevent EMF-induced mechanical resonance that impaired the quality of image recording. Emission ratios were calculated for each 0.5-sec. interval after subtraction of the background. Spontaneous activity of cells was measured using excitation/emission wavelengths 380 nm/510 nm and sampling rate ≤500 ms. A system for rapid superfusion of the cultured cells was used for drug application [26]. The control experiments were performed for each electromagnetic exposure system during the same day for comparison.

Electrophysiology

Whole-cell membrane currents were recorded by employing an Axopatch 200B amplifier and pCLAMP 10 software (Molecular Devices), exactly as described previously [27]. The extracellular bath solutions contained the following: 160 mM NaCl, 2.5 mM KCl, 1 mM $CaCl_2$, 2 mM $MgCl_2$, 10 mM HEPES, 10 mM glucose, adjusted to pH 7.3 and 320 mOsm. The internal pipette solution contained 125 mM K^+-gluconate, 15 mM KCl, 5 mM EGTA, 0.5 mM $CaCl_2$, 10 mM HEPES and 2 mM MgATP, 0.3 mM NaGTP, 10 mM creatine phosphate adjusted with KOH to pH 7.2 and 300 mOsm. Only one recording was performed on any one coverslip of cells to ensure that recordings were made from cells not previously exposed to chemical stimuli.

Statistical analysis

All of the data were analysed using ImageJ software (NIH, Bethesda, MD, USA), pCLAMP 10 (Molecular Devices) and SigmaPlot 10 (Systat Software Inc., San Jose, CA, USA). Statistical significance was determined by Student's t-test; differences were considered significant at $P < 0.05$ where not stated otherwise. The data are presented as means $\pm$ S.E.M.

Results

LF-EMF inhibits bradykinin-induced calcium responses in F11 cells

We examined the effects of three distinct sources of repetitive LF-EMF on endogenous Ca^{2+} responses of F11 cells to repeated applications of 10 nM bradykinin (BK). We applied two subsequent BK exposures, each lasting 30 sec. and separated by 3 min. In the control experiments (without EMF1 or EMF2), the first application of BK induced Ca^{2+} responses with peak amplitudes of 1.96 ± 0.11 and 1.93 ± 0.09 ($n = 85$ and 28; ratio 340/380 nm in arbitrary units). The second response was largely reduced (to 0.85 ± 0.04 and 0.57 ± 0.04; $P = {<}0.001$). As shown in Figure 1, continuous exposure to EMF1 or EMF2 did not significantly influence the average initial response to BK (1.94 ± 0.11 and 2.12 ± 0.15, $n = 46$ and 28; $P = 0.907$ and 0.287), but the subsequent response to BK applied three minutes later was markedly suppressed ($P = 0.047$ and 0.031) and delayed. Upon exposure to EMF1, the 80–20% decay time of the second response was significantly slowed from 26 ± 2 to 37 ± 3 sec. ($P = 0.005$). Exposure to EMF3 caused a significantly delayed onset and reduction of the first average response from 2.7 ± 0.1 to 2.3 ± 0.1 ($n = 160$ and 315; $P = {<}0.001$) (Fig. 1B). The 20–80% rise time of the first BK responses significantly increased from 2.3 ± 0.1 sec. to 3.7 ± 0.1 sec. ($P < 0.001$). The second average BK response upon exposure to EMF3 was no different from control cells. To gain qualitative information about the overall effects of bradykinin on F11 cell excitability, we used patch-clamp technique and measured membrane currents in response to 20-ms voltage pulses from -40 mV to $+60$ mV in the absence and in the presence of 10 nM bradykinin (Fig. 1C). The inward currents, which are typical for voltage-gated Na^+ channels, were significantly inhibited by bradykinin (from -1.39 ± 0.10 nA to -0.98 ± 0.11 nA; $n = 3$, $P < 0.05$) and the resting membrane current increased (Fig. 1C and D). The outward voltage-dependent potassium currents were only slightly affected (Fig. 1E).

F11 cells exhibit spontaneous activity, that is increased in response to LF-EMF

We regularly observed spontaneous Ca^{2+} activity in a subset of F11 cells (Fig. 2A) that could be better monitored using one excitation wavelength (380 nm) and subsecond sampling rates (Fig. 2B). The occurrence of spontaneous activity depended on the extent of differentiation of F11 cells. The highest activity was observed in cells 4–8 days after passaging. The percentage of spontaneously active cells was $19 \pm 3\%$ (calculated from 2363 cells from 28 independent experiments conducted at eight different days). Although not obvious at first sight, the spontaneous activity seemed to be promoted by EMF2 and EMF3, but this effect was not apparently reversible and was seen only in some cells. In a small proportion of cells (21/894 in case of EMF3), switching off the magnetic field, on the contrary, increased the
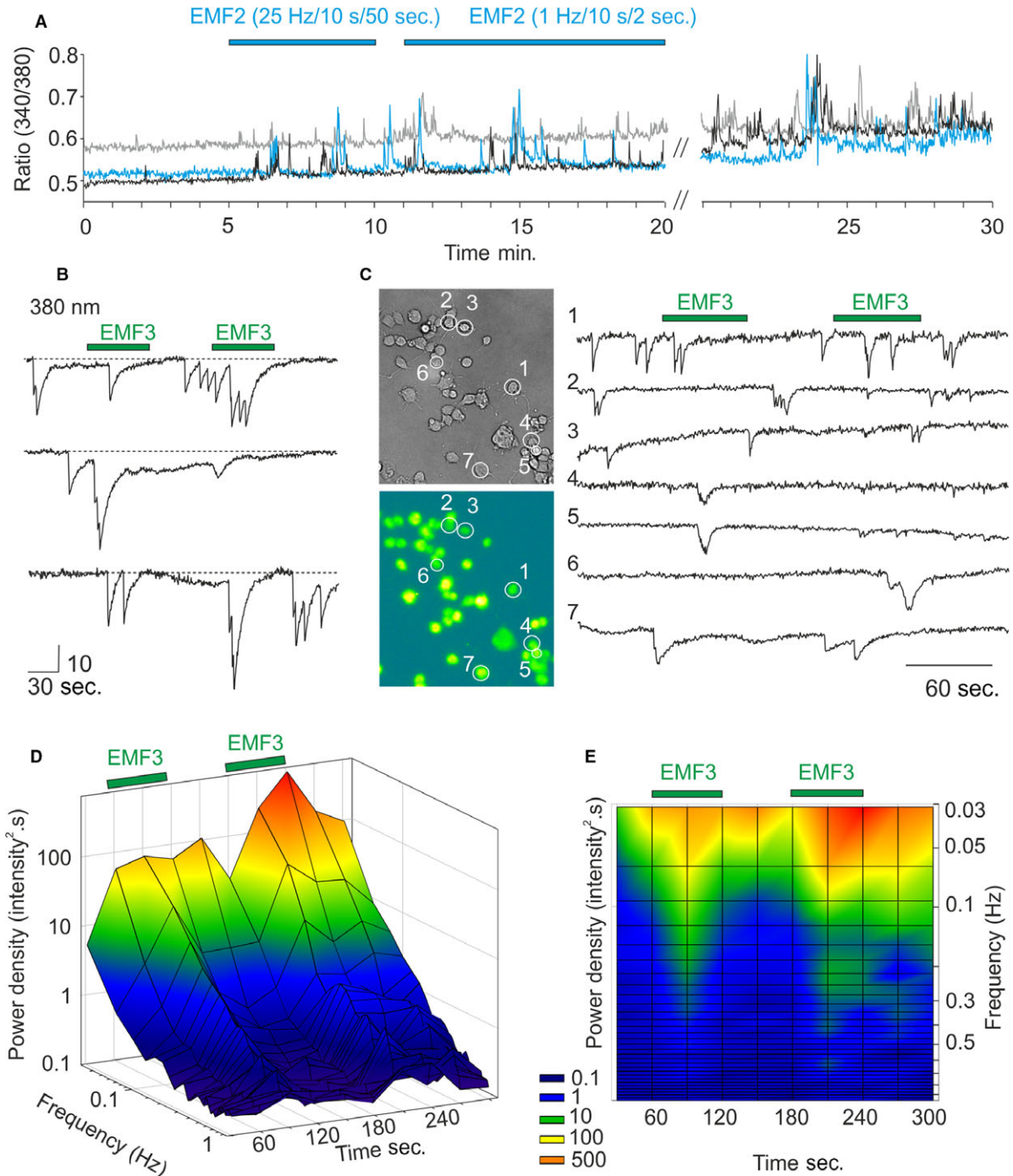
Fig. 2 F11 cells exhibit spontaneous activity that is increased in response to LF-EMF. (**A**) Spontaneous Ca^{2+} activity in three representative F11 cells exposed to EMF2 (with two different settings of parameters), measured as the relative calcium increase, expressed by the 340/380 fluorescence ratio. (**B**) Spontaneous Ca^{2+} activity in three representative F11 cells exposed to EMF3. The spontaneous activity could be monitored at a better time resolution using one excitation wavelength (380 nm) and the 500-msec. sampling rate. The vertical scale is in arbitrary intensity units. (**C**) Recording from seven representative Fura-2-loaded cells exposed twice to 60 sec. to EMF3 (indicated by green bar above the records). (**D**) and (**E**) The spontaneous Ca^{2+} activity was analysed using Fast Fourier Transformation (using Von Hann windowing function available in Clampfit). Average power spectrum obtained from 154 cells reveals a clear and reversible increase in activity upon EMF3 stimulation.

© 2017 The Authors.

Journal of Cellular and Molecular Medicine published by John Wiley & Sons Ltd and Foundation for Cellular and Molecular Medicine.

1359

activity. To quantify these observations, we decided to apply EMF3 that had most pronounced effects on F11 responses (Fig. 2B and C), and the Fast Fourier Transformation that converts a signal to its representation in the frequency domain. The resulting average power spectra obtained from 154 cells exposed twice to ELF3 for 60 sec. with 60-sec. interval revealed a clear increase in power spectral density within the frequency range of ~0.03–0.3 Hz (Fig. 2D and E).

LF-EMF affects crosstalk among F11 cells heterologously expressing human transient receptor potential TRPA1

The reported beneficial effects of high-induction electromagnetic field on acute and persistent pain [11–15] prompted us to further explore whether LF-EMF may be able to influence some of the known prototypical nociceptor-specific ion channels. As an example, we have selected the transient receptor potential ankyrin subtype 1 (TRPA1) which is an excitatory ion channel expressed by nociceptive neurons of the dorsal root and trigeminal ganglia. There it mediates acute and chronic pain and plays an important role in initiation and maintenance of chronic inflammatory diseases and tissue injuries (e.g. Ref. [28–33] and references therein). TRPA1 transcript is completely absent in F11 cells [19]; therefore, these cells are well suitable for studying this channel under close-to-native conditions [34]. We co-expressed human TRPA1 with green fluorescent protein (GFP, as a marker) and measured Ca^{2+} responses to EMF2. As we previously described [34], TRPA1-expressing cells exhibited increased basal levels of intracellular Ca^{2+} and we occasionally observed spontaneous calcium transients in a subset of cells (usually 1–2 per experiment). Figure 3 shows a representative recording obtained from one of three independent experiments. Among five interconnected cells, cell 1 (black line) and cell 2 (red line) were GFP positive and, thus, most likely, expressed TRPA1 channels. Prolonged application of EMF2 did not induce any response, but after discontinuation of the magnetic field, calcium transients occurred simultaneously in three of the cells. Six minutes later, EMF2 triggered activity in these cells, but it did not affect those cells that exhibited low basal Ca^{2+} levels. Such cells consistently responded to repeated application of 50 mM KCl (see cell 5 in Fig. 3B and C).

Discussion

Together, our results demonstrate that repetitive electromagnetic stimulation has acute effects on calcium responses in model peripheral sensory neurons. We show that short-term exposure of naïve F11 cells to LF-EMF reduces calcium transients in response to bradykinin (Fig. 1) and demonstrate a potentiating effect of LF-EMF on spontaneous activity of F11 cells under two different conditions (Figs. 2 and 3). The main result of this pilot study is the demonstration that sensory neuron-derived cell line is a suitable and physiologically relevant tool for studying the mechanisms underlying the effects of LF-EMF at the cellular and molecular level. The information gleaned from studies on the cellular processes that might be involved in such effects is scattered in the literature and does not permit yet to integrate the results into an explicit mechanism for several main reasons: (i) the cell types, (ii) parameters of electromagnetic field, (iii) the
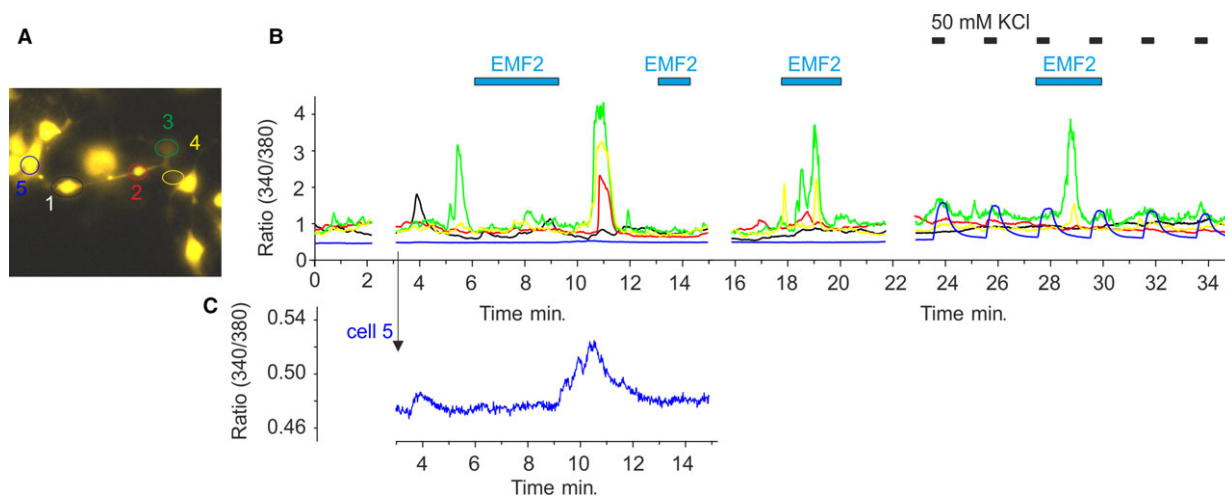

Fig. 3 Crosstalk among interconnected F11 cells is affected by LF-EMF. (**A**) F11 cells transfected with human TRPA1. (**B**) Time course of Fura-2 ratiometric responses from cells shown in A. Cell 1 (black line) and cell 2 (red line) were GFP positive and, thus, most likely, expressed TRPA1. Ca^{2+} responses to EMF2 (intensity 79%, frequency 25 Hz, packet 10 sec., pause 50 sec.). The cell 5 (blue trace) which exhibited a lower basal level of intracellular Ca^{2+} was affected after switching off the EMF2 stimulator. This portion of the graph is enlarged below (**C**). The low activity of cell 5 could trigger the robust Ca^{2+} transients in cells 2, 3 and 4. The cell 5 responded to repeated application of 50 mM KCl (horizontal bars above the record). Similar effects were seen in three independent experiments.

length of exposure, (iv) the pharmacological and biochemical tools and (v) a biased focus on only one aspect of cellular responsiveness were different in each study. The identification of a plausible mechanism that could be extrapolated in the therapeutic context can be still quite difficult due to the complexity of effects. We demonstrate that exposure to high-induction EMF attenuates responses to 10 nM bradykinin. Under voltage-clamp conditions, bradykinin reduced Na+ inward currents and increased the resting membrane current, indicating alterations in neuronal excitability. Bradykinin stimulates the hydrolysis of phosphatidylinositol 4,5-bisphosphate. This membrane phospholipid is a necessary and general cofactor whose requirement is clearly established for many ion channels, receptors and transporters [23, 35, 36]. Thus, to further explain the multiple mechanisms whereby LF-EMF may affect the cellular signalling would require careful characterization of responses in a particular native cell type and the use of novel approaches to identify receptors and cellular pathways involved. Interestingly, Ambrosino *et al.* [22] previously reported that Ca^{2+} responses do not desensitize when BK is repeatedly applied on F11 cells at a concentration of 250 nM. The authors used three subsequent BK exposures, each lasting 30 sec. and separated by >15 min. This time interval was probably sufficient for full resensitization of BK receptors and their signalling pathways, in contrast to 3-min. interval used in our application protocol. Whereas LF-EMF seemed to affect the signalling pathways involved in the desensitization, the effects on resensitization cannot be assessed from our recordings. Given that the bradykinin B2 receptors exhibit two different apparent affinities in F11 cells (EC50s of 1.8×10^{-9} and 3.7×10^{-12} M) [20], the strong desensitization of Ca^{2+} responses observed in our experiments indicates that LF-EMF may affect the higher affinity signalling pathway of the BK receptor.

We examined a possible contribution of TRPA1 in EMF-induced responses (Fig. 3). This ion channel is considered to be mechanosensitive [37, 38], and we hypothesized that such a channel might be also physically prone to be modulated by high-induction electromagnetic field. The overexpression of TRPA1 heightened the sensitivity of F11 cells to EMF, but this effect was rather due to increased basal levels of intracellular Ca^{2+}. Additional studies, which are currently ongoing, are necessary to further elucidate whether and to what extent LF-EMF may influence other mechanotransduction ion channels that modulate nociceptor excitability and/or contribute to action potential propagation in sensory neurons [39]. Such ion channels are expected to be intrinsically capable of stimulus-specific conformational changes, and their putative involvement in magnetosensation would take us one step closer to understanding how these processes might occur.

Acknowledgements

Conflict of interest

The authors confirm that there is no conflict of interests.

References

1. **Clapham DE.** Calcium signaling. *Cell.* 2007; 131: 1047–58.

2. **Pall ML.** Electromagnetic fields act via activation of voltage-gated calcium channels to produce beneficial or adverse effects. *J Cell Mol Med.* 2013; 17: 958–65.

3. **Sun ZC, Ge JL, Guo B, et al.** Extremely low frequency electromagnetic fields facilitate vesicle endocytosis by increasing presynaptic calcium channel expression at a central synapse. *Sci Rep.* 2016; 6: 21774.

4. **Piacentini R, Ripoli C, Mezzogori D, et al.** Extremely low-frequency electromagnetic fields promote in vitro neurogenesis via upregulation of Ca(v)1-channel activity. *J Cell Physiol.* 2008; 215: 129–39.

5. **Cui Y, Liu X, Yang T, et al.** Exposure to extremely low-frequency electromagnetic fields inhibits T-type calcium channels via AA/LTE4 signaling pathway. *Cell Calcium.* 2014; 55: 48–58.

6. **Marchionni I, Paffi A, Pellegrino M, et al.** Comparison between low-level 50 Hz and

900 MHz electromagnetic stimulation on single channel ionic currents and on firing frequency in dorsal root ganglion isolated neurons. *Biochim Biophys Acta.* 2006; 1758: 597–605.

7. **He YL, Liu DD, Fang YJ, et al.** Exposure to extremely low-frequency electromagnetic fields modulates Na+ currents in rat cerebellar granule cells through increase of AA/PGE2 and EP receptor-mediated cAMP/PKA pathway. *PLoS ONE.* 2013; 8: e54376.

8. **Yang G, Ren Z, Mei YA.** Exposure to 50 Hz magnetic field modulates GABAA currents in cerebellar granule neurons through an EP receptor-mediated PKC pathway. *J Cell Mol Med.* 2015; 19: 2413–22.

9. **Santini MT, Rainaldi G, Indovina PL.** Cellular effects of extremely low frequency (ELF) electromagnetic fields. *Int J Radiat Biol.* 2009; 85: 294–313.

10. **Rossini PM, Burke D, Chen R, et al.** Non-invasive electrical and magnetic stimulation of the brain, spinal cord, roots and

peripheral nerves: basic principles and procedures for routine clinical and research application. An updated report from an I.F.C.N. Committee. *Clin Neurophysiol.* 2015; 126: 1071–107.

11. **Masse-Alarie H, Beaulieu LD, Preuss R, et al.** Repetitive peripheral magnetic neurostimulation of multifidus muscles combined with motor training influences spine motor control and chronic low back pain. *Clin Neurophysiol.* 2017; 128: 442–53.

12. **Smania N, Corato E, Fiaschi A, et al.** Therapeutic effects of peripheral repetitive magnetic stimulation on myofascial pain syndrome. *Clin Neurophysiol.* 2003; 114: 350–8.

13. **Lo YL, Fook-Chong S, Huerto AP, et al.** A randomized, placebo-controlled trial of repetitive spinal magnetic stimulation in lumbosacral spondylotic pain. *Pain Med.* 2011; 12: 1041–5.

14. **Khedr EM, Ahmed MA, Alkady EA, et al.** Therapeutic effects of peripheral magnetic

stimulation on traumatic brachial plexopathy: clinical and neurophysiological study. *Neurophysiol Clin*. 2012; 42: 111–8.

15. **Beaulieu LD, Schneider C.** Repetitive peripheral magnetic stimulation to reduce pain or improve sensorimotor impairments: a literature review on parameters of application and afferents recruitment. *Neurophysiol Clin*. 2015; 45: 223–37.

16. **Usoskin D, Furlan A, Islam S, et al.** Unbiased classification of sensory neuron types by large-scale single-cell RNA sequencing. *Nat Neurosci*. 2015; 18: 145–53.

17. **Yekkirala AS, Roberson DP, Bean BP, et al.** Breaking barriers to novel analgesic drug development. *Nat Rev Drug Discovery*. 2017; 16: 545–64.

18. **von Hehn CA, Baron R, Woolf CJ.** Deconstructing the neuropathic pain phenotype to reveal neural mechanisms. *Neuron*. 2012; 73: 638–52.

19. **Yin K, Baillie GJ, Vetter I.** Neuronal cell lines as model dorsal root ganglion neurons: a transcriptomic comparison. *Mol Pain*. 2016; 12: 1–17.

20. **Vetter I, Lewis RJ.** Characterization of endogenous calcium responses in neuronal cell lines. *Biochem Pharmacol*. 2010; 79: 908–20.

21. **Francel PC, Harris K, Smith M, et al.** Neurochemical characteristics of a novel dorsal root ganglion X neuroblastoma hybrid cell line, F-11. *J Neurochem*. 1987; 48: 1624–31.

22. **Ambrosino P, Soldovieri MV, Russo C, et al.** Activation and desensitization of TRPV1 channels in sensory neurons by the PPARalpha agonist palmitoylethanolamide. *Br J Pharmacol*. 2013; 168: 1430–44.

23. **Petho G, Reeh PW.** Sensory and signaling mechanisms of bradykinin, eicosanoids, platelet-activating factor, and nitric oxide in peripheral nociceptors. *Physiol Rev*. 2012; 92: 1699–775.

24. **Bassett CA, Pawluk RJ, Pilla AA.** Acceleration of fracture repair by electromagnetic fields. A surgically noninvasive method. *Ann N Y Acad Sci*. 1974; 238: 242–62.

25. **Markov MS.** Expanding use of pulsed electromagnetic field therapies. *Electromagn Biol Med*. 2007; 26: 257–74.

26. **Dittert I, Benedikt J, Vyklicky L, et al.** Improved superfusion technique for rapid cooling or heating of cultured cells under patch-clamp conditions. *J Neurosci Methods*. 2006; 151: 178–85.

27. **Hynkova A, Marsakova L, Vaskova J, et al.** N-terminal tetrapeptide T/SPLH motifs contribute to multimodal activation of human TRPA1 channel. *Sci Rep*. 2016; 6: 28700.

28. **Nilius B, Appendino G, Owsianik G.** The transient receptor potential channel TRPA1: from gene to pathophysiology. *Pflugers Arch*. 2012; 464: 425–58.

29. **Viana F.** TRPA1 channels: molecular sentinels of cellular stress and tissue damage. *J Physiol*. 2016; 594: 4151–69.

30. **Zygmunt PM, Hogestatt ED.** Trpa1. *Handb Exp Pharmacol*. 2014; 222: 583–630.

31. **Vilceanu D, Stucky CL.** TRPA1 mediates mechanical currents in the plasma membrane of mouse sensory neurons. *PLoS ONE*. 2010; 5: e12177.

32. **Moparthi L, Kichko TI, Eberhardt M, et al.** Human TRPA1 is a heat sensor displaying intrinsic U-shaped thermosensitivity. *Sci Rep*. 2016; 6: 28763.

33. **Moran MM.** Transient receptor potential ankyrin 1 as a target for perioperative pain management. *Anesthesiology*. 2012; 117: 8–9.

34. **Kadkova A, Synytsya V, Krusek J, et al.** Molecular basis of TRPA1 regulation in nociceptive neurons. A review. *Physiol Res*. 2017; 66: 425–39.

35. **Suh BC, Hille B.** PIP2 is a necessary cofactor for ion channel function: how and why? *Annu Rev Biophys*. 2008; 37: 175–95.

36. **Cruzblanca H, Koh DS, Hille B.** Bradykinin inhibits M current via phospholipase C and Ca^{2+} release from IP3-sensitive Ca^{2+} stores in rat sympathetic neurons. *Proc Natl Acad Sci U S A*. 1998; 95: 7151–6.

37. **Meotti FC, Figueiredo CP, Manjavachi M, et al.** The transient receptor potential ankyrin-1 mediates mechanical hyperalgesia induced by the activation of B1 receptor in mice. *Biochem Pharmacol*. 2017; 125: 75–83.

38. **Zappia KJ, O'Hara CL, Moehring F, et al.** Sensory neuron-specific deletion of TRPA1 results in mechanical cutaneous sensory deficits. *eNeuro*. 2017; 4: 1–14.

39. **Ranade SS, Syeda R, Patapoutian A.** Mechanically activated ion channels. *Neuron*. 2015; 87: 1162–79.

REVIEW

Molecular Basis of TRPA1 Regulation in Nociceptive Neurons. A Review

A. KÁDKOVÁ[1], V. SYNYTSYA[1,2], J. KRUSEK[1], L. ZÍMOVÁ[1], V. VLACHOVÁ[1]

[1]Department of Cellular Neurophysiology, Institute of Physiology of the Czech Academy of Sciences, Prague, Czech Republic, [2]Department of Physical and Macromolecular Chemistry, Faculty of Science, Charles University in Prague, Prague, Czech Republic

Summary

Transient receptor potential A1 (TRPA1) is an excitatory ion channel that functions as a cellular sensor, detecting a wide range of proalgesic agents such as environmental irritants and endogenous products of inflammation and oxidative stress. Topical application of TRPA1 agonists produces an acute nociceptive response through peripheral release of neuropeptides, purines and other transmitters from activated sensory nerve endings. This, in turn, further regulates TRPA1 activity downstream of G-protein and phospholipase C-coupled signaling cascades. Despite the important physiological relevance of such regulation leading to nociceptor sensitization and consequent pain hypersensitivity, the specific domains through which TRPA1 undergoes post-translational modifications that affect its activation properties are yet to be determined at a molecular level. This review aims at providing an account of our current knowledge on molecular basis of regulation by neuronal inflammatory signaling pathways that converge on the TRPA1 channel protein and through modification of its specific residues influence the extent to which this channel may contribute to pain.

Corresponding authors

A. Kádková and V. Vlachová, Department of Cellular Neurophysiology, Institute of Physiology AS CR, Videnska 1083, 142 20 Prague 4, Czech Republic. Fax. 420-29644-2488. E-mail: Anna.Kadkova@fgu.cas.cz or Viktorie.Vlachova@fgu.cas.cz

Introduction

The Transient Receptor Potential Ankyrin 1 (TRPA1) channel, originally called ANKTM1 (Story *et al.* 2003), is an ion channel dominantly expressed in a subset of nociceptive somatosensory neurons where it acts as a polymodal sensor for diverse physical and chemical stimuli of extracellular or intracellular origin. This channel is characterized by a marked activating agent promiscuity towards painful or potentially harming stimuli, including natural and exogenous electrophilic compounds, ultraviolet radiation, oxygen, extreme temperatures, chemical irritants and endogenous inflammatory mediators (Nilius *et al.* 2011, Nilius *et al.* 2012, Laursen *et al.* 2014, Zygmunt and Hogestatt 2014, Chen and Hackos 2015, Viana 2016). Studies using TRPA1 knock-out mice and specific antagonists have linked the function of TRPA1 to the regulation of temperature perception, inflammation, mechanosensation, pain, itching, but also the homeostatic balance between the nociceptive and the immune system (Bandell *et al.* 2004, Kwan *et al.* 2006, Viana 2016). In peptidergic nociceptors, TRPA1 is extensively co-expressed with the structurally related vanilloid receptor subtype 1 channel TRPV1. These two channels functionally interact and share multiple and overlapping signaling pathways that lead to their post-translational modifications regulating their activity and thus the nociceptor excitability (Story *et al.* 2003, Bandell *et al.* 2004, Jordt *et al.* 2004, Staruschenko *et al.* 2010). A clear demonstration of functional interaction between TRPV1 and TRPA1 in the bradykinin signaling pathways was first

shown in 2006 when the TRPA1-deficient mice were generated (Bautista *et al.* 2006). The authors demonstrated that the magnitude of bradykinin-evoked responses in trigeminal neurons from control mice correlated with the size of TRPA1-mediated responses induced by the selective agonist allyl isothiocyanate but not with those induced by the specific TRPV1 agonist capsaicin. The bradykinin-evoked responses were significantly attenuated and the correlation was completely lost in both TRPA1- and TRPV1-deficient neurons.

The activation of TRPA1 at nerve terminals results in membrane depolarization mainly due to Na^+ influx and induces a local calcium influx through the channel which further releases neuropeptides such as calcitonin gene-related peptide (CGRP), substance P, or neurokinin A from large dense-core vesicles *via* Ca^{2+}-dependent exocytosis (Gustavsson *et al.* 2012). The presence of neuropeptides causes a further amplification of nociception, recruitment of immune cells, vasodilatation and neurogenic inflammation (Geppetti *et al.* 2008). Accordingly, TRPA1 has been functionally linked to a number of chronic pain conditions associated with inflammation, including visceral pain, arthritic pain, cancer pain, and migraine. It is generally assumed that proinflammatory agents released at the site of injury, such as prostaglandins, bradykinin, serotonin and extracellular proteases, modulate TRPA1 *via* G-protein-coupled receptors and phospholipase C-coupled signaling cascades (Fig. 1). These mediators can directly activate TRPA1 (Taylor-Clark *et al.* 2008) or stimulate protein kinase A (PKA), protein kinase C (PKC), and phospholipase C (PLC) pathways to induce phosphorylation of TRPA1 (Dai *et al.* 2007, Wang *et al.* 2008a, Andrade *et al.* 2012, Petho and Reeh 2012). Phosphorylation, in turn, significantly affects the activation threshold of TRPA1, rendering nociceptors more sensitive to noxious stimulation. The putative roles of the PKA- and PLC-dependent signaling pathways in TRPA1-mediated nociception have recently been very well reviewed by previous authors (Andrade *et al.* 2012, Nilius *et al.* 2012, Bautista *et al.* 2013, Zygmunt and Hogestatt 2014, Viana 2016). Despite the presumed physiological importance of TRPA1 post-translational modifications, little is known about the specific domains and residues through which the TRPA1 protein undergoes conformational changes that affect the activation properties of this channel (Voolstra and Huber 2014). This review aims at providing an overview of the currently available results of site-directed mutagenesis studies on TRPA1 and summarizes the data on the functionally important amino acids which are involved in TRPA1 activation and may represent the residues through which this channel is regulated by phosphorylation or other post-translational modifications.
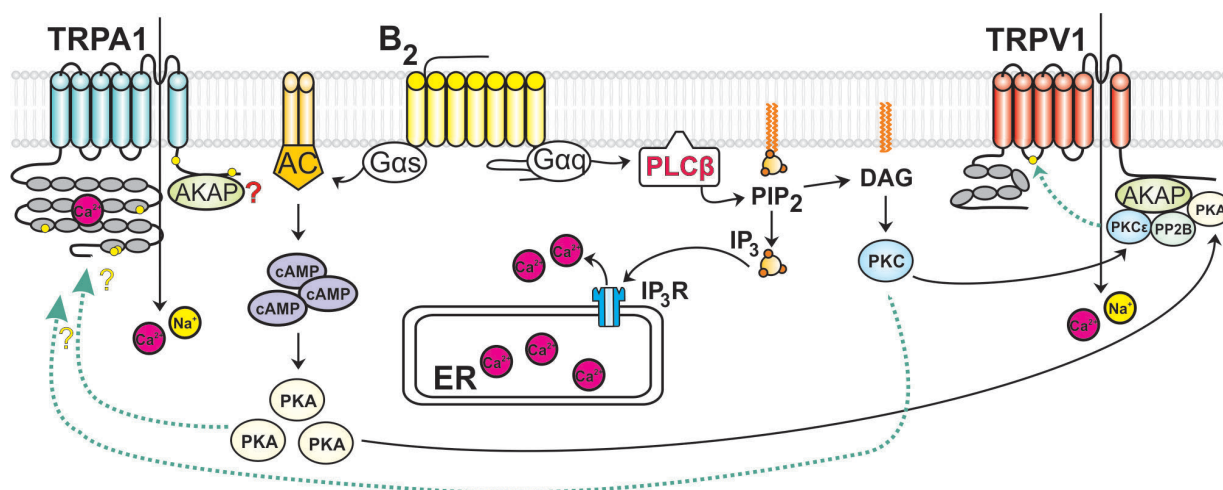

Fig. 1. Different but interconnected signaling pathways contribute to the sensitization of TRPA1 (adapted from Andrade *et al.* 2012). The binding of an agonist to the bradykinin receptor 2 (B₂) triggers phospholipase Cβ (PLCβ) through Gαq protein. PLCβ cleaves phosphatidylinositol-4,5-bisphosphate (PIP₂) into diacylglycerol (DAG) and inositol triphosphate (IP₃). Ca^{2+} release from the endoplasmic reticulum (ER) induced by binding of IP₃ to the inositol triphosphate receptor (IP₃R) probably directly sensitizes TRPA1. The activation of protein kinase Cε (PKCε) by DAG results into the binding of the kinase to the anchoring protein AKAP79/150 (AKAP) bound to the C-terminus of TRPV1 and into phosphorylation of TRPV1 which, in turn, sensitizes this channel to an agonist, promoting Ca^{2+} influx. AKAP79/150 binds also to TRPA1 (Zhang *et al.* 2008). The B₂ receptor can also stimulate the Gαs protein that activates the synthesis of cyclic adenosine monophosphate (cAMP) by adenylate cyclase (AC). The activation of protein kinase A (PKA) by cAMP or the activation of protein kinase C (PKC) by DAG sensitizes TRPA1 (putative phosphorylatable serine/threonine residues are indicated as yellow circles). In addition, PKA can also bind to the AKAP79/150 protein on TRPV1 together with PKCε and the phosphatase calcineurin (PP2B) to either phosphorylate or dephosphorylate the receptor at serine S502, depicted as a yellow circle.

Structural characteristics of TRPA1

All TRP channels share a similar general topology consisting of four pore-forming subunits, each of which contains six transmembrane segments (S1-S6) comprised of a sensor module S1-S4 and an ion conduction pore-forming region S5-S6. Both amino- and carboxyl-terminal domains are located cytoplasmically (Owsianik *et al.* 2006). Among mammalian TRP channels, TRPA1 is unique in bearing an extensive cytoplasmic amino terminus (720 of 1119 amino acids), comprised of a prominent ankyrin repeat domain (ARD; amino acids 1-639) and a linker (amino acids 640-720) consisting of a β-hairpin loop followed by two α-helices and the pre-S1 helix that connects ARD with the first transmembrane segment (Cvetkov *et al.* 2011, Brewster and Gaudet 2015, Paulsen *et al.* 2015). The proximal C-terminus is divided into a TRP-like domain, a putative β-sheet and a long coiled-coil. Atomic resolution structures of the distal cytoplasmic termini have not been resolved yet. Recent advances in electron cryo-microscopy allowed determining the first atomic-level structure of human TRPA1 captured in a closed-pore conformation (Paulsen *et al.* 2015). Also recently, a unified model of gating mechanism based on a comparative sequence analysis of the transmembrane regions from almost three thousand different TRP proteins has been proposed (Palovcak *et al.* 2015). Combined with the known structures of three related channels, TRPV1, TRPV2 and TRPV6 in open, closed or desensitized states, these findings offer new approaches to the further understanding of the TRPA1 channel and the general principles of TRP channel functioning (Cao *et al.* 2013, Liao *et al.* 2013, Gao *et al.* 2016, Huynh *et al.* 2016, Saotome *et al.* 2016, Zubcevic *et al.* 2016). These new structures enable precise molecular modelling of different activation states of TRPA1 and allow to overlay the available information obtained from point mutagenesis experiments on an accurate spatial model (Brewster and Gaudet 2015).

Activation, potentiation and inactivation of TRPA1

TRPA1 constitutes a target for a range of pungent and irritating chemical substances of endogenous origin (reviewed in Laursen *et al.* 2014, Zygmunt and Hogestatt 2014). Algogenic and pro-inflammatory agents, such as prostaglandins, bradykinin, histamine, and trypsin, acting on G protein-coupled receptors, stimulate the production of intracellular mediators that directly or indirectly activate TRPA1. Oxygen, reactive oxygen species and reactive nitrogen species directly activate TRPA1. Molecular mechanism underlying O_2-sensing involves prolyl hydroxylation of conserved proline P394 within the N-terminal ankyrin repeat 10 and oxidation of cysteines C633 and/or C856 (Miyamoto *et al.* 2009, Takahashi *et al.* 2011).

The origin of the exogenous chemicals activating TRPA1 is either natural, or synthetic. Pungent compounds from cinnamon (cinnamaldehyde), horseradish and wasabi (allyl isothiocyanate) or garlic (allicin) belong to the first aforementioned group, whereas some synthetic drugs (general anesthetics isoflurane or propofol) and acrolein, an irritant in tear gas and vehicle exhaust fumes, are only a few examples from the second group (recent comprehensive reviews – Nilius *et al.* 2012, Zygmunt and Hogestatt 2014, Viana 2016). From chemical point of view, modulators of TRPA1 can be both electrophilic and non-electrophilic compounds. The electrophilic activators bind covalently to reactive cysteines C621, C641, C665 within the N-terminus of TRPA1. Of these, the most important is cysteine C621 that possesses an exceptionally high reactivity imparted by the neighboring lysine residue K620 (Bahia *et al.* 2016). The variability of TRPA1 covalent agonists is enormous and the reactions include nitrosylation (nitric oxide), sulfhydration (sulfane), forming of a disulphide bond (hydrogen peroxide) and alkylation. The electrophiles alkylate TRPA1 by the mechanism known as the Michael addition. The unsaturated bond of α,β-unsaturated aldehydes such as acrolein, cinnamaldehyde or allyl isothiocyanate is attacked by a nucleophilic mercapto-group of a cysteine or an amino group of a lysine (Hinman *et al.* 2006, Macpherson *et al.* 2007).

Probably the most important physiological activators and modulators of TRPA1 are calcium ions, which enter through the channel or are released from internal stores and, depending on the activation state, dynamically control the critical properties of the channel (Story *et al.* 2003, Nagata *et al.* 2005, Wang *et al.* 2008b, Nilius *et al.* 2011). Although TRPA1 is often referred to as nonselective cation channel, its favoring of calcium is noticeable. Its selectivity for mono- and divalent cations is determined by a selectivity filter formed by the sequence glycine-aspartate-isoleucine (^{914}GDI^{916}), located in the loop between the two pore helices (Wang *et al.*

2008b). Combined patch-clamp and Fura-2 fluorescence measurements revealed that the fraction of TRPA1 inward current that is carried by Ca^{2+} is much higher than in the case of a non-selective channel (Karashima *et al.* 2010). This phenomenon probably arises from a partial block (~35 %) of the monovalent cation current caused by binding of Ca^{2+} in the lumen of the pore. The intracellular Ca^{2+} influences the most important properties of the channel: conductance, ion selectivity and opening probability (Cavanaugh *et al.* 2008, Karashima *et al.* 2010, Nilius *et al.* 2011). Moreover, the increase of the TRPA1 surface expression level, which can be induced by an agonist exposure, is not observed in Ca^{2+}-free solution suggesting the role of calcium ions in TRPA1 membrane trafficking (Schmidt *et al.* 2009). The agonist- and voltage-induced TRPA1 currents are strongly amplified by the intracellular Ca^{2+}. The potentiation of TRPA1 currents is followed by an inactivation (desensitization), which is almost complete and irreversible and both these processes can be accelerated by the increasing concentration of Ca^{2+}. The potentiation and the inactivation are independent processes. The elevation of intracellular Ca^{2+} causes the TRPA1 potentiation, whereas the extracellular Ca^{2+} are required for the inactivation (Wang *et al.* 2008b). However, the exact molecular mechanisms of these processes have not yet been fully understood. The negatively charged residues within a loop between the N-terminal ankyrin repeats 12 and 13 have been thought to be a Ca^{2+}-binding site in TRPA1. However, the role of this so-called EF-hand in both Ca^{2+}-dependent potentiation and inactivation has been disputed by several studies (Wang *et al.* 2008b, Sura *et al.* 2012). Thus, further studies are needed to find other calcium-binding sites within the TRPA1 protein. TRPA1 is activated by intracellular Ca^{2+} ions at micromolar concentrations and the activation mechanism does not depend on calmodulin or other Ca^{2+}-binding proteins, neither it depends on the interaction of TRPA1 with phosphatidylinositol 4,5-bisphosphate (PIP_2) (Doerner *et al.* 2007, Zurborg *et al.* 2007). Although several studies supported the role of PIP_2 in TRPA1 modulation (Rohacs 2009), the newly developed methods for PIP_2 level manipulation indicate that agonist responses of TRPA1 are probably not significantly influenced by changes in PIP_2 levels (Wang *et al.* 2008b, Nilius *et al.* 2011).

Putative phosphorylation pathways involved in TRPA1-mediated bradykinin-induced nociception

Bradykinin is one of the most potent pronociceptive mediators produced under inflammation. Two types of G protein-coupled receptors (GPCR) for bradykinin have been characterized in nociceptive neurons, B_1 and B_2, both signaling through $G_{q/11}$ (in Fig. 1 shown as Gαq subunit) to increase intracellular concentrations of calcium (Petho and Reeh 2012). While B_2 is widely expressed in many tissues including the nervous system, B_1 protein expression is rapidly increased under tissue injury or inflammation (Chen and Johnson 2007). Stimulation of B_1 or B_2 by bradykinin can initiate either the phospholipase C (PLC) pathway or activation of adenylate cyclase (AC) to produce cyclic adenosine monophosphate (cAMP), which further activates protein kinase A (PKA) (Fig. 1). After the PLC pathway is initiated, PLC breaks down PIP_2 into diacylglycerol (DAG) and inositol triphosphate (IP_3). Diacylglycerol either activates protein kinase C (PKC) or it can be converted into polyunsaturated fatty acids, such as arachidonic acid, by DAG lipase. IP_3, in turn, induces release of calcium ions from the intracellular stores in endoplasmic reticulum (Bandell *et al.* 2004, Mizumura *et al.* 2009, Andrade *et al.* 2012). The influx of extracellular calcium ions together with Ca^{2+} released from intracellular stores directly activate TRPA1 (Doerner *et al.* 2007, Zurborg *et al.* 2007).

In nociceptive neurons, the regulation of TRPV1 by protein kinases PKA and PKC and the phosphatase calcineurin strongly depends on an interaction with the A kinase anchoring protein AKAP79/150, which enables the formation of a signaling complex between these enzymes and TRPV1 and thus a dynamic modulation of the channel (balancing phosphorylation and dephosphorylation). In addition, binding of AKAP79/150 is necessary for membrane trafficking of TRPV1 (Zhang *et al.* 2008). A similar mechanism of sensitization by protein kinases can be predicted also in TRPA1 as the interaction between AKAP79/150 and TRPA1 has been confirmed by co-immunoprecipitation experiments (Zhang *et al.* 2008). The primary sequence of human TRPA1 clearly predicts several phosphorylation sites for PKA kinase (Table 1) and potentiation of agonist-induced responses by bradykinin can be inhibited by PKA and PLC inhibitors or mimicked by PLC or PKA activators (Wang *et al.* 2008a). Several putative

PKC phosphorylation sites are predicted from the primary sequence of TRPA1, though their functional roles have not been systematically studied. From published experiments in which the PLC or PKA activators and inhibitors were used by several authors, it is not always clear whether the effects on TRPA1 reflect phosphorylation because calcium ions were usually present in extracellular solution and their direct effect cannot be excluded. In addition, TRPA1-mediated responses gradually increase during prolonged application of agonist and this intrinsic sensitization precludes from clearly differentiating the effects of kinase modulators (Meents *et al.* 2016). The situation is further complicated by the fact that the choice of the expression system for TRPA1 has been shown to be critical as the channel is constitutively activated at physiological membrane potentials, leading to a massive increase in cellular Ca^{2+} (Karashima *et al.* 2008).

Figure 2 shows how heterologous expression of TRPA1 in a neuronal cell line may influence cellular responses to membrane depolarization. To illustrate this point, for the purpose of this review, we measured responses from cells that are derived from rat dorsal root ganglion neurons F11 as *in vitro* model of native peripheral sensory neurons (Francel *et al.* 1987). This cell line lacks TRPA1 and exhibits a specific combination of action potential properties and cell markers, including those for nociceptive sensory neurons (Vetter and Lewis 2010, Yin *et al.* 2016): the F11 cells endogenously express voltage gated K^+ and Na^+ channels (particularly $K_V11.1$, $Na_V1.6$ and $Na_V1.7$), and many other ion channels and receptors with recognized roles in nociception. We used whole-cell patch clamp technique exactly as described in (Hynkova *et al.* 2016). The cells repeatedly stimulated with depolarizing pulses from -60 mV to +60 mV exhibited inward currents, which are typical for voltage-gated Na^+ channels (Fig. 2A). Then, we transiently expressed TRPA1 in F11 cells using a standard transfection method as we previously described in (Sura *et al.* 2012) and (Hynkova *et al.* 2016). In contrast to naïve cells, when TRPA1 were relatively more expressed in F11, the voltage-gated Na^+ currents were fully dampened (Fig. 2B, C). Thus, the activation of TRPA1 by depolarization, or its presence itself, affects cellular excitability to a large extent.
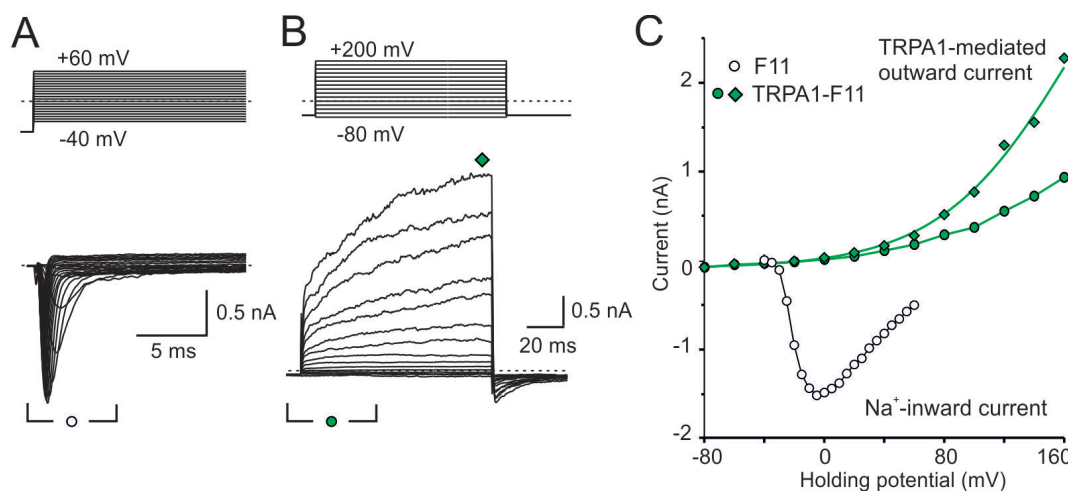

Fig. 2. Transfection of F11 cells with TRPA1 produces large outward currents upon depolarizing steps and reduces inward currents at negative membrane potentials. (**A**), Untransfected F11 cells displayed characteristic voltage-gated sodium channels in depolarizing step recordings (depolarizing pulses from -40 mV to +60 mV, voltage step protocol indicated above). (**B**) TRPA1 transfected cells stimulated by depolarizing pulses from -80 mV to +200 mV (voltage step protocol indicated above). The voltage-gated Na^+ currents were fully dampened. (**C**) Current-voltage relationship constructed from A and B at the times indicated by symbols: naïve F11, inward currents (open circle), TRPA1-expressing F11, inward currents (green circle), outward currents (green diamond). Whole-cell membrane currents were recorded using the extracellular bath solution containing 160 mM NaCl, 2.5 mM KCl, 1 mM $CaCl_2$, 2 mM $MgCl_2$, 10 mM HEPES, 10 mM glucose, pH 7.3, 320 mOsm. The whole-cell pipette solution contained 145 mM CsCl, 5 mM EGTA, 3 mM $CaCl_2$, 10 mM HEPES, 2 mM MgATP, pH 7.3, 290 mOsm. Methods of transfection and recording were as described in (Hynkova *et al.* 2016).

Recently, a comprehensive pharmacological and transcriptomic studies performed on immortalized cell lines derived from dorsal root ganglion neurons demonstrated that F11 cells highly express bradykinin B_2 receptor and exhibit robust responses to subnanomolar concentrations of bradykinin (Vetter and Lewis 2010, Yin *et al.* 2016). These findings prompted us to explore whether the known proalgesic effects of bradykinin could

involve a direct regulation of TRPA1 under *ex vivo* conditions. We used calcium imaging technique as described previously by us in (Marsakova *et al.* 2012) and measured responses from F11 cells. In our hands, bradykinin at a concentration of 10 nM elicited large Ca^{2+} transients in all naïve F11 cells (Fig. 3A), similarly as previously described by Vetter and Lewis (2010). The amplitude of the second response to bradykinin applied 3 min later was substantially lower than the initial response. Next, we co-transfected F11 cells with cDNA encoding human TRPA1 together with green fluorescent protein (GFP) and measured intracellular Ca^{2+} responses to addition of 10 nM bradykinin. As shown in Figures 3B, C and D, TRPA1-expressing cells exhibited increased basal calcium levels likely due to constitutively opened TRPA1 channels (Karashima *et al.* 2008). The cells responded to bradykinin in a very similar manner as GFP-negative cells, indicating no sensitizing effects on TRPA1. Only occasionally, we observed spontaneous calcium transients in TRPA1-expressing cells. When bradykinin was applied to cells pre-activated by allyl-isothiocyanate (Fig. 3D), the Ca^{2+} responses were only transient and at least in part additive, indicating that, most likely, TRPA1 channels do not undergo long-term modulation caused by bradykinin-triggered phosphorylation.
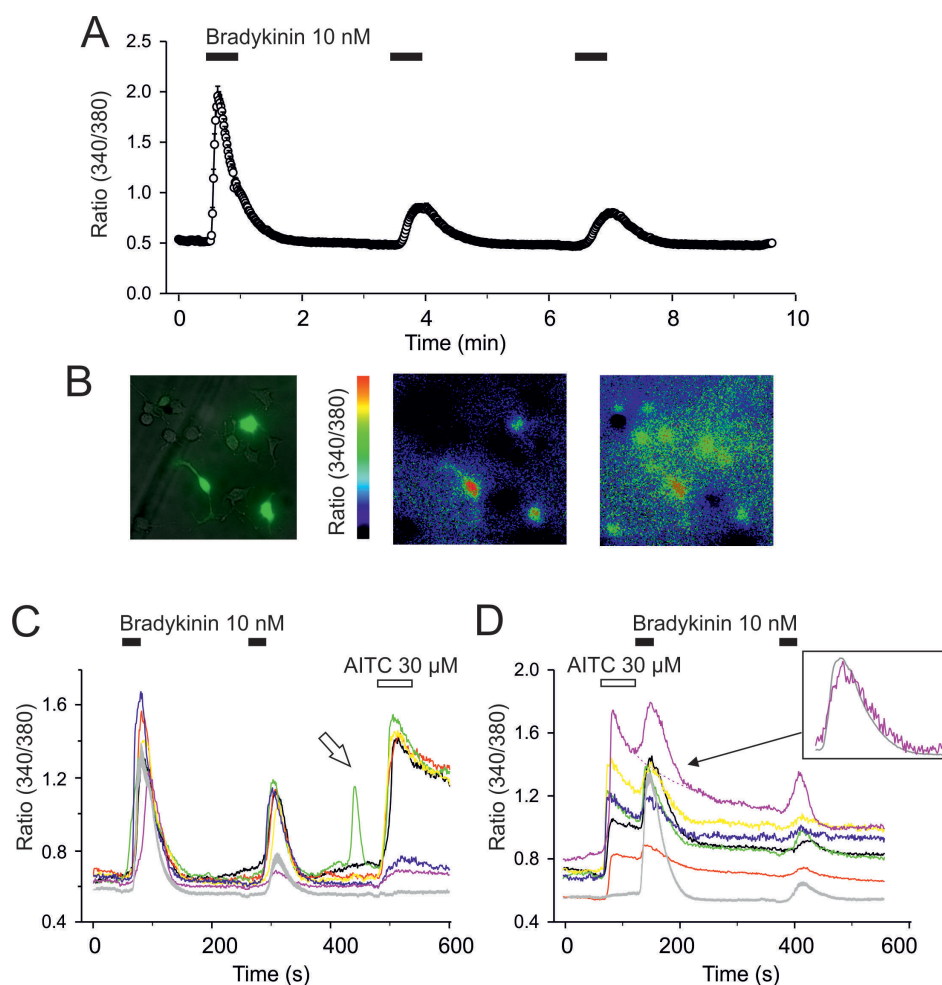

Fig. 3. Calcium imaging experiments in F11 cells. (**A**) Changes in the Fura-2 ratio measured in naïve F11 cells exposed to 3 subsequent applications of 10 nM bradykinin. Data are represented as mean ± SEM of n=85 cells and are representative of 5 independent experiments. (**B**) GFP-fluorescence marks the cells expressing TRPA1 (left). Pseudocolored images of the 340/380 nm Fura-2 ratio show cells captured at the peak of AITC-induced (middle) and at the peak of bradykinin-induced transients (right), as shown in D. (**C**) Bradykinin induced large calcium transients but did not affect TRPA1 channels. Representative traces for individual TRPA1-expressing cells are shown in color, the average calcium response of F11 cells unresponsive to allyl isothiocyanate (AITC, 30 µM) is shown as a gray line surrounded by the gray area representing SEM (n=14). The white arrow denotes spontaneous calcium transient. (**D**) Expression of TRPA1 did not affect the magnitude or duration of the Ca^{2+} response to bradykinin compared to F11 control cells. The average calcium response for F11 cells unresponsive to AITC (30 µM) is shown as a gray line surrounded by the gray area representing SEM (n=19). The inset shows the averaged response from cells unresponsive to AITC (gray line) and the response obtained by digital subtraction of the AITC response interpolated by exponential fitting over the interval 120-210 s (purple dashed line) from the original AITC trace (purple solid line). It is apparent that normalized responses overlap in time.
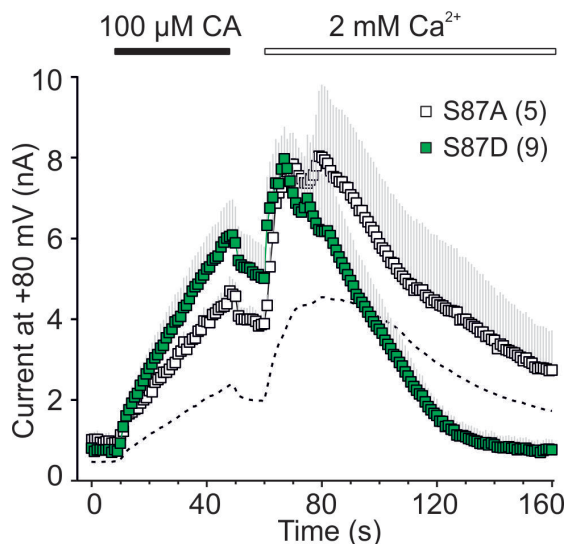
Fig. 4. Phospho-mimicking and phospho-null substitutions at serine S87. Time course of average whole-cell currents through the wild-type human TRPA1 (dashed line, n=70) and the S87A (n=5) and S87D (n=9) mutants measured at +80 mV. The average currents are shown with gray bars indicating SEM. The number of cells is given in parentheses. Whole-cell membrane currents were measured first in the absence of extracellular Ca^{2+} and in the presence of the partial agonist cinnamaldehyde (CA, 100 μM for 40 s). CA was then washed out for 10 s and Ca^{2+} at a concentration of 2 mM was added to the extracellular solution. The membrane potential was ramped up each second from -80 mV to +80 mV (1 V/s; data are shown only at +80 mV). Intracellular Ca^{2+} was buffered to low levels with 5 mM EGTA in the patch pipette to assess the effects of permeating calcium ions. The application of 100 μM CA and subsequent addition of 2 mM Ca^{2+} are indicated above. The experimental methods and solutions used for whole-cell recordings are described in detail in Hynkova *et al.* (2016).

Although further experiments are necessary to fully understand the mechanisms, the apparent conclusion from these illustrative examples is that the over-expression of TRPA1 may lead to an increase in cellular Ca^{2+}, which ultimately activates the intracellular pathways enormously and makes their specific regulation more difficult. So what are the implications of these findings in relation to the potential phosphorylation targets on TRPA1 for kinases activated by inflammatory mediators? General and kinase-specific phosphorylation site predictions point to a number of serine and threonine residues within the primary sequence of human TRPA1 (Table 1). To decisively identify these sites would require an in-depth, systematic examination of a number of mutants in which individual serines, threonines or tyrosines are replaced either by a nonphosphorylatable residue (alanine or phenylalanine) or by an acidic residue mimicking phosphorylation (aspartate or glutamate). While this approach can provide information on putative role of the predicted sites, it also has several

limitations that must be taken into account when interpreting the data. An example of an electrophysiological experiment, in which mutations at one of the predicted phosphorylation sites for PKA lead to a dramatic increase in TRPA1-mediated responses to cinnamaldehyde, is shown in Figure 4. Our unpublished electrophysiological results (Hynkova *et al.*) indicate that this increase in responsiveness was observed for both the alanine (open squares) and the aspartate (green squares) mutants. One may speculate that phosphorylation at serine S87 influences the functioning or targeting of TRPA1, however, a nonphosphorylatable residue at this position increased the responses as well. By considering that S87 is located at the beginning of the finger loop of predicted N-terminal ankyrin repeat 1, it is tempting to conclude that the effects we observe result from structural changes in this region. Another explanation, similarly plausible and not mutually exclusive, is that mutations at S87 influence immediately preceding serine S86 that is also predicted to be a phosphorylation site (Table 1).

Cyclin-dependent kinase 5-mediated phosphorylation of TRPA1

Cyclin-dependent kinase 5 (Cdk5), a serine/threonine kinase, is predominantly expressed in neuronal tissues and plays an important role in inflammation-induced pain signaling (Pareek and Kulkarni 2006, Pareek *et al.* 2007, Utreras *et al.* 2009). It is involved in several cellular processes such as regulation of neuronal migration, axon guidance, synaptic structure and plasticity or membrane transport (Dhavan and Tsai 2001). Cdk5 belongs to a large group of cyclin-dependent kinases, however, it is neither activated by cyclins, nor does it participate in the cell cycle progression. Instead, association of Cdk5 with myristoylated p35 (or its splice variant p25) and/or p39 cofactors is required for activation of the kinase. As the p35 is a membrane-bound protein, physiological substrates of Cdk5 are likely to be transmembrane or membrane-associated proteins. Cdk5 is a proline-directed kinase that phosphorylates serine or threonine residues immediately preceding a proline residue. Its consensus motif is (S/T)PX(K/H/R), where S and T are the phosphorylatable serine or threonine, P is a proline residue in the +1 position, and X is any amino acid (Songyang *et al.* 1996).

Table 1. Predictions for putative phosphorylation sites in human TRPA1.

S/T	PKA			PKC			CDK5			Src		
	NetPhos	Scan-Site	GPS	NetPhos	Scan-Site	GPS	NetPhos	Scan-Site	GPS	NetPhos	Scan-Site	GPS
S4	-	-	-	0.8	-	13	-	-	-	-	-	-
Y22	-	-	-	-	-	-	-	-	-	0.542	0.553	9.8
S35	-	0.724	-	0.612	0.447	11.034	-	-	-	-	-	-
S86	0.773	0.711	3.893	-	-	-	-	-	-	-	-	-
S87	0.559	0.562	3.714	-	0.493	5.455	-	-	-	-	-	-
Y97	-	-	-	-	-	-	-	-	-	0.481	-	5.75
T100	-	-	-	-	-	-	0.424	0.571	14.6	-	-	-
T241	-	-	5.333	-	-	-	0.376	0.578	13.7	-	-	-
T274	0.517	0.676	4.018	-	-	-	-	-	-	-	-	-
S317	0.781	0.458	4.429	-	-	-	-	-	-	-	-	-
S344	-	-	-	-	-	-	0.535	0.672	11.6	-	-	-
T415	-	-	-	-	-	-	0.405	0.571	22.3	-	-	-
S438	-	-	-	-	0.472	4.059	-	-	-	-	-	-
S443	-	-	-	0.793	-	7.424	-	-	-	-	-	-
S448	-	0.673	6.333	-	-	-	0.465	0.433	18.2	-	-	-
T484	-	-	-	-	-	-	0.518	0.543	20.1	-	-	-
T598	-	-	-	0.824	0.537	-	-	-	-	-	-	-
S616	-	-	-	-	-	-	0.471	0.546	9.3	-	-	-
T673	-	0.617	4.667	-	-	-	0.478	0.616	11	-	-	-
Y680	-	-	-	-	-	-	-	-	-	0.461	0.533	12.813
S972	0.27	0.657	4.043	0.71	0.498	9.96	-	-	-	-	-	-
S1012	0.627	0.72	-	-	-	-	-	-	-	-	-	-
T1055	-	0.623	1.037	-	-	-	-	-	-	-	-	-
S1101	0.751	0.737	4.607	-	-	-	-	-	-	-	-	-
T1105	0.234	0.599	-	0.672	-	10.813	-	-	-	-	-	-
T1114	-	-	-	0.537	-	11.672	-	-	-	-	-	-

Comparisons of the score values for the predicted residues obtained from three prediction servers NetPhosK2.0: http://www.cbs.dtu.dk/services/NetPhos/, ScanSite3: http://scansite3.mit.edu/, and GPS: http://gps.biocuckoo.org/. Phosphorylation sites predicted unanimously are highlighted by yellow.

The co-expression of TRPA1 with the p35 alone or with Cdk5 and p35 in HEK 293T cells significantly increased the cinnamaldehyde-evoked responses of human TRPA1 (Hynkova *et al.* 2016), indicating that TRPA1 may be a substrate for the Cdk5/p35 complex and/or its interaction with p35 may stabilize the activated state of the channel (Fig. 5A). As candidate residues for phosphorylation by Cdk5 in TRPA1, the N-terminal threonines T100, T241, T415, T484 and serine S448, which are located in highly conserved T/SPLH ankyrin motifs, were predicted in our recent study (Hynkova *et al.* 2016) at a high stringency level (Table 1). The N-terminal part of TRPA1, constituting more than a half

of the protein size, encompasses a tandem array of 17 ankyrin repeats (AR1-AR17) that have been described as an integrator of various activation stimuli: electrophilic agents, cold or calcium ions (Hinman *et al.* 2006, Macpherson *et al.* 2007, Zurborg *et al.* 2007, Jabba *et al.* 2014). The ankyrin repeat is a common structural motif, typically of 33 amino acid residues, which forms an anti-parallel helix-turn-helix structure followed by a β-hairpin loop. Five of seventeen ARs of human TRPA1 contain a tetrapeptide motif T/SPLH, which is highly conserved among ankyrin proteins. In such a motif, proline initiates the first α-helix, whereas the pair of threonine and histidine forms intra- and inter-repeat

bonds thus contributing to local conformational stability of the AR (Li *et al.* 2006, Gaudet 2008, Guo *et al.* 2010). The neighboring ankyrin repeats tend to stack together and form elongated domains, which are important for protein-protein interactions (Corey *et al.* 2004, Sotomayor *et al.* 2005) and can serve as the binding sites for non-protein ligands such as adenosine triphosphate (Lishko *et al.* 2007).

Based on the consensus sequence, the N-terminal tetrapeptide T/SPLH motifs in TRPA1 can serve as putative phosphorylation sites TRPA1 for proline-targeted Ser/Thr kinases such as Cdk5. On the other hand, even subtle structural changes introduced by mutations at ankyrin repeat consensus residues can profoundly impact the structure or result in an unstable protein (Gaudet 2008). Indeed, recently the site-directed mutagenesis and patch clamp experiments suggested that the examined serine and threonine residues within these T/SPLH motifs are not likely to be involved in phosphorylation because the phosphonull alanine mutations and phosphorylation mimicking aspartate mutations did not lead to opposite changes in the channel functioning. It has been previously shown that a 58-AA peptide (C421-D479) containing S448 was phosphorylated by Cdk5 *in vitro* (Sulak 2011). However, the phospho-mimicking aspartate mutation of this serine residue in the TRPA1 channel resulted in a non-functional phenotype (Hynkova *et al.* 2016).

Further sequence prediction analysis of the TRPA1 N-terminus revealed additional three putative phosphorylation sites for Cdk5: serine and threonine residues S344, S616, and T673. Among these, only the T673D mutation resulted in channels whose responses to the agonist cinnamaldehyde were increased almost threefold compared with wild-type (Fig. 5B). According to the TRPA1 structure, threonine T673 is solvent-accessible and located in a flexible loop connecting the β-strands to the helix-turn-helix motif preceding the pre-S1 helix, indicating that it may represent a candidate target for Ser/Thr phosphorylation.

In sensory neurons expressing TRPV1, increased activity of Cdk5 is associated with elevated levels of phosphorylated threonine T407 at TRPV1, increased surface distribution and TRPV1-mediated Ca^{2+} influx (Liu *et al.* 2015, Rozas *et al.* 2016). Although two threonine and one serine residues in the primary sequence of TRPV1 correspond to the consensus, only the threonine T407 is a target residue for Cdk5 (Pareek *et al.* 2007). The co-expression of Cdk5 and p35 with TRPV1
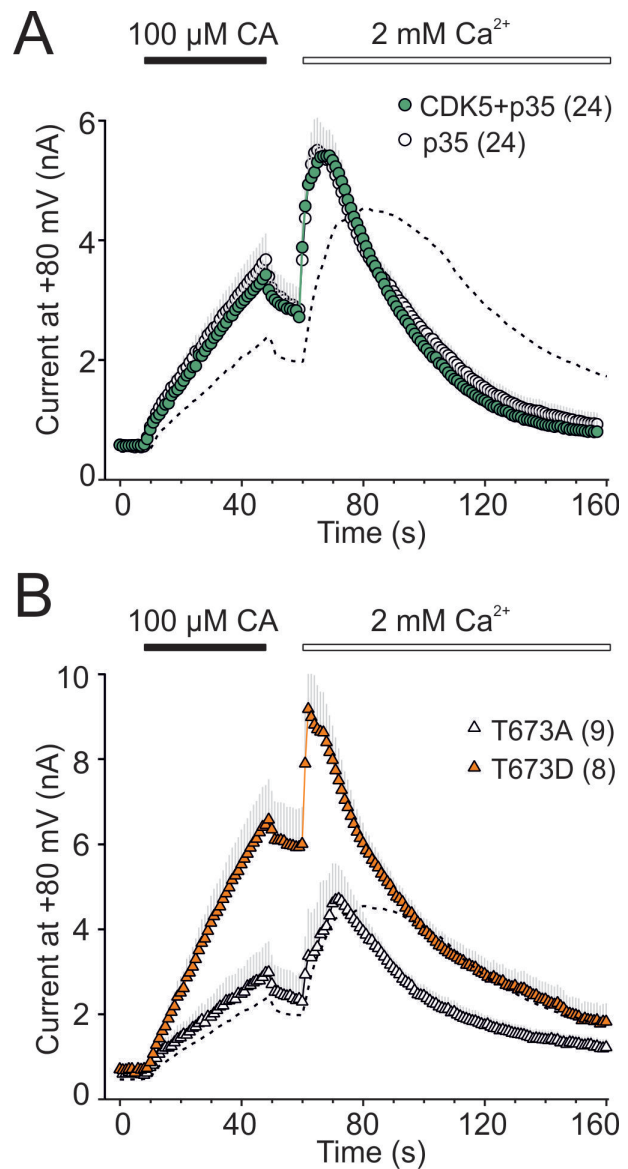

Fig. 5. Threonine T673 as a putative phosphorylation site for Cdk5. (**A**) Co-expression of TRPA1 with Cdk5 kinase and p35, a Cdk5-specific activator, significantly increased TRPA1-mediated responses to cinnamaldehyde (CA), indicating that TRPA1 may be a substrate for the CDK5/p35 complex and/or its interaction with p35 may stabilize the activated state. Whole-cell recordings were obtained using the same protocol as in Figure 4. The number of cells is given in parentheses. (**B**) The T673D mutation resulted in channels whose responses to cinnamaldehyde were increased almost threefold, whereas the mutant T673A channels remained largely unchanged. Threonine T673 is solvent-accessible and located in a flexible loop connecting the β-strands to the helix-turn-helix motif preceding the pre-S1 helix, i.e. well situated in a locus especially important for the detection, integration and transmission of activation stimuli (Paulsen *et al.* 2015). Thus, T673 may represent a candidate target for Ser/Thr phosphorylation by Cdk5 (adapted Fig. 7, panel C, and Fig. 8, panel B from Hynkova *et al.* 2016).

as well as the mutation of threonine T407 to aspartate had the same effect on the function of the channel – both reduced the TRPV1 Ca^{2+}-dependent desensitization

(Jendryke *et al.* 2016). TRPV1 and TRPA1 are expressed in partially overlapping subsets of nociceptive neurons and thus it is likely that both ion channels act in tandem as the important targets for Cdk5.

C-terminus of TRPA1 as a putative target for protein kinase CK2?

Protein kinase CK2, formerly known as casein kinase II, is a ubiquitous and highly conserved protein serine/threonine kinase whose activity is independent of cyclic nucleotides and calcium. It has been linked to a number of human disorders, including neuro-degenerative diseases and inflammatory response (Singh and Ramji 2008, Perez *et al.* 2011). CK2 is an acidophilic kinase, requiring an acidic residue (either aspartate or glutamate) three residues from the C-terminal of the phosphate acceptor site. In the consensus motif S/T–X–X–D/E, serine is favored over threonine; X can be any nonbasic amino acid. Additional acidic residues in positions +1, +2, +4, and +5 increase the phosphorylation rate and aspartate is preferred to glutamate (St-Denis *et al.* 2015). Within the C-terminal region of human TRPA1, there are two strong consensus phosphorylation motifs containing the serine S1076 and the threonine T1078 ([1071]KMEII**S**ETEDD[1081] and [1073]EIISE**T**EDDDS[1083]), both predicted to be targeted by casein kinase CK2 (NetPhorest Posterior probability of 0.6386 and 0.6261; (Sura *et al.* 2012). A similar acidic cluster has been reported to constitute a cytosolic sorting motif that, upon CK2 phosphorylation, controls the trafficking and surface expression of TRPA1-related TRPP2 and TRPV4 channels (Kottgen *et al.* 2005). In our recent study by Sura *et al.* (2012), we compared four constructs of human TRPA1 in which either serine or threonine were replaced by either alanine or aspartate to mimic the non-phosphorylated and phosphorylated forms of the protein, respectively. In this study, we showed that the aspartate mutation T1078D exhibited the gain of function phenotype. The alanine mutations S1076A and T1078A and the phosphorylation mimicking mutation S1076D resembled the wild-type phenotype which indicates that the functional changes caused by substitutions in this region are not likely to be caused by disturbed phosphorylation. Instead, we demonstrated that the highly conserved sequence [1077]ETEDDD[1082] may act as a binding site for calcium ions, similar as the Ca^{2+}-binding domain found in the Ca^{2+}-binding domain of the superfamily of BK channels (Sura *et al.* 2012).

Regulation of TRPA1 by Src tyrosine kinase

Nerve growth factor (NGF) regulates chronic inflammatory hyperalgesia by controlling gene expression in sensory neurons. NGF, acting on the receptor TrkA, initiates a signaling pathway in which phosphoinositide 3-kinase plays an essential early role. A downstream element of this signaling cascade is the tyrosine-protein Src kinase which binds to and phosphorylates proteins at tyrosine residues. One of the Src-kinase targets is TRPV1 in which phosphorylation at a single residue Y200 promotes trafficking of the receptor to the surface membrane (Zhang *et al.* 2005). In the presence of NGF, TRPA1 expression is also up-regulated (Obata *et al.* 2005, Diogenes *et al.* 2007); however, a direct evidence of Src kinase mediated phosphorylation of TRPA1 is still lacking. The apparent candidates are tyrosines Y22, Y97 and Y680, predicted with high stringency by a number of prediction servers (Table 1). Recently, TRPA1 has been shown to be regulated by a Src family tyrosine kinase inhibitor PP2 in the SH-SY5Y cell line (Morgan *et al.* 2014). The cells expressing TRPA1 gradually lost detectable response to agonist when cultured for more than 10-15 passages but the responses could be retrieved rapidly by short pre-treatment with PP2. The authors individually mutated several tyrosine residues with the aim to identify the putative tyrosine residues responsible for this effect (Y69C, Y97F, Y226F, and Y654F/Y655F). Of these, only Y69C was not affected by pre-treatment with PP2. Interestingly, the authors could not repeat this experiment in HEK293 cells because the PP2 inhibitor elicited large elevations in intracellular Ca^{2+}.

N-linked glycosylation of TRPA1

Among other TRP channels, TRPA1 has a distinctive structural feature: its outer pore domain contains two pore helices instead of the typical solitary one present in TRPV1, TRPV2, TRPV6 and in the TRP-related family of voltage-gated potassium (K_V) channels (Paulsen *et al.* 2015). Another apparent difference, related to the presumptive gating mechanism, resides in the existence of a short linker connecting S1 and S2. In TRPV1, the S1-S2 linker lies atop the S1-S4 bundle and is static (Cao *et al.* 2013). In TRPA1, this region extends into the extracellular space. A poorly resolved density map in this region suggests that the S1-S2 linker possesses intrinsic structural flexibility, and

thus may be actively involved in channel gating. Within this region, two putative glycosylation sites ([747]NSTG and [753]NETS) have been predicted (Jaquemar *et al.* 1999). Independent mutagenesis studies confirmed the structural importance of both asparagine residues. Despite the glycosylation of TRPA1 has not been identified in native cells yet, a population of "mature" FLAG-tagged human TRPA1 receptor expressed in HEK293 cells was recently described (Egan *et al.* 2016). These authors show that both of these predicted sites can be modified with an N-glycan and that the glycan at position N747 modulates agonist-sensitivity of TRPA1 *in vitro*. The authors showed that the agonist sensitivity of TRPA1 was significantly decreased in mutants N747Q and N747Q-N753Q but not in N753Q and the expression level of the double mutant was significantly lower. Moreover, the N747Q mutation influenced the efficiency of glycoprocessing of the N-glycan bound at N753. Another study showed that alanine mutations of these two asparagines are comparably sensitive to electrophiles AITC and 3,5-*di-tert*-butylphenol. The N753A mutant was much less sensitive to coal fly ash, the prototype particulate matter pollutant, indicating that this residue is involved in mechanical activation of TRPA1 (Deering-Rice *et al.* 2015).

In our laboratory, using GFP-tagged TRPA1 in HEK 293T cells, we failed to observe any glycosylation (Marsakova *et al.* 2017). The sensitivity to agonist was not different from control measurements in cells that were treated with tunicamycin that prevents N-glycosylation of proteins. The AITC responses through the N747T-N753T double mutant were much less rectified at negative membrane potentials whereas immunoblot analysis showed that this double mutant achieved in average only about 80 % of the total wild-type TRPA1 surface expression. The functional changes were thus attributed to structural changes in the S1-S2 loop that is crucial for proper expression.

Concluding remarks

Better knowledge of the structural mechanisms underlying phosphorylation and other post-translational modifications is an important prerequisite if one wishes to understand how the signaling pathways may contribute to changes in nociception during normal and pathological states. It has been recognized that the study of these processes is very challenging due to tissue specificity, thus the experiments in heterologous expression systems must be interpreted with caution. Nevertheless, there is a progress in the identification of various signaling pathways involved in the sensitization of the TRP channels by pro-inflammatory agents. At the same time, the unknown identity of specific sites underlying these processes signifies a gap in our understanding of how these channels are capable of transducing and modulating pain.

Author Note

During the review process, a study was published identifying four amino acid residues (S86, S317, S428, and S972) as the principal targets of PKA-mediated phosphorylation and sensitization of human TRPA1 (Meents *et al.* 2017). The findings confirm our predictions and may partly explain our data presented in Figure 4 of this review.

Conflict of Interest

There is no conflict of interest.

Acknowledgements

References

ANDRADE EL, MEOTTI FC, CALIXTO JB: TRPA1 antagonists as potential analgesic drugs. *Pharmacol Ther* **133**: 189-204, 2012.

BAHIA PK, PARKS TA, STANFORD KR, MITCHELL DA, VARMA S, STEVENS SM, JR, TAYLOR-CLARK TE: The exceptionally high reactivity of Cys 621 is critical for electrophilic activation of the sensory nerve ion channel TRPA1. *J Gen Physiol* **147**: 451-465, 2016.

BANDELL M, STORY GM, HWANG SW, VISWANATH V, EID SR, PETRUS MJ, EARLEY TJ, PATAPOUTIAN A: Noxious cold ion channel TRPA1 is activated by pungent compounds and bradykinin. *Neuron* **41**: 849-857, 2004.

BAUTISTA DM, JORDT SE, NIKAI T, TSURUDA PR, READ AJ, POBLETE J, YAMOAH EN, BASBAUM AI, JULIUS D: TRPA1 mediates the inflammatory actions of environmental irritants and proalgesic agents. *Cell* **124**: 1269-1282, 2006.

BAUTISTA DM, PELLEGRINO M, TSUNOZAKI M: TRPA1: A gatekeeper for inflammation. *Annu Rev Physiol* **75**: 181-200, 2013.

BREWSTER MS, GAUDET R: How the TRPA1 receptor transmits painful stimuli: Inner workings revealed by electron cryomicroscopy. *Bioessays* **37**: 1184-1192, 2015.

CAO E, LIAO M, CHENG Y, JULIUS D: TRPV1 structures in distinct conformations reveal activation mechanisms. *Nature* **504**: 113-118, 2013.

CAVANAUGH EJ, SIMKIN D, KIM D: Activation of transient receptor potential A1 channels by mustard oil, tetrahydrocannabinol and Ca(2+) reveals different functional channel states. *Neuroscience* **154**: 1467-1476, 2008.

CHEN J, HACKOS DH: TRPA1 as a drug target--promise and challenges. *Naunyn Schmiedebergs Arch Pharmacol* **388**: 451-463, 2015.

CHEN JJ, JOHNSON EJ: Targeting the bradykinin B1 receptor to reduce pain. *Expert Opin Ther Targets* **11**: 21-35, 2007.

COREY DP, GARCIA-ANOVEROS J, HOLT JR, KWAN KY, LIN SY, VOLLRATH MA, AMALFITANO A, CHEUNG EL, DERFLER BH, DUGGAN A, ET AL.: TRPA1 is a candidate for the mechanosensitive transduction channel of vertebrate hair cells. *Nature* **432**: 723-730, 2004.

CVETKOV TL, HUYNH KW, COHEN MR, MOISEENKOVA-BELL VY: Molecular architecture and subunit organization of TRPA1 ion channel revealed by electron microscopy. *J Biol Chem* **286**: 38168-38176, 2011.

DAI Y, WANG S, TOMINAGA M, YAMAMOTO S, FUKUOKA T, HIGASHI T, KOBAYASHI K, OBATA K, YAMANAKA H, NOGUCHI K: Sensitization of TRPA1 by PAR2 contributes to the sensation of inflammatory pain. *J Clin Invest* **117**: 1979-1987, 2007.

DEERING-RICE CE, SHAPIRO D, ROMERO EG, STOCKMANN C, BEVANS TS, PHAN QM, STONE BL, FASSL B, NKOY F, UCHIDA DA, ET AL.: Activation of transient receptor potential ankyrin-1 by insoluble particulate material and association with asthma. *Am J Respir Cell Mol Biol* **53**: 893-901, 2015.

DHAVAN R, TSAI LH: A decade of CDK5. *Nat Rev Mol Cell Biol* **2**: 749-759, 2001.

DIOGENES A, AKOPIAN AN, HARGREAVES KM: NGF up-regulates TRPA1: implications for orofacial pain. *J Dent Res* **86**: 550-555, 2007.

DOERNER JF, GISSELMANN G, HATT H, WETZEL CH: Transient receptor potential channel A1 is directly gated by calcium ions. *J Biol Chem* **282**: 13180-13189, 2007.

EGAN TJ, ACUÑA MA, ZENOBI-WONG M, ZEILHOFER HU, URECH D: Effects of N-Glycosylation of the human cation channel TRPA1 on agonist-sensitivity. *Biosci Rep* **36**: e00390, 2016.

FRANCEL PC, HARRIS K, SMITH M, FISHMAN MC, DAWSON G, MILLER RJ: Neurochemical characteristics of a novel dorsal root ganglion X neuroblastoma hybrid cell line, F-11. *J Neurochem* **48**: 1624-1631, 1987.

GAO Y, CAO E, JULIUS D, CHENG Y: TRPV1 structures in nanodiscs reveal mechanisms of ligand and lipid action. *Nature* **534**: 347-351, 2016.

GAUDET R: A primer on ankyrin repeat function in TRP channels and beyond. *Mol Biosyst* **4**: 372-379, 2008.

GEPPETTI P, NASSINI R, MATERAZZI S, BENEMEI S: The concept of neurogenic inflammation. *BJU Int* **101** (Suppl 3): 2-6, 2008.

GUO Y, YUAN C, TIAN F, HUANG K, WEGHORST CM, TSAI MD, LI J: Contributions of conserved TPLH tetrapeptides to the conformational stability of ankyrin repeat proteins. *J Mol Biol* **399**: 168-181, 2010.

GUSTAVSSON N, WU B, HAN W: Calcium sensing in exocytosis. *Adv Exp Med Biol* **740**: 731-757, 2012.

HINMAN A, CHUANG HH, BAUTISTA DM, JULIUS D: TRP channel activation by reversible covalent modification. *Proc Natl Acad Sci U S A* **103**: 19564-19568, 2006.

HUYNH KW, COHEN MR, JIANG J, SAMANTA A, LODOWSKI DT, ZHOU ZH, MOISEENKOVA-BELL VY: Structure of the full-length TRPV2 channel by cryo-EM. *Nat Commun* **7**: 11130, 2016.

HYNKOVA A, MARSAKOVA L, VASKOVA J, VLACHOVA V: N-terminal tetrapeptide T/SPLH motifs contribute to multimodal activation of human TRPA1 channel. *Sci Rep* **6**: 28700, 2016.

JABBA S, GOYAL R, SOSA-PAGAN JO, MOLDENHAUER H, WU J, KALMETA B, BANDELL M, LATORRE R, PATAPOUTIAN A, GRANDL J: Directionality of temperature activation in mouse TRPA1 ion channel can be inverted by single-point mutations in ankyrin repeat six. *Neuron* **82**: 1017-1031, 2014.

JAQUEMAR D, SCHENKER T, TRUEB B: An ankyrin-like protein with transmembrane domains is specifically lost after oncogenic transformation of human fibroblasts. *J Biol Chem* **274**: 7325-7333, 1999.

JENDRYKE T, PROCHAZKOVA M, HALL BE, NORDMANN GC, SCHLADT M, MILENKOVIC VM, KULKARNI AB, WETZEL CH: TRPV1 function is modulated by Cdk5-mediated phosphorylation: insights into the molecular mechanism of nociception. *Sci Rep* **6**: 22007, 2016.

JORDT SE, BAUTISTA DM, CHUANG HH, McKEMY DD, ZYGMUNT PM, HOGESTATT ED, MENG ID, JULIUS D: Mustard oils and cannabinoids excite sensory nerve fibres through the TRP channel ANKTM1. *Nature* **427**: 260-265, 2004.

KARASHIMA Y, PRENEN J, MESEGUER V, OWSIANIK G, VOETS T, NILIUS B: Modulation of the transient receptor potential channel TRPA1 by phosphatidylinositol 4,5-biphosphate manipulators. *Pflugers Arch* **457**: 77-89, 2008.

KARASHIMA Y, PRENEN J, TALAVERA K, JANSSENS A, VOETS T, NILIUS B: Agonist-induced changes in Ca(2+) permeation through the nociceptor cation channel TRPA1. *Biophys J* **98**: 773-783, 2010.

KOTTGEN M, BENZING T, SIMMEN T, TAUBER R, BUCHHOLZ B, FELICIANGELI S, HUBER TB, SCHERMER B, KRAMER-ZUCKER A, HOPKER K, ET AL.: Trafficking of TRPP2 by PACS proteins represents a novel mechanism of ion channel regulation. *EMBO J* **24**: 705-716, 2005.

KWAN KY, ALLCHORNE AJ, VOLLRATH MA, CHRISTENSEN AP, ZHANG DS, WOOLF CJ, COREY DP: TRPA1 contributes to cold, mechanical, and chemical nociception but is not essential for hair-cell transduction. *Neuron* **50**: 277-289, 2006.

LAURSEN WJ, BAGRIANTSEV SN, GRACHEVA EO: TRPA1 channels: chemical and temperature sensitivity. *Curr Top Membr* **74**: 89-112, 2014.

LI J, MAHAJAN A, TSAI MD: Ankyrin repeat: a unique motif mediating protein-protein interactions. *Biochemistry* **45**: 15168-15178, 2006.

LIAO M, CAO E, JULIUS D, CHENG Y: Structure of the TRPV1 ion channel determined by electron cryo-microscopy. *Nature* **504**: 107-112, 2013.

LISHKO PV, PROCKO E, JIN X, PHELPS CB, GAUDET R: The ankyrin repeats of TRPV1 bind multiple ligands and modulate channel sensitivity. *Neuron* **54**: 905-918, 2007.

LIU J, DU J, YANG Y, WANG Y: Phosphorylation of TRPV1 by cyclin-dependent kinase 5 promotes TRPV1 surface localization, leading to inflammatory thermal hyperalgesia. *Exp Neurol* **273**: 253-262, 2015.

MacPHERSON LJ, DUBIN AE, EVANS MJ, MARR F, SCHULTZ PG, CRAVATT BF, PATAPOUTIAN A: Noxious compounds activate TRPA1 ion channels through covalent modification of cysteines. *Nature* **445**: 541-545, 2007.

MARSAKOVA L, BARVIK I, ZIMA V, ZIMOVA L, VLACHOVA V: The first extracellular linker is important for several aspects of the gating mechanism of human TRPA1 channel. *Front Mol Neurosci* **10**: 16, 2017.

MARSAKOVA L, TOUSKA F, KRUSEK J, VLACHOVA V: Pore helix domain is critical to camphor sensitivity of transient receptor potential vanilloid 1 channel. *Anesthesiology* **116**: 903-917, 2012.

MEENTS JE, FISCHER MJ, McNAUGHTON PA: Agonist-induced sensitisation of the irritant receptor ion channel TRPA1. *J Physiol* **594**: 6643-6660, 2016.

MEENTS JE, FISCHER MJ, McNAUGHTON PA: Sensitization of TRPA1 by protein kinase A. *PloS One* **12**: e0170097, 2017.

MIYAMOTO T, DUBIN AE, PETRUS MJ, PATAPOUTIAN A: TRPV1 and TRPA1 mediate peripheral nitric oxide-induced nociception in mice. *PLoS One* **4**: e7596, 2009.

MIZUMURA K, SUGIURA T, KATANOSAKA K, BANIK RK, KOZAKI Y: Excitation and sensitization of nociceptors by bradykinin: what do we know? *Exp Brain Res* **196**: 53-65, 2009.

MORGAN K, SADOFSKY LR, CROW C, MORICE AH: Human TRPM8 and TRPA1 pain channels, including a gene variant with increased sensitivity to agonists (TRPA1 R797T), exhibit differential regulation by SRC-tyrosine kinase inhibitor. *Biosci Rep* **34**: e00131, 2014.

NAGATA K, DUGGAN A, KUMAR G, GARCIA-ANOVEROS J: Nociceptor and hair cell transducer properties of TRPA1, a channel for pain and hearing. *J Neurosci* **25**: 4052-4061, 2005.

NILIUS B, APPENDINO G, OWSIANIK G: The transient receptor potential channel TRPA1: from gene to pathophysiology. *Pflugers Arch* **464**: 425-458, 2012.

NILIUS B, PRENEN J, OWSIANIK G: Irritating channels: the case of TRPA1. *J Physiol* **589**: 1543-1549, 2011.

OBATA K, KATSURA H, MIZUSHIMA T, YAMANAKA H, KOBAYASHI K, DAI Y, FUKUOKA T, TOKUNAGA A, TOMINAGA M, NOGUCHI K: TRPA1 induced in sensory neurons contributes to cold hyperalgesia after inflammation and nerve injury. *J Clin Invest* **115**: 2393-2401, 2005.

OWSIANIK G, TALAVERA K, VOETS T, NILIUS B: Permeation and selectivity of TRP channels. *Annu Rev Physiol* **68**: 685-717, 2006.

PALOVCAK E, DELEMOTTE L, KLEIN ML, CARNEVALE V: Comparative sequence analysis suggests a conserved gating mechanism for TRP channels. *J Gen Physiol* **146**: 37-50, 2015.

PAREEK TK, KELLER J, KESAVAPANY S, AGARWAL N, KUNER R, PANT HC, IADAROLA MJ, BRADY RO, KULKARNI AB: Cyclin-dependent kinase 5 modulates nociceptive signaling through direct phosphorylation of transient receptor potential vanilloid 1. *Proc Natl Acad Sci U S A* **104**: 660-665, 2007.

PAREEK TK, KULKARNI AB: Cdk5: a new player in pain signaling. *Cell Cycle* **5**: 585-588, 2006.

PAULSEN CE, ARMACHE JP, GAO Y, CHENG Y, JULIUS D: Structure of the TRPA1 ion channel suggests regulatory mechanisms. *Nature* **520**: 511-517, 2015.

PEREZ DI, GIL C, MARTINEZ A: Protein kinases CK1 and CK2 as new targets for neurodegenerative diseases. *Med Res Rev* **31**: 924-954, 2011.

PETHO G, REEH PW: Sensory and signaling mechanisms of bradykinin, eicosanoids, platelet-activating factor, and nitric oxide in peripheral nociceptors. *Physiol Rev* **92**: 1699-1775, 2012.

ROHACS T: Phosphoinositide regulation of non-canonical transient receptor potential channels. *Cell Calcium* **45**: 554-565, 2009.

ROZAS P, LAZCANO P, PINA R, CHO A, TERSE A, PERTUSA M, MADRID R, GONZALEZ-BILLAULT C, KULKARNI AB, UTRERAS E: Targeted overexpression of tumor necrosis factor-alpha increases cyclin-dependent kinase 5 activity and TRPV1-dependent Ca2+ influx in trigeminal neurons. *Pain* **157**: 1346-1362, 2016.

SAOTOME K, SINGH AK, YELSHANSKAYA MV, SOBOLEVSKY AI: Crystal structure of the epithelial calcium channel TRPV6. *Nature* **534**: 506-511, 2016.

SCHMIDT M, DUBIN AE, PETRUS MJ, EARLEY TJ, PATAPOUTIAN A: Nociceptive signals induce trafficking of TRPA1 to the plasma membrane. *Neuron* **64**: 498-509, 2009.

SINGH NN, RAMJI DP: Protein kinase CK2, an important regulator of the inflammatory response? *J Mol Med* **86**: 887-897, 2008.

SONGYANG Z, LU KP, KWON YT, TSAI LH, FILHOL O, COCHET C, BRICKEY DA, SODERLING TR, BARTLESON C, GRAVES DJ, DEMAGGIO AJ, HOEKSTRA MF, BLENIS J, HUNTER T, CANTLEY LC: A structural basis for substrate specificities of protein Ser/Thr kinases: primary sequence preference of casein kinases I and II, NIMA, phosphorylase kinase, calmodulin-dependent kinase II, CDK5, and Erk1. *Mol Cell Biol* **16**: 6486-6493, 1996.

SOTOMAYOR M, COREY DP, SCHULTEN K: In search of the hair-cell gating spring elastic properties of ankyrin and cadherin repeats. *Structure* **13**: 669-682, 2005.

ST-DENIS N, GABRIEL M, TUROWEC JP, GLOOR GB, LI SS, GINGRAS AC, LITCHFIELD DW: Systematic investigation of hierarchical phosphorylation by protein kinase CK2. *J Proteomics* **118**: 49-62, 2015.

STARUSCHENKO A, JESKE NA, AKOPIAN AN: Contribution of TRPV1-TRPA1 interaction to the single channel properties of the TRPA1 channel. *J Biol Chem* **285**: 15167-15177, 2010.

STORY GM, PEIER AM, REEVE AJ, EID SR, MOSBACHER J, HRICIK TR, EARLEY TJ, HERGARDEN AC, ANDERSSON DA, HWANG SW, McINTYRE P, JEGLA T, BEVAN S, PATAPOUTIAN A: ANKTM1, a TRP-like channel expressed in nociceptive neurons, is activated by cold temperatures. *Cell* **112**: 819-829, 2003.

SULAK MA: Modulation of transient receptor potential cation channel, subfamily A, member 1 (TRPA1) activity by CDK5. In: *Kent State University PhD Thesis*, 2011, 84 p.

SURA L, ZIMA V, MARSAKOVA L, HYNKOVA A, BARVIK I, VLACHOVA V: C-terminal acidic cluster is involved in Ca2+-induced regulation of human transient receptor potential ankyrin 1 channel. *J Biol Chem* **287**: 18067-18077, 2012.

TAKAHASHI N, KUWAKI T, KIYONAKA S, NUMATA T, KOZAI D, MIZUNO Y, YAMAMOTO S, NAITO S, KNEVELS E, CARMELIET P, OGA T, KANEKO S, SUGA S, NOKAMI T, YOSHIDA J, MORI Y: TRPA1 underlies a sensing mechanism for O2. *Nat Chem Biol* **7**: 701-711, 2011.

TAYLOR-CLARK TE, UNDEM BJ, MacGLASHAN DW JR, GHATTA S, CARR MJ, McALEXANDER MA: Prostaglandin-induced activation of nociceptive neurons via direct interaction with transient receptor potential A1 (TRPA1). *Mol Pharmacol* **73**: 274-281, 2008.

UTRERAS E, FUTATSUGI A, PAREEK TK, KULKARNI AB: Molecular roles of Cdk5 in pain signaling. *Drug Discov Today Ther Strateg* **6**: 105-111, 2009.

VETTER I, LEWIS RJ: Characterization of endogenous calcium responses in neuronal cell lines. *Biochem Pharmacol* **79**: 908-920, 2010.

VIANA F: TRPA1 channels: molecular sentinels of cellular stress and tissue damage. *J Physiol* **594**: 4151-4169, 2016.

VOOLSTRA O, HUBER A: Post-translational modifications of TRP channels. *Cells* **3**: 258-287, 2014.

WANG S, DAI Y, FUKUOKA T, YAMANAKA H, KOBAYASHI K, OBATA K, CUI X, TOMINAGA M, NOGUCHI K: Phospholipase C and protein kinase A mediate bradykinin sensitization of TRPA1: a molecular mechanism of inflammatory pain. *Brain* **131**: 1241-1251, 2008a.

WANG YY, CHANG RB, WATERS HN, McKEMY DD, LIMAN ER: The nociceptor ion channel TRPA1 is potentiated and inactivated by permeating calcium ions. *J Biol Chem* **283**: 32691-32703, 2008b.

YIN K, BAILLIE GJ, VETTER I: Neuronal cell lines as model dorsal root ganglion neurons: A transcriptomic comparison. *Mol Pain* **12**: 2016.

ZHANG X, HUANG J, McNAUGHTON PA: NGF rapidly increases membrane expression of TRPV1 heat-gated ion channels. *EMBO J* **24**: 4211-4223, 2005.

ZHANG X, LI L, McNAUGHTON PA: Proinflammatory mediators modulate the heat-activated ion channel TRPV1 via the scaffolding protein AKAP79/150. *Neuron* **59**: 450-461, 2008.

ZUBCEVIC L, HERZIK MA JR, CHUNG BC, LIU Z, LANDER GC, LEE SY: Cryo-electron microscopy structure of the TRPV2 ion channel. *Nat Struct Mol Biol* **23**: 180-186, 2016.

ZURBORG S, YURGIONAS B, JIRA JA, CASPANI O, HEPPENSTALL PA: Direct activation of the ion channel TRPA1 by Ca2+. *Nat Neurosci* **10**: 277-279, 2007.

ZYGMUNT PM, HOGESTATT ED: Trpa1. *Handb Exp Pharmacol* **222**: 583-630, 2014.

Article

Phospho-Mimetic Mutation at Ser602 Inactivates Human TRPA1 Channel

Kristyna Barvikova [1], **Ivan Barvik** [2], **Viktor Sinica** [1], **Lucie Zimova** [1] and **Viktorie Vlachova** [1,*]

[1]   Department of Cellular Neurophysiology, Institute of Physiology Czech Academy of Sciences, 142 20 Prague, Czech Republic; tynabarvikova@seznam.cz (K.B.); viktor.synytsya@fgu.cas.cz (V.S.); lucie.zimova@fgu.cas.cz (L.Z.)
[2]   Division of Biomolecular Physics, Institute of Physics, Faculty of Mathematics and Physics, Charles University, 121 16 Prague, Czech Republic; ibarvik@karlov.mff.cuni.cz
*   Correspondence: viktorie.vlachova@fgu.cas.cz; Tel.: +420-29644-2711

check for updates

Abstract: The Transient Receptor Potential Ankyrin 1 (TRPA1) channel is an integrative molecular sensor for detecting environmental irritant compounds, endogenous proalgesic and inflammatory agents, pressure, and temperature. Different post-translational modifications participate in the discrimination of the essential functions of TRPA1 in its physiological environment, but the underlying structural bases are poorly understood. Here, we explored the role of the cytosolic N-terminal residue Ser602 located near a functionally important allosteric coupling domain as a potential target of phosphorylation. The phosphomimetic mutation S602D completely abrogated channel activation, whereas the phosphonull mutations S602G and S602N produced a fully functional channel. Using mutagenesis, electrophysiology, and molecular simulations, we investigated the possible structural impact of a modification (mutation or phosphorylation) of Ser602 and found that this residue represents an important regulatory site through which the intracellular signaling cascades may act to reversibly restrict or "dampen" the conformational space of the TRPA1 channel and promote its transitions to the closed state.

---

1. Introduction

Phosphorylation is supposed to be one of the most important post-translational mechanisms reversibly regulating the Transient Receptor Potential Ankyrin 1 (TRPA1) channel under various physiological and pathophysiological conditions [1,2]. This channel is abundantly expressed in a subset of nociceptive somatosensory neurons where it acts as a polymodal detector of diverse pain-producing chemical and physical stimuli [3,4]. The expression of TRPA1 is also detected in a wide variety of non-neuronal cells [5–8], such as lung fibroblast and epithelial cells, smooth muscle cells [9,10], hair cells [11], astrocytes [12], oligodendrocytes [13], Schwann cells [14], odontoblasts [15], and synoviocytes [16], indicating the involvement of the channel in the (patho)physiology of multiple organ systems. Activation of TRPA1 produces an acute nociceptive response through peripheral release of neuropeptides from sensory nerve endings or from non-neural tissues. Under a number of chronic conditions associated with inflammation, tissue damage, or oxidative stress, endogenous substances released at the site of injury modulate TRPA1 via the G-protein-coupled receptor and phospholipase C-coupled signaling cascades. Among such agents are extracellular proteases, prostaglandins, bradykinin, serotonin, substance P, calcitonin gene related peptide, nerve growth factor (NGF), tumor

necrosis factor α (TNFα), and many more [17–20]. These mediators can directly activate TRPA1 [21–23] or stimulate protein kinase A (PKA) [24–27], protein kinase C (PKC) [25], p38 mitogen-activated protein kinases [28], cyclin dependent kinase 5 [29,30], or phospholipase C (PLC) pathways [24,31] to induce phosphorylation of TRPA1. Phosphorylation, in turn, significantly alters the activation threshold and/or membrane expression of TRPA1, amplifying the inflammation and rendering nociceptors more sensitive to noxious stimulation.

For effective phosphorylation by PKA and PKC, TRPA1 needs the presence of the scaffolding A-kinase anchoring protein 79/150 (AKAP) [25]. AKAP directly interacts with TRPA1 [32], spatially constrains phosphorylation, and most likely serves as a molecular hub that contributes to the efficiency and specificity of the cellular signaling network regulating the channel under various physiological or pathophysiological conditions [33]. Importantly, the sensitization of TRPA1 through the PKA-AKAP pathway is responsible for persistent mechanical hypersensitivity [25], carboplatin-induced mechanical allodynia, and cold hyperalgesia [34]. While most of the kinases described so far that act on TRPA1 functionally up-regulate the channel's function, 5′ adenosine monophosphate-activated protein kinase (AMPK), on the contrary, down-regulates TRPA1 plasma membrane expression in dorsal root ganglion neurons which might represent a potential mechanism underlying painful diabetic peripheral neuropathy and other diseases with a similar pathophysiological profile of metabolic dysfunction [35]. In addition, several tyrosine residues located at the N-terminus have been proposed to be involved in the inhibition of TRPA1 by Src kinase in SH-SY5Y human neuroblastoma cells [36]. Despite the presumed physiological importance of the molecular mechanisms that establish and control the subtle balance between phosphorylated and dephosphorylated states of TRPA1, information regarding the specific sites underlying these processes remains scarce (reviewed in [1,18,37,38]).

Recently, it has been proposed that natural or exogenous thiol-reactive electrophilic compounds activate TRPA1 through a two-step mechanism that involves conformational changes within a specific cytoplasmic membrane proximal domain (Figure 1A). This functionally key part of the protein, dubbed the allosteric nexus [39] or coupling domain [40], is composed of seven N-terminal and one C-terminal short helices, three β-strands that form an antiparallel β-sheet, and the TRP-like helix. In the process of electrophile-induced activation, covalent modification of Cys621 is followed by partial modification of Cys665 and repositioning of Lys671 that is stabilized through its interaction with backbone carbonyl oxygens at the C-terminus of the TRP-like domain, leading to pore widening [39]. Structurally, the allosteric nexus is immediately preceded by Ser602 (Figure 1B), a residue from ankyrin repeat 16 that is predicted by various servers [41] to be a potential phosphorylation site for several kinases, including AGC, CMGC, and Ca^{2+}/calmodulin-dependent protein kinase families. Interestingly, the side chain of this serine is exposed to the cytoplasm in TRPA1 structures obtained in the ligand-free state (PDB ID: 6PQQ; [40]) or in the presence of the covalent agonists allyl isothiocyanate (3J9P; [42]), benzyl isothiocyanate (6PQP; [40]), and JT010 (6PQO; [40]). In contrast, in other structures resolved recently in various closed and activated conformations (6V9V, 6V9W, 6V9X, and 6V9Y; [39]), the side chain of Ser602 is oriented towards the protein by forming hydrogen bonds with main chain carbonyls. This indicates that the role of this putative consensus phosphorylation site may depend on the conformational state of the channel. We reasoned that being located near the functionally important allosteric nexus, a modification of Ser602 may have a strong impact on TRPA1 channel gating. Therefore, in this study, we explored the role of this residue as a potential target of phosphorylation.
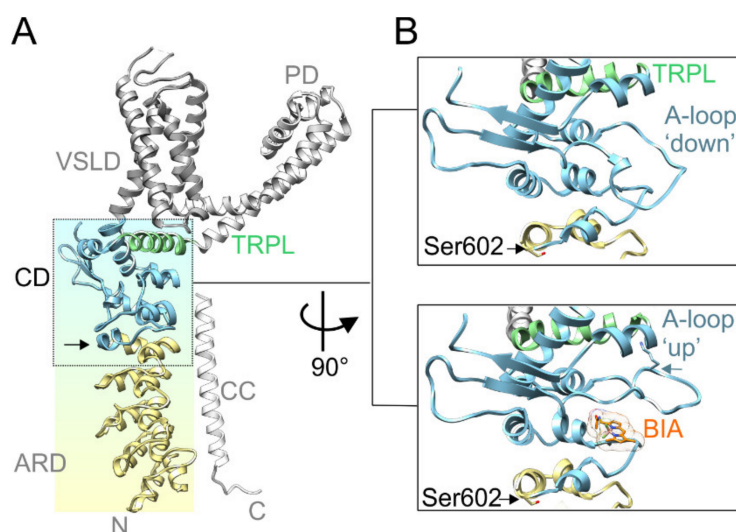
Figure 1. Serine 602 (Ser602) precedes the functionally key coupling domain. (**A**) The structure overview of a Transient Receptor Potential Ankyrin 1 (TRPA1) subunit (PDB ID: 6V9W [39]) with indicated voltage-sensor like domain (VSLD; grey ribbon), pore domain (PD; light grey ribbon), coupling domain, also dubbed as allosteric nexus (CD; light blue ribbon), ankyrin repeat domain (ARD; yellow ribbon), C-terminal coiled-coil domain (CC; white ribbon), and TRP-like domain (TRPL; light green ribbon). Black vertical arrow indicates the position of Ser602. (**B**) Close-up view of the coupling domain in two conformations: Upper box, activation loop (A-loop) in a "down" conformation (PDB ID: 6V9W). Lower box, activation loop in an "up" conformation (PDB ID: 6V9V), enabling binding of BODIPY-iodoacetamide (BIA) and stabilization of the A-loop through the interaction of Lys671 (indicated by horizontal blue arrow) with backbone carbonyls at the C-terminus of the TRP-like helix. Black horizontal arrows indicate position of Ser602.

2. Results

2.1. Phophomimetic Mutation S602D Abrogates Voltage-Dependent Activation of TRPA1

In order to explore the role of Ser602 as a potential phosphorylation site, we constructed the phosphomimetic and phoshonull mutants of human TRPA1, S602D, and S602G, and tested their voltage-dependent activation properties in transiently transfected HEK 293T cells under whole-cell patch clamp conditions (Figure 2). At the beginning of the recording from each cell, we ensured that a series of depolarizing pulses from −80 mV to +140 mV applied in the presence of extracellular control solution produced typical outwardly rectifying membrane currents (Figure 2A). Afterwards, we repeatedly applied voltage ramps from −100 mV to +120 mV (1 V/s; holding potential −70 mV) with 5-s intervals (Figure 2B,C). Whereas S602G exhibited outwardly rectifying membrane currents that were not significantly different from wild-type TRPA1 (*n* = 10), the S602D construct was nonfunctional in all cells tested within a recording period of at least 120 s (*n* = 9). To investigate if the S602D mutation affects the surface expression of TRPA1, we expressed tGFP-tagged wild-type TRPA1 or S602D in HEK 293T cells and performed confocal microscopy by using CellBrite^{TM} Fix 640 to visualize plasma membrane (Figure 2D,E). The colocalization analysis of fluorescence intensity profiles measured along a rectangle drawn across the cell membrane confirmed that the areas of high intensity were observed at the cell periphery similarly in both constructs. Although not quantitatively, together these findings indicate that the S602D mutant is significantly expressed on the cell membrane, but it is not active.
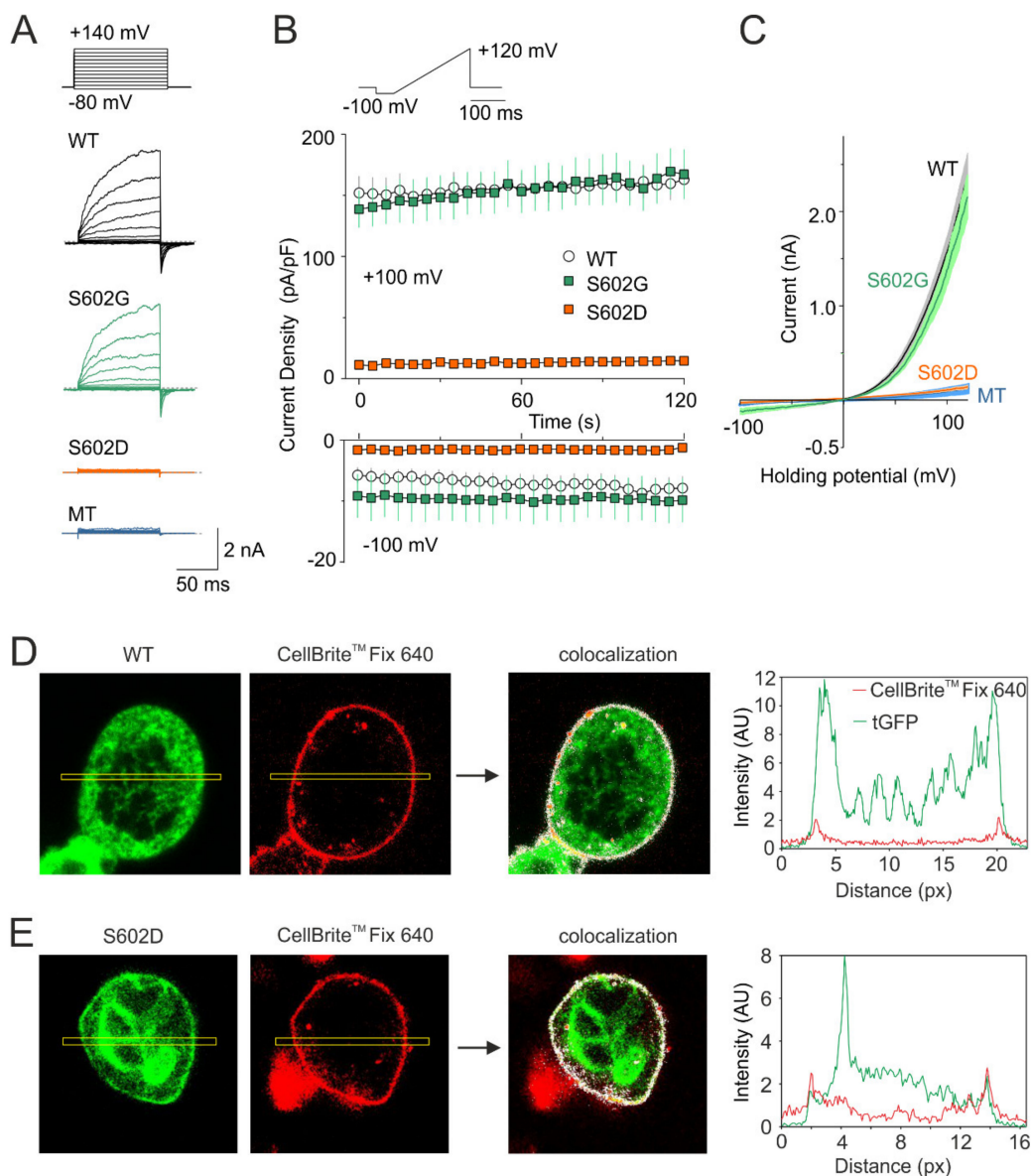
Figure 2. Mutation S602D abrogates voltage-dependent activation of TRPA1. (**A**) Currents through wild-type TRPA1 (WT), S602G, and S602D channels and currents from HEK 293T cells transfected with control plasmid (MT) induced by voltage-step protocol (shown above): 100-ms steps from −80 mV to +140 mV (increment +20 mV), holding potential −70 mV. (**B**) Average whole-cell current densities induced by depolarizing voltage measured from HEK 293T cells expressing TRPA1 (white circles indicating mean ± S.E.M.; *n* = 21), S602G (green squares ± S.E.M.; *n* = 10), or S602D (orange squares ± S.E.M.; *n* = 9). Voltage ramp protocol (shown in upper trace) was applied repeatedly each 5 s for 3 min. Amplitudes were measured at −100 mV and +100 mV and plotted as a function of time. (**C**) Mean current-voltage relations (mean as thin darker curves, ± SEM as lighter-colored envelopes) plotted for the initial response from cells expressing wild-type TRPA1, S602G, S602D or mock-transfected (MT) cells, exposed to the protocol shown in B. (**D**,**E**) Fluorescence colocalization analysis of HEK 293T cells transfected with tGFP-tagged (green) wild-type TRPA1 (D) or S602D mutant (E). Images are shown at 130× magnification. Cells were stained with the membrane dye CellBrite[TM] Fix 640 (red). An ImageJ plugin Colocalization Finder (see the Methods section) was used to highlight corresponding pixels on a RGB overlap (colocalization image indicated by arrow). Right graphs: the fluorescence intensity profiles (in arbitrary units, AU) were measured along rectangle drawn across the cell shown left. Similar results were obtained from nine WT-expressing and five S602D-expressing cells from three independent transfections.

2.2. Salt-Bridge Formation is Not Involved in the Effects Caused by the S602D Mutation

The structural role of Ser602 in TRPA1 channel functioning was next investigated by substituting this residue with asparagine, a polar amino acid of a similar size as negatively charged aspartate. We also evaluated the possibility that the disruptive effect of S602D may be caused by salt-bridge formation with proximal residues Lys603 or Arg604. Moreover, we tested the structural role of Trp605, a residue contained in the allosteric nexus. According to various prediction servers (e.g., http://cam.umassmed.edu/ and http://calcium.uhnres.utoronto.ca/), the region around Trp605 may represent not only a putative phosphorylation site but also a putative consensus binding site for Ca^{2+}/calmodulin [33]. Figure 3 summarizes the whole-cell current measurements from the S602D, S602N, S602D/K603A, S602D/R604A, and W605A mutants. To test the general role of these residues in channel gating, we examined not only the sensitivity of the constructs to depolarizing voltage and the electrophilic agonist allyl isothiocyanate (AITC; 100 µM), but also to the nonelectrophilic agonist carvacrol (50 µM) that activates the channel through a different, more classical noncovalent mechanism. The S602D mutant failed to produce any appreciable currents in response to agonist stimulation and its function was not rescued by either the K603A or R604A mutation. The S602D mediated currents measured in extracellular control solution or in the presence of AITC or carvacrol were not significantly different from the currents measured in mock-transfected cells ($p = 0.905$, 0.682 and 0.620 at +120 mV and $p = 0.970$, 0.676 and 0.845 at −100 mV; $n = 4$). The currents through S602N were not significantly different from wild-type channels (Figure 3B). The W605A mutant was sensitive to both agonists, although its responses to carvacrol were significantly lower than in wild-type channels ($p = 0.006$; $n = 5$), which indicates structural involvement of the tryptophan 605 in the process of channel activation. These data together suggest that the introduction of a negatively charged amino acid at position 602 mimics the phosphorylated state of the channel and that possible phosphorylation at Ser602 may cause the channel to be irresponsive to voltage and chemical stimuli.
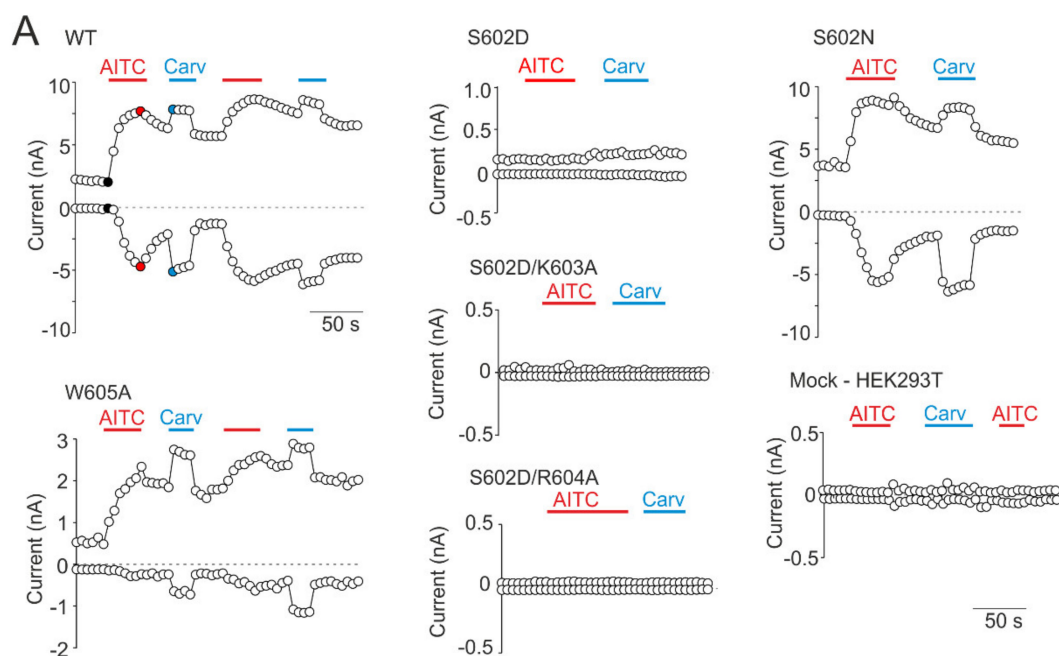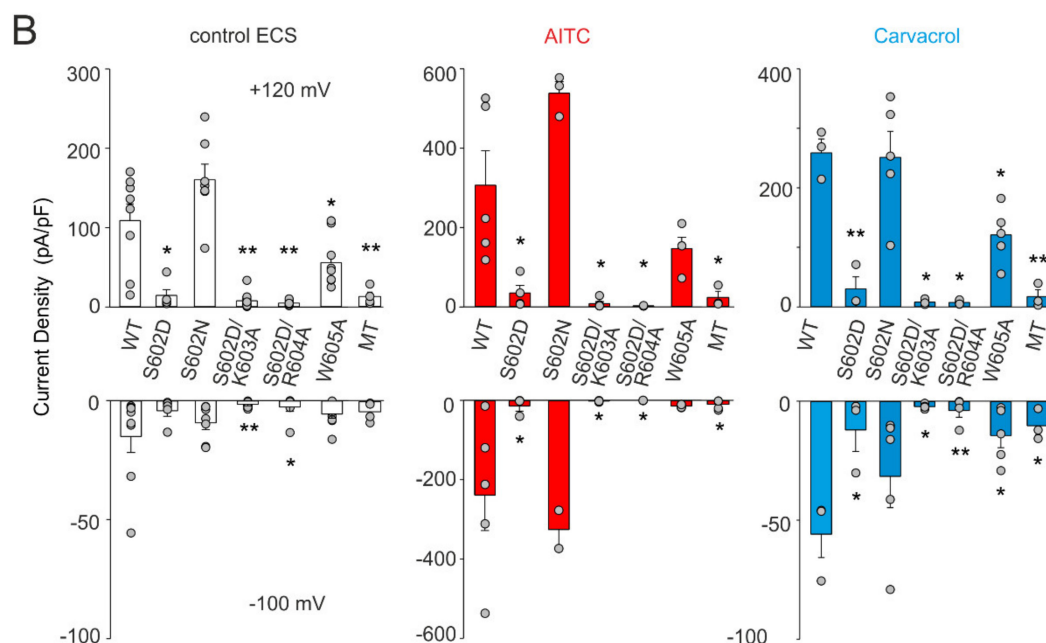

Figure 3. *Cont.*

Figure 3. Effects of mutations at Ser602 and contiguous residues on TRPA1 responses. (**A**) Time course of whole-cell current responses induced by voltage ramp (−100 mV, +120 mV; protocol shown in Figure 2B), applied in the presence of extracellular control solution (ECS), allyl isothiocyanate (AITC; 100 μM) or carvacrol (Carv; 50 μM). (**B**) Maximal amplitude of currents measured from recordings such as shown in A for indicated mutants (*n* = 3–10) and for mock-transfected cells (MT). The amplitudes were measured at times indicated by the colored points shown for the wild-type (WT) in A. The error bars represent the standard error of the mean. * *p* < 0.05; ** *p* < 0.005; Student's *t*-test.

2.3. Molecular Dynamics Simulations of the Phosphorylation of TRPA1 at Ser602

To further investigate how conformational changes induced by modification of Ser602 can be transduced to the channel gate, we conducted molecular dynamics (MD) simulations using the published cryo-electron microscopic structure of human TRPA1 captured in the open, ligand-occupied state (PDB ID: 6V9X; [39]). The simulations were performed with the "wild-type" structure, the S602D and S602N mutants, and with the phosphorylated state of Ser602, p-Ser602 (Figure 4, Supplementary Figures S1–S3).

The molecular dynamics (MD) trajectory reached 42–44-ns and the root mean square deviation (RMSD) measured for individual subunits and for the channel complex indicated that the models were stable (Supplementary Figure S1). Obvious differences were observed in local conformations around the position 602 among the wild-type, S602N, S602D, and the p-Ser602 structures (Figure 4A–D). In the wild-type structure and in S602N, the side chain of the amino acid at position 602 forms H-bonds with backbone carbonyl groups of Thr598 and Ile599 from the outer helix of ankyrin repeat 16 (AR16) (Figure 4A–C). In contrast, p-Ser602 phosphorylation and the S602D mutation orient the side chain into the aqueous environment where it forms salt bridges with the neighboring Lys603 (Figure 4B,D). In S602D, the backbone NH group of Asp602 interacts with the backbone carbonyl groups of Thr598 and Ile599 which slightly prolongs the end of the outer helix of AR16. Notably, this is similar to the interactions observed in the TRPA1 structure 3J9P [42], which has been obtained in the presence of covalent agonist but captured the channel in a closed state. In p-Ser602, the phosphoryl group forms extensive contacts with Arg601, a residue that interacts with Phe640 and through which the signal can be transmitted upwards through the allosteric nexus. On the other hand, such an extensive contact network was not observed in the S602D structure, suggesting that Arg601 is not the key to explaining the main impact of the mutation and/or phosphorylation.
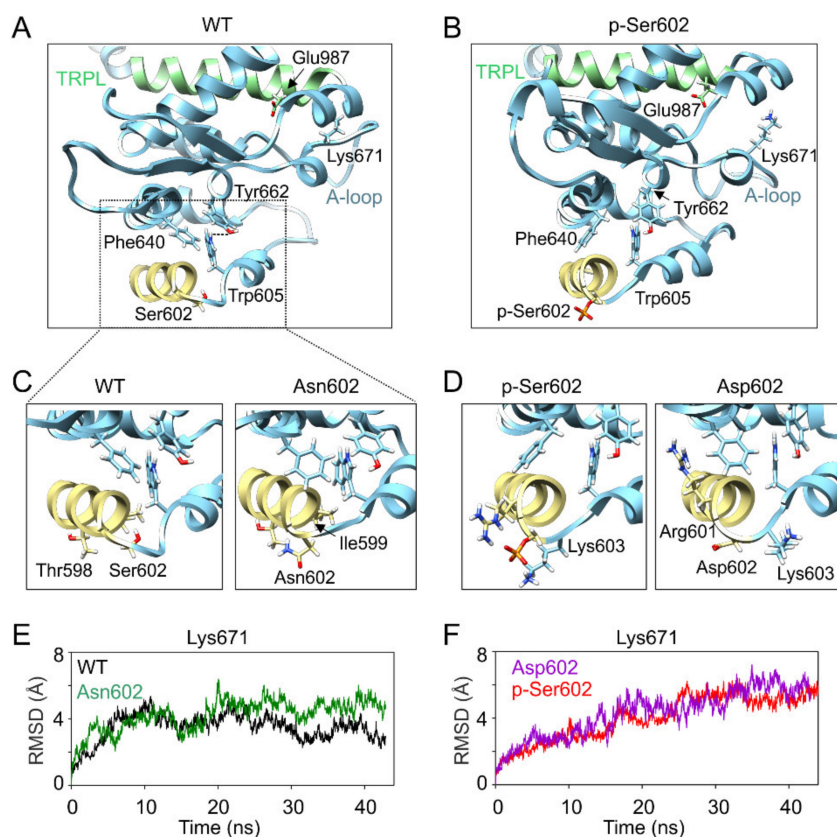
Figure 4. MD simulations indicate possible structural changes induced by modification at Ser602. (**A**,**B**) Close up view of the cluster of bulky amino acids Phe640, Trp605, and Tyr662 (chain B) through which the signal from Ser602 can be transduced to the activation loop (A-loop). Distances between Trp605 and Tyr662 shown in Supplementary Figure S2 were measured as indicated by dashed line in A. (**C**,**D**) Close up view of the local conformations of the outer helix of ankyrin repeat 16 obtained from MD simulations of the indicated constructs. (**E**,**F**) Time course of the average root mean square deviation (RMSD) values for Lys671, measured from the indicated TRPA1 constructs.

Figure 4A shows that Phe640 forms a cluster of bulky amino acids with neighboring Trp605 and Tyr662. The relative positions of these two amino acids usually did not change much over the wild-type and S602N MD simulations (Supplementary Figure S2) so that their distances were less than 3 Å for about 50% and 42% of MD simulation time in three subunits. Conversely, in the case of S602D and p-Ser602, the changes in the distances were more pronounced (7.5% and 22% respectively). These changes appear to be efficiently transmitted to the crucial TRP-like helix, so they can undoubtedly influence channel gating. Specifically, this can be seen in the time evolution of the average root mean square deviation of Lys671 (Figure 4E,F) and the time course of the distances between amino acids Lys671 and Glu987 (measured between Cα atoms, Supplementary Figure S3). While in the case of wild-type and S602 structures, these distances were below ~10 Å for about 60% of the MD simulation time in all subunits, in the case of S602D and p-Ser602, the relative time spent below ~10 Å was only 26% and 30%, respectively. These results suggest that the possible structural mechanism through which the modification at Ser602 produces inactivation of the channel involves changes in the coordination between Ly671 and the TRP-like helix, which are the critical components of the channel gating machinery.

3. Discussion

Our present data show that the single mutation of Ser602 to aspartate renders the TRPA1 channel inactive, whereas the replacement of this serine with asparagine, a residue of a similar side-chain as

aspartate but lacking its negative charge, or with a flexible glycine, fully retains channel functionality. The data show further that the phosphomimetic mutant S602D is expressed on the plasma membrane, and thus appears to retain key protein functions. These results raise the possibility that Ser602 represents a potential phosphorylation site through which specific intracellular signaling cascade(s) may act to promote the transition of the channel to the closed state.

Although phosphomimetic/phosphonull substitution studies have proved to be instrumental and highly informative in obtaining new insights into the mechanisms of TRPA1 regulation by phosphorylation [26,29,36,43,44], the results should be interpreted with caution. First, the negative charge introduced by aspartate substitution (−1) does not match that of the phosphorylated residue (generally, −1.5) at physiological pH. Second, if the Ser602 serves as a recognition signal for an adaptor protein, a phosphomimetic mutant should not fit into its binding pocket. The third significant aspect is that a phosphomimetic substitution mimics long-term protein phosphorylation. Physiologically, phosphorylation is a dynamic process, often transient in response to various stimuli or cellular signaling events [45,46]. Thus, due to steric and intrinsic activity differences, the aspartate mutation does not necessarily imitate the effects of a phosphorylated residue. Our molecular simulations indicate that the structural impact of covalently attached phosphate produced by a phosphate group at position 602 is very similar to that of negatively charged amino acid aspartate, and so the overall chemical environment introduced by the mutation can be similar to phosphorylation. The proximity of Ser602 to the functionally crucial allosteric nexus makes it tempting to speculate that conformational changes at or near this residue may readily propagate to the gates of the channel. Indeed, our molecular simulations are in agreement with our functional data and suggest that the negative charge introduced by aspartate substitution at position 602 significantly alters local conformation of the activation loop through affecting the interaction of Trp605, Phe640, and Tyr662 and, subsequently, weakening the coordination between Lys671 and backbone carbonyl oxygens at the TRP-like domain C-terminus. Our electrophysiological data demonstrate that substitution of Trp605 by alanine notably reduced but did not abolish voltage- and carvacrol-induced activation (Figure 3). This suggests that Trp605 is important but not necessary for channel activation. Structural comparisons indicate that Tyr662 is located in a completely different position in the 3J9P structure of the closed TRPA1 [42]. In fact, Tyr662 is shifted several tens of Ångströms from the place where we observe it in the 6V9X structure. It is therefore possible that the conformational changes observed by us—with respect to the relative position of Trp605 and Tyr662 in the S602D and p-Ser602 MD simulations (see Supplementary Figure S2)—could ultimately lead to a broader conformational transition that could promote channel closure.

More than 900,000 different protein phosphorylation sites, including predicted, have been reported in various literature-curated databases and numerous bioinformatics resources and tools are available for the prediction of phosphorylation sites (see [41] and references therein). However, despite intensive research over many years, only about a few percent (~3%) of phosphorylation sites reported have been attributed to an experimentally confirmed human kinase and have their biological role clearly identified [41,47,48]. At least, the present state of knowledge enables to identify several kinases that may phosphorylate TRPA1 at Ser602 using various phosphorylation site prediction tools (reviewed in [41]; Table 1).

Most likely, the protein kinases A and C can be excluded from consideration because direct activation of protein kinase A (by 8-Br-cAMP or forskolin) or protein kinase C (by phorbol 12-myristate 13-acetate or phorbol 12,13-dibutyrate) has been already shown to up-regulate TRPA1 [24–26], which is opposite to the observed effects of the S602D mutation. Recent technological advances in mass spectrometry-based phosphoproteomic profiling are steadily increasing the scope of a global exploration of protein phosphorylation [46,48]. A key focus for future research can be to experimentally assess the phosphorylation status of Ser602 under various physiologically relevant conditions.

Table 1. Protein kinases predicted at a high or medium stringency level/threshold to phosphorylate human Transient Receptor Potential Ankyrin 1 (TRPA1) at Ser602.

Predicted Protein Kinase	Prediction Server
Protein kinase A	GPS 5.0 [49], PhosphoPICK [50]
Protein kinase C	GPS 5.0, NetPhos [51], NetPhorest, NetworKIN [52]
Protein kinase D1	GPS 5.0 [49], PhosphoPICK [50]
Glycogen synthase kinase-3	GPS 5.0 [49]
AKT2 kinase	GPS 5.0 [49]
Rho-associated protein kinase	PhoScan [53]
Mitogen-activated protein (MAP) kinase 3	Musite [54]
MAP kinase-activated protein kinase 5	GPS 5.0 [49]
ULK1 protein kinase	GPS 5.0 [49]

The enormous variability of the mechanisms found in relation to the role of TRPA1 in various physiological processes is a major challenge for the future. Most of the kinases described so far act on TRPA1 to functionally up-regulate the channel's function. The region around Ser602, on the contrary, might represent a potential site from which the activity of the channel can be effectively down-regulated under some pathophysiological conditions. Future studies, perhaps using a co-expression of TRPA1 with the predicted kinases (see Table 1) or examining various kinase modulators and mass spectrometry in a native system (i.e., DRG neurons), will be required to determine whether the mechanisms regulating TRPA1 channel involve Ser602. One of the general aspects that are usually considered when deciding whether or not the identified residue may represent a potential phosphorylation site is its evolutionary conservation [55,56]. Ser602 is not conserved across all species but is completely conserved in primates including human and any missense polymorphism at this site and the neighboring Lys603 have been identified in human. On the other hand, a total of 14 missense variants in the *TRPA1* gene have been detected at positions immediately preceding and following these two residues: T598M (rs147715599), I599V (rs145600263), I599N (rs745749488), I600V (rs1236229851), R601S (rs148585412), R601T (rs1347666288), R604I (rs377764138), R604T, W605R (rs748788882), D606N, D606Y (rs1352827754), E607K (rs755681762), C608Y (rs747708313), and C608R (rs955642376). In particular, some of these polymorphisms may affect the phosphorylation consensus or gating and deserve further investigation to elucidate their potential involvement in human pathophysiology.

4. Materials and Methods

4.1. Cell Culture, Constructs, and Transfection

Human embryonic kidney 293T cells (HEK 293T; ATCC, Manassas, VA, USA) were cultured in Opti-MEM I media (Invitrogen, Carlsbad, CA, USA) supplemented with 5% fetal bovine serum. The magnet-assisted transfection (IBA GmbH, Gottingen, Germany) technique was used to transiently co-transfect the cells in a 15.6 mm well on a 24-well plate coated with poly-L-lysine and collagen (Sigma-Aldrich, Prague, Czech Republic) with 200 ng of green fluorescent protein (GFP) plasmid (TaKaRa, Shiga, Japan) and with 400 ng of cDNA plasmid-encoding wild-type or mutant human TRPA1 (pCMV6-XL4 vector, OriGene Technologies, Rockville, MD, USA) or control plasmid. The cells were used 24–48 h after transfection. At least three independent transfections were used for each experimental group. The wild-type channel was regularly tested in the same batch as the mutants. The mutants were generated by PCR by using a QuikChange II XL Site-Directed Mutagenesis Kit (Agilent Technologies, Santa Clara, CA, USA), and they were confirmed by DNA sequencing (Eurofins Genomics, Ebersberg, Germany).

4.2. Electrophysiology

Whole-cell membrane currents were filtered at 2 kHz by using the low-pass Bessel filter of the Axopatch 200B amplifier, and they were digitized (5–10 kHz) with a Digidata 1440 unit

and the pCLAMP 10 software (Molecular Devices, San Jose, CA, USA). Patch electrodes were pulled from borosilicate glass and heat-polished to a final resistance of between 3 and 5 MΩ. Series resistance was compensated by at least 60%. The experiments were performed at room temperature (23–25 °C). Only one recording was performed on any one coverslip of cells to ensure that recordings were made from cells that had not been previously exposed to chemical stimuli. Extracellular bath solution was Ca^{2+}-free and contained: 140 mM NaCl, 5 mM KCl, 2 mM $MgCl_2$, 5 mM EGTA (ethylene glycol-bis (β-aminoethyl ether)-N,N,N′,N′-tetraacetic acid), 10 mM 4-(2-Hydroxyethyl)piperazine-1-ethanesulfonic acid (HEPES), 10 mM glucose, and pH 7.4 was adjusted by tetramethylammonium hydroxide. The intracellular solution contained 125 mM Cs-gluconate, 15 mM CsCl, 5 mM EGTA, 0.5 mM $CaCl_2$, 10 mM HEPES, 2 mM adenosine 5′-triphosphate magnesium salt, 0.3 mM guanosine 5′-triphosphate sodium salt hydrate, adjusted with CsOH to pH 7.4. The chemicals were purchased from Sigma-Aldrich (Prague, Czech Republic). The current-voltage relationships were recorded by using 50-ms steps ranging from holding potential of −70 mV to −100 mV, followed by a 220-ms ramp from −100 mV to +120 mV.

4.3. Confocal Microscopy

HEK 293T cells transfected with wild-type or S602D mutant of human TRPA1 tagged with tGFP (turbo GFP; Origene Technologies, Rockville, MD, USA) were stained with the cytoplasmic membrane labeling dye CellBrite[TM] Fix 640 (Biotium, Fremont, CA, USA) according to the manufacturer's protocol. Briefly, the cells were incubated in phosphate-buffered saline (1 mL) containing the dye (1 μL) for 20 min at 37 °C in a 5% CO_2. After treatment, cells were washed and imaged in Opti-MEM I media (Invitrogen, Carlsbad, CA, USA) supplemented with 5% fetal bovine serum. The colocalization analysis was performed using the Colocalization Finder plugin in ImageJ and fluorescence intensity profiles measured along a rectangle drawn across the cell membrane.

4.4. Molecular Modeling

To elucidate the possible structural mechanism through which the substitution S602D produces inactivation of the channel and compare the impact of phosphorylation at Ser602, we used the human TRPA1 structure with PDB ID: 6V9X, determined by cryo-electron microscopy [39]. First, the mutations S602D and S602N were created using the „Mutate residue" plugin in VMD [57]. The phosphorylated state of Ser602 (dianionic phosphate group) was created using the "Automatic PSF Builder" plugin with an appropriate parameter file (toppar_all36_prot_na_combined.par) within VMD software. The TRPA1 tetrameric structures (wild-type, mutated and phosphorylated) were inserted into the patch of the 1-palmitoyl-2-oleoylphosphatidylcholine (POPC) bilayer and solvated in transferable intermolecular potential 3-point (TIP3P) [58] water molecules to ensure at least 10 Å of solvent on both sides of the membrane and ionized in 0.5 M NaCl. This gives a periodic box size of 120 × 120 × 160 Å for a simulated system consisting of ~225,000 atoms. All atom structure and topology files were generated using VMD software [57]. Forces were computed using CHARMM27 force field for proteins, lipids, and ions [59–61]. All molecular dynamics (MD) simulations were produced with the aid of the software package NAMD2.13 [62] running on computers equipped with NVIDIA graphics processing units. First, Langevin dynamics was used for temperature control with the target temperature set to 310 K; the Langevin piston method was applied to reach an efficient pressure control with a target pressure of 1 atm [62]. The integration timestep was set to 2 fs. Simulated systems were energy-minimized, heated to 310 K, and production MD runs reached a length of 42–44 ns. Data were recorded every 20 ps and distances and contacts were analyzed using CPPTRAJ module from Amber Tools suite [63]. MD trajectories were visualized with the aid of the VMD 1.9 software package [57]. Figures were produced with the software packages UCSF Chimera 1.13 [64] and CorelDraw X7 (Corel Corporation, Otawa, Canada).

5. Conclusions

Our data identify an important N-terminal serine residue from which the channel functioning can be abrogated by a phospho-mimetic mutation. Beyond that, our data suggest that conformational changes produced by a substitution of Ser602 affect not only electrophilic- but also non-electrophilic- and voltage-dependent activation. This indicates that these activation mechanisms may converge and involve changes in the coordination between Ly671 and the TRP-like helix. Whether this serine residue indeed represents a phosphorylation site in vitro and in vivo is an interesting topic for future studies.

Abbreviations

TRPA1	Transient receptor potential ankyrin subtype 1
JT010	2-chloro-N-(4-(4-methoxyphenyl)thiazol-2-yl)-N-(3-methoxypropyl)-acetamide
AGC	Kinase family named after the protein kinase A, G, and C families
CMGC	Kinase family named after the initials of its subfamily members, including cyclin-dependent kinase, mitogen-activated protein kinase, glycogen synthase kinase and CDC-like kinase
AR16	Ankyrin repeat 16

References

1. Voolstra, O.; Huber, A. Post-Translational Modifications of TRP Channels. *Cells* **2014**, *3*, 258–287. [CrossRef] [PubMed]

2. Andrade, E.L.; Meotti, F.C.; Calixto, J.B. TRPA1 antagonists as potential analgesic drugs. *Pharmacol. Ther.* **2012**, *133*, 189–204. [CrossRef] [PubMed]

3. Story, G.M.; Peier, A.M.; Reeve, A.J.; Eid, S.R.; Mosbacher, J.; Hricik, T.R.; Earley, T.J.; Hergarden, A.C.; Andersson, D.A.; Hwang, S.W.; et al. ANKTM1, a TRP-like channel expressed in nociceptive neurons, is activated by cold temperatures. *Cell* **2003**, *112*, 819–829. [CrossRef]

4. Bautista, D.M.; Jordt, S.E.; Nikai, T.; Tsuruda, P.R.; Read, A.J.; Poblete, J.; Yamoah, E.N.; Basbaum, A.I.; Julius, D. TRPA1 mediates the inflammatory actions of environmental irritants and proalgesic agents. *Cell* **2006**, *124*, 1269–1282. [CrossRef]

5. Atoyan, R.; Shander, D.; Botchkareva, N.V. Non-neuronal expression of transient receptor potential type A1 (TRPA1) in human skin. *J. Investig. Dermatol.* **2009**, *129*, 2312–2315. [CrossRef]

6. Earley, S.; Gonzales, A.L.; Crnich, R. Endothelium-dependent cerebral artery dilation mediated by TRPA1 and Ca2+-Activated K+ channels. *Circ. Res.* **2009**, *104*, 987–994. [CrossRef]

7. Nozawa, K.; Kawabata-Shoda, E.; Doihara, H.; Kojima, R.; Okada, H.; Mochizuki, S.; Sano, Y.; Inamura, K.; Matsushime, H.; Koizumi, T.; et al. TRPA1 regulates gastrointestinal motility through serotonin release from enterochromaffin cells. *Proc. Natl. Acad. Sci. USA* **2009**, *106*, 3408–3413. [CrossRef]

8. Okada, Y.; Reinach, P.S.; Shirai, K.; Kitano-Izutani, A.; Miyajima, M.; Yamanaka, O.; Sumioka, T.; Saika, S. Transient Receptor Potential Channels and Corneal Stromal Inflammation. *Cornea* **2015**, *34* (Suppl. 11), S136–S141. [CrossRef]

9. Nassini, R.; Pedretti, P.; Moretto, N.; Fusi, C.; Carnini, C.; Facchinetti, F.; Viscomi, A.R.; Pisano, A.R.; Stokesberry, S.; Brunmark, C.; et al. Transient receptor potential ankyrin 1 channel localized to non-neuronal airway cells promotes non-neurogenic inflammation. *PLoS ONE* **2012**, *7*, e42454. [CrossRef]

10. Mukhopadhyay, I.; Gomes, P.; Aranake, S.; Shetty, M.; Karnik, P.; Damle, M.; Kuruganti, S.; Thorat, S.; Khairatkar-Joshi, N. Expression of functional TRPA1 receptor on human lung fibroblast and epithelial cells. *J. Recept. Signal Transduct.* **2011**, *31*, 350–358. [CrossRef]

11. Corey, D.P.; Garcia-Anoveros, J.; Holt, J.R.; Kwan, K.Y.; Lin, S.Y.; Vollrath, M.A.; Amalfitano, A.; Cheung, E.L.; Derfler, B.H.; Duggan, A.; et al. TRPA1 is a candidate for the mechanosensitive transduction channel of vertebrate hair cells. *Nature* **2004**, *432*, 723–730. [CrossRef] [PubMed]

12. Shigetomi, E.; Tong, X.; Kwan, K.Y.; Corey, D.P.; Khakh, B.S. TRPA1 channels regulate astrocyte resting calcium and inhibitory synapse efficacy through GAT-3. *Nat. Neurosci.* **2011**, *15*, 70–80. [CrossRef] [PubMed]

13. Hamilton, N.B.; Kolodziejczyk, K.; Kougioumtzidou, E.; Attwell, D. Proton-gated Ca(2+)-permeable TRP channels damage myelin in conditions mimicking ischaemia. *Nature* **2016**, *529*, 523–527. [CrossRef] [PubMed]

14. De Logu, F.; Nassini, R.; Materazzi, S.; Carvalho Goncalves, M.; Nosi, D.; Rossi Degl'Innocenti, D.; Marone, I.M.; Ferreira, J.; Li Puma, S.; Benemei, S.; et al. Schwann cell TRPA1 mediates neuroinflammation that sustains macrophage-dependent neuropathic pain in mice. *Nat. Commun.* **2017**, *8*, 1887. [CrossRef]

15. El Karim, I.A.; Linden, G.J.; Curtis, T.M.; About, I.; McGahon, M.K.; Irwin, C.R.; Lundy, F.T. Human odontoblasts express functional thermo-sensitive TRP channels: Implications for dentin sensitivity. *Pain* **2011**, *152*, 2211–2223. [CrossRef]

16. Kochukov, M.Y.; McNearney, T.A.; Fu, Y.; Westlund, K.N. Thermosensitive TRP ion channels mediate cytosolic calcium response in human synoviocytes. *Am. J. Physiol. Cell Physiol.* **2006**, *291*, C424–C432. [CrossRef]

17. Nilius, B.; Appendino, G.; Owsianik, G. The transient receptor potential channel TRPA1: From gene to pathophysiology. *Pflug. Arch.* **2012**, *464*, 425–458. [CrossRef]

18. Talavera, K.; Startek, J.B.; Alvarez-Collazo, J.; Boonen, B.; Alpizar, Y.A.; Sanchez, A.; Naert, R.; Nilius, B. Mammalian transient receptor potential TRPA1 channels: From structure to disease. *Physiol. Rev.* **2019**, *100*, 725–803. [CrossRef]

19. Viana, F. TRPA1 channels: Molecular sentinels of cellular stress and tissue damage. *J. Physiol.* **2016**, *594*, 4151–4169. [CrossRef]

20. Zygmunt, P.M.; Hogestatt, E.D. TRPA1. *Handb. Exp. Pharmacol.* **2014**, *222*, 583–630. [CrossRef]

21. Taylor-Clark, T.E.; Undem, B.J.; Macglashan, D.W., Jr.; Ghatta, S.; Carr, M.J.; McAlexander, M.A. Prostaglandin-induced activation of nociceptive neurons via direct interaction with transient receptor potential A1 (TRPA1). *Mol. Pharmacol.* **2008**, *73*, 274–281. [CrossRef] [PubMed]

22. Cruz-Orengo, L.; Dhaka, A.; Heuermann, R.J.; Young, T.J.; Montana, M.C.; Cavanaugh, E.J.; Kim, D.; Story, G.M. Cutaneous nociception evoked by 15-delta PGJ2 via activation of ion channel TRPA1. *Mol. Pain* **2008**, *4*, 30. [CrossRef] [PubMed]

23. Redmond, W.J.; Gu, L.; Camo, M.; McIntyre, P.; Connor, M. Ligand determinants of fatty acid activation of the pronociceptive ion channel TRPA1. *PeerJ* **2014**, *2*, e248. [CrossRef]

24. Wang, S.; Dai, Y.; Fukuoka, T.; Yamanaka, H.; Kobayashi, K.; Obata, K.; Cui, X.; Tominaga, M.; Noguchi, K. Phospholipase C and protein kinase A mediate bradykinin sensitization of TRPA1: A molecular mechanism of inflammatory pain. *Brain* **2008**, *131*, 1241–1251. [CrossRef] [PubMed]

25. Brackley, A.D.; Gomez, R.; Guerrero, K.A.; Akopian, A.N.; Glucksman, M.J.; Du, J.; Carlton, S.M.; Jeske, N.A. A-Kinase Anchoring Protein 79/150 Scaffolds Transient Receptor Potential A 1 Phosphorylation and Sensitization by Metabotropic Glutamate Receptor Activation. *Sci. Rep.* **2017**, *7*, 1842. [CrossRef] [PubMed]

26. Meents, J.E.; Fischer, M.J.; McNaughton, P.A. Sensitization of TRPA1 by Protein Kinase A. *PLoS ONE* **2017**, *12*, e0170097. [CrossRef] [PubMed]

27. Anand, U.; Otto, W.R.; Facer, P.; Zebda, N.; Selmer, I.; Gunthorpe, M.J.; Chessell, I.P.; Sinisi, M.; Birch, R.; Anand, P. TRPA1 receptor localisation in the human peripheral nervous system and functional studies in cultured human and rat sensory neurons. *Neurosci. Lett.* **2008**, *438*, 221–227. [CrossRef]

28. Obata, K.; Katsura, H.; Mizushima, T.; Yamanaka, H.; Kobayashi, K.; Dai, Y.; Fukuoka, T.; Tokunaga, A.; Tominaga, M.; Noguchi, K. TRPA1 induced in sensory neurons contributes to cold hyperalgesia after inflammation and nerve injury. *J. Clin. Investig.* **2005**, *115*, 2393–2401. [CrossRef]

29. Sulak, M.A.; Ghosh, M.; Sinharoy, P.; Andrei, S.R.; Damron, D.S. Modulation of TRPA1 channel activity by Cdk5 in sensory neurons. *Channels* **2018**, *12*, 65–75. [CrossRef]

30. Hall, B.E.; Prochazkova, M.; Sapio, M.R.; Minetos, P.; Kurochkina, N.; Binukumar, B.K.; Amin, N.D.; Terse, A.; Joseph, J.; Raithel, S.J.; et al. Phosphorylation of the Transient Receptor Potential Ankyrin 1 by Cyclin-dependent Kinase 5 affects Chemo-nociception. *Sci. Rep.* **2018**, *8*, 1177. [CrossRef]

31. Dai, Y.; Wang, S.; Tominaga, M.; Yamamoto, S.; Fukuoka, T.; Higashi, T.; Kobayashi, K.; Obata, K.; Yamanaka, H.; Noguchi, K. Sensitization of TRPA1 by PAR2 contributes to the sensation of inflammatory pain. *J. Clin. Investig.* **2007**, *117*, 1979–1987. [CrossRef] [PubMed]

32. Zhang, X.; Li, L.; McNaughton, P.A. Proinflammatory mediators modulate the heat-activated ion channel TRPV1 via the scaffolding protein AKAP79/150. *Neuron* **2008**, *59*, 450–461. [CrossRef] [PubMed]

33. Zimova, L.; Barvikova, K.; Macikova, L.; Vyklicka, L.; Sinica, V.; Barvik, I.; Vlachova, V. Proximal C-Terminus Serves as a Signaling Hub for TRPA1 Channel Regulation via Its Interacting Molecules and Supramolecular Complexes. *Front. Physiol.* **2020**, *11*, 189. [CrossRef] [PubMed]

34. Miyano, K.; Shiraishi, S.; Minami, K.; Sudo, Y.; Suzuki, M.; Yokoyama, T.; Terawaki, K.; Nonaka, M.; Murata, H.; Higami, Y.; et al. Carboplatin Enhances the Activity of Human Transient Receptor Potential Ankyrin 1 through the Cyclic AMP-Protein Kinase A-A-Kinase Anchoring Protein (AKAP) Pathways. *Int. J. Mol. Sci.* **2019**, *20*, 3271. [CrossRef] [PubMed]

35. Wang, S.; Kobayashi, K.; Kogure, Y.; Yamanaka, H.; Yamamoto, S.; Yagi, H.; Noguchi, K.; Dai, Y. Negative Regulation of TRPA1 by AMPK in Primary Sensory Neurons as a Potential Mechanism of Painful Diabetic Neuropathy. *Diabetes* **2018**, *67*, 98–109. [CrossRef] [PubMed]

36. Morgan, K.; Sadofsky, L.R.; Morice, A.H. Genetic variants affecting human TRPA1 or TRPM8 structure can be classified in vitro as 'well expressed', 'poorly expressed' or 'salvageable'. *Biosci. Rep.* **2015**, *35*, e00255. [CrossRef]

37. Kadkova, A.; Synytsya, V.; Krusek, J.; Zimova, L.; Vlachova, V. Molecular basis of TRPA1 regulation in nociceptive neurons. A review. *Physiol. Res.* **2017**, *66*, 425–439. [CrossRef]

38. Meents, J.E.; Ciotu, C.I.; Fischer, M.J.M. TRPA1: A molecular view. *J. Neurophysiol.* **2019**, *121*, 427–443. [CrossRef]

39. Zhao, J.; Lin King, J.V.; Paulsen, C.E.; Cheng, Y.; Julius, D. Irritant-evoked activation and calcium modulation of the TRPA1 receptor. *Nature* **2020**, *585*, 141–145. [CrossRef]

40. Suo, Y.; Wang, Z.; Zubcevic, L.; Hsu, A.L.; He, Q.; Borgnia, M.J.; Ji, R.R.; Lee, S.Y. Structural insights into Electrophile Irritant Sensing by the human TRPA1 channel. *Neuron* **2020**, *105*, 882–894. [CrossRef]

41. Savage, S.R.; Zhang, B. Using phosphoproteomics data to understand cellular signaling: A comprehensive guide to bioinformatics resources. *Clin. Proteom.* **2020**, *17*, 27. [CrossRef] [PubMed]

42. Paulsen, C.E.; Armache, J.P.; Gao, Y.; Cheng, Y.; Julius, D. Structure of the TRPA1 ion channel suggests regulatory mechanisms. *Nature* **2015**, *520*, 511–517. [CrossRef]

43. Sura, L.; Zima, V.; Marsakova, L.; Hynkova, A.; Barvik, I.; Vlachova, V. C-terminal Acidic Cluster Is Involved in Ca2+-induced Regulation of Human Transient Receptor Potential Ankyrin 1 Channel. *J. Biol. Chem.* **2012**, *287*, 18067–18077. [CrossRef] [PubMed]

44. Hynkova, A.; Marsakova, L.; Vaskova, J.; Vlachova, V. N-terminal tetrapeptide T/SPLH motifs contribute to multimodal activation of human TRPA1 channel. *Sci. Rep.* **2016**, *6*, 28700. [CrossRef] [PubMed]

45. Hunter, T. Why nature chose phosphate to modify proteins. *Philos. Trans. R. Soc. B-Biol. Sci.* **2012**, *367*, 2513–2516. [CrossRef]

46. Dephoure, N.; Gould, K.L.; Gygi, S.P.; Kellogg, D.R. Mapping and analysis of phosphorylation sites: A quick guide for cell biologists. *Mol. Biol. Cell* **2013**, *24*, 535–542. [CrossRef]

47. Hornbeck, P.V.; Kornhauser, J.M.; Latham, V.; Murray, B.; Nandhikonda, V.; Nord, A.; Skrzypek, E.; Wheeler, T.; Zhang, B.; Gnad, F. 15 years of PhosphoSitePlus(R): Integrating post-translationally modified sites, disease variants and isoforms. *Nucleic Acids Res.* **2019**, *47*, D433–D441. [CrossRef]

48. Needham, E.J.; Parker, B.L.; Burykin, T.; James, D.E.; Humphrey, S.J. Illuminating the dark phosphoproteome. *Sci. Signal.* **2019**, *12*, eaau8645. [CrossRef]

49. Wang, C.; Xu, H.; Lin, S.; Deng, W.; Zhou, J.; Zhang, Y.; Shi, Y.; Peng, D.; Xue, Y. GPS 5.0: An Update on the Prediction of Kinase-specific Phosphorylation Sites in Proteins. *Genom. Proteom. Bioinform.* **2020**, *18*, 72–80. [CrossRef]

50. Patrick, R.; Kobe, B.; Le Cao, K.A.; Boden, M. PhosphoPICK-SNP: Quantifying the effect of amino acid variants on protein phosphorylation. *Bioinformatics* **2017**, *33*, 1773–1781. [CrossRef]

51. Blom, N.; Sicheritz-Ponten, T.; Gupta, R.; Gammeltoft, S.; Brunak, S. Prediction of post-translational glycosylation and phosphorylation of proteins from the amino acid sequence. *Proteomics* **2004**, *4*, 1633–1649. [CrossRef] [PubMed]

52. Horn, H.; Schoof, E.M.; Kim, J.; Robin, X.; Miller, M.L.; Diella, F.; Palma, A.; Cesareni, G.; Jensen, L.J.; Linding, R. KinomeXplorer: An integrated platform for kinome biology studies. *Nat. Methods* **2014**, *11*, 603–604. [CrossRef]

53. Li, T.; Li, F.; Zhang, X. Prediction of kinase-specific phosphorylation sites with sequence features by a log-odds ratio approach. *Proteins* **2008**, *70*, 404–414. [CrossRef] [PubMed]

54. Gao, J.; Thelen, J.J.; Dunker, A.K.; Xu, D. Musite, a tool for global prediction of general and kinase-specific phosphorylation sites. *Mol. Cell. Proteom. MCP* **2010**, *9*, 2586–2600. [CrossRef] [PubMed]

55. Pearlman, S.M.; Serber, Z.; Ferrell, J.E., Jr. A mechanism for the revolution of phosphorylation sites. *Cell* **2011**, *147*, 934–946. [CrossRef]

56. Gnad, F.; Ren, S.; Cox, J.; Olsen, J.V.; Macek, B.; Oroshi, M.; Mann, M. PHOSIDA (phosphorylation site database): Management, structural and evolutionary investigation, and prediction of phosphosites. *Genome Biol.* **2007**, *8*, R250. [CrossRef]

57. Humphrey, W.; Dalke, A.; Schulten, K. VMD: Visual molecular dynamics. *J. Mol. Graph.* **1996**, *14*, 33–38. [CrossRef]

58. Jorgensen, W.L.; Chandrasekhar, J.; Madura, J.D.; Impey, R.W.; Klein, M.L. Comparison of Simple Potential Functions for Simulating Liquid Water. *J. Chem. Phys.* **1983**, *79*, 926–935. [CrossRef]

59. Beglov, D.; Roux, B. Finite Representation of an Infinite Bulk System-Solvent Boundary Potential for Computer-Simulations. *J. Chem. Phys.* **1994**, *100*, 9050–9063. [CrossRef]

60. Schlenkrich, M.; Brickmann, J.; MacKerell, A.D., Jr.; Karplus, M. An Empirical Potential Energy Function for Phospholipids: Criteria for Parameter Optimization and Applications. In *Biological Membranes: A Molecular Perspective from Computation and Experiment*; Merz, K., Jr., Roux, B., Eds.; Birkhauser Boston: Cambridge, MA, USA, 1996; pp. 31–81.

61. MacKerell, A.D.; Bashford, D.; Bellott, M.; Dunbrack, R.L.; Evanseck, J.D.; Field, M.J.; Fischer, S.; Gao, J.; Guo, H.; Ha, S.; et al. All-atom empirical potential for molecular modeling and dynamics studies of proteins. *J. Phys. Chem. B* **1998**, *102*, 3586–3616. [CrossRef]

62. Phillips, J.C.; Braun, R.; Wang, W.; Gumbart, J.; Tajkhorshid, E.; Villa, E.; Chipot, C.; Skeel, R.D.; Kale, L.; Schulten, K. Scalable molecular dynamics with NAMD. *J. Comput. Chem.* **2005**, *26*, 1781–1802. [CrossRef] [PubMed]

63. Roe, D.R.; Cheatham, T.E. PTRAJ and CPPTRAJ: Software for Processing and Analysis of Molecular Dynamics Trajectory Data. *J. Chem. Theory Comput.* **2013**, *9*, 3084–3095. [CrossRef]

64. Pettersen, E.F.; Goddard, T.D.; Huang, C.C.; Couch, G.S.; Greenblatt, D.M.; Meng, E.C.; Ferrin, T.E. UCSF Chimera–a visualization system for exploratory research and analysis. *J. Comput. Chem.* **2004**, *25*, 1605–1612. [CrossRef]

BIOCHEMISTRY

Intracellular cavity of sensor domain controls allosteric gating of TRPA1 channel

Lucie Zimova,[1]* Viktor Sinica,[1]* Anna Kadkova,[1] Lenka Vyklicka,[1] Vlastimil Zima,[2]
Ivan Barvik,[2] Viktorie Vlachova[1]†

Transient receptor potential ankyrin 1 (TRPA1) is a temperature-sensitive ion channel activated by various pungent and irritant compounds that can produce pain in humans. Its activation involves an allosteric mechanism whereby electrophilic agonists evoke interactions within cytosolic domains and open the channel pore through an integrated nexus formed by intracellular membrane proximal regions that are densely packed beneath the lower segment of the S1–S4 sensor domain. Studies indicate that this part of the channel may contain residues that form a water-accessible cavity that undergoes changes in solvation during channel gating. We identified conserved polar residues facing the putative lower crevice of the sensor domain that were crucial determinants of the electrophilic, voltage, and calcium sensitivity of the TRPA1 channel. This part of the sensor may also comprise a domain capable of binding to membrane phosphoinositides through which gating of the channel is regulated in a state-dependent manner.

INTRODUCTION

Sensory neurons receive and react to a variety of extracellular stimuli, including those that cause or threaten tissue damage. To detect pungent and proalgesic agents, these neurons use a sophisticated system of transduction molecules that respond to noxious stimuli by opening intrinsic ion channel gates. One such molecule, the transient receptor potential ankyrin 1 (TRPA1) channel (*1*), gates in response to a wide range of thiol-reactive electrophiles and oxidants and to a number of chemically unrelated irritants such as menthol, carvacrol, camphor, certain cannabinoids, and many others [reviewed in (*2*–*4*)]. The opening of this cation channel leads to an increase in intracellular calcium concentration, depletion of membrane lipids, and depolarization of the membrane, and all these signals, in turn, modulate the channel's activity. Such a complexity of TRPA1 regulation at the molecular level requires the presence of a significant number of interacting domains, and despite the large number of identified sites to date, we are still far from a complete identification of them and understanding of their functions (*5*, *6*).

All transient receptor potential (TRP) channels form functional tetramers, with each subunit consisting of six transmembrane segments (S1 to S6) flanked by N- and C-terminal cytosolic domains (Fig. 1A). The helices S1–S4 form isolated sensor domains (S1–S4) arranged radially around the periphery of the central ion-conducting pore, which is lined with four S5-reentrant pore loop-S6 domains. The recent high-resolution structures of TRPA1 and its relatives TRPV1, TRPV2, TRPV6, TRPP1, and TRPN1, captured in different conformations, have yielded valuable new insights into the general principles of TRP channel functioning (*5*–*12*). In particular, the structures of three of these channels (TRPV1, TRPP1, and TRPN1) were determined in a native bilayer environment, adding especially important information about the putative sites of the TRP channel's interactions with annular and regulatory lipids (*11*, *13*–*15*). At the same time, the recent structures and sequence comparisons among TRPs point to apparent differences, suggesting different regulatory mechanisms (Fig. 1, B to D).

Using approaches from information theory and probabilistic modeling, Palovcak *et al.* (*16*) recently performed a comparative sequence analysis of almost 3000 different TRP proteins and a large comprehensive ensemble (>3700) of distantly related voltage-gated potassium (Kv) channel sequences. Remarkable differences in the evolutionarily conserved features of these two families were found between their S1–S4 sensor domains. In Kv channels, the sensors can be hydrated from both the intracellular and extracellular sides of the membrane bilayer (*17*). Penetrating water interacts with polar residues and regulates the Kv channel's voltage gating by shaping the transmembrane electric field (*18*). In contrast, solvation of the TRP's sensor is predicted to be limited to the intracellular side, whereas its upper part is packed with hydrophobic and aromatic residues (*16*, *19*). In the structurally and functionally best-characterized TRPV1 and TRPV2, the lower segment of the S1–S4 sensor domain contains highly conserved hydrophilic residues that may facilitate the solvation of this region (*7*, *8*, *16*). This portion of the channels directly interacts with endogenous lipids and C-terminal amino acids following the TRP box that probably help to stabilize the sensor during channel gating (*9*, *13*, *20*). The TRPA1's sensor is also occupied by polar residues at the base of the S1–S4 helices and the S2-S3 loop (Fig. 1, B and C), but there is practically no clear homology across this domain between TRPV1, TRPV2, and TRPA1 at the primary sequence level (Fig. 1D).

The role that the lower vestibule of the S1–S4 sensor domain plays in TRPA1 regulation is of particular interest, because this region is an important component of an allosteric nexus at which activation signals are integrated and transmitted through the TRP-like domain to the intracellular channel gate (Fig. 1A). The specific structural features of TRPA1 apparently distinct from those of TRPV channels (*5*) raise intriguing questions and prompted us to use electrophysiology combined with molecular dynamics (MD) simulations and systematic mutagenesis to explore the hypothesis that conserved polar residues form a uniquely charged and functionally important cavity in the lower part of the TRPA1 sensor domain. We show that this region does more than just act to regulate the electrophilic, voltage, and calcium sensitivity of

[1]Department of Cellular Neurophysiology, Institute of Physiology Czech Academy of Sciences, 14220 Prague, Czech Republic. [2]Division of Biomolecular Physics, Institute of Physics, Faculty of Mathematics and Physics, Charles University, 12116 Prague, Czech Republic.
*These authors contributed equally to this work.
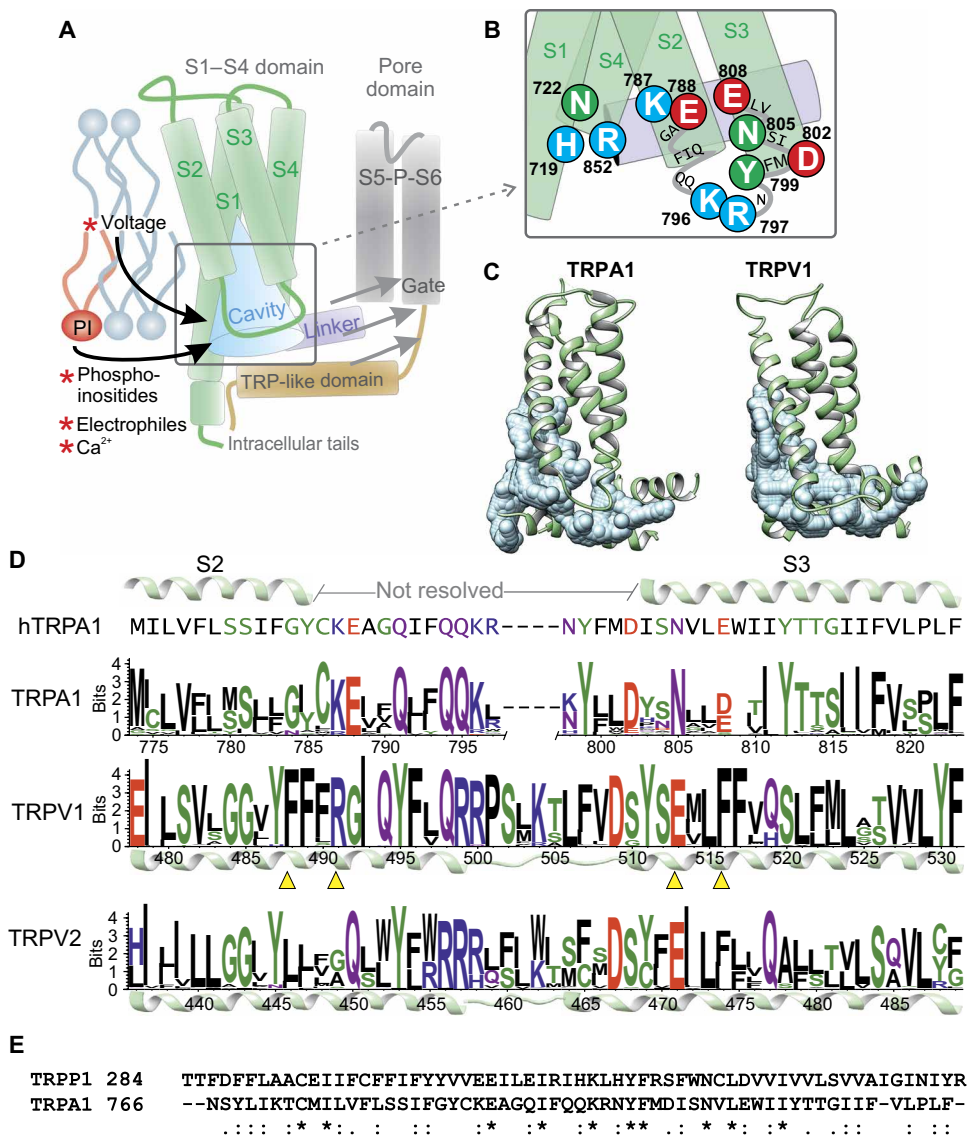†Corresponding author. Email: viktorie.vlachova@fgu.cas.cz

Fig. 1. Schematic of TRPA1 channel sensor domain. (**A**) Inner cavity (light blue funnel) formed by the lower part of the S1–S4 sensor domain and adjacent structures. S5-P-S6 refers to the central ion-conducting pore. The cavity regulates the gating of the channel (gray arrows) right in the center of the integrated nexus formed by the web of interactions between the transient receptor potential (TRP)–like domain (brown), pre-S1 helix (helix preceding S1), and S4-S5 linker (violet). Red asterisks indicate TRPA1-activating stimuli. (**B**) The positions of the cavity-facing polar residues. Amino acids are annotated by their single-letter abbreviation and residue number. (**C**) The HOLLOW script (53) was used for a "casting" of the inner cavity of TRPA1 (model constructed in this study; based on the TRPA1 3J9P structure and TRPP1 structure 5K47) and TRPV1 (5IRZ) by filling the voids with dummy atoms defined on a grid. The inner cavity of the sensor in TRP channels is predicted to be hydrated, and the extracellular part is tightly packed with bulky hydrophobic residues (16). Note the differences between the predicted hydration in TRPV1 and TRPA1 sensors. (**D**) Amino acid sequence conservation within the S2-S3 region of TRPA1, TRPV1, and TRPV2 proteins (222, 183, and 293 sequences) represented as sequence logo (54). Residues participating in phosphatidylcholine binding to TRPV1 (yellow triangles). (**E**) Sequence alignment of the human TRPP1 and TRPA1 channels used for the homology modeling. The identical, strongly conserved, and weakly conserved residues are denoted with asterisk, double dots, and single dot marks, respectively.

RESULTS

The intracellular side of the S1–S4 sensor domain forms a hydrated cavity

We constructed a model of human TRPA1 with the S1–S4 sensor domain using the 3J9P structure determined by cryo-electron microscopy (5). The intracellular loop connecting helices S2 and S3 was modeled with the use of sequence homology with the polycystin-2 TRP channel TRPP1 (Fig. 1E) on the basis of its structures with Protein Data Bank (PDB) IDs: 5K47 (12), 5T4D (14), and 5MKE and 5MKF (15) (see Materials and Methods for a detailed description of the procedure used for homology modeling and subsequent MD and ligand docking studies). The model showed that the lower cavity inside the S1–S4 sensor domain was highly hydrophilic. The following residues were oriented inward: His[719] and Asn[722] (S1); Lys[787], Gln[791], and Gln[794] (S2); Lys[796] (S2 and S3); Asp[802], Ser[804], Asn[805], and Glu[808] (S3); Tyr[849] and Arg[852] (S4); and Lys[989] (TRP-like box). The S1–S4 sensor domain was surrounded by phospholipids; however, its bottom part was in contact with water molecules. MD simulations confirmed that water molecules can permeate and reside in the lower cavity of the S1–S4 sensor domain (Fig. 2A). Further, we calculated the electrostatic potential around the TRPA1 channel (3J9P completed with the S2-S3 linker as described above) and compared it with the electrostatic potential obtained for TRPV1 [PDB ID: 5IRZ (13)] (Fig. 2B). In TRPA1, there were a negative electrostatic potential in the selectivity filter and inside the pore and a positive electrostatic potential around the intracellular ankyrin moieties. Compared to TRPV1, a notable feature of TRPA1 was that the positive electrostatic potential permeated into the intracellular part of the S1–S4 sensor domain, where there is a cluster of basic amino acids composed of Lys[787], Lys[796], Arg[852], Lys[989], and, possibly, protonated His[719].

The S1–S4 sensor domain contains a putative PIP₂ binding site

Recently, the determined structures of the TRPV1 and TRPV2 channels [PDB IDs: 5IRZ (13), 5AN8 (9), and 5HI9 (20)] revealed membrane lipids bound to the crevice formed by the S1–S4 helical bundle of the sensor

the TRPA1 channel. The sensor's cavity is capable of directly binding membrane phosphoinositides, such as phosphatidylinositol 4,5-bisphosphate [PI(4,5)P₂; also known as PIP₂], through which the channel's gating can be regulated in a state-dependent manner.

above the TRP domain. Here, we found by ligand docking that TRPA1 was also capable of binding phospholipids including PIP₂ at an analogous position. Subsequent MD simulations performed with TRPA1 in solution showed that the negatively charged inositol trisphosphate head group

Fig. 2. Modeling the sensor domain of human TRPA1. (**A**) Model of the intracellular side of the S1–S4 sensor domain, which forms a hydrated cavity. The intracellular loop connecting helices S2 and S3 was modeled using sequence homology with TRPP1 (5K47, 5T4D, 5MKE, and 5MKF) as described in Materials and Methods. Residues His[719], Asn[722], Lys[787], Lys[796], Asp[802], Asn[805], Glu[808], Arg[852], and Lys[989] were mutated in this study. (**B**) Schematic of electrostatic potential surrounding TRPA1 [Protein Data Bank (PDB) ID: 3J9P] and TRPV1 (PDB ID: 3J5P) structures was determined by means of visual molecular dynamics (*41*). Red mesh indicates a negative electrostatic potential in the selectivity filter and inside the pore. Compared to TRPV1, a notable feature of TRPA1 is that the positive electrostatic potential (blue mesh) permeates into the intracellular part of the S1–S4 sensor domain. (**C**) Model of the putative phosphatidylinositol 4,5-bisphosphate (PIP$_2$) binding site on the S1–S4 sensor domain of TRPA1. Left: Homology model of the S1–S4 sensor domains of TRPA1. The negatively charged inositol trisphosphate head group of PIP$_2$ contacts residues His[719], Asn[722], Lys[787], Lys[796], Arg[852], and Lys[989]. Right: Four PIP$_2$ molecules located in the four identical binding pockets (left) shown in the context of the template 3J9P structure completed with the model of the S1-S2 and S3-S4 linkers.
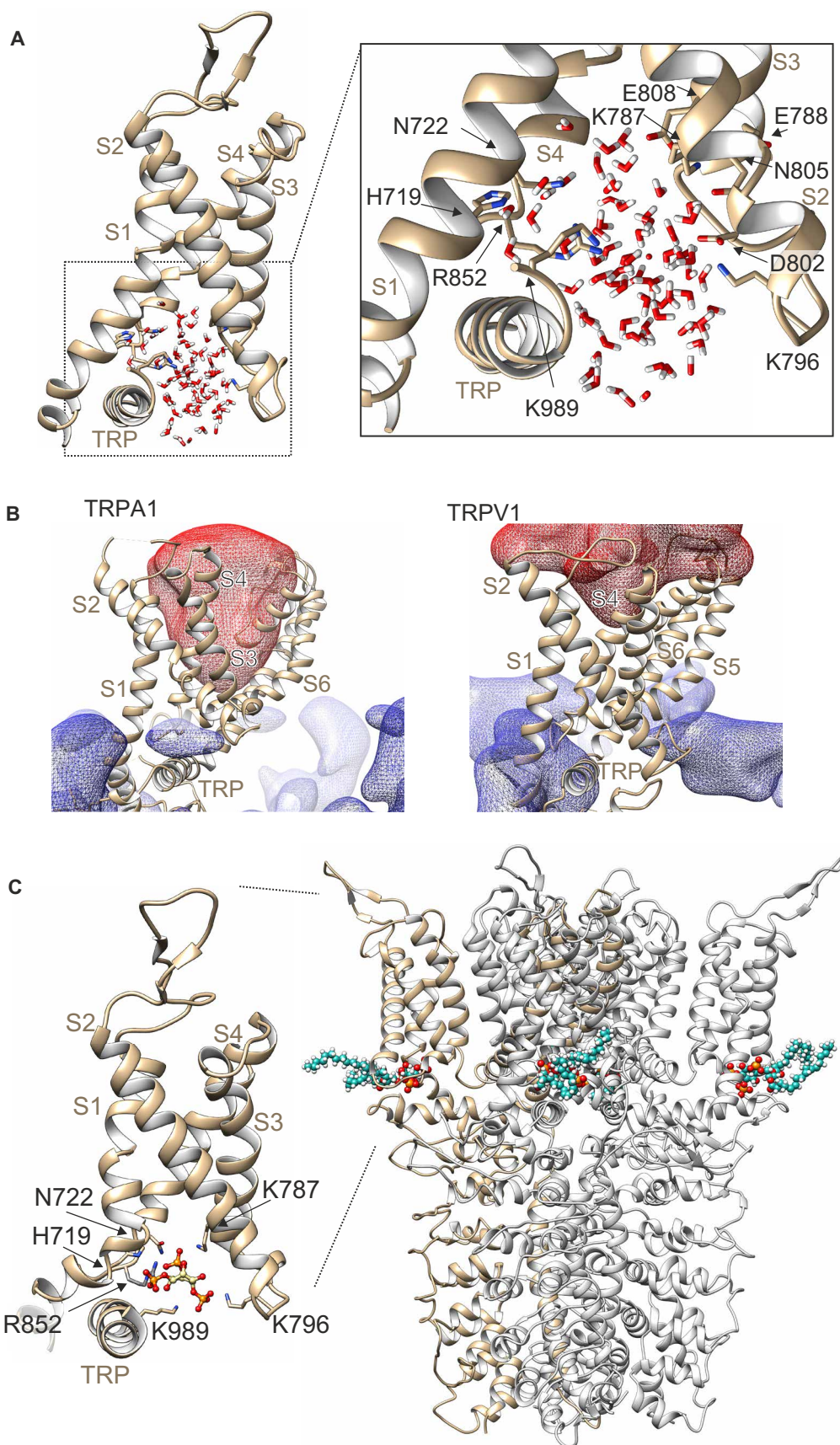
of PIP$_2$ may adopt several different conformations within the S1–S4 sensor domain of TRPA1 to contact residues His[719], Asn[722], Lys[787], Lys[796], Arg[852], and Lys[989] (Fig. 2C).

Polar residues in the inner cavity of the sensor regulate the voltage-dependent gating of TRPA1

To assess the functional roles of polar amino acids predicted to face the cavity of the sensor domain of TRPA1, we individually mutated the polar residues located in this region (Figs. 1B and 2A) and measured the voltage-dependent activation properties of the mutants transiently expressed in human embryonic kidney (HEK) 293T cells using whole-cell electrophysiology. The conductance-to-voltage (*G-V*) relationships were assessed in control bath solution using a voltage step protocol from −80 to +200 mV, in 20-mV increments (Fig. 3A). Intracellular Ca^{2+} was routinely buffered to low levels
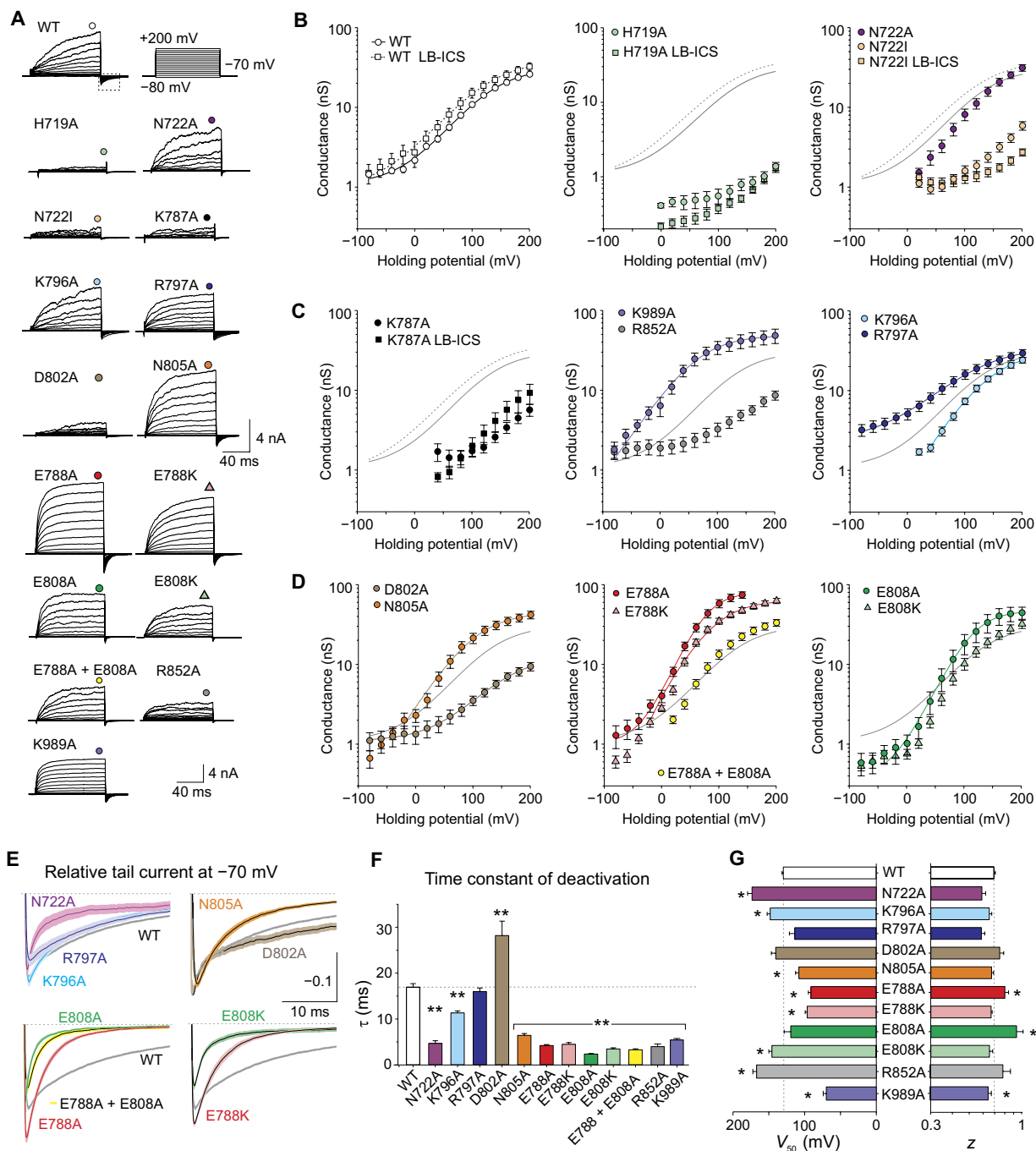
Fig. 3. Voltage-dependent gating of TRPA1 mutants. (**A**) Representative family of whole-cell currents recorded from human embryonic kidney (HEK) 293T cells transfected with either wild-type human TRPA1 channel (WT) or the indicated mutants elicited with a voltage step protocol consisting of 100-ms depolarizing pulses from −80 up to +200 mV in steps of 20 mV and a holding potential of −70 mV. The voltage protocol is shown in the top right panel. Bath solution contained 160 mM NaCl, 2.5 mM KCl, 1 mM CaCl₂, 2 mM MgCl₂, 10 mM Hepes, and 10 mM glucose (adjusted to pH 7.3 and 320 mosmol). The currents were recorded ~1 min after whole-cell formation. Steady-state currents were measured at the end of the pulses as indicated by colored symbols atop each record. (**B** to **D**) Average conductances obtained from recordings as in (A). Data are means ± SEM (n = 132 cells for wild-type and n = 6 to 30 cells for mutants from at least two independent transfections). The lines represent the best fit to a Boltzmann function for wild-type and mutant TRPA1 (gray and colored lines) using high-buffer (solid lines) or low-buffer intracellular solution [(LB-ICS); dashed lines]. (**E**) Deactivation kinetics of TRPA1 mutants. Averaged tail currents normalized to the maximum amplitude at +200 mV obtained as indicated by dashed box in (A, top left) for the wild-type channel. The average currents are shown with color bars indicating means ± SEM [number of cells indicated in (B) to (D)]. The gray lines with gray bars (SEM) represent the averaged tail currents obtained from data for wild-type TRPA1. Dashed lines indicate zero current. (**F**) The average time constants obtained from single exponential fits of tail currents. The asterisks indicate a significant difference from wild-type channels [**P < 0.001; n as in (B) to (D)]. (**G**) Summary of half-activation voltage (V_{50}) and apparent number of gating charges (z) from experiments in (B) to (D). *P < 0.05; analysis of variance (ANOVA) on ranks followed by Dunn's test versus WT.

with 5 mM EGTA in the patch pipette to prevent the synergistic potentiation of voltage-induced currents by permeating calcium ions (*21*). In other experiments, low-buffer intracellular solution (LB-ICS) containing 100 µM instead of 100 nM free Ca^{2+} was additionally used to assess the activation capacity of the less responsive mutants (Fig. 3B).

In cells expressing the H719A, N722A, N722I, K787A, K796A, R852A, and E808K mutant channels, the *G-V* curves were significantly shifted rightward compared to wild-type channels (Fig. 3, B to D). Notably, currents through the H719A and N722I channels were significantly suppressed by using LB-ICS in the pipette (Fig. 3B, middle and right), whereas currents through the less responsive K787A mutant channels were not significantly affected (Fig. 3C, left), indicating the involvement of these residues in Ca^{2+} sensitivity. The E788A, E788K, N805A, E808A, and K989A mutants exhibited significantly increased currents at positive membrane potentials. The E788A and E808A constructs had much steeper *G-V* relationships, reflecting a changed apparent number of gating charges from $z = 0.69\ e_o$ for wild-type channels to 0.80 and 0.94 e_o for E788A and E808A, respectively. The most notable effect of the mutations at His[719], Asn[722], Lys[787], Lys[796], Glu[788], and Glu[808] was that these channels closed extremely quickly upon repolarization from +200 to −70 mV, resulting in faster tail currents (Fig. 3, A, E, and F). Because inward currents were significantly attenuated at hyperpolarized voltages in these mutants, the steady-state half-activation voltage (V_{50}) values and z derived from *G-V* relationships could only be reliably estimated over the positive voltage range (Fig. 3, B to D and G). D802A channels opened slowly and exhibited slowly decaying tail currents that remained transiently open upon repolarization to −70 mV (Fig. 3E). The R797A mutant displayed significantly increased basal conductance at negative potentials (Fig. 3C, right), suggesting that this mutation disturbed the closed-open equilibrium in favor of the open state.

Together, these data indicated that the neutralizations of negative charges quite deep in the cavity facilitated conformational transitions upon voltage stimulation, and the other polar residues also critically contributed to the voltage-dependent gating of TRPA1. Of these, H719 and K787 appeared to play a central role, because their neutralization mostly disrupted the ability of the channel to gate in response to depolarization. Likewise, substitution of the crevice facing asparagine N722 with a large hydrophobic residue disrupted voltage-dependent gating.

Mutations deep in the cavity strengthen Ca^{2+}-induced inactivation

To test the overall chemical sensitivity of the mutants, we used a previously established protocol (*21*, *22*) in which currents were first induced by the electrophilic agonist in the absence of external Ca^{2+} (Fig. 4, A to L, and fig. S1). The agonist was then washed out for 10 s, and 2 mM Ca^{2+} was added to the extracellular solution to assess the allosteric effects of permeating calcium ions. The membrane potential was linearly ramped up each second from −80 to +80 mV (1 V/s). In the standard procedure, cinnamaldehyde (100 µM) or allyl isothiocyanate (AITC; 100 µM) was used as a partial and a full agonist, whereas intracellular Ca^{2+} was buffered to low levels with 5 mM EGTA in the patch pipette. The less responsive mutants were also tested using the LB-ICS. The average responses through wild-type channels (Fig. 4, A and G) were in full accordance with the ones from previous papers (*21*, *22*). In H719A, N722I, and K787A, the AITC-induced currents were slowly developing and outwardly rectifying (Fig. 4, B, D, and E).

These changes were even more evident from the rectification ratio (−current at −80 mV/current at +80 mV) plotted as a function of time (fig. S2). The currents through N722A channels activated slowly but, ultimately, within 40 s, reached their maximum amplitude at +80 mV similar to the wild-type channels (Fig. 4C). K787A was partially rescued by increasing intracellular Ca^{2+} in the patch pipette (Fig. 4E), and the currents resembled the AITC responses obtained from R852A channels [Fig. 4F; (*23*)]. In the above mutants, the addition of Ca^{2+} to the bath solution induced an immediate inactivation that was almost complete at negative membrane potentials. The average responses to cinnamaldehyde (100 µM) through the K796A and R797A channels were consistently much larger than those through wild-type channels (Fig. 4, H and I), and their rectification ratio was apparently increased in the presence of external Ca^{2+} (fig. S2, H and I). Responses to cinnamaldehyde through D802A were initially smaller, but the addition of Ca^{2+} to the bath solution potentiated the currents so that their magnitudes reached the maximum responses of the wild-type TRPA1 (Fig. 4J). The AITC currents through D802A were slower, their average amplitudes exceeded the wild-type responses at negative potentials, and the addition of external Ca^{2+} inactivated the currents more intensively than in the wild type (Fig. 4K). The K989A channels were constitutively active in the absence of external Ca^{2+} and characterized by saturating cinnamaldehyde-induced currents that were not further potentiated by external calcium (Fig. 4L).

Together, these results suggested that the mutations at residues His[719], Asn[722], Lys[787], Asp[802], Arg[852], and Lys[989] induced functional defects manifested as significant changes in rectification that depend on the activation state of the channel, indicating that these residues are important for the allosteric coupling between voltage and agonist sensing and gate opening. Moreover, the prominent and immediate inactivation by external Ca^{2+} observed in some of these mutants suggested that neutralizations in the inner cavity of the sensor may also strengthen the allosteric coupling between putative domain(s) responsible for Ca^{2+}-dependent inactivation and the channel's gate. In D802A, the time constant of Ca^{2+} inactivation was independent of the agonist used and the extent of channel activation (23 ± 1 s and 25 ± 1 s for cinnamaldehyde and AITC, respectively; Fig. 4, J and K), suggesting that the external Ca^{2+} stimulus avoids the electrophile-dependent activation machinery and works through a separate pathway.

Glu[808] interacts with key Lys[787], whereas Glu[788] helps to transduce the signals to the gate

The E788A and E808A mutants displayed robust responses to cinnamaldehyde, reaching more than twice the maximum currents obtained from the WT-TRPA1 at +80 mV (Fig. 5, A and B). The cinnamaldehyde-induced currents mediated by E808A exhibited a slow onset at negative membrane potentials, as was visible from the time course of the rectification ratio (Fig. 5B, bottom). Although, in wild-type channels, the rectification ratio typically increased slightly upon stimulation with cinnamaldehyde from about 0.5 to 0.7 in 40 s; the currents through E808A reached a maximum rectification of only about 0.4 and displayed a shift in gating equilibrium toward positive membrane potentials and a hindered opening at negative potentials. The mutation E788K produced channels that readily opened in response to cinnamaldehyde, exhibiting a rectification ratio of about 0.9, suggesting a close-to-saturation state (Fig. 5C, bottom). The charge-reversal mutant E808K closely resembled the double-mutant E788A/E808A in that the currents recorded

Fig. 4. Mutations in the inner cavity of sensor module affect chemical-dependent gating of TRPA1. (**A**) Time course of average whole-cell currents induced by 100 μM allyl isothiocyanate (AITC) measured at +80 and −80 mV in HEK293T cells transfected with wild-type TRPA1 (open circles). Inset shows voltage-ramp protocol used for measuring currents. The cells were first exposed to the electrophilic agonist (AITC) in the absence of external Ca^{2+} using the bath solution containing 2 mM HEDTA. The agonist was then washed out for 10 s, and 2 mM Ca^{2+} was added to the extracellular solution as indicated above the current traces. Data are mean + SEM (open circles; $n = 34$ cells). In some cases, the error bars are smaller than the symbol. The dashed line represents the average currents obtained for WT using low-buffer intracellular solution (LB-ICS) ($n = 11$ cells). Zero current is indicated by the horizontal line. (**B** to **F**) Time course of average AITC-induced currents recorded from the indicated mutant channels using either high-buffer intracellular solution (circles) or LB-ICS (squares). Data are means + SEM ($n = 6$ to 13 cells). The average current for WT is overlaid as a gray line with gray bars indicating mean + SEM (high-buffer pipette solution) or dashed gray line representing the average current for WT obtained with LB-ICS. (**G**) Average whole-cell currents induced by 100 μM cinnamaldehyde (CA) in Ca^{2+}-free solution and then exposed to 2 mM Ca^{2+} measured at +80 and −80 mV in WT. The application of CA and subsequent addition of 2 mM Ca^{2+} are indicated above. Data are mean + SEM ($n = 45$ cells). (**H** to **L**) Average currents recorded from mutant channels. The average current for the WT is shown as a gray line with bars indicating + SEM. Data are mean + SEM ($n = 7$ to 9 cells). In some cases, the error bars are smaller than the symbol.
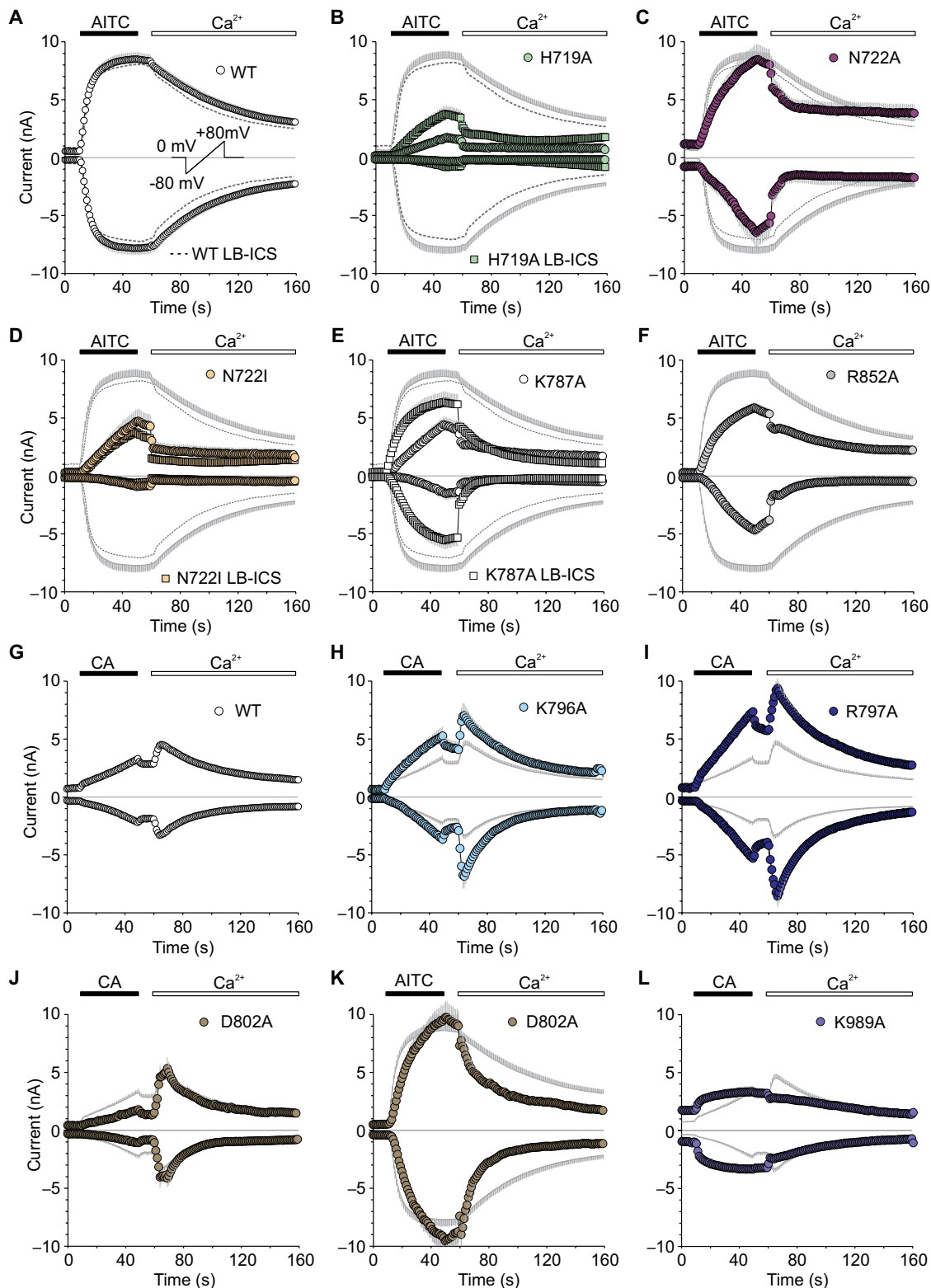

during the 40-s application of cinnamaldehyde were fully superimposable onto those obtained with WT-TRPA1 (Fig. 5, D and E). Notably, in all the constructs above, the subsequent exposure to extracellular Ca^{2+} caused a rapid inactivation of cinnamaldehyde-induced currents, in-

stead of potentiation seen with wild-type channels. Except for E788K, the Ca^{2+}-induced block was more pronounced at negative membrane potentials. AITC-induced responses were saturated in E788A, E788K, and E808A, whereas in E808K and E788A/E808A, they did not reach the

Fig. 5. Mutations in internal sensor domain increase the sensitivity of TRPA1 and strengthen Ca²⁺-induced inactivation. (**A** to **E**) Time course of average cinnamaldehyde (100 μM)–induced currents recorded from HEK293T cells transfected with either wild-type TRPA1 channel (WT) or the indicated mutants. The overlaid gray line with gray bars represents the average currents + SEM obtained for wild-type TRPA1 as in Fig.4G. Below each panel, average rectification of currents shown above (−current at −80 mV/current at +80 mV) plotted as a function of time. Colored symbols and lines with gray bars indicate means + SEM (n = 45 cells for WT and n = 7 to 9 cells for mutants). (**F**) Bottom view of the inner cavity of TRPA1 sensor domain. (**G**) Representative current traces from E788I in response to voltage step protocol shown in Fig.3A recorded in control extracellular solution containing 1 mM Ca²⁺ (left; indicated above as 1 mM [Ca²⁺]ₒ) or in Ca²⁺-free bath solution (right; indicated above as 0 mM [Ca²⁺]ₒ). Bottom: Averaged tail currents recorded from cells expressing E788I (lines with yellow and pink bars indicating means ± SEM; n = 20 and 16 cells, respectively) and WT (superimposed gray lines with gray bars indicating means ± SEM; n = 132 and 10 cells, respectively). (**H** to **I**) Average conductances obtained from HEK293T cells transfected with the indicated mutants compared with WT human TRPA1 channel. The currents elicited with a voltage step protocol were measured at the end of the pulses as indicated by colored circles atop the traces in (G). The average conductance obtained from the WT in control extracellular solution (n = 132 cells) is shown as a gray line. Data are means ± SEM for WT measured in Ca²⁺-free bath solution (open circles; n = 10 cells) and for N805A and Y799A recorded in control extracellular solution containing 1 mM Ca²⁺ (colored circles; n = 15 and 13 cells, respectively). Solid lines are best fits to a Boltzmann function. (**J** to **L**) Time course of average CA-induced currents through indicated mutants measured at +80 and −80 mV. The average current for the WT is shown as a gray line with bars indicating means ± SEM (n = 45 cells for WT and n = 8 cells for each of the mutants). Bottom: Mean rectification ratio for the cells shown above (colored lines with gray bars indicating means + SEM) plotted against time.

wild-type level (fig. S1), indicating the activation-dependent roles of these residues.

These distinctive effects of mutations argued against a mechanism of simple electrostatic interactions among the charged residues in the internal sensor cavity. Rather, they indicated that some other factor is required as an intermediary for a series of allosteric steps that are necessary for a proper regulation of TRPA1. One possibility emerging from our molecular modeling was that conformational changes underlying the transition of the channel between
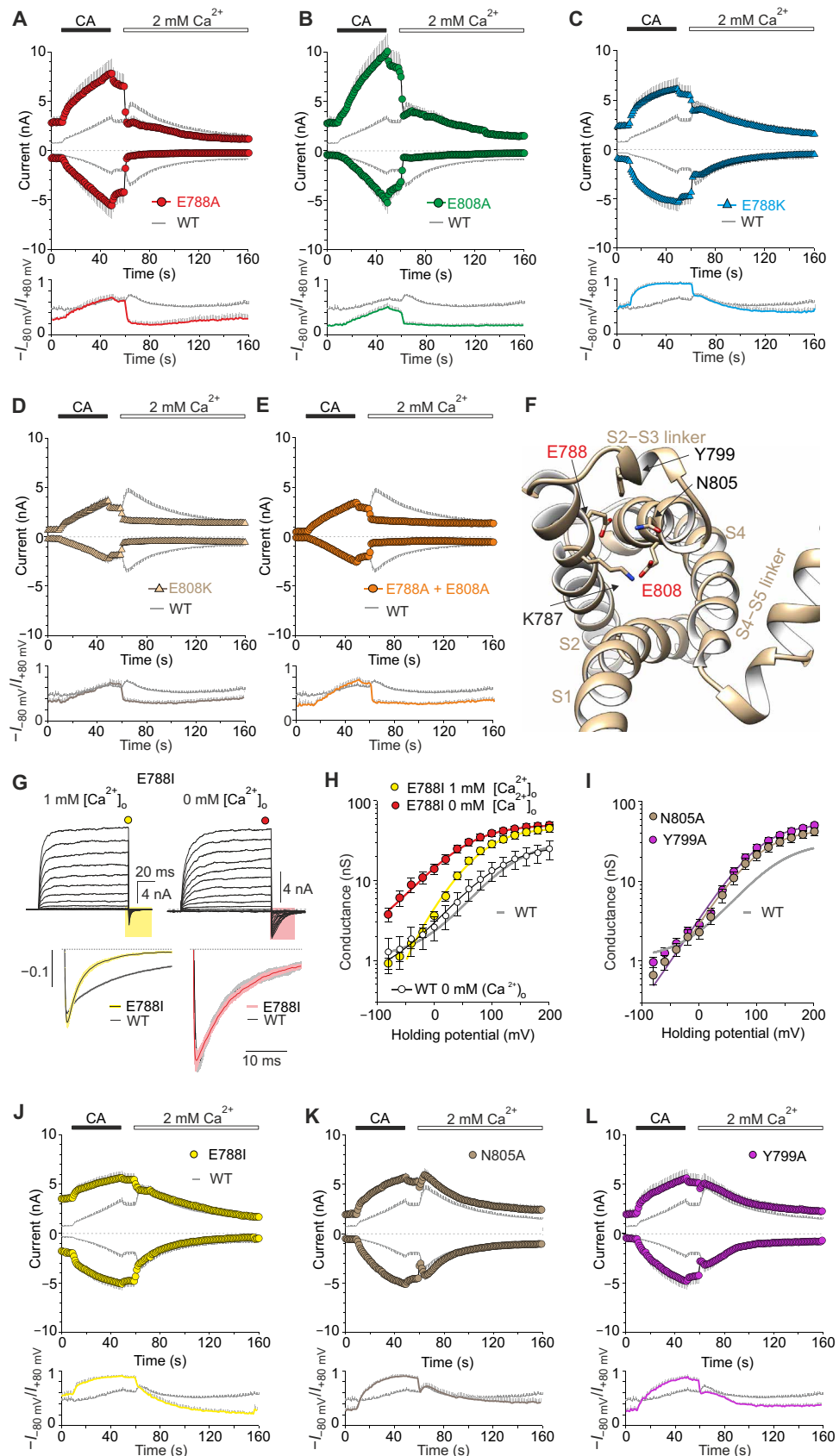
the closed and open states are influenced by changes in the water accessibility of the inner crevice of the sensor domain. The other possibility was indicated by our docking studies implying that Asn^{722}, and Lys^{787}, together with His^{719}, Lys^{796}, Arg^{852}, and Lys^{989} may constitute a binding site for phosphoinositides (Fig. 2C). These models are not mutually exclusive, because changing the occupancy of water within the crevice and/or a disruption of the binding pocket may, in a state-dependent manner, affect the strength of allosteric coupling between the putative voltage- and Ca^{2+}-sensing domains and the gate.

Inner cavity of the sensor is a Ca^{2+}-sensing domain

In our structural model, the key lysine residue, K787, forms salt bridge interactions with one glutamate residue, Glu^{808}, whereas the neighboring Glu^{788} is oriented away from the cavity (Fig. 5F) and located about 2 to 3 Å from Tyr^{799}, which, in turn, is about 3 Å from Asn^{805}. Because the size and not the charge of the residue at position Glu^{788} was important for effective gating, we further substituted Glu^{788} with a bulky hydrophobic isoleucine to explore whether Glu^{788} might contribute to the processes by which the various signals from the cavity could be propagated throughout the sensor domain (Fig. 5, G and H). The voltage-induced currents through E788I mutant channels closely resembled those mediated by E788K mutant channels (Fig. 3D). The tail currents upon repolarization from +200 to −70 mV normalized to the maximum amplitude at +200 mV, measured in the standard bath solution, which contained 1 mM Ca^{2+}, were much faster in E788I mutant channels, but upon the removal of Ca^{2+}, the traces were superimposable onto those obtained with wild-type TRPA1 (Fig. 5G). Upon the removal of Ca^{2+} from the extracellular medium, the G-V relationship of E788I channels was significantly shifted leftward by −35 mV (z from 0.7 to 0.6 e_o; Fig. 5H). This result supported the involvement of Glu^{788} in the Ca^{2+}-dependent regulation of TRPA1 and argued against the relevance of the polarity of this residue for channel deactivation under Ca^{2+}-free conditions. Also consistent with our hypothesis, the voltage- and agonist-induced currents through N805A and Y799A channels almost completely overlapped, resembled those of the E788I channels, and were characterized by large and saturating cinnamaldehyde-induced currents that were not further potentiated by Ca^{2+}, indicating that these residues use the same transduction pathway and participate in the putative mechanism through which TRPA1 is modulated by permeating Ca^{2+} (Fig. 5, J to L; note the striking resemblance of the mutant phenotypes).

On the basis of this information, we further explored a working model of channel activation that can account for the observed voltage- and calcium-dependent TRPA1 current characteristics (Fig. 6). In this model, we hypothesized that the lower cavity needs to be occupied by a phospholipid (as in the wild-type channels) to enable proper gating upon voltage stimulation and upon agonist stimulation (Fig. 6A). When the mutations (H719A, K787A, and N722A/I) prevent the stabilization of the sensor domain by phospholipids, the channel tends to be closed (Fig. 6B), whereas mutations (E788A and E808A) with putative propitious effects on PIP_2 binding cause gain-of-function phenotypes (Fig. 6C), perhaps by keeping the channel in a state that is primed for activation. Moreover, any alternation of the polarity balance deep in the cavity causes a Ca^{2+}-dependent block of currents at negative membrane potentials (Fig. 6D).

Structural comparisons of the lipid binding site densities among the TRPV1 and TRPV2 at different conformations suggested that interaction of the crevice formed by the S1–S4 helical bundle above the TRP domain with lipids is dynamic and possibly depends on the
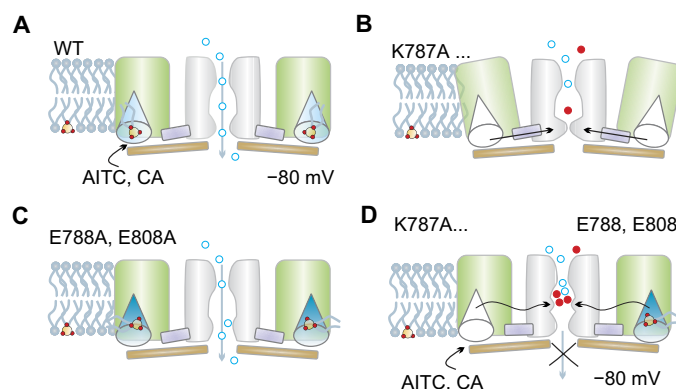
Fig. 6. Proposed mechanism for regulation of human TRPA1 by the inner cavity of sensor domain. The diagram of the transmembrane part of the TRPA1 channel only shows two of the four subunits for clarity. The sensor domains (S1–S4; green) are connected through the S4-S5 linkers (lilac) to the pore domains (S5 and S6; gray). The TRP-like domain (brown) interacts with the S4-S5 linker through hydrophobic interactions. The inner cavities of the sensor domains are shown as a light blue cone for the wild-type channel. Sodium and calcium ions (blue and red circles) are indicated. (**A**) In the absence of external Ca^{2+}, the cavity can be occupied by a phospholipid (PIP_2; lipids with yellow and red phosphate head groups) to enable proper gating at negative membrane potentials. (**B** and **C**) When the mutations (K787A, H719A, N722A/I, and R852A) prevent the stabilization of the sensor by phospholipids (indicated with a white cone), the channel tends to be closed (B), whereas mutations (E788A and E808A) with putative beneficial effects on phosphoinositide binding (indicated with a dark blue cone) cause an increase in currents in the absence of external Ca^{2+} (C). (**D**) Any alteration to the polarity balance deep in the cavity causes a Ca^{2+}-dependent block of currents elicited by electrophilic agonists.

channel activation state (20). Our results supported a similar role of lipids for TRPA1. In our model, the residues Asn^{722}, Lys^{787}, and Glu^{808} directly contact Tyr^{726} (fig. S3, A and B) and help to keep its side chain in an orientation analogous to Tyr^{400} in TRPV2. This tyrosine is in a direct contact with the membrane lipid in TRPV2 (20). It is noteworthy that in TRPA1, the neighboring residue of the cognate Tyr^{726} is the reactive cysteine Cys^{727} and its reactivity depends on the extent of TRPA1 activation (24). This may indicate that this part of the channel undergoes structural changes during electrophilic activation. To test this hypothesis, we measured cinnamaldehyde- and AITC-induced whole-cell currents from the C727A and C727S mutants (fig. S3, C and D). In the absence of external Ca^{2+}, these mutants did not exhibit changes in their responsiveness to electrophilic agonists. However, the addition of Ca^{2+} to the bath solution induced a significantly stronger inactivation of cinnamaldehyde-induced responses than in wild-type channels but not of the currents induced by the full agonist AITC. This result supported the hypothesis that the sensor domain was involved in Ca^{2+}-induced inactivation and that this process was activity-dependent.

Membrane PIP_2 may stabilize TRPA1 in an open conformation

Reports are inconsistent regarding the effects of PIP_2 on TRPA1 [reviewed in (25)]. Although there are indications that PIP_2 has a positive modulatory effect on TRPA1 (26, 27), some reports suggest that PIP_2 either does not affect (21, 28) or down-regulates TRPA1 (29, 30). In our study, mutations of the residues putatively involved in PIP_2 binding (His^{719}, Asn^{722}, Lys^{787}, Lys^{796}, Arg^{852}, and Lys^{989}) resulted in a partial loss of functional response to voltage and the low-affinity electrophilic agonist cinnamaldehyde (Figs. 3 and 4). Thus, if phosphoinositides (particularly

PIP$_2$) bind the TRPA1 channel through the inner cavity of the sensor domain, then we would expect that the depletion of membrane PIP$_2$ could down-regulate the wild-type channels (Fig. 6). To clarify this issue, we used three different approaches to manipulate the membrane PIP$_2$ levels and measured responses from wild-type TRPA1 (Fig. 7).

First, we coexpressed TRPA1 with myristoylated alanine-rich C-kinase substrate (MARCKS). This protein has basic domains capable of laterally sequestering membrane PIP$_2$, depending on a local increase in intracellular Ca^{2+} concentration (31, 32). The expression of MARCKS in HEK293T cells should cause membrane PIP$_2$ to be sequestered by MARCKS and, therefore, less available for the supposed interaction with coexpressed TRPA1. In line with our hypothesis, we observed that the sequestration of PIP$_2$ by MARCKS had detrimental effects on wild-type TRPA1 functioning (Fig. 7A). Upon voltage stimulation, the responses were completely inactivated at negative potentials, resembling the currents mediated by H719A, K787A, N722I, and K796A. The G-V curves were significantly shifted rightward, and the cinnamaldehyde-evoked currents were significantly smaller than the wild-type responses. Moreover, the onset of agonist-induced responses was delayed at negative membrane potentials as in the mutants N722A, K787A, and R852A, which we predicted to be disruptive of the TRPA1-phospholipid interaction. The addition of external Ca^{2+} to cells preactivated for 40 s with cinnamaldehyde caused an immediate influx of Ca^{2+}, which should result in a release of PIP$_2$ sequestered by MARCKS. Next, we assumed that the neutralization of Glu^{808} might positively influence a putative channel-phosphoinositide interaction. We hypothesized that if the interacting lipid is PIP$_2$, then its sequestration by MARCKS should attenuate the current responses of E808A. The actual changes observed in HEK293T cells coexpressing MARCKS with E808A channels matched this assumption reasonably well (Fig. 7B). The voltage-gated currents were suppressed to the wild-type level at positive holding potentials, and the channels were completely blocked at negative potentials. The cinnamaldehyde-induced currents also decreased to the wild-type level, and a subsequent exposure to Ca^{2+} caused an immediate block, as was previously observed for E808K and E788A/E808A.

In the second approach, we coexpressed TRPA1 with growth-associated protein 43 (GAP43; also known as neuromodulin). Whereas MARCKS sequesters PIP$_2$ under low-Ca^{2+} conditions, GAP43 sequesters PIP$_2$ when the cytoplasmic Ca^{2+} concentration is increased (31, 32). Furthermore, only one point mutation in GAP43, R43A, produces a phenotype that sequesters PIP$_2$ regardless of the Ca^{2+} concentration (33), thus providing an excellent control for our experiments. The same series of experiments as with MARCKS was performed with either the wild-type GAP43 (WT-GAP43) or R43A-GAP43 mutant coexpressed with wild-type TRPA1 (Fig. 7, C and D). Coexpression of WT-GAP43 did not change the TRPA1 profiles of current responses induced by cinnamaldehyde in the absence of external calcium, as expected for these control measurements. Switching to the extracellular solution containing 2 mM calcium sensitized the responses to a greater extent than that observed for the wild-type TRPA1 alone. Coexpression of the mutant R43A-GAP43, which was expected to sequester PIP$_2$ independently of calcium concentration, resulted in reduced current amplitudes, practically identical to those obtained with the expression of MARCKS (Fig. 7A), which supported the idea that the observed changes in activation kinetics of TRPA1 may be caused by a lack of available PIP$_2$ in the plasma membrane.

In the third approach, we used a voltage-sensitive lipid 5-phosphatase from *Danio rerio* (Dr-VSP). The activity of this enzyme can be induced by depolarization greater than +50 mV and results in the hydrolysis of PIP$_2$ [PI(4,5)P$_2$ to PI(4)P] (34, 35). Whereas the above coexpression approaches allow for the equilibration of free PIP$_2$ with closed channels, the acute stimulation of Dr-VSP only dynamically affects the channels upon depolarization to +80 mV. At these potentials, the channels opened with a probability of about 25% in the absence of any agonist (Fig. 3B). We coexpressed Dr-VSP with TRPA1 and stimulated the cells with a 2-s depolarizing prepulse to +80 mV before each application of the standard voltage step protocol (Fig. 7E). In cotransfected cells, the rightward shift in the G-V curves was similar to the effects seen with MARCKS and R43A-GAP43, in support of a PIP$_2$-promoting role in voltage-dependent gating. In the next series of experiments, we measured responses to cinnamaldehyde using a standard protocol in which the membrane potential was linearly ramped up each second from −80 to +80 mV (1 V/s). The cinnamaldehyde-induced currents measured from the cells coexpressing TRPA1 with Dr-VSP were selectively suppressed at negative membrane potentials (Fig. 7E). The subsequent addition of extracellular Ca^{2+} potentiated the currents at both positive and negative membrane potentials, more than we observed in cells expressing TRPA1 alone. Collectively, the results indicated that a reduction in PIP$_2$ leads to a rightward shift in G-V characteristics and, unambiguously at least at negative membrane potentials, a reduction in cinnamaldehyde-induced currents.

Apparently, the effects of PIP$_2$ modulation by the "pipmodulins" MARCKS, GAP43, R43A-GAP43, and Dr-VSP were obscured upon the addition of external Ca^{2+} (Fig. 7, A to E). This indicated that PIP$_2$ may modulate TRPA1 in a state-dependent manner, with PIP$_2$ preferentially occupying closed states until the potentiating effect of Ca^{2+} prevails. To further clarify this observation, we measured the cinnamaldehyde-induced responses from cells coexpressing TRPA1 with MARCKS, GAP43, or R43A-GAP43 while using the LB-ICS containing 100 μM free Ca^{2+}. The channels appeared to more readily respond to cinnamaldehyde and exhibited a greater degree of inactivation upon the addition of Ca^{2+} to the extracellular medium (fig. S4, A to C). Notably, the presence of GAP43, but not of R43A-GAP43, significantly increased the currents, suggesting a specific and Ca^{2+}-dependent action of GAP43 on TRPA1 (fig. S4, B and C). This observation indicated that PIP$_2$ may compete with Ca^{2+} to confer the potentiation of TRPA1.

Glu^{808} regulates activation of TRPA1 under physiological temperatures

Because TRPA1 is considered as a thermosensitive channel, we further explored whether the identified residue Glu^{808} plays a general role in channel activation under physiological temperatures. We measured currents at 25° and 35°C using 200-ms voltage ramps from −100 to +100 mV (fig. S5, A to H). Currents through wild-type and mutant channels measured in control extracellular solution at 25°C exhibited outward rectification that was significantly more pronounced by increasing the temperature to 35°C (fig. S5, A to E). The outward currents at +80 mV were potentiated 1.9-fold in wild-type channels, which is in agreement with a previously reported finding (36). E808A mutation produced currents that were potentiated only 1.5-fold at 35°C. In the presence of an agonist (50 μM carvacrol), increasing the temperature from 25° to 35°C reduced the rectification ratio about 2-fold in wild-type channels but only ~1.5-fold in E808A (fig. S5, F to H). This mutation rendered the channel insensitive to the agonist at negative membrane potentials and significantly decreased its temperature dependence. This result demonstrated that Glu^{808} may participate in temperature regulation of TRPA1. The significant
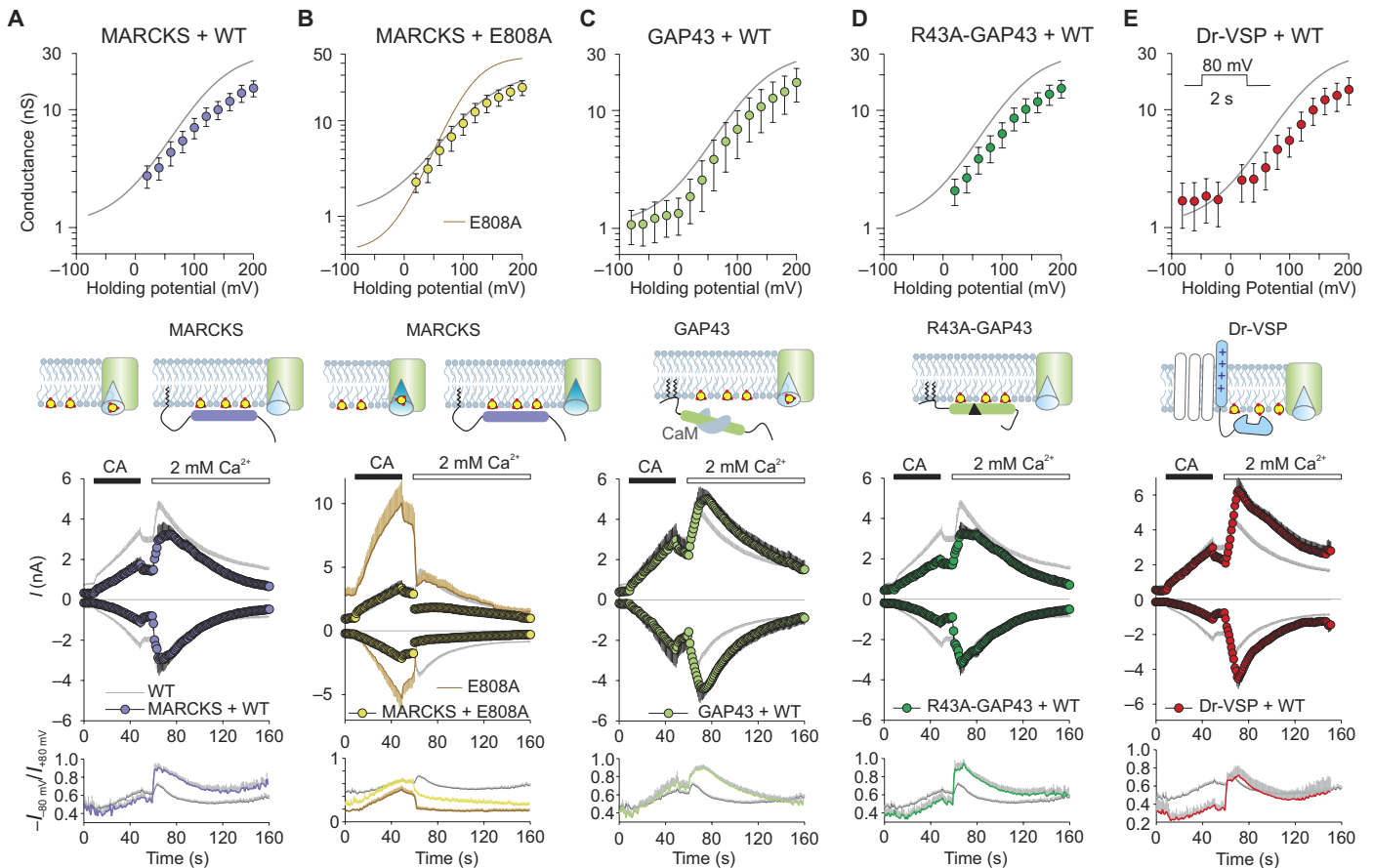
Fig. 7. Sequestering or reducing membrane PIP$_2$ inhibits voltage- and cinnamaldehyde-induced TRPA1 currents. (**A** to **D**) Top: Average conductances obtained from HEK293T cells transfected with the indicated protein combinations measured in control bath solution containing 160 mM NaCl, 2.5 mM KCl, 1 mM CaCl$_2$, 2 mM MgCl$_2$, 10 mM Hepes, and 10 mM glucose (adjusted to pH 7.3 and 320 mosmol). The solid lines of the WT (gray) or E808A mutant (brown) are the best fits to a Boltzmann function, as described in Materials and Methods and shown in Fig.3 (B and D). Data are means ± SEM (n = 7 to 13 cells from at least two independent transfections). Bottom: The time course of average currents induced by cinnamaldehyde (100 μM) and by external Ca^{2+} (2 mM) measured at +80 and −80 mV, as described in Fig.4G. The average current through TRPA1 expressed alone is overlaid as a gray line, with bars indicating SEM (n = 45 cells) for comparison. A schematic model of the mechanism is indicated for each "pipmodulin" above. PIP$_2$ molecules are indicated as lipids with yellow and red phosphate head groups. Data are means ± SEM (n = 7 to 11 cells from at least two independent transfections). Bottom: Average rectification of currents shown above expressed as absolute values of the amplitudes of inward currents at −80 mV divided by outward currents at +80 mV and plotted as a function of time. The average rectification of TRPA1 expressed alone is overlaid as a gray line with gray bars indicating SEM (n = 45 cells) for comparison. MARCKS, myristoylated alanine-rich C-kinase substrate; GAP43, growth-associated protein 43. (**E**) The same experiments described in (A) to (D) performed with TRPA1 coexpressed with voltage-sensitive lipid 5-phosphatase from *Danio rerio* (Dr-VSP). The voltage step protocol was preceded by a 2-s depolarization to +80 mV. Colored symbols and lines with gray bars indicate average ± SEM (n = 7 to 9 cells).

effects of the alanine mutation causing the channel to remain closed at physiological membrane potentials and to be less affected by warm temperatures indicated that this residue is, in essence, irreplaceable for the proper functioning of the TRPA1 channel under close to physiological conditions.

DISCUSSION

TRPA1 is the only known ion channel that is capable of responding to both cold and heat (*36*). Such a bidirectional temperature dependency has been recently explained by a theoretical possibility that the conformational changes that occur upon opening the channel may cause a transfer of specific residues between hydrophobic and aqueous environments, which leads to changes in the heat capacity of the channel protein complex (*37–39*). When premodified with redox-active compounds or noncovalent ligands, TRPA1-mediated currents

were sensitized by warm and cold temperatures (*36*), indicating that conformational changes induced by chemical agonists may be associated with changes in the solvent accessibility of residues within a putative allosteric nexus converging on the region that encompasses the TRP-like domain, pre-S1 helix, and S4-S5 linker (*5*). The inner cavity of the sensor is an integral part of this key region, and thus, it may represent an important locus that undergoes changes in solvation when the channel opens. Our results have identified possible candidate residues in the lower sensor domain that may be the main determinants of water occupancy. Among these, Glu^{788}, Glu^{808}, and Lys^{787} seem to play important roles. In the presence of external Ca^{2+}, mutations at His^{719}, Asn^{722}, Lys^{796}, Glu^{788}, and Glu^{808} biased the channel toward the closed state at negative membrane potentials, indicating that PIP$_2$ binding or changes in hydration of these residues may provide the energy required to open the channel. On the other hand, the mutations E788I, N805A, Y799A, and K989A biased the channel toward

the open state in the absence of Ca^{2+}, suggesting that this may be an inherently less stable conformation and that calcium provides the energy required to adopt the closed conformation. Although this hypothesis awaits confirmation by future experiments, our results demonstrate that substitutions of polar residues predicted to face the crevice lead to large changes in TRPA1 sensitivity to voltage and chemical stimuli. In addition, our molecular model indicated that the inner cavity is also capable of binding phosphoinositides, such as PIP_2, which might further increase the number of allosteric states that depend on the degree of channel activation and phospholipid environment.

Our current understanding of how the TRPA1 channel gates is based on the electron cryo-microscopic structure obtained with an agonist and two antagonists (5) and on the recent structural analyses of related TRPV1, TRPV2, TRPV6, and TRPP1 channels (7–10, 14, 15). The remarkable sequence variability among the TRP proteins observed in the lower part of the sensor and the S2-S3 intracellular linker (16) indicates that this domain might serve a specific function in TRPA1 channel gating. The lower sensor domain in TRPA1 may contain a putative site for interactions with annular or regulatory lipids as seen in its relative TRPV1 (13). Using several approaches to manipulate PIP_2 levels in cells, we found that the depletion of membrane PIP_2 down-regulates the wild-type TRPA1 channels in the absence of external Ca^{2+}. An even more selective effect of PIP_2 depletion observed with Dr-VSP indicated that TRPA1 needs PIP_2 to be properly activated at negative membrane potentials. When the channel is weakly activated by depolarization or cinnamaldehyde, the intracellular cavity of the sensor domain can bind PIP_2 and then release it in response to a local increase in Ca^{2+}. Our observation that the increased cinnamaldehyde-induced activity of the gain-of-function mutant E808A can be suppressed to wild-type levels by PIP_2 sequestration is a strong indication of the role of the internal sensor cavity in TRPA1 regulation.

During the preparation of this work, a study reported that calmodulin binds to TRPA1 in a Ca^{2+}-dependent manner and that this binding is essential for the basal sensitivity and Ca^{2+} potentiation and inactivation of the channel (40). MARCKS and GAP43, but not R43A-GAP43, interact with the Ca^{2+}/calmodulin complex and the free calmodulin, respectively, and this interaction tightly depends on intracellular calcium concentration (33). We have found here that TRPA1 coexpressed with the pipmodulins MARCKS, GAP43, or R43A-GAP43 exhibited a higher maximum rectification ratio (~0.9) than TRPA1 alone and that this effect was seen when the intracellular calcium concentration was raised. This means that the channels come close to saturation, which could indicate that PIP_2 modulates TRPA1 in a Ca^{2+}-dependent manner or vice versa. This could explain the divergent results on the effect of PIP_2 in reports from groups using different activation states of the channel. Whether PIP_2 and calmodulin agonistically regulate TRPA1 through direct or indirect competition should be further analyzed, and such analysis could reveal important details about the activation mechanisms of TRPA1.

MATERIALS AND METHODS
Homology modeling, ligand docking, MD simulations
To obtain a model of human TRPA1 with the S1–S4 sensor domain, we used the structure with PDB ID: 3J9P determined by cryo-electron microscopy (5). The intracellular loop connecting helices S2 and S3 was modeled with the use of sequence homology with the polycystin-2 TRP channel TRPP1 [structures with PDB IDs: 5K47 (12), 5T4D (14), 5MKE and 5MKF (15)]. The homology model of the S2-S3 linker of

TRPA1 was created using the Swiss-Model web server (https://swissmodel.expasy.org/). UCSF Chimera (www.cgl.ucsf.edu/chimera/) and AutoDock Vina (http://vina.scripps.edu/) were used for the docking of phospholipids into the S1–S4 sensor domain of TRPA1. The electrostatic potential surrounding TRPA1 and TRPV1 channels was determined by means of Visual Molecular Dynamics (VMD) (41). The TRPA1 tetrameric structure was inserted into the patch of the 1-palmitoyl-2-oleoylphosphatidylcholine (POPC) bilayer and solvated in transferable intermolecular potential 3-point (TIP3P) (42) water molecules to ensure at least 10 Å of solvent on both sides of the membrane and neutralized in 0.5 M NaCl. This gives a periodic box with a size of ~133, ~133, and ~164 Å for a simulated system consisting of ~239,000 atoms. All-atom structure and topology files were generated using VMD (41). Forces were computed using a CHARMM27 force field for proteins, lipids, and ions (43–45). All MD simulations were produced with the aid of the software package NAMD2.9 (46) running on a local workstation equipped with an NVIDIA graphics processing unit. The particle mesh Ewald method with a grid size of $128 \times 128 \times 192$ was used for long-range electrostatic forces (47). The nonbonded cutoff was set to 12 Å. The SETTLE algorithm (tolerance, 1×10^{-8}) was applied to constrain bonds in water molecules (48). Langevin dynamics was used for temperature control with the target temperature set to 310 K, and the Langevin piston method was applied to reach an efficient pressure control with a target pressure of 1 atm (46). The integration time step was set to 2 fs. Simulated systems were energy-minimized and heated to 310 K, and production MD runs reached lengths of 200 ps. Data were recorded every 1 ps and analyzed using the CPPTRAJ module from the AmberTools suite (49). MD trajectories were visualized with the aid of the VMD 1.9 software package (41). Figures were produced with the software packages UCSF Chimera (50), ICM (Molsoft LLC), and CorelDraw X7 (Corel Corporation).

Cell culture, constructs, and transfection
HEK293T cells were cultured in Opti-MEM I medium (Invitrogen) supplemented with 5% fetal bovine serum as described previously (51). The magnet-assisted transfection (IBA GmbH) technique was used to transiently cotransfect the cells in a 15.6-mm well on a 24-well plate with 200 ng of plasmid encoding green fluorescent protein (TaKaRa), 300 ng of plasmid encoding wild-type or mutant human TRPA1 (pCMV6-XL4 vector, OriGene), and, for particular experiments, 200 ng of plasmid of wild-type or mutant GAP43 (pCMV6-XL5 vector, OriGene) or 100 ng of plasmid encoding MARCKS (pCMV6-XL5 vector, OriGene). The cells were used 24 to 48 hours after transfection. At least two independent transfections were used for each experimental group. The wild-type channel was regularly tested in the same batch as the mutants. The mutants were generated by polymerase chain reaction using the QuikChange II XL Site-Directed Mutagenesis Kit (Agilent Technologies) and confirmed by DNA sequencing (GATC Biotech).

Electrophysiology
Whole-cell membrane currents were recorded by using an Axopatch 200B amplifier and pCLAMP 10 software (Molecular Devices). Patch electrodes were pulled from borosilicate glass and heat-polished to a final resistance between 3 and 5 megohms. Series resistance was compensated by at least 70% in all recordings. The experiments were performed at room temperature (23° to 25°C). Only one recording was performed on any one coverslip of the cells to ensure that recordings were made from cells not previously exposed to chemical stimuli. A system for rapid superfusion and heating of the cultured cells was

used for drug application (*52*). The extracellular bath solutions contained 150 mM NaCl and 10 mM Hepes, with an added 2 mM HEDTA [N-(2-hydroxyethyl)ethylenediamine-N,N′,N′-triacetic acid] for the Ca^{2+}-free solution and 2 mM $CaCl_2$ for the Ca^{2+}-containing solutions (adjusted to pH 7.3 with NaOH and to 300 mosmol). The current-to-voltage (*I*-*V*) relationships were measured in control bath solution containing 160 mM NaCl, 2.5 mM KCl, 1 mM $CaCl_2$, 2 mM $MgCl_2$, 10 mM Hepes, and 10 mM glucose (adjusted to pH 7.3 and 320 mosmol). The *I*-*V* relationships were recorded using 100-ms voltage steps from −80 to +200 mV (+20-mV increments) and a holding potential of −70 mV recorded in control extracellular solution ~1 min after whole-cell formation. The high-buffer internal pipette solution containing 145 mM CsCl, 5 mM EGTA, 3 mM $CaCl_2$, 10 mM Hepes, and 2 mM MgATP (adjusted to pH 7.3 with CsOH and to 290 mosmol) was used unless the usage of low-buffer internal solution (LB-ICS) is noted, which contained 145 mM CsCl, 10 mM EGTA, 10.24 mM $CaCl_2$ (corresponding to 100 μM free Ca^{2+}), 10 mM Hepes, and 2 mM MgATP (adjusted to pH 7.3 with CsOH and to 290 mosmol). For experiments shown in fig. S5, extracellular control solution contained 140 mM NaCl, 5 mM KCl, 2 mM $MgCl_2$, 5 mM EGTA, 10 mM Hepes, and 10 mM glucose (pH 7.4 was adjusted by tetramethylammonium hydroxide). Intracellular solution contained 140 mM KCl, 5 mM EGTA, 2 mM $MgCl_2$, and 10 mM Hepes (adjusted to pH 7.4 with KOH). Cinnamaldehyde and AITC solution was prepared before use from a 0.1 M stock solution in Me_2SO. All of the chemicals were purchased from Sigma-Aldrich. The agonist sensitivity was tested with a standard protocol where the membrane potential was ramped every second from −80 to +80 mV (1 V/s) or from −80 to +160 mV (1 V/s) for the inactivating mutations H719A and K787A. In experiments with Dr-VSP, the voltage step protocol was preceded by a 2-s depolarization to +80 mV. The current responses for further processing were always measured at −80 and +80 mV.

Statistical analysis

The electrophysiological data were analyzed using pCLAMP 10 (Molecular Devices), and the curve fitting and statistical analyses were done in SigmaPlot 10 (Systat Software Inc.). *G*-*V* relationships were obtained from steady-state whole-cell currents measured at the end of voltage steps from −80 to +200 mV in increments of +20 mV. Voltage-dependent gating parameters were estimated by fitting the conductance $G = I/(V − V_{rev})$ as a function of the test potential *V* to the Boltzmann equation: $G = [(G_{max} − G_{min})/(1 + exp(−zF(V − V_{50})/RT))] + G_{min}$, where *z* is the apparent number of gating charges; V_{50} is the half-activation voltage; G_{min} and G_{max} are the minimum and maximum whole-cell conductance, respectively; V_{rev} is the reversal potential; and *F*, *R*, and *T* have their usual thermodynamic meanings. Statistical significance was determined by Student's *t* test or the analysis of variance (ANOVA), as appropriate; differences were considered significant at $P < 0.05$ unless stated otherwise. Data are means ± SEM.

SUPPLEMENTARY MATERIALS

www.sciencesignaling.org/cgi/content/full/11/514/eaan8621/DC1

Fig. S1. Mutations in the inner cavity of the sensor module affect chemical-dependent gating of TRPA1.

Fig. S2. Average rectification of whole-cell currents through the mutant channels.

Fig. S3. Structural comparison with TRPV2 and a central role for Tyr^{726}.

Fig. S4. LB-ICS containing Ca^{2+} abolishes the inhibitory effects of MARCKS and mutant GAP43.

Fig. S5. Polar residues in the sensor cavity regulate the activity of TRPA1 under physiological temperatures.

REFERENCES AND NOTES

1. G. M. Story, A. M. Peier, A. J. Reeve, S. R. Eid, J. Mosbacher, T. R. Hricik, T. J. Earley, A. C. Hergarden, D. A. Andersson, S. W. Hwang, P. McIntyre, T. Jegla, S. Bevan, A. Patapoutian, ANKTM1, a TRP-like channel expressed in nociceptive neurons, is activated by cold temperatures. *Cell* **112**, 819–829 (2003).
2. B. Nilius, G. Appendino, G. Owsianik, The transient receptor potential channel TRPA1: From gene to pathophysiology. *Pflugers Arch.* **464**, 425–458 (2012).
3. P. M. Zygmunt, E. D. Högestätt, TRPA1. *Handb. Exp. Pharmacol.* **222**, 583–630 (2014).
4. F. Viana, TRPA1 channels: Molecular sentinels of cellular stress and tissue damage. *J. Physiol.* **594**, 4151–4169 (2016).
5. C. E. Paulsen, J. P. Armache, Y. Gao, Y. Cheng, D. Julius, Structure of the TRPA1 ion channel suggests regulatory mechanisms. *Nature* **520**, 511–517 (2015).
6. M. S. J. Brewster, R. Gaudet, How the TRPA1 receptor transmits painful stimuli: Inner workings revealed by electron cryomicroscopy. *Bioessays* **37**, 1184–1192 (2015).
7. M. Liao, E. Cao, D. Julius, Y. Cheng, Structure of the TRPV1 ion channel determined by electron cryo-microscopy. *Nature* **504**, 107–112 (2013).
8. E. Cao, M. Liao, Y. Cheng, D. Julius, TRPV1 structures in distinct conformations reveal activation mechanisms. *Nature* **504**, 113–118 (2013).
9. L. Zubcevic, M. A. Herzik Jr., B. C. Chung, Z. Liu, G. C. Lander, S.-Y. Lee, Cryo-electron microscopy structure of the TRPV2 ion channel. *Nat. Struct. Mol. Biol.* **23**, 180–186 (2016).
10. K. Saotome, A. K. Singh, M. V. Yelshanskaya, A. I. Sobolevsky, Crystal structure of the epithelial calcium channel TRPV6. *Nature* **534**, 506–511 (2016).
11. P. Jin, D. Bulkley, Y. Guo, W. Zhang, Z. Guo, W. Huynh, S. Wu, S. Meltzer, T. Cheng, L. Y. Jan, Y.-N. Jan, Y. Cheng, Electron cryo-microscopy structure of the mechanotransduction channel NOMPC. *Nature* **547**, 118–122 (2017).
12. M. Grieben, A. C. Pike, C. A. Shintre, E. Venturi, S. El-Ajouz, A. Tessitore, L. Shrestha, S. Mukhopadhyay, P. Mahajan, R. Chalk, N. A. Burgess-Brown, R. Sitsapesan, J. T. Huiskonen, E. P. Carpenter, Structure of the polycystic kidney disease TRP channel Polycystin-2 (PC2). *Nat. Struct. Mol. Biol.* **24**, 114–122 (2017).
13. Y. Gao, E. Cao, D. Julius, Y. Cheng, TRPV1 structures in nanodiscs reveal mechanisms of ligand and lipid action. *Nature* **534**, 347–351 (2016).
14. P. S. Shen, X. Yang, P. G. DeCaen, X. Liu, D. Bulkley, D. E. Clapham, E. Cao, The structure of the polycystic kidney disease channel PKD2 in lipid nanodiscs. *Cell* **167**, 763–773.e11 (2016).
15. M. Wilkes, M. G. Madej, L. Kreuter, D. Rhinow, V. Heinz, S. De Sanctis, S. Ruppel, R. M. Richter, F. Joos, M. Grieben, A. C. W. Pike, J. T. Huiskonen, E. P. Carpenter, W. Kuhlbrandt, R. Witzgall, C. Ziegler, Molecular insights into lipid-assisted Ca^{2+} regulation of the TRP channel Polycystin-2. *Nat. Struct. Mol. Biol.* **24**, 123–130 (2017).
16. E. Palovcak, L. Delemotte, M. L. Klein, V. Carnevale, Comparative sequence analysis suggests a conserved gating mechanism for TRP channels. *J. Gen. Physiol.* **146**, 37–50 (2015).
17. E. Palovcak, L. Delemotte, M. L. Klein, V. Carnevale, Evolutionary imprint of activation: The design principles of VSDs. *J. Gen. Physiol.* **143**, 145–156 (2014).
18. D. Krepkiy, M. Mihailescu, J. A. Freites, E. V. Schow, D. L. Worcester, K. Gawrisch, D. J. Tobias, S. H. White, K. J. Swartz, Structure and hydration of membranes embedded with voltage-sensing domains. *Nature* **462**, 473–479 (2009).
19. L. Marsakova, I. Barvik, V. Zima, L. Zimova, V. Vlachova, The first extracellular linker is important for several aspects of the gating mechanism of human TRPA1 channel. *Front. Mol. Neurosci.* **10**, 16 (2017).
20. K. W. Huynh, M. R. Cohen, J. Jiang, A. Samanta, D. T. Lodowski, Z. H. Zhou, V. Y. Moiseenkova-Bell, Structure of the full-length TRPV2 channel by cryo-EM. *Nat. Commun.* **7**, 11130 (2016).
21. Y. Y. Wang, R. B. Chang, H. N. Waters, D. D. McKemy, E. R. Liman, The nociceptor ion channel TRPA1 is potentiated and inactivated by permeating calcium ions. *J. Biol. Chem.* **283**, 32691–32703 (2008).
22. L. Sura, V. Zima, L. Marsakova, A. Hynkova, I. Barvik, V. Vlachova, C-terminal acidic cluster is involved in Ca^{2+}-induced regulation of human transient receptor potential ankyrin 1 channel. *J. Biol. Chem.* **287**, 18067–18077 (2012).
23. V. Zima, K. Witschas, A. Hynkova, L. Zimova, I. Barvik, V. Vlachova, Structural modeling and patch-clamp analysis of pain-related mutation TRPA1-N855S reveal inter-subunit salt bridges stabilizing the channel open state. *Neuropharmacology* **93**, 294–307 (2015).
24. L. Wang, T. L. Cvetkov, M. R. Chance, V. Y. Moiseenkova-Bell, Identification of in vivo disulfide conformation of TRPA1 ion channel. *J. Biol. Chem.* **287**, 6169–6176 (2012).
25. T. Rohacs, Phosphoinositide regulation of TRP channels. *Handb. Exp. Pharmacol.* **223**, 1143–1176 (2014).
26. Y. Karashima, J. Prenen, V. Meseguer, G. Owsianik, T. Voets, B. Nilius, Modulation of the transient receptor potential channel TRPA1 by phosphatidylinositol 4,5-biphosphate manipulators. *Pflugers Arch.* **457**, 77–89 (2008).
27. A. N. Akopian, N. B. Ruparel, N. A. Jeske, K. M. Hargreaves, Transient receptor potential TRPA1 channel desensitization in sensory neurons is agonist dependent and regulated by TRPV1-directed internalization. *J. Physiol.* **583**, 175–193 (2007).

28. D. Kim, E. J. Cavanaugh, Requirement of a soluble intracellular factor for activation of transient receptor potential A1 by pungent chemicals: Role of inorganic polyphosphates. *J. Neurosci.* **27**, 6500–6509 (2007).

29. Y. Dai, S. Wang, M. Tominaga, S. Yamamoto, T. Fukuoka, T. Higashi, K. Kobayashi, K. Obata, H. Yamanaka, K. Noguchi, Sensitization of TRPA1 by PAR2 contributes to the sensation of inflammatory pain. *J. Clin. Invest.* **117**, 1979–1987 (2007).

30. D. Kim, E. J. Cavanaugh, D. Simkin, Inhibition of transient receptor potential A1 channel by phosphatidylinositol-4,5-bisphosphate. *Am. J. Physiol. Cell Physiol.* **295**, C92–C99 (2008).

31. J. Wang, A. Gambhir, G. Hangyás-Mihályné, D. Murray, U. Golebiewska, S. McLaughlin, Lateral sequestration of phosphatidylinositol 4,5-bisphosphate by the basic effector domain of myristoylated alanine-rich C kinase substrate is due to nonspecific electrostatic interactions. *J. Biol. Chem.* **277**, 34401–34412 (2002).

32. S. McLaughlin, D. Murray, Plasma membrane phosphoinositide organization by protein electrostatics. *Nature* **438**, 605–611 (2005).

33. V. Kumar, V. P. Chichili, L. Zhong, X. Tang, A. Velazquez-Campoy, F.-S. Sheu, J. Seetharaman, N. Z. Gerges, J. Sivaraman, Structural basis for the interaction of unstructured neuron specific substrates neuromodulin and neurogranin with calmodulin. *Sci. Rep.* **3**, 1392 (2013).

34. M. I. Hossain, H. Iwasaki, Y. Okochi, M. Chahine, S. Higashijima, K. Nagayama, Y. Okamura, Enzyme domain affects the movement of the voltage sensor in ascidian and zebrafish voltage-sensing phosphatases. *J. Biol. Chem.* **283**, 18248–18259 (2008).

35. Y. Okamura, Y. Murata, H. Iwasaki, Voltage-sensing phosphatase: Actions and potentials. *J. Physiol.* **587**, 513–520 (2009).

36. L. Moparthi, T. I. Kichko, M. Eberhardt, E. D. Högestätt, P. Kjellbom, U. Johanson, P. W. Reeh, A. Leffler, M. R. Filipovic, P. M. Zygmunt, Human TRPA1 is a heat sensor displaying intrinsic U-shaped thermosensitivity. *Sci. Rep.* **6**, 28763 (2016).

37. D. E. Clapham, C. Miller, A thermodynamic framework for understanding temperature sensing by transient receptor potential (TRP) channels. *Proc. Natl. Acad. Sci. U.S.A.* **108**, 19492–19497 (2011).

38. M. F. Tsai, C. Miller, Building a temperature-sensitive ion channel. *Cell* **158**, 977–979 (2014).

39. S. Chowdhury, B. W. Jarecki, B. Chanda, A molecular framework for temperature-dependent gating of ion channels. *Cell* **158**, 1148–1158 (2014).

40. R. Hasan, A. T. Leeson-Payne, J. H. Jaggar, X. Zhang, Calmodulin is responsible for Ca^{2+}-dependent regulation of TRPA1 channels. *Sci. Rep.* **7**, 45098 (2017).

41. W. Humphrey, A. Dalke, K. Schulten, VMD: Visual molecular dynamics. *J. Mol. Graph.* **14**, 33–38 (1996).

42. W. L. Jorgensen, J. Chandrasekhar, J. D. Madura, R. W. Impey, M. L. Klein, Comparison of simple potential functions for simulating liquid water. *J. Chem. Phys.* **79**, 926–935 (1983).

43. A. D. MacKerell Jr., D. Bashford, M. Bellott, R. L. Dunbrack Jr., J. D. Evanseck, M. J. Field, S. Fischer, J. Gao, H. Guo, S. Ha, D. Joseph-McCarthy, L. Kuchnir, K. Kuczera, F. T. K. Lau, C. Mattos, S. Michnick, T. Ngo, D. T. Nguyen, B. Prodhom, W. E. Reiher, B. Roux, M. Schlenkrich, J. C. Smith, R. Stote, J. Straub, M. Watanabe, J. Wiorkiewicz-Kuczera, D. Yin, M. Karplus, All-atom empirical potential for molecular modeling and dynamics studies of proteins. *J. Phys. Chem. B* **102**, 3586–3616 (1998).

44. M. Schlenkrich, J. Brickmann, A. D. MacKerell Jr., M. Karplus, An empirical potential energy function for phospholipids: Criteria for parameter optimization and applications, in *Biological Membranes: A Molecular Perspective from Computation and Experiment*, K. M. Merz, B. Roux, Eds. (Birkhäuser Boston, 1996), pp. 31–81.

45. D. Beglov, B. Roux, Finite representation of an infinite bulk system: Solvent boundary potential for computer simulations. *J. Chem. Phys.* **100**, 9050–9063 (1994).

46. J. C. Phillips, R. Braun, W. Wang, J. Gumbart, E. Tajkhorshid, E. Villa, C. Chipot, R. D. Skeel, L. Kalé, K. Schulten, Scalable molecular dynamics with NAMD. *J. Comput. Chem.* **26**, 1781–1802 (2005).

47. T. E. Cheatham, J. L. Miller, T. Fox, T. A. Darden, P. A. Kollman, Molecular dynamics simulations on solvated biomolecular systems: The particle mesh Ewald method leads to stable trajectories of DNA, RNA, and proteins. *J. Am. Chem. Soc.* **117**, 4193–4194 (1995).

48. J.-P. Ryckaert, G. Ciccotti, H. J. C. Berendsen, Numerical integration of the Cartesian equations of motion of a system with constraints: Molecular dynamics of *n*-alkanes. *J. Comput. Phys.* **23**, 327–341 (1977).

49. D. R. Roe, T. E. Cheatham III, PTRAJ and CPPTRAJ: Software for processing and analysis of molecular dynamics trajectory data. *J. Chem. Theory Comput.* **9**, 3084–3095 (2013).

50. E. F. Pettersen, T. D. Goddard, C. C. Huang, G. S. Couch, D. M. Greenblatt, E. C. Meng, T. E. Ferrin, UCSF Chimera—A visualization system for exploratory research and analysis. *J. Comput. Chem.* **25**, 1605–1612 (2004).

51. J. Benedikt, J. Teisinger, L. Vyklicky, V. Vlachova, Ethanol inhibits cold-menthol receptor TRPM8 by modulating its interaction with membrane phosphatidylinositol 4,5-bisphosphate. *J. Neurochem.* **100**, 211–224 (2007).

52. I. Dittert, J. Benedikt, L. Vyklicky, K. Zimmermann, P. W. Reeh, V. Vlachová, Improved superfusion technique for rapid cooling or heating of cultured cells under patch-clamp conditions. *J. Neurosci. Methods* **151**, 178–185 (2006).

53. B. K. Ho, F. Gruswitz, HOLLOW: Generating accurate representations of channel and interior surfaces in molecular structures. *BMC Struct. Biol.* **8**, 49 (2008).

54. G. E. Crooks, G. Hon, J.-M. Chandonia, S. E. Brenner, WebLogo: A sequence logo generator. *Genome Res.* **14**, 1188–1190 (2004).

Citation: L. Zimova, V. Sinica, A. Kadkova, L. Vyklicka, V. Zima, I. Barvik, V. Vlachova, Intracellular cavity of sensor domain controls allosteric gating of TRPA1 channel. *Sci. Signal.* **11**, eaan8621 (2018).

Putative interaction site for membrane phospholipids controls activation of TRPA1 channel at physiological membrane potentials

Lucie Macikova[1,2,3], Viktor Sinica[2], Anna Kadkova[2], Sandrine Villette[1], Alexandre Ciaccafava[1], Jonathan Faherty[4], Sophie Lecomte[1], Isabel D. Alves[1] and Viktorie Vlachova[2] (iD)

1 CBMN-UMR 5248 CNRS, IPB, University of Bordeaux, Pessac, France
2 Department of Cellular Neurophysiology, Institute of Physiology, Academy of Sciences of the Czech Republic, Prague, Czech Republic
3 Department of Physiology, Faculty of Science, Charles University in Prague, Czech Republic
4 Fluidic Analytics Unit 5, Chesterton Mill, Cambridge, UK

The transient receptor potential ankyrin 1 (TRPA1) channel is a polymodal sensor of environmental irritant compounds, endogenous proalgesic agents, and cold. Upon activation, TRPA1 channels increase cellular calcium levels via direct permeation and trigger signaling pathways that hydrolyze phosphatidylinositol-4,5-bisphosphate (PIP_2) in the inner membrane leaflet. Our objective was to determine the extent to which a putative PIP_2-interaction site (Y1006-Q1031) is involved in TRPA1 regulation. The interactions of two specific peptides (L992-N1008 and T1003-P1034) with model lipid membranes were characterized by biophysical approaches to obtain information about affinity, peptide secondary structure, and peptide effect in the lipid organization. The results indicate that the two peptides interact with lipid membranes only if PIP_2 is present and their affinities depend on the presence of calcium. Using whole-cell electrophysiology, we demonstrate that mutation at F1020 produced channels with faster activation kinetics and with a rightward shifted voltage-dependent activation curve by altering the allosteric constant that couples voltage sensing to pore opening. We assert that the presence of PIP_2 is essential for the interaction of the two peptide sequences with the lipid membrane. The putative phosphoinositide-interacting domain comprising the highly conserved F1020 contributes to the stabilization of the TRPA1 channel gate.

Introduction

The human transient receptor potential (TRP) subtype A1 (TRPA1) is a chemosensitive ion channel involved in nociception and inflammatory pain [1–4]. It is considered to be one of the key physiological sensors for many pungent and irritant compounds being activated by thiol-reactive electrophiles such as cinnamaldehyde, oxidants, and various nonelectrophilic agonists such as carvacrol or menthol [5,6]. Cytosolic calcium modulates the activity of TRPA1 in a bimodal manner so that Ca^{2+} activates or potentiates the channel at low concentrations and inactivates it at higher concentrations [7]. The proposed molecular mechanism involves

Ca^{2+}-sensing calmodulin that preassociates with the C-terminal region of TRPA1 (L992-N1008) and enables the channel to distinctly respond to diverse Ca^{2+} signals [8]. Further adding to the complexity of TRPA1 regulation are early signaling events linked to Ca^{2+}-dependent phosphoinositide-specific phospholipase C (PLC) enzymes that hydrolyze phosphatidylinositol-4,5-bisphosphate (PtdIns(4,5)P$_2$; PIP$_2$) in the inner membrane leaflet. The PLC-mediated PIP$_2$ depletion may represent an important mechanism involved in TRPA1-mediated nociception triggered by pro-inflammatory agents such as bradykinin [9] and protease-activated receptor PAR2 [10]. Up to date, however, reports are inconsistent regarding the effects of membrane phosphoinositides on TRPA1 [reviewed in refs. [11–13]]. The sites at which these may interact with TRPA1 are not resolved, but most likely involve the membrane proximal regions of the N- and C termini and inter-subunit regions near the inner leaflet of the membrane [14–16]. Indeed, we have previously shown that 29-residue peptide (I964-L992) from the C terminus exhibits a high affinity to PIP$_2$-containing membranes, relative to other lipids, suggesting that important electrostatic interactions with the negatively charged lipid head groups occur [15]. These results fitted well with a later structural study that attributed the predicted region (then, called H1 in our study) to the TRP-like helix that runs parallel to the inner leaflet of the membrane and forms a central nexus of activating signal convergence [17].

From the TRPA1 electron density map, another putative site for interaction with membrane phospholipids has been proposed that is formed by a poorly resolved flexible linker connecting the TRP-like domain with the C-terminal coiled coil [17]. This part of the channel (Y1006-Q1031) forms an intracellular vestibule between adjacent subunits connected to the bulk solution through a side fenestration that could provide means for hydrophobic modulators and lipids to affect channel functioning. The flexible linker contains a short α-helix (shown in violet in Fig. 1A,B) that is almost buried in the inner membrane leaflet. The linker is integrated with a putative three-stranded β-sheet formed by two antiparallel β-strands from the N terminus and a contacting strand that follows the C-terminal TRP-like helix. The latter, peripherally exposed β-strand binds the carboxy-lobe of calmodulin and even under resting concentrations of Ca^{2+} (~ 100 nM) may form a tight complex with the channel [8]. Calmodulin binds to TRPA1 within the region L992-N1008 and it may compete for the same or overlapping binding site with PIP$_2$ or other phosphoinositides.

Here, we examined the functional role of both the above regions (L992-N1008 and Y1006-Q1031) with the aim to extend available knowledge about the putative role of membrane PIP$_2$ in TRPA1 channel functioning. Using electrophysiological and biophysical studies, we tested the hypothesis that the binding specificity of PIP$_2$ may depend not only on the presence of positively charged residues in the TRP-like domain that likely interact with polar head groups as demonstrated in [15] and [18] but also on specific hydrophobic residues presumably involved in contacting the lipid hydrophobic tails.

Results

Specific peptides corresponding to the flexible linker or calmodulin-binding site rely on the presence of PIP$_2$ to establish superficial contacts with the lipid membrane

Different biophysical approaches were employed to characterize the peptide–lipid interaction in terms of the affinity (Plasmon Waveguide Resonance—PWR and Microfluidic Diffusional Sizing—MDS), effect in lipid membrane organization (PWR and polarized ATR-FTIR—p ATR-FTIR), membrane integrity (Rhodamine leakage), and peptide secondary structure (Circular Dichroism—CD) (Fig. 2A–D). To investigate the importance of PIP$_2$ in these interactions, lipid model systems such as planar membranes, large unilamellar vesicles (LUVs), and polymer-based nanodiscs (styrene maleic acid lipid particles, SMALPs) composed of palmitoyl-oleoyl-phosphatidylcholine (POPC) (main lipid of mammalian cell membranes) and POPC with PIP$_2$ (5–20%) were employed. To test the binding of the peptides to the lipid model systems, three different approaches were employed: polarized ATR-FTIR [19], PWR [20], and MDS, a new technology developed by Fluidic Analytics that allows to determine the concentration and size of proteins or peptides or any primary amine containing molecule [21,22]. Since the higher resolution limit in terms of size is about 30 nm of radius, herein we have chosen polymer-based nanodiscs (SMALPs) that have a diameter of about 10–15 nm as our lipid model system. MDS was used to follow peptide binding to SMALPs composed of POPC and POPC/PIP$_2$ (9/1 mol·mol^{-1}) by following the changes in size occurring upon the interaction (further details can be found in the Materials and methods). From the PWR and MDS data it is evident that PIP$_2$ is essential for lipid interaction as no binding was observed in the case of pure POPC membranes (Fig. 2A,B). For POPC/PIP$_2$ membranes, binding was

A

sensor domain

short helix

S1 S2 S3 S4 S5 P1P2 S6

TRP- helix

...N ...C

992-1008: LWFLRKVDQKSTIVYPN
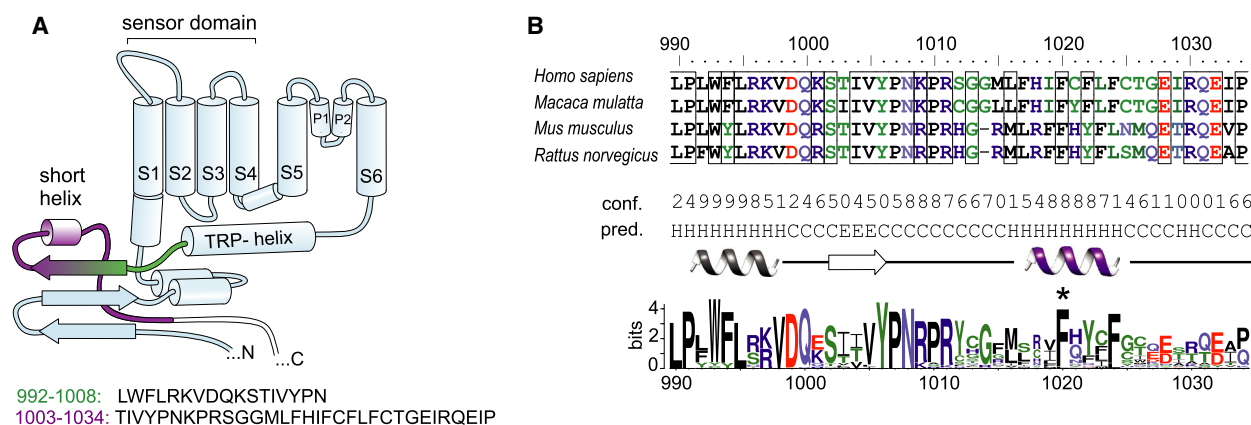1003-1034: TIVYPNKPRSGGMLFHIFCFLFCTGEIRQEIP

B

Fig. 1. Schematic representation of TRPA1 receptor showing regions predicted to interact with membrane lipids. (A) Schematic illustration of human TRPA1 subunit with depicted position of a poorly resolved flexible linker connecting the TRP-like domain with the C-terminal coiled coil linker region (colored region containing the calmodulin-binding domain in green, and an overlapping violet region containing predicted short α-helix). Below, the sequences of the peptides used in this study. (B) Amino acid sequence conservation within the linker of TRPA1 proteins represented as a sequence logo generated from 65 sequences of vertebrate TRPA1 by WebLogo server [52]. The height of the amino acid at each position indicates its probability of occurrence at that position. F1020 in the middle of the short helix (indicated by asterisk) is highly conserved.

observed for both peptides with affinities ranging from about 300 to 700 nM for L992-N1008 and T1003-P1034 peptides, respectively, as determined by MDS (Table 1). The peptide L992-N1008 showed a stronger affinity than T1003-P1034. This could be related to the difference in the net charge (2 for L992-N1008 and 1 for T1003-P1034) as the peptide L992-N1008 could establish stronger electrostatic interactions with the negatively charged lipid. PWR failed to provide accurate affinities, although a hyperbolic saturating curve was obtained for $POPC/PIP_2$ membranes, as the spectral changes induced by peptide addition are quite small ($\leq$ 5 mdeg, at saturating peptide concentrations whereas the instrument angular resolution $\geq$ 0.5 mdeg) (Fig. 2A). Increasing the PIP_2 content to 20% relative to POPC did not increase the PWR signal amplitude (data not shown). This suggests that peptide binding to lipids induces weak perturbations in the lipid ordering. Indeed, this hypothesis is further supported by p ATR-FTIR data that show no significant changes in the lipid fatty acid. Similar position and dichroic ratio for CH_2 symmetric (at 2852 cm^{-1}) and antisymmetric (at 2923 cm^{-1}) stretching bonds (Fig. 2D) are observed after incubation with both peptides. To observe only the signal from the membrane-bound peptide, following peptide incubation, the cell was rinsed with buffer to remove all nonmembrane bound peptide. In the present studies, the amide I (1640 cm^{-1}) and the amide II (1535 cm^{-1}) were observed before peptide rinsing but became extremely small (detection limit) after rinsing the peptide. Therefore, ATR-FTIR data deconvolution of the amide I and amide II region with the intention of

obtaining the peptide secondary structure and orientation was not performed here. p ATR-FTIR data agree well with PWR and MDS data in that no peptide interaction was observed in the absence of PIP_2. The presence of Ca^{2+} in the buffer decreased the affinity of both peptides to $POPC/PIP_2$ lipid membranes as shown by MDS (Table 1). Peptide effect in rhodamine leakage from LUVs was tested to determine if peptide interaction affects membrane integrity (e.g., pore formation). No membrane leakage was observed even at peptide/lipid ratios of 1/10 (Table 2). Those two findings suggest that peptide binding to lipid occurs if PIP_2 is present and that the binding is superficial, most probably involving electrostatic interactions between the anionic lipid and positive charges in the peptide. In terms of the peptide secondary structure, CD data indicate that both peptides are highly nonstructured (random coil), with a certain degree of antiparallel β-sheet (Fig. 2C and Table 3). The peptide L992-N1008 also presents a certain degree of helical content. The data suggest no significant peptide conformational changes from a buffer system and upon interaction with POPC or $POPC/PIP_2$ (9.5/0.5 and 8/2 mol·mol^{-1}) at P/L ratios ranging from 1/50 to 1/10 (Fig. 2C and Table 3).

Glycine mutation of central phenylalanine F1020 produces strongly rectifying channels

Based on the multiple sequence alignment of TRPA1 proteins over the flexible linker region, the most conserved residue within the putative short α-helix is the central phenylalanine 1020 (Fig. 1B). We substituted
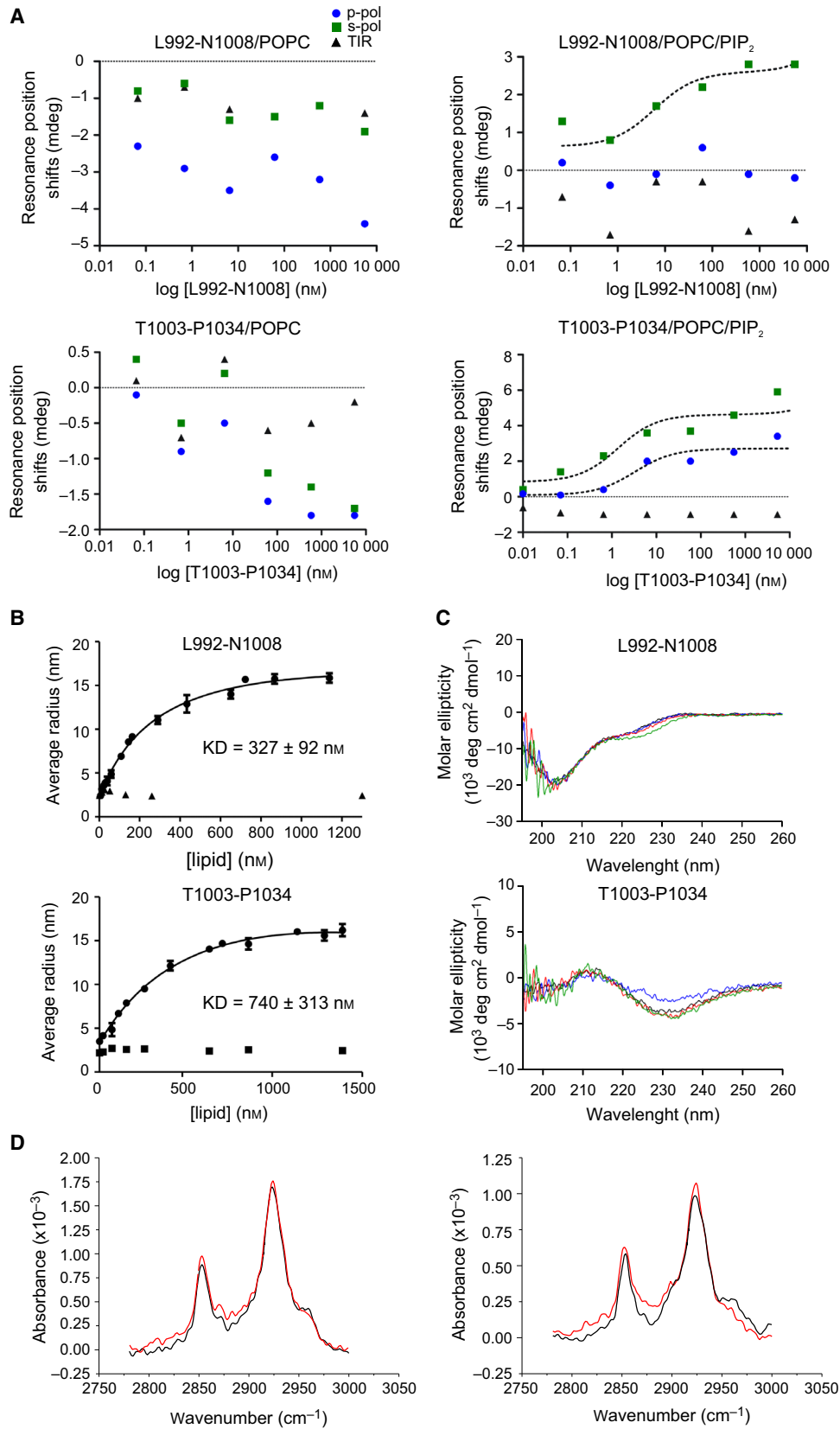
Fig. 2. Interaction of the L992-N1008 and T1003-P1034 peptides with model membranes composed of POPC and POPC/PIP$_2$. (A) PWR resonance position shifts obtained in the p- (blue circles) and s- (green squares) polarization and total internal reflection angle (TIR; black triangles) upon incremental addition of peptide to a planar model membrane composed of POPC and POPC/PIP$_2$ (95/5 mol·mol^{-1}). No binding affinities were determined due to the rather small shifts relative to the instrument limits (see text for details). (B) Average radius of the indicated peptides upon titration with increasing concentrations of SMALPs composed of POPC (triangles and squares) and POPC/PIP$_2$ (9/1 mol/mol) (circles). For experiments performed with POPC/PIP$_2$, data are presented as mean ± SD (n = 3). Binding affinities are presented in Table 1. (C) Secondary peptide structure determined by CD for the two peptides alone in buffer (black) and upon incubation with POPC (blue) and POPC/PIP$_2$ at 5% (red) and 20% (green) liposomes at P/L ratios of 1/10. Secondary structure content has been calculated and presented in Table 2. (D) Polarized ATR-FTIR spectra obtained with the p- (left panel) and s- (right panel) polarized light of a solid-supported lipid membrane composed of POPC/PIP$_2$ (8/2 mol·mol^{-1}) in the absence (black) and presence (red) of L992-N1008 peptide.

Table 1. Binding affinity (in nM) for the peptides L992-N1008 and T1003-P1034 for SMALPs composed of POPC and POPC/PIP$_2$ (9/1 mol·mol^{-1}) in the absence and presence of 2 mM Ca^{2+} obtained by MDS. Data are presented as mean ± SD (n = 3)

LIPID/PEPTIDE	L992-N1008	T1003-P1034
POPC	No binding	No binding
POPC/PIP$_2$ (9/1 mol·mol^{-1}) no Ca^{+2}	330 ± 68	685 ± 114
POPC/PIP$_2$ (9/1 mol·mol^{-1}) with Ca^{+2}	425 ± 95	720 ± 123

Table 2. Rhodamine leakage induced by the peptides L992-N1008 and T1003-P1034 in POPC and POPC/PIP$_2$ (9.5/0.5 mol·mol^{-1}) liposomes encapsulating rhodamine. Experiments have been performed two times

Rhodamine leakage

P/L ratio	T1003-P1034		L992-L1008	
	100% POPC	5% PIP$_2$ + 95% POPC	100% POPC	5% PIP$_2$ + 95% POPC
1/100	2.5 ± 0.3	0	2.4 ± 0.6	0
1/50	1.3 ± 0.2	0	1.6 ± 0.4	0
1/25	2.9 ± 0.3	0	1.9 ± 0.2	0
1/10	2.5 ± 0.4	0	2.5 ± 0.3	0

this residue with glycine to disrupt the predicted helical structure and measured agonist-induced responses from transfected HEK293T cells using whole-cell patch-clamp electrophysiology (Fig. 3). To stimulate the cells, we used a previously established protocol [23–25] in which currents were first induced by the electrophilic agonist in the absence of external Ca^{2+}. The agonist was then washed out for 10 s, and 2 mM Ca^{2+} was added to the extracellular solution to assess the allosteric effects of permeating calcium ions. The membrane potential was linearly ramped up each second from −80 to +80 mV (1 V·s^{-1}) (Fig. 3A). Cinnamaldehyde, a partial agonist of TRPA1, was sufficient to activate the mutant channels at a concentration of 100 μM. Compared to wild-type channels, mutation F1020G produced a strong outward rectification of currents measured in the absence of Ca^{2+} (Fig. 3B) as was visible from the current–voltage relationships obtained after 30 s application of agonist (Fig. 3C,D) and from the time course of rectification ratio measured at −80 mV and at +80 mV (Fig. 3E, F). At negative membrane potentials, the average peak inward currents through F1020G channels were almost three times smaller (−1.0 ± 0.1 nA vs. −2.9 ± 0.5 nA for wild-type; $P \leq 0.001$; n = 13 and 10). The F1020G-mediated currents were not significantly different when external calcium was added (−4.0 ± 0.5 nA vs. −4.4 ± 0.5 nA at −80 mV; P = 0.554; and 5.6 ± 0.7 nA vs. 6.1 ± 0.8 nA at +80 mV; P = 0.637; n = 13 and 10). The mutation thus affected primarily the voltage dependence of the channel under weakly activated conditions.

Table 3. Secondary structure content of the peptides L992-N1008 and T1003-P1034 in buffer and in contact with POPC, POPC/PIP$_2$ (5% and 20% of PIP$_2$ were used). Secondary structure content was calculated using BeStSel software as indicated in Materials and methods

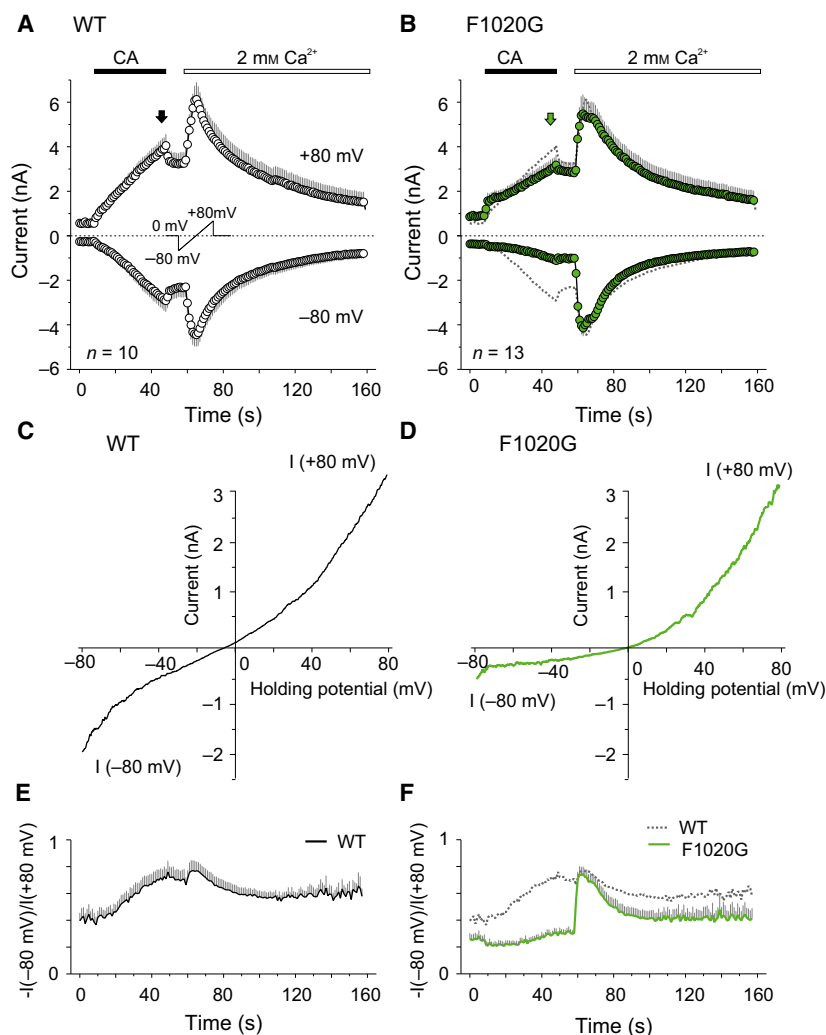| Secondary structure	L992-N1008				T1003-P1034			
	Buffer	POPC	5% PIP$_2$	20% PIP$_2$	Buffer	POPC	5% PIP$_2$	20% PIP$_2$
α-helix	6.4	3.1	6.9	6.9	1.0	0.9	1.1	0.8
Antiparallel β-sheet	30.2	27.5	26.2	30.1	33.9	34.2	33	31.5
Parallel β-sheet	0.0	0.0	0.0	0.0	0.0	0.0	0.0	0.0
Turn	15.3	15.4	15.3	15.3	16.5	16.1	16.4	17.0
Random coil	48.1	54.1	51.7	47.7	48.6	48.9	49.5	50.8

Fig. 3. Mutation F1020G affects chemical- and voltage-induced gating of TRPA1. (A) Average whole-cell currents induced by 100 µM cinnamaldehyde (CA) in Ca^{2+}-free solution and then exposed to 2 mM Ca^{2+}, measured at +80 and −80 mV in wild-type TRPA1 (WT). The membrane potential was linearly ramped up each second from −80 to +80 mV (1 V s^{-1}) (inset). Gray bars indicate SEM (number of cells; $n = 10$). In some cases, the error bars are smaller than the symbol. (B) Average currents recorded from 13 HEK293T cells expressing the F1020G mutant channels. The average current for the WT is overlaid as a gray dashed line for comparison. (C) and (D) Current–voltage relationships of traces measured at times indicated by arrows in panels *A* and *B* for wild-type (black arrow) and indicated mutant (green arrow). (E) and (F) Average rectification of currents shown in A and B plotted as a function of time. Colored lines with gray bars indicate average ± SEM. The average rectification of currents through the WT is overlaid as a gray dashed line for comparison.

Mutation F1020G shifts the voltage dependence of activation

To further assess the changes in the intrinsic voltage dependence of the F1020G mutant channels, we measured responses to a voltage step protocol from −80 to +200 mV, in 20 mV increments, applied in extracellular control solution containing either 1 mM Ca^{2+} or 0 mM Ca^{2+}. In both cases, the currents through F1020G exhibited apparently much faster activation and deactivation kinetics (Fig. 4A,B). Mutation F1020G produced a large shift in the steady-state voltage-dependent activation toward more positive potentials (V_{50} from 112 to 146 mV; Fig. 4C). The steepness of the Boltzmann relationship (reflecting the apparent number of gating charges z) significantly increased from $z = 0.61 \pm 0.03$ e$_0$ to 0.75 ± 0.02 e$_0$ ($P \leq 0.001$; $n = 13$ and 16), indicating that PIP$_2$ may interact with potentially voltage-sensing residues. When Ca^{2+} was omitted from the extracellular

solution, mutation F1020G also resulted in an ∼ 30-mV rightward shift in the V_{50} of the G–V curve, the estimated z was not significantly different from wild-type channels ($P = 0.343$; $n = 10$ and 15), indicating that Ca^{2+} affects the gating of the wild-type and the F1020G mutant channels to a different extent (Fig. 4D).

The activation kinetics of wild-type TRPA1-mediated currents elicited by a depolarizing step from −80 to +200 mV in extracellular control solution containing 1 mM Ca^{2+} were best described by the sum of two exponential functions in 7 of 12 cells ($\tau_{slow} = 47.2 \pm 9.0$ ms, $60.8 \pm 6.6\%$, $\tau_{fast} = 9.6 \pm 2.2$ ms; $n = 7$). In five cells, the activation process was best fit by one exponential function (41.0 ± 5.6 ms; $n = 5$). The activation kinetics of F1020G were characterized by $\tau_{slow} = 32.7 \pm 6.9$ ms, $31.7 \pm 4.9\%$, $\tau_{fast} = 4.8 \pm 0.5$ ms in 6 of 16 cells. In 10 cells, the activation process was best fit by one exponential function (12.1 ± 1.8 ms). Repolarization to the
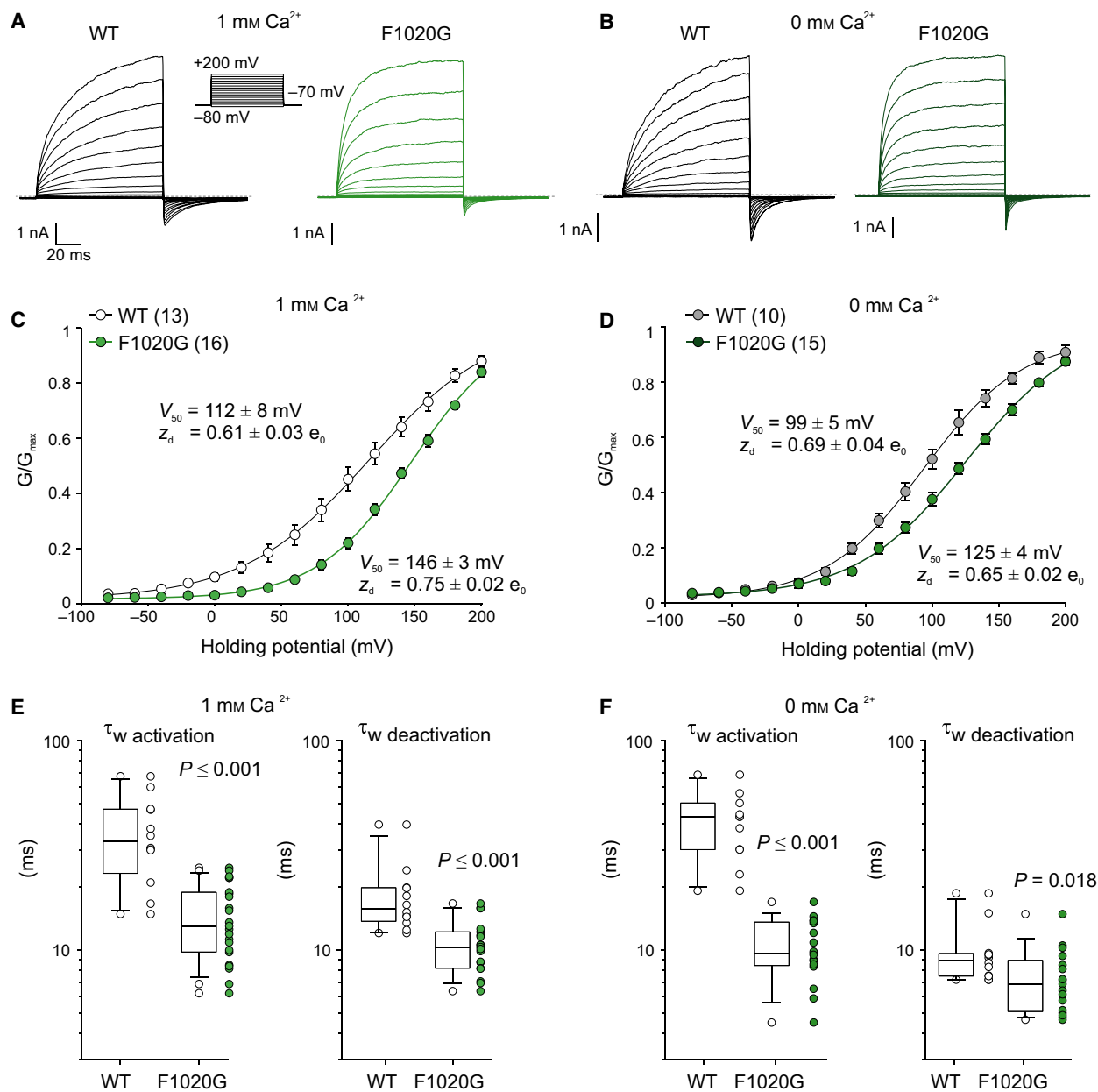
Fig. 4. Mutation F1020G affects the voltage dependence of activation. (A) and (B) Representative current traces in response to voltage step protocol indicated above (holding potential −70 mV; 100-ms voltage steps from −80 to +200 mV; increment +20 mV) recorded *A* in extracellular control solution containing 1 mM Ca^{2+} or *B* in Ca^{2+}-free extracellular solution. (C) and (D) Average conductances obtained from voltage step protocols as in A and B. Data represent the means ± SEM (number of cells *n* indicated in parentheses). The solid lines represent the best fit to a Boltzmann function as described in Materials and methods. (E) and (F) Activation and deactivation kinetics of TRPA1 and the F1020G mutant. Parameters of the time course of currents elicited by a depolarizing step from −80 to +200 mV in extracellular control solution containing 1 mM Ca^{2+} (E left) or in Ca^{2+}-free extracellular solution (F left) was fitted by one or two exponential terms and the weighted time constant (τ_w) was used for statistics. Similarly, the deactivation time constant was obtained from tail currents elicited by stepping from +200 to −70 mV (E right and F right). Data are represented as vertical point plots and summary box plots. Boxes encompass the 25th through 75th percentile of the data, the horizontal bar represents the median, and whiskers extend to the 10th and 90th percentile of the data. Number of cells is indicated in panels C and D. The Mann–Whitney rank sum test was used to determine whether there is a statistically significant difference between F1020G and wild-type channels (*P* values are indicated).

holding membrane potential of −70 mV produced pronounced inward 'tail currents' that could be fitted by one exponential function in 8 of 12 cells expressing wild-type channels (16.7 ± 1.4 ms). In four cells, the deactivation process was best fit by a sum of two exponential functions (τ_{slow} = 39.2 ± 6.0 ms, 44.1 ± 10.8-%, τ_{fast} = 5.6 ± 0.5 ms). Detailed analysis of the F1020G-mediated deactivation kinetics revealed a slow (22.9 ± 2.5 ms; 35.9 ± 4.2%) and a fast time constant (3.9 ± 0.4 ms). Because the relative weights of fast and slow components differed between the cells, the overall statistics was performed with the weighted, average time constants of the fast and slow components (Fig. 4E,F).

Docking experiments suggest different PIP₂ conformations within the sensor domain

The lower segment of the S1–S4 sensor domain with the C-terminal TRP-like helix below forms an integrated nexus that has been previously proposed to be capable of binding membrane phosphoinositides including PIP₂ [25]. Our ligand docking studies showed that the negatively charged inositol trisphosphate head group of PIP₂ may adopt several different conformations within the inner crevice formed by the S1–S4 helical bundle of the sensor to contact polar residues in the inner cavity of the sensor (H719, N722, K787, K796, R852) and the TRP-like helix (K989). Mutations at these residues resulted in a partial loss of functional response to depolarizing voltage in the absence or presence of electrophilic agonists and similar effects are observed as a consequence of the depletion of membrane PIP₂ [18,25]. However, the identification of the positively charged residues that might interact with PIP₂ head group is usually not sufficient to support a conclusion that these are the major binding sites. It is possible that mutations of other contacting residues would give similar defects in channel functioning once they are identified [26]. To gain further insights into possible orientations of PIP₂ within the inner sensor cavity, we performed subsequent ligand docking experiments and found that hydrophobic regions near the PIP₂ hydrocarbon chains may also contribute to the stabilization of the TRPA1–PIP₂ complex (Fig. 5A-C). The density map for the flexible loop T1003-Q1031 at one side extends to the vicinity of the poorly resolved intracellular S2–S3 linker of the S1–S4 sensor domain. At its other side, it contacts the sensor from an adjacent subunit through stacking interactions with the side chains of F716 and H719 from S1 helix and F853 from the S4–S5 linker (Fig. 5B). We have previously shown that the substitution of H719 by a small residue alanine induced serious functional defects manifested as significant changes in rectification and kinetics

of the currents that were blocked but not potentiated by external calcium [25]. To further substantiate the functional importance of this putative contact region, we constructed the F853A mutant and tested its chemical sensitivity (Fig. 5D). The electrophilic full agonist allyl isothiocyanate at a concentration of 100 μM was used because cinnamaldehyde, a partial agonist of TRPA1, was not sufficient to activate the mutant channels. Control cells transfected with wild-type TRPA1 responded robustly to application of agonist in agreement with our previous reports (e.g., [23–25]). In contrast, the HEK293T cells expressing F853A produced only very small currents in response to allyl isothiocyanate even when combined with voltage-ramp stimulus from −80 to +80 mV. The currents developed slowly and were further diminished by the addition of external calcium, thus resembling H719A [25]. These results together support the structurally predicted importance of the stacking interactions within the S1 and S4 helices of the sensor domain and indicate that the channel functioning can be strongly affected through this region.

Putative mechanism of coupling of PIP₂ signal to the gate involves serine 972

The TRPA1 density map indicates another possible mechanism through which the region T1003-Q1031 might directly affect functional coupling of stimulus sensing and gate opening. The C-terminal end of the flexible linker (I1033) is located only about 4 Å from serine 972 (Fig. 5B). This serine residue is situated at the beginning of the TRP-like helix, a critically important locus of channel regulation that is directly connected to the lower gate (Fig. 5B). To explore the possibility of such interaction, we compared responses from two TRPA1 constructs in which the serine 972 was substituted with either smaller (alanine) or larger (aspartate) residue (Fig. 6A–F). As above (Fig. 5D), the transfected cells were first activated by the electrophilic agonist in the absence of external Ca²⁺. The agonist was then washed out for 10 s, and 2 mM Ca²⁺ was added to the extracellular solution to assess the allosteric effects of permeating calcium ions. The membrane potential was linearly ramped up each second from −80 to +80 mV (1 V·s⁻¹). Compared to wild-type channels, S972A-mediated whole-cell currents were not significantly different, producing only a slight relative decrease in the rectification throughout the time course of the experiment (Fig. 6A, C and E). In contrast, S972D produced a strong outward rectification of currents measured in the absence of Ca²⁺ (Fig. 6B) as was visible from the current–voltage relationships obtained after 30 s application of agonist
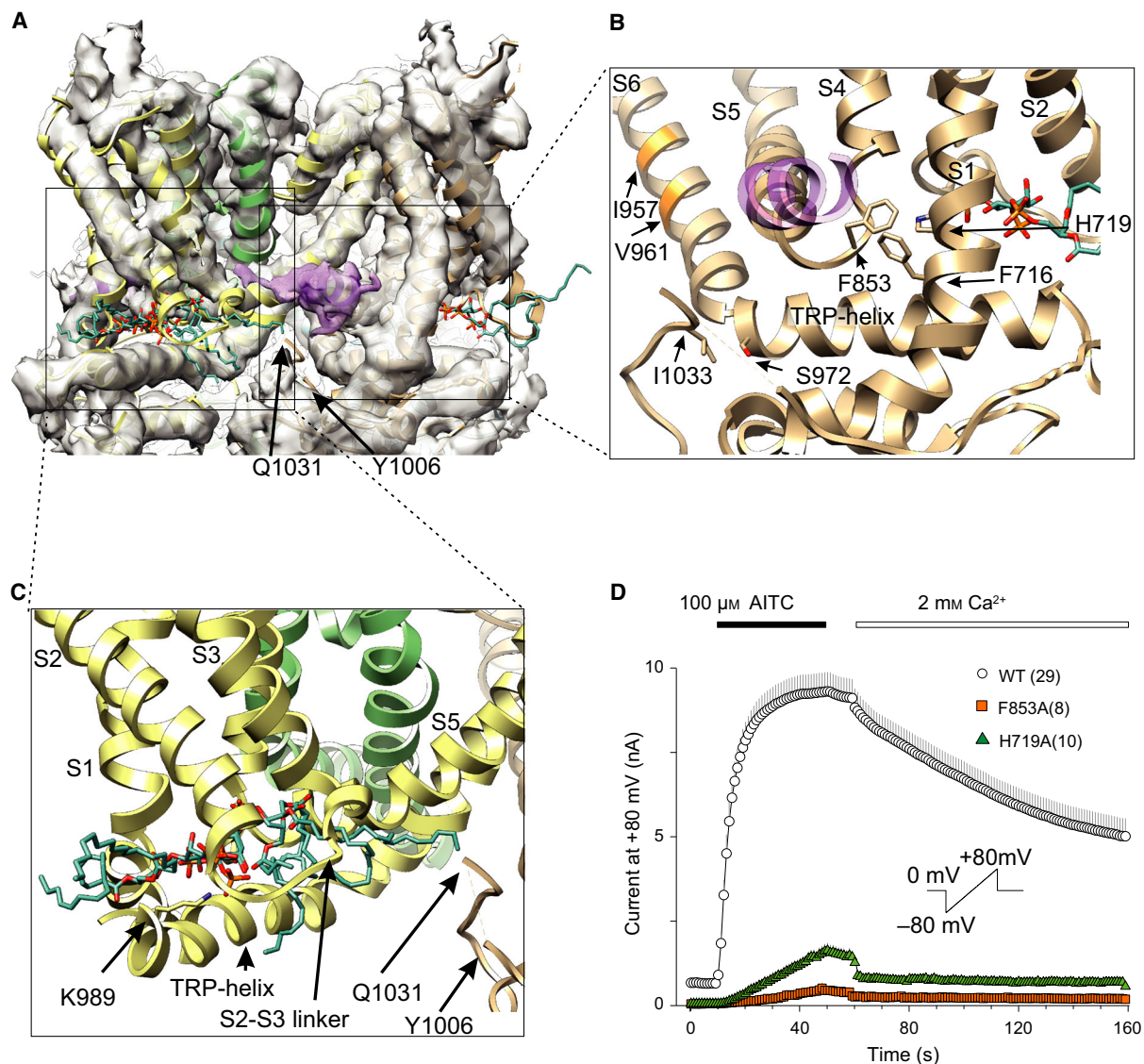
Fig. 5. Docking and functional studies indicate importance of the putative PIP$_2$-interacting region. (A) Cryo-EM density with superimposed model of TRPA1 with the completed intracellular loop connecting helices S2 and S3, modeled as described in [25]. The intracellular side of the sensor cavity has been proposed by Paulsen *et. al.* [17] to form a putative PIP$_2$ binding pocket. The negatively charged inositol triphosphate head group of PIP$_2$ may adopt several different conformations within the sensor domain. The lowest energy configurations of PIP$_2$ in the binding pocket obtained by ligand docking experiments are shown. Density map showing the location of a poorly resolved flexible loop between Y1006 and Q1031 with the schematically indicated density map for the α-helix (violet) in the inner membrane leaflet. (B) The loop may contact the sensor domain through stacking interactions with the side chains of F716, F853, and H719. Approximate position of the putative α-helix within the flexible loop is schematically shown (transparent violet). The close proximity of I1033 from the linker and S972 from the TRP-like helix suggests the possibility of a direct impact of the putative PIP$_2$-interacting region on channel gating. The lower gate of the channel is formed by I957 and V961, indicated in orange. (C) A detailed view from *A* showing the putative interaction site for PIP$_2$ centered above the TRP-helix. (D) Time course of average whole-cell currents induced by 100 μM AITC in Ca^{2+}-free solution and then exposed to 2 mM Ca^{2+}, obtained from wild-type and indicated mutants according to the voltage-ramp protocol depicted as an inset, measured at +80 mV (open circles with gray bars indicating SEM; *n* indicated in brackets). In some cases, the error bars are smaller than the symbol. The application of AITC and subsequent addition of 2 mM Ca^{2+} are indicated above.

(Fig. 6D) and from the time course of rectification ratio measured at −80 mV and at +80 mV (Fig. 6F). This result, analogous to that obtained from F1020G

(see Fig. 3), indicates that the two residues may share a common intramolecular pathway for affecting the gating of the channel. PIP$_2$ could then regulate
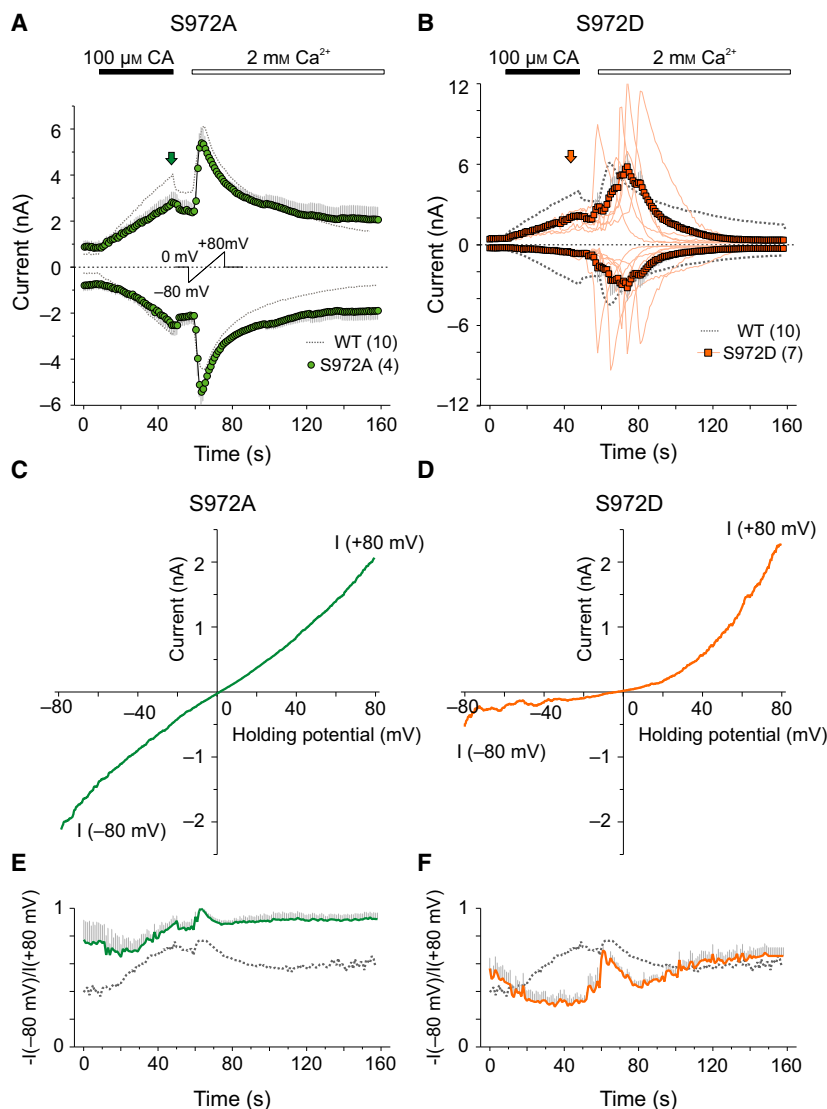
Fig. 6. Mutations at S972 affect chemical- and voltage-induced gating of TRPA1. (A) Average whole-cell currents induced by 100 μM cinnamaldehyde (CA) in Ca^{2+}-free solution and then exposed to 2 mM Ca^{2+}, measured at +80 and −80 mV in S972A mutant. The membrane potential was linearly ramped up each second from −80 to +80 mV (1 V·s^{-1}) (inset). Gray bars indicate SEM (*n* = 4). In some cases, the error bars are smaller than the symbol. The average current for the WT is overlaid as a gray dashed line for comparison. (B) Average currents (orange squares) and individual traces (light orange lines) recorded from seven HEK293T cells expressing the S972D mutant channels. The average current for the WT is overlaid as a gray dashed line for comparison. Note the desynchronized responses to 2 mM Ca^{2+}, most likely due to a low activity at negative potentials that do not permit Ca^{2+} to permeate and modulate the channel from the intracellular side. The number of cells is indicated in brackets for each construct. (C) and (D) Current–voltage relationships of traces measured at times indicated by arrows in panels A and B for S972A (green arrow) and S972D (orange arrow). (E) and (F) Average rectification of currents shown in panels A and B plotted as a function of time. Colored lines with gray bars indicate average ± SEM. The average rectification of currents through the WT is overlaid as a gray dashed line for comparison.

TRPA1 specifically at negative membrane potentials, whereas it loses its activity upon strong depolarization or in the presence of calcium. When external calcium was added, the maximum S972A-mediated currents were not significantly different from wild-type TRPA1 (−5.5 ± 0.6 nA vs. −4.4 ± 0.5 nA at −80 mV;

$P = 0.230$; and 5.5 ± 0.7 nA vs. 6.1 ± 0.8 nA at +80 mV; $P = 0.667$; $n = 4$ and 10). The maximum currents measured in the presence of Ca^{2+} were significantly increased in S972D at both negative and positive membrane potentials (to −9.9 ± 0.8 nA, $P = 0.027$ at −80 mV and to 9.6 ± 0.8 nA at +80 mV;

$P = 0.01$; $n = 7$). This latter result indicates changes in voltage-dependent gating rather than in trafficking or expression. Secondly, S972 is a residue involved in Ca^{2+} dependence of TRPA1.

Allosteric model indicates changes in voltage coupling and basal-open equilibrium induced by mutation F1020G

The double exponential fit needed for fitting the activation phase of voltage-induced responses and the decay of the tail currents (Fig. 4) reflects a complex gating process, apparently including multiple closed and open states. Such analysis does not indicate a possible mechanism through which the mutation may affect the channel gating. The faster voltage-induced activation of F1020G compared with the wild-type channels suggests that the mutation may strengthen the allosteric coupling of putative voltage sensor activation to channel opening. A rightward shift in V_{50} could be related to a direct change in gate equilibrium or a decrease in the voltage sensor equilibrium constant. By plotting the G–V curves described in Fig. 4C, D on a semi-logarithmic scale (Fig. 7A,B), it is obvious that the G–V shift in F1020G observed in the presence of external Ca^{2+} could be due to changes in the (basal-open) gate equilibrium [27]. An allosteric model to explain the activation of thermosensitive TRP ion channels by voltage has been previously proposed by Brauchi *et al.* [28]. This model is based on the presumption that an independent voltage sensor exists that is coupled to channel gating. At a constant temperature and low voltages, the channel is confined to the equilibrium between closed (C$_1$) and open (O$_1$) states with a small equilibrium constant L. Voltage drives transitions between resting and activated states of the sensor (C$_1$–C$_2$) with equilibrium constant $J = J_0\exp(zFV/RT)$, where J_0 is the equilibrium constant for the transition at 0 mV. In turn, the voltage sensor is coupled to channel gating by an allosteric coupling constant D. A simplifying assumption is that the voltage sensors from each subunit act in concert. The open probability is then given by $P_o = 1/[1 + (1 + J)/(L(1 + JD))]$.

We found that this simple allosteric model could reproduce voltage-dependent activation of the wild-type and the mutant F1020G channels. By simultaneously fitting the normalized steady-state G–V data and the time course of the activation phase of normalized conductances induced by depolarization to +200 mV, we obtained parameters D, L, and J_0 for representative cells (Fig. 7C–F and Table 4). For wild-type TRPA1 measured in the presence of external Ca^{2+}, a good fit

yielded the equilibrium constant L of 0.0200 ± 0.0027 and the allosteric factor D of $29\ 562 \pm 3571$ ($n = 10$). Mutation F1020G did not affect the equilibrium constant L (0.0172 ± 0.0031; $P = 0.490$; $n = 9$) but significantly decreased the allosteric factor D ($P \leq 0.001$; Fig. 7G). The estimated value of the voltage sensor equilibrium J_0 was significantly increased ($P = 0.020$) and this effect was particularly pronounced ($P \leq 0.001$; $n = 11$) when Ca^{2+} was not present in the extracellular solution (see Fig. 7G and Table 4). This result suggests that the F1020G mutation could abolish the allosteric coupling of the putative voltage sensor to channel gating and increase the equilibrium constant for the transitions between resting and activated states of the sensor. External Ca^{2+} affected the basal-open gate equilibrium (L) in F1020G but not in wild-type channels, indicating Ca^{2+} dependence of conformational changes caused by mutation.

Specific peptides interfere with TRPA1 calcium-dependent potentiation

It has been previously shown that Ca^{2+}/calmodulin complex binds to TRPA1 within the region L992-N1008 and potentiates the channel under resting conditions [8]. This study suggested that basal intracellular Ca^{2+} concentration is sufficient to cause preassociation of calmodulin with TRPA1, but the channels are far from saturated by endogenous calmodulin. Our results indicate that the peptide L992-N1008 interacts with lipid membranes if PIP$_2$ is present and its affinity decreases in the presence of calcium. We reasoned that if PIP$_2$ binds at the same site under native conditions, then chelating background Ca^{2+} should release the prebound Ca^{2+}/calmodulin complex from the channel and enable it to interact with PIP$_2$. It has been previously shown that the role of PIP$_2$ in TRPA1 activation and desensitization is complex and involves the related channel TRPV1 in sensory neurons [29]. In order to explore the possible contribution of the putative PIP$_2$-interaction site (Y1006-Q1031) in TRPA1 regulation under close-to-native conditions, we used neuronal F11 cells transfected with human TRPA1. We and others have previously shown that this cell line is a suitable model which maintains broad functional similarities with dorsal root ganglia neurons [30,31], including phospholipase C pathway and PIP$_2$ signaling [32,33]. *TRPA1* and *TRPV1* genes are absent from this cell line [31], which provides an opportunity to observe the human TRPA1 activity in isolation from the TRPV1-dependent pathways.

In our experiments, we aimed: (a) to generalize the previously published observations by Hasan *et al.* [8]

Fig. 7. Allosteric model reproduces voltage-dependent activation of TRPA1. (A) and (B) Average normalized conductances obtained as explained in Fig. 4, in the presence or absence of external Ca^{2+}, plotted on a semi-logarithmic scale. Data represent the means $\pm$ SEM (n indicated in Fig. 4C,D). The solid and dashed lines represent the best fit to a Boltzmann function as described in Materials and methods. (C) The time course of the activation phase of normalized currents measured for a representative cell expressing the wild-type TRPA1, induced by depolarization to +200 mV. (D) The normalized steady-state G–V data simultaneously fitted using a simple allosteric model (shown as inset in C). (E) and (F) The same as in C and D for the mutant F1020G. (G) Bar graph summarizing the results from allosteric model fitted to experimental data obtained for wild-type TRPA1 and F1020G in the presence (white and light green bars; $n = 10$ and 9) or absence (gray and dark green bars; $n = 8$ and 11) of external Ca^{2+}. Asterisk indicates a statistically significant difference from the first bar (Student's t-test; $P < 0.05$). The data are presented as means $\pm$ SEM.
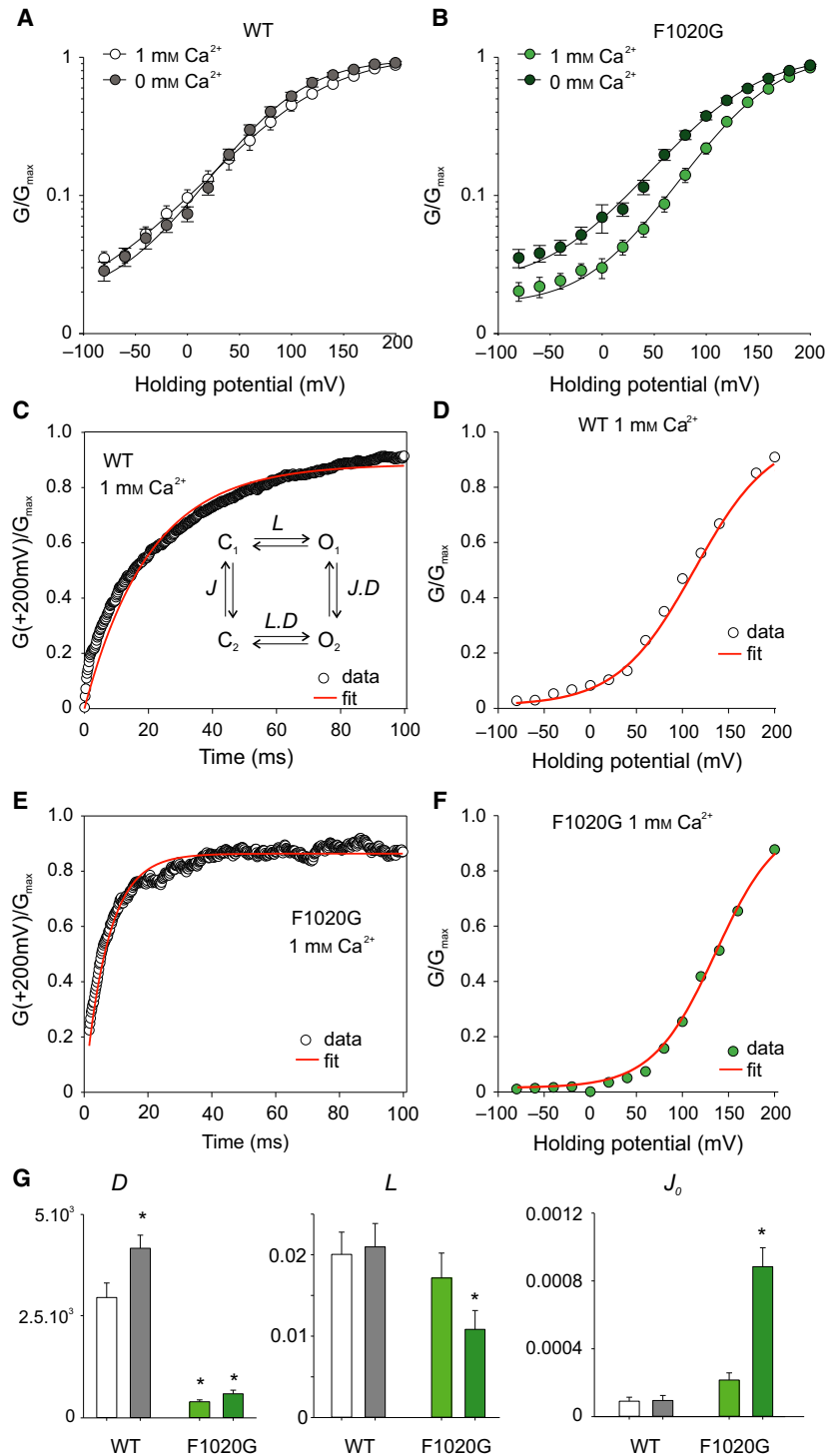
that Ca^{2+}/calmodulin-dependent potentiation of mouse TRPA1 is prevented by including the dominant negative peptide L992-N1008 in the pipette solution, (b) to explore, whether intracellular perfusion with the longer peptide T1003-P1034 has a similar dominant-negative

effect as the shorter peptide L992-N1008, and (c) to examine, whether PIP$_2$ and Ca^{2+}/calmodulin may compete for the same site at TRPA1 and influence the stability/sensitivity of the channel under resting conditions (i.e., at negative membrane potentials and

Table 4. Parameters of allosteric model fitted to experimental data obtained in the presence or absence of external Ca^{2+}. The data are presented as means $\pm$ SEM

Construct/[Ca^{2+}]$_o$	D	L	J$_0$	n
TRPA1/1 mM	29 562 $\pm$ 3571	0.0200 $\pm$ 0.0027	9.1 $\pm$ 2.3 $\times$ 10^{-5}	10
F1020G/1 mM	3967 $\pm$ 454	0.0172 $\pm$ 0.0031	2.2 $\pm$ 0.4 $\times$ 10^{-4}	9
TRPA1/0 mM	41 663 $\pm$ 3231	0.0210 $\pm$ 0.0029	9.5 $\pm$ 2.9 $\times$ 10^{-5}	8
F1020G/0 mM	5897 $\pm$ 899	0.0108 $\pm$ 0.0023	8.8 $\pm$ 1.1 $\times$ 10^{-4}	11

in the absence of calcium). Using the same experimental solutions and application protocol as Hasan *et al.* [8], we measured the extent of potentiation of carvacrol (100 μM) responses by external calcium (0.5 mM) under three situations: (a) within 30–50 s after whole-cell formation, (b) after 5–6 min perfusion with intracellular solution, and (c) after 5–6 min perfusion with intracellular solution containing either the L992-N1008 or T1003-P1034 peptide (Fig. 8). Figure 8A shows that initial TRPA1-mediated carvacrol responses recorded in nominal 0 Ca^{2+} 30–50 s after whole-cell formation had a much slower onset than responses measured from cells perfused for 5–6 min with internal solution with or without the peptide. As an apparent consequence, the carvacrol-induced current densities measured at the end of 10s application were significantly smaller in nonperfused cells (median 18.7 pA/pF vs. 8.5 pA/pF for the T1003-P1034 peptide; n = 12 and 6; P = 0.044; Fig. 8C). Intriguingly, Ca^{2+} potentiation was strongly (8.3 $\pm$ 1.6 fold) enhanced in the cells recorded within 30–50 s after whole-cell formation (Fig. 8D) and there were no correlation between the peak current amplitudes and the extent of Ca^{2+}-induced potentiation (correlation coefficient −0.0979, P = 0.749; n = 12). Inclusion of the T1003-P1034 peptide in the pipette solution significantly (P = 0.028; n = 6) prevented Ca^{2+}-dependent potentiation similarly as previously seen with L992-N1008 peptide [8]. These results suggest that the T1003-P1034 region is important for Ca^{2+}-dependent potentiation and that Ca^{2+}/calmodulin complex may compete for the same or overlapping binding site with PIP$_2$.

Discussion

Although TRPA1 does not necessarily require PIP$_2$ for function [34], a number of studies have shown that phosphoinositides are involved in TRPA1 regulation under different conditions [10,29,35,36] and a number putative sites of interaction have been proposed [15,18,25,36]. Structural studies [17], together with our results, support the possibility that PIP$_2$ can regulate TRPA1 either from the inner vestibule of the S1–S4

sensor domain or through a lateral fenestration between two adjacent subunits. Generally, proteins bind phosphoinositides mainly through electrostatic interactions of their positively charged residues and contributing nearby hydrophobic residues. Previous predictions for mouse TRPA1 protein sequence pointed to several prototypical PIP$_2$-interacting (pleckstrin homology) domains located in the N terminus (R46-K56, K443-K448, K592-R605) and the distal C terminus (K1092-R1097)[36]; based on later structural [17] and mutagenesis [18,23] studies, the latter region cannot be excluded. Another bioinformatics approach was used by Witschas *et al.* [15] who mapped the C terminus of human TRPA1 for prediction of antibacterial activity with AntiBP Server (http://crdd.osdd.net/raghava/antibp/index.html). Antibacterial peptides are capable of distinguishing bacterial from mammalian cells based on the differences in plasma membrane composition due to their significant affinity for negatively charged phospholipids [37,38]. Prediction results identified a high propensity for membrane-active region within the most proximal C-terminal region (later recognized as TRP-like domain) and subsequent biophysical studies indeed confirmed a strong interaction of the corresponding peptide I964-L992 with membranes containing anionic lipids [15]. This assay was complementary to previous electrophysiological studies that identified several positively charged residues within this region (K969, R975, K988, and K989) as critically involved in TRPA1 channel gating [18]. The mapping of antibacterial peptides within the C terminus predicted also another sequence, with even the highest score: F1017-Q1031. This region has a net charge of zero and contains only one basic residue. Thus, the predicted interaction with phosphoinositides should be predominantly facilitated by hydrophobic/aromatic residues. In this context, it is noteworthy that a missense mutation of a histidine residue two amino acids upstream of F1020 was recently found to be associated with childhood asthma [39]. It could be envisaged that the histidine-to-arginine mutation (rs959976) increases the affinity of PIP$_2$ to TRPA1 and, thus, influences the gating of the channel at physiological membrane potentials.
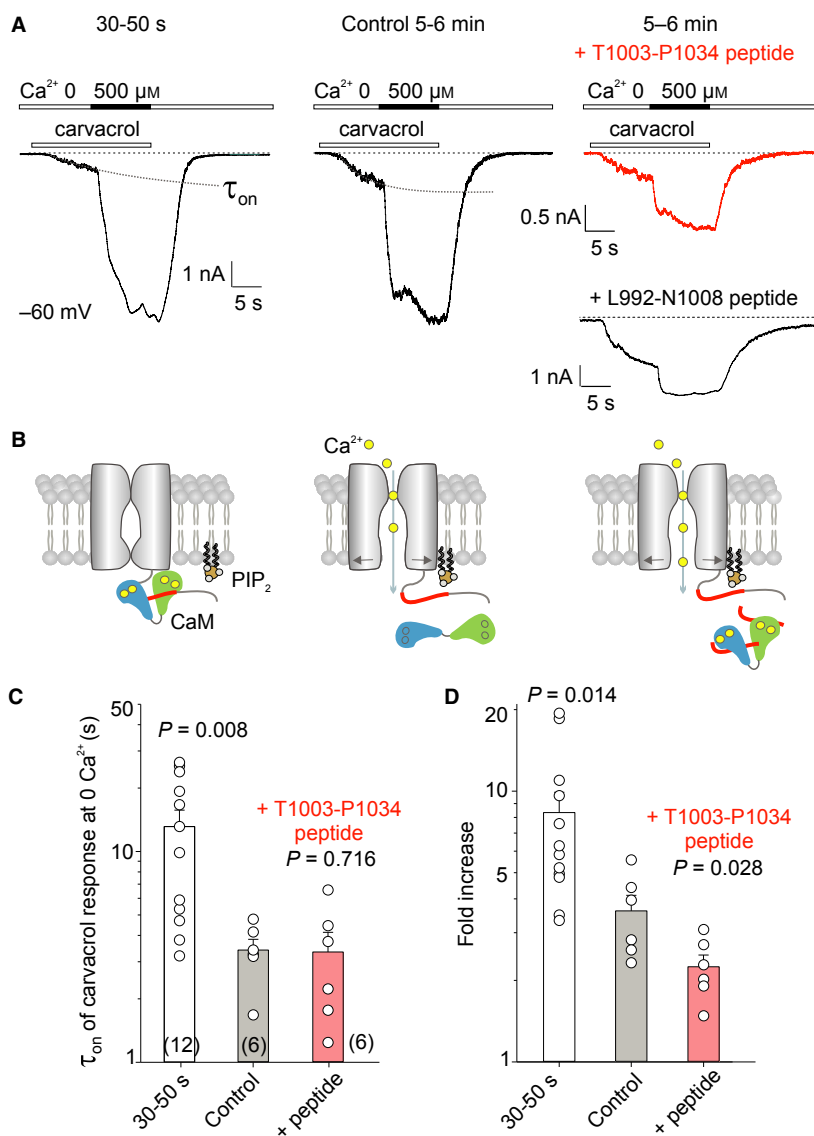
Fig. 8. Putative interaction site for membrane phosphoinositides may compete with Ca^{2+}/calmodulin complex. (A) Representative recordings from F11 cells expressing human TRPA1. The cells were exposed to 100 μM carvacrol in the absence (10 s) and presence (10 s) of extracellular Ca^{2+} (500 μM) either 30–50 s after whole-cell formation (left), after 5–6 min perfusion with internal solution (middle), or after 5–6 min perfusion with internal solution containing indicated peptide (right). For the L992-N1008 control peptide, three similar recordings as shown in right panel were measured (not statistically evaluated). (B) Proposed mechanism for regulation of human TRPA1 by Ca^{2+}/calmodulin and PIP$_2$. Under basal concentrations of Ca^{2+}, the channels bind Ca^{2+}/calmodulin (left). Chelation of Ca^{2+} upon 5–6 min perfusion with internal solution releases calmodulin from TRPA1, enables PIP$_2$ to bind at the same site and promote the channel activation by carvacrol (middle). When the specific peptide is included in the pipette solution (5–6 min perfusion), binding of PIP$_2$ increases and Ca^{2+}-dependent potentiation is reduced because of the dominant-negative effect of peptide (right). (C) Bar and all point plot summary of time constant (τ_{on}) of TRPA1 activation by 100 μM carvacrol applied in the absence of Ca^{2+}, obtained by monoexponential fit from experiments similar to those in (A) gray dotted line. Significance (*P*) tested using Student's paired *t*-test is indicated above the bars. The number of experiments is given in parentheses. (D) Summary of TRPA1 potentiation induced by 500 μM Ca^{2+} in experiments similar to those in (A). The data in panels C and D are presented as means ± SEM.

We demonstrate that PIP$_2$ is essential for the interaction of the peptide comprising the above region (T1003-P1034) with membrane lipids. The binding is strong and superficial, inducing only small perturbation in the lipid ordering. By looking at the published structure of TRPA1 [17] and integrating our current knowledge about the interaction capacity of specific TRPA1 peptides with PIP$_2$, it is tempting to speculate that there

might exist at least two sites with separate functions from which PIP$_2$ can regulate the channel activity. The first, formed by the inner cavity of the sensor and contributed by K989 from the TRP-like domain, and the second, explored within this study, localized between adjacent subunits, capable of directly affecting gating of the channel through the S4–S5 linker and R975 from the TRP-like domain. This scenario also predicts that the effectiveness of PIP$_2$ in inhibiting or promoting the activity of TRPA1 could strictly depend on conformational states of the channel. Our previous mutagenesis study demonstrated that neutralization of either K989 or R975 from the TRP-like domain produced gain of function phenotypes with strong outward rectification upon stimulation by depolarizing pulses. In the presence of a high concentration of agonist (200 μM allyl isothiocyanate), the gating of K989A became voltage independent whereas the gating of R975A remained strongly voltage dependent and outwardly rectifying [18]. These experiments were performed in the presence of 1 mM concentration of external Ca^{2+}, and thus, we cannot distinguish which of the reported effects may result exclusively from PIP$_2$ interaction. Given the recently revealed critical and dual role of Ca^{2+}/calmodulin in the regulation of TRPA1 [8], we could only hypothesize that PIP$_2$ may act in concert with Ca^{2+} and calmodulin to regulate the channel. Notably, the R975A mutant characterized in [18] and the S972D mutant studied here (Fig. 6) could have similar impact on the voltage sensitivity of the channel due to disrupted contacts with E1032 and I1033 (residues included in the region explored in this study). In any case, our data demonstrate that the peptide corresponding to the calmodulin binding site (L992-N1008) and the peptide overlapping with this site (T1003-P1034) are capable of binding PIP$_2$ and their affinities are decreased in the presence of Ca^{2+}. Under what physiological circumstances might the PIP$_2$-dependent regulation of TRPA1 be relevant? TRPA1 is extensively coexpressed with TRPV1 in sensory neurons and these channels form a complex and functionally interact [29,40]. Future studies should focus on establishing the physiological relevance of our proposed mechanism (Fig. 8B) in various nociceptive neurons and, particularly, in relation to the TRPV1 expression pattern. Our data demonstrate that lowering the concentration of Ca^{2+} below basal levels increases the apparent affinity of the channel to nonelectrophilic agonist carvacrol (Fig. 8A,C). It can thus be imagined that PIP$_2$ competes with Ca^{2+}/calmodulin for binding at TRPA1 under basal conditions. Because the Ca^{2+}/calmodulin complex primes the channel for activation under weakly activating conditions and inactivates it at higher Ca^{2+}

concentrations [8], the effects of PIP$_2$ should be consequentially complex and Ca^{2+} dependent. For that matter, a similar degree of complexity of regulation by PIP$_2$ has been demonstrated (after nearly 15 years of intensive research) for related channel TRPV1 [41,42].

Materials and methods

Cell culture, constructs, and transfection

Human embryonic kidney 293T (HEK293T, CRL-3216; ATCC, Manassas, VA, USA) cells were cultured in Opti-MEM I media (Invitrogen, Carlsbad, CA, USA) supplemented with 5% fetal bovine serum. The magnet-assisted transfection (IBA GmbH, Göttingen, Germany) technique was used to transiently cotransfect the cells in a 15.6-mm well on a 24-well plate with 200 ng of GFP plasmid (TaKaRa, Shiga, Japan) and with 300 ng of cDNA plasmid encoding wild-type or mutant human TRPA1 (pCMV6-XL4 vector, OriGene Technologies, Rockville, MD, USA). The cells were used 24–48 h after transfection. At least two independent transfections were used for each experimental group. The wild-type channel was regularly tested in the same batch as the mutant. The mutants were generated by PCR using a QuikChange II XL Site-Directed Mutagenesis Kit (Agilent Technologies, Santa Clara, CA, USA) and confirmed by DNA sequencing (GATC Biotech, Konstanz, Germany). F11 cells (The European Collection of Authenticated Cell Cultures, ECACC 08062601, Porton Down, UK) cultured in Dulbecco's modified Eagle's medium supplemented with 2 mM glutamine and 10% fetal bovine serum were passaged once a week using trypsin-EDTA (Invitrogen) and grown under 5% CO$_2$ at 37 °C. One to two days before transfection, cells were plated in 24-well plates (2×10^5 cells per well) in 0.5 mL of medium and became confluent on the day of transfection. The cells were transiently cotransfected with 300 ng of cDNA plasmid encoding human TRPA1 (in the pCMV6-XL4 vector, OriGene Technologies) and with 200 ng of GFP plasmid (TaKaRa, Shiga) with the use of Lipofectamin 2000 (Invitrogen) and then plated on poly-L-lysine-coated glass coverslips.

Electrophysiology

Whole-cell membrane currents were recorded by employing an Axopatch 200B amplifier and pCLAMP10 software (Molecular Devices). Patch electrodes were pulled from borosilicate glass and heat-polished to a final resistance between 3 and 5 MΩ. Series resistance was compensated by at least 70% in all recordings. The experiments were performed at room temperature (23–25 °C). Only one recording was performed on any one coverslip of cells to ensure that recordings were made from cells not previously exposed to chemical stimuli. A system for rapid superfusion of the cultured cells was used for drug application [43]. For

HEK293T cell recordings, the extracellular bath solutions contained: 150 mM NaCl and 10 mM HEPES, with an added 2 mM HEDTA for the Ca^{2+}-free solution, and 2 mM CaCl$_2$ for the Ca^{2+}-containing solutions, adjusted to pH 7.3 with NaOH, 300 mOsm. The current to voltage (*I/V*) relationships were measured in control bath solution containing 160 mM NaCl, 2.5 mM KCl, 1 mM CaCl$_2$, 2 mM MgCl$_2$, 10 mM HEPES, 10 mM glucose, adjusted to pH 7.3 and 320 mOsm, or in the Ca^{2+}-free solution. The *I/V* relationships were recorded using 100 ms voltage steps from −80 to +200 mV (increment +20 mV), holding potential −70 mV, recorded in control extracellular solution ~ 1 min after whole-cell formation. The internal pipette solution contained 145 mM CsCl, 5 mM EGTA, 3 mM CaCl$_2$, 10 mM HEPES, and 2 mM MgATP, adjusted with CsOH to pH 7.3 and 290 mOsm. The agonist sensitivity was tested with a protocol described previously [25] where the membrane potential was ramped every second from −80 to +80 mV (1 V·s^{-1}). For F11 cell recordings, the extracellular bath solution (nominal 0 Ca^{2+}) contained: 140 mM NaCl, 4 mM KCl, 1 mM MgCl$_2$, 10 mM HEPES, 5 mM glucose, pH 7.4 adjusted with NaOH. Internal pipette solution contained 140 mM KCl, 2 mM MgCl$_2$, 5 mM EGTA, 10 mM HEPES, pH 7.4 adjusted with KOH. Allyl isothiocyanate, cinnamaldehyde, and carvacrol solutions were prepared prior to use from a 0.1 M stock solution in Me$_2$SO. To study the effects of peptides on TRPA1-mediated currents in F11 cells, peptides were included in the pipette. All of the chemicals were purchased from Sigma-Aldrich (Prague, Czech Republic).

Preparation of small unilamellar vesicles, large unilamellar vesicles, and polymer-based nanodiscs (SMALPs)

Liposomes were prepared by dissolving the appropriate amount of lipid into chloroform or a mixture of chloroform and methanol 2/1 (v/v), followed by solvent evaporation under nitrogen to deposit the lipid as a film on the wall of a test tube. Final traces of solvent were removed in a vacuum chamber attached to a liquid nitrogen trap during 2–3 h. Dried lipid films were hydrated with TBS buffer, pH 7.6 or with 10 mM phosphate buffer, pH 7.6 (for CD experiments), and thoroughly vortexed at a temperature superior to the phase transition temperature of the lipid to obtain multilamellar vesicles (MLVs). To better mimic biological conditions, the peptide was added to the lipids after vesicle/liposome formation. To form LUVs, the MLV dispersion was subjected to six freeze/thawing cycles and passed 11 times through a mini-extruder equipped with two stacked 0.1 µm polycarbonate filters (Avanti, Alabaster, AL, USA). For forming small unilamellar vesicles (SUVs), MLVs were tip sonicated on ice, amplitude 40, time 2 × 10 min.

Styrene maleic acid lipid particles were prepared by incubating MLVs (1.3 mM) with SMA solution (6.5 mM) both in PBS. To ensure complete solubilization of the MLVs, a ratio of 0.5 ([SMA]/[lipid]) was used that is above the reported Rsol value (ratio above which the liposome solubilization is complete) for POPC liposomes [44]. Formation of SMALPs was followed by Dynamic Light Scattering (Vasco, Cordouan) and also by MDS (microfluidic diffusional sizing; in this case, we have included 10% palmitoyl-oleoyl-phosphatidylserine in the lipid system in order to have a reactive primary amine for fluorescent labeling). SMALP formation occurred promptly after the mixing and they remained stable for a couple of weeks. SMALPs of about 10–15 nm in size were obtained by this procedure. All lipids were purchased from Avanti Polar Lipids. The peptides (TIVYPNKPR SGGMLFHIFCFLFCTGEIRQEIP, herein named T1003-P1034 and LWFLRKVDQKSTIVYPN, herein named L992-N1008) were purchased from Biomatik (Cambridge, ON, Canada) and used without further purification.

Liposome leakage

Sulforhodamine B-containing LUVs were prepared using the same protocol used to make regular LUVs, except for the hydration step made with 0.5xTBS buffer of the lipid films, which contained 50 mM Sulforhodamine B. Free rhodamine was separated from rhodamine-containing LUVs using size exclusion column chromatography (Sephadex G-75) with TBS as elution buffer. The concentration of lipids was estimated using Rouser protocol [45]. For the assay, the lipid concentration was set at 1 µM and peptide concentration varied from 1 to 500 nM (P/L ratio of 1/100 to 1/10, respectively). All measurements were performed with a BMG Labtech plate reader. Data were collected every 1 s at room temperature using a λ_{exc} = 565 nm and λ_{em} = 586 nm with an emission and excitation slit of 2.5 nm in a cuvette of 2 mL. The fluorescence from rhodamine at 50 mM concentration was low due to self-quenching, but increased considerably upon dilution. The fluorescence intensity at equilibrium was measured after 60 min. At the end of the assay, complete leakage of LUVs was achieved by adding 100 µL of 10% Triton X-100 solution dissolving the lipid membrane without interfering with the fluorescence signal. The percentage of rhodamine release was calculated according to the following equation:

$$\% \, leakage = (F_t - F_0)/(F_f - F_0) * 100, \qquad (1)$$

where the percentage of leakage is the fraction of dye released (normalized membrane leakage), F_t is the measured fluorescence intensity at time t, and F_0 and F_f are the fluorescence intensities at times $t = 0$, and after final addition of Triton X-100, respectively. A dilution correction was applied to the fluorescence intensity after injection of the Triton X-100.

Circular dichroism (CD)

CD data were recorded on a Jasco J-815 CD spectrophotometer with a 1-mm path length. Far-UV spectra were recorded from 185 or 195 to 250 nm with a 0.5-nm step resolution and a 1-nm bandwidth at 300 K. The scan speed was 50 nm·min^{-1} (1 s response time), and the spectra were averaged over seven scans. CD spectra were collected for peptide samples in a 10-mM phosphate buffer at concentrations varying from 20 to 120 μM for the peptide alone and in the presence of the lipid at concentrations of 1220 μM (20% PIP$_2$ + 80% POPC), 1290 μM (5% PIP$_2$ + 95% POPC), and 1320 μM (POPC) (P/L ratios investigated ranged from 1/50 to 1/10). For each sample, the background (buffer or liposome/micelle in the absence of peptide) was automatically subtracted from the signal. Data were evaluated using BeStSel.org database [46].

Plasmon waveguide resonance spectroscopy

Plasmon waveguide resonance experiments were performed on a homemade PWR instrument that had a spectral angular resolution of ≥ 0.5 mdeg. Resonances can be obtained with light whose electric vector is either parallel (s-polarization) or perpendicular (p-polarization) to the plane of the resonator surface. The principles behind the technique and information obtained have been reported elsewhere (see, e.g., [20,47,48]). The sample to be analyzed (a lipid bilayer membrane) was immobilized on the resonator surface and placed in contact with an aqueous medium (TBS buffer, pH 7.6), into which the peptides were then introduced. The solid-supported lipid bilayer was made by incubation of SUVs of lipids with the sensor surface that leads to the spontaneous burst of the vesicles in the silica surface to form a bilayer (further details can be found in ref. [49]). After bilayer formation, a peptide was incrementally added to the cell sample compartment and the spectral changes monitored with both polarizations. Affinities between the peptide and the lipids were obtained by plotting the PWR spectral changes that occur upon incremental additions of ligand to the cell. Data fitting (GraphPad Prism, San Diego, CA, USA) through a hyperbolic saturation curve provides the apparent dissociation constants.

Attenuated total reflection infrared spectroscopy (ATR-FTIR)

ATR-FTIR spectra were recorded on a Nicolet 6700 FT-IR spectrometer (Nicolet Instrument, Madison, WI, USA) equipped with a liquid nitrogen cooled mercury–cadmium–telluride detector (ThermoFisher Scientific, San Jose, CA, USA), with a spectral resolution of 4 cm^{-1} and a one-level zero filling. Lipid bilayers adsorbed on a germanium ATR crystal were obtained by spontaneous fusion of SUVs of pure POPC or a mixture of POPC with PIP$_2$. The total lipid concentration used was 1.5 mg·mL^{-1} (ca. 1.96 mM). SUV was prepared by tip sonication for 30 min after direct hydration of lipid films by TBS buffer. TBS was used instead of PBS to avoid phosphate contribution from the buffer. After bilayer formation at the crystal surface, the excess of SUV was removed by a TBS buffer. Since ATR spectroscopy is sensitive to the orientation of the lipid and peptide [50], spectra were recorded with a parallel (p) and perpendicular (s) polarization of the incident light. All the orientation information is then contained in the dichroic ratio $R_{ATR} = Ap/As$, where Ap and As represent the absorbance of the considered band for the p or s polarization of the incident light, respectively (for more details, see [19]). A peptide at a concentration of 1 mM was incubated for 10 min with the bilayer, the noninteracting peptide was removed by washing three times with TBS buffer.

Microfluidic diffusional sizing

Microfluidic diffusional sizing was performed using the Fluidity One instrument developed by Fluidic Analytics. This newly developed and very sensitive method provides information about sample concentration and size by measuring the rate of diffusion of proteins. Streams of a protein sample and an auxiliary fluid are run in parallel under steady-state laminar flow, with no convective mixing. Consequently, the only way the protein can migrate from the sample into the auxiliary fluid is by diffusion. This is the measurement step in the Fluidity One system, and occurs while the proteins are in their native state, before a label is introduced. Following measurement, the streams are split and the analytes are labeled via primary amines present in the peptides and lipids (in case of phosphatidylserine or phosphatidylethanolamine lipid headgroups). The hydrodynamic radius of the vesicles is directly related to their diffusion coefficient, D, through the Stokes–Einstein equation

$$D = K_B T / \pi \eta \, R_h, \qquad (2)$$

where K_B is the Boltzmann constant, T is the temperature, and η is the viscosity of the buffer used for coflow and for suspending the sample. Herein, we have used this method to follow the interaction of the two peptides with SMALPs composed of POPC and POPC/PIP$_2$ (9/1). By titrating the peptides (450 μg·mL^{-1}) with increasing concentration of lipids and measuring the size at each point, a binding curve can be obtained based on the size changes occurring upon the peptide–lipid interaction. From the binding curve, the dissociation constant can be obtained by fitting the data with a hyperbolic binding equation (PRISM, GraphPad Software). To note that the peptides alone have a size of about 1.5–2 nm and the SMALPs have a size of about 10 nm.

Data analysis, statistics, and modeling

All of the electrophysiological data were analyzed using pCLAMP10 (Molecular Devices, San Jose, CA, USA), and curve fitting and statistical analyses were done in SIGMAPLOT 10 (Systat Software Inc.) or PRISM (GraphPad Software). Conductance–voltage (*G–V*) relationships were obtained from steady-state whole-cell currents measured at the end of voltage steps from −80 to +200 mV in increments of +20 mV. Voltage-dependent gating parameters were estimated by fitting the conductance $G = I/(V - V_{rev})$ as a function of the test potential *V* to the Boltzmann equation:

$$G = [(G_{max} - G_{min})/(1 + \exp(-zF(V - V_{50})/RT))] + G_{min},$$

(3)

where *z* is the apparent number of gating charges, V_{50} is the half-activation voltage, G_{min} and G_{max} are the minimum and maximum whole-cell conductance, V_{rev} is the reversal potential, and *F*, *R*, and *T* have their usual thermodynamic meanings. Statistical significance was determined by Student's *t*-test or the analysis of variance, as appropriate; differences were considered statically significant at $P < 0.05$ where not stated otherwise. The data are presented as means ± SEM.

Activation time constants (τ_{fast} and τ_{slow}) were measured directly from outward currents by performing a double exponential Chebyshev fit to the rising phase of the activating currents. Fast and slow deactivation was characterized by a single or a double exponential fit to the current upon repolarization from +200 to −70 mV. Initial 1.3-ms interval was ignored. Because the relative weights of fast and slow deactivation components differed between the cells tested, we calculated a weighted, average time constant of the fast and slow components of activation/deactivation based on the amplitude of each component.

$$\tau_w = A_{fast}/(A_{fast} + A_{slow}) \times \tau_{fast} + A_{slow}/(A_{fast} + A_{slow}) \times \tau_{slow}.$$

(4)

Fitting to an allosteric model was performed with COPASI 4.22 [51]. Molecular docking of PIP$_2$ into the TRPA1 sensor domain was performed as described previously [25] with the program AutoDoc Vina integrated in UCSF CHIMERA 1.12 software using a cubic box of $100 \times 100 \times 100$ Å^3 with default docking parameters.

Acknowledgements

Conflict of interest

The authors declare no conflict of interest.

Author contributions

VV and LM conceived the project; VV and IDA designed the experiments; LM, VS, AK, AC, and IDA performed experiments; LM, VS, SV, JF, SL, IDA, and VV analyzed data; VV and IDA wrote the manuscript.

References

1 Story GM, Peier AM, Reeve AJ, Eid SR, Mosbacher J, Hricik TR, Earley TJ, Hergarden AC, Andersson DA, Hwang SW *et al.* (2003) ANKTM1, a TRP-like channel expressed in nociceptive neurons, is activated by cold temperatures. *Cell* **112**, 819–829.

2 Jordt SE, Bautista DM, Chuang HH, McKemy DD, Zygmunt PM, Hogestatt ED, Meng ID & Julius D (2004) Mustard oils and cannabinoids excite sensory nerve fibres through the TRP channel ANKTM1. *Nature* **427**, 260–265.

3 Nilius B, Appendino G & Owsianik G (2012) The transient receptor potential channel TRPA1: from gene to pathophysiology. *Pflugers Arch* **464**, 425–458.

4 Laursen WJ, Bagriantsev SN & Gracheva EO (2014) TRPA1 channels: chemical and temperature sensitivity. *Curr Top Membr* **74**, 89–112.

5 Baraldi PG, Preti D, Materazzi S & Geppetti P (2010) Transient receptor potential ankyrin 1 (TRPA1) channel as emerging target for novel analgesics and anti-inflammatory agents. *J Med Chem* **53**, 5085–5107.

6 Zygmunt PM & Hogestatt ED (2014) Trpa1. *Handb Exp Pharmacol* **222**, 583–630.

7 Wang YY, Chang RB, Allgood SD, Silver WL & Liman ER (2011) A TRPA1-dependent mechanism for the pungent sensation of weak acids. *J Gen Physiol* **137**, 493–505.

8 Hasan R, Leeson-Payne AT, Jaggar JH & Zhang X (2017) Calmodulin is responsible for Ca2 + -dependent regulation of TRPA1 Channels. *Sci Rep* **7**, 45098.

9 Bandell M, Story GM, Hwang SW, Viswanath V, Eid SR, Petrus MJ, Earley TJ & Patapoutian A (2004) Noxious cold ion channel TRPA1 is activated by pungent compounds and bradykinin. *Neuron* **41**, 849–857.

10 Dai Y, Wang S, Tominaga M, Yamamoto S, Fukuoka T, Higashi T, Kobayashi K, Obata K, Yamanaka H & Noguchi K (2007) Sensitization of TRPA1 by PAR2 contributes to the sensation of inflammatory pain. *J Clin Invest* **117**, 1979–1987.

11 Rohacs T (2014) Phosphoinositide regulation of TRP channels. *Handb Exp Pharmacol* **223**, 1143–1176.

12 Rohacs T (2013) Regulation of transient receptor potential channels by the phospholipase C pathway. *Adv Biol Regul* **53**, 341–355.

13 Rohacs T (2016) Phosphoinositide signaling in somatosensory neurons. *Adv Biol Regul* **61**, 2–16.

14 Nilius B, Prenen J & Owsianik G (2011) Irritating channels: the case of TRPA1. *J Physiol (Lond)* **589**, 1543–1549.

15 Witschas K, Jobin ML, Korkut DN, Vladan MM, Salgado G, Lecomte S, Vlachova V & Alves ID (2015) Interaction of a peptide derived from C-terminus of human TRPA1 channel with model membranes mimicking the inner leaflet of the plasma membrane. *Biochim Biophys Acta* **1848**, 1147–1156.

16 Gao Y, Cao E, Julius D & Cheng Y (2016) TRPV1 structures in nanodiscs reveal mechanisms of ligand and lipid action. *Nature* **534**, 347–351.

17 Paulsen CE, Armache JP, Gao Y, Cheng Y & Julius D (2015) Structure of the TRPA1 ion channel suggests regulatory mechanisms. *Nature* **520**, 511–517.

18 Samad A, Sura L, Benedikt J, Ettrich R, Minofar B, Teisinger J & Vlachova V (2011) The C-terminal basic residues contribute to the chemical- and voltage-dependent activation of TRPA1. *Biochem J* **433**, 197–204.

19 Castano S & Desbat B (2005) Structure and orientation study of fusion peptide FP23 of gp41 from HIV-1 alone or inserted into various lipid membrane models (mono-, bi- and multibi-layers) by FT-IR spectroscopies and Brewster angle microscopy. *Biochim Biophys Acta* **1715**, 81–95.

20 Salamon Z, Macleod HA & Tollin G (1997) Coupled plasmon-waveguide resonators: a new spectroscopic tool for probing proteolipid film structure and properties. *Biophys J* **73**, 2791–2797.

21 Arosio P, Muller T, Rajah L, Yates EV, Aprile FA, Zhang Y, Cohen SI, White DA, Herling TW, De Genst EJ *et al.* (2016) Microfluidic diffusion analysis of the sizes and interactions of proteins under native solution conditions. *ACS Nano* **10**, 333–341.

22 Gang H, Galvagnion C, Meisl G, Muller T, Pfammatter M, Buell AK, Levin A, Dobson CM, Mu B & Knowles TPJ (2018) Microfluidic diffusion platform for characterizing the sizes of lipid vesicles and the thermodynamics of protein-lipid interactions. *Anal Chem* **90**, 3284–3290.

23 Sura L, Zima V, Marsakova L, Hynkova A, Barvik I & Vlachova V (2012) C-terminal acidic cluster is involved in Ca2 +-induced regulation of human transient receptor potential ankyrin 1 channel. *J Biol Chem* **287**, 18067–18077.

24 Hynkova A, Marsakova L, Vaskova J & Vlachova V (2016) N-terminal tetrapeptide T/SPLH motifs contribute to multimodal activation of human TRPA1 channel. *Sci Rep* **6**, 28700.

25 Zimova L, Sinica V, Kadkova A, Vyklicka L, Zima V, Barvik I & Vlachova V (2018) Intracellular cavity of sensor domain controls allosteric gating of TRPA1 channel. *Sci Signal* **11**. https://doi.org/10.1126/scisigna l.aan8621

26 Suh BC & Hille B (2008) PIP2 is a necessary cofactor for ion channel function: how and why? *Annu Rev Biophys* **37**, 175–195.

27 Horrigan FT & Aldrich RW (2002) Coupling between voltage sensor activation, Ca2 + binding and channel opening in large conductance (BK) potassium channels. *J Gen Physiol* **120**, 267–305.

28 Brauchi S, Orio P & Latorre R (2004) Clues to understanding cold sensation: thermodynamics and electrophysiological analysis of the cold receptor TRPM8. *Proc Natl Acad Sci USA* **101**, 15494–15499.

29 Akopian AN, Ruparel NB, Jeske NA & Hargreaves KM (2007) Transient receptor potential TRPA1 channel desensitization in sensory neurons is agonist dependent and regulated by TRPV1-directed internalization. *J Physiol* **583**, 175–193.

30 Vetter I & Lewis RJ (2010) Characterization of endogenous calcium responses in neuronal cell lines. *Biochem Pharmacol* **79**, 908–920.

31 Yin K, Baillie GJ & Vetter I (2016) Neuronal cell lines as model dorsal root ganglion neurons: a transcriptomic comparison. *Mol Pain* **12**, 1–17.

32 Kadkova A, Synytsya V, Krusek J, Zimova L & Vlachova V (2017) Molecular basis of TRPA1 regulation in nociceptive neurons. A review. *Physiol Res* **66**, 425–439.

33 Prucha J, Krusek J, Dittert I, Sinica V, Kadkova A & Vlachova V (2018) Acute exposure to high-induction electromagnetic field affects activity of model peripheral sensory neurons. *J Cell Mol Med* **22**, 1355–1362.

34 Moparthi L, Survery S, Kreir M, Simonsen C, Kjellbom P, Hogestatt ED, Johanson U & Zygmunt PM (2014) Human TRPA1 is intrinsically cold- and chemosensitive with and without its N-terminal ankyrin repeat domain. *Proc Natl Acad Sci USA* **111**, 16901–16906.

35 Hirono M, Denis CS, Richardson GP & Gillespie PG (2004) Hair cells require phosphatidylinositol 4,5-bisphosphate for mechanical transduction and adaptation. *Neuron* **44**, 309–320.

36 Karashima Y, Prenen J, Meseguer V, Owsianik G, Voets T & Nilius B (2008) Modulation of the transient receptor potential channel TRPA1 by

phosphatidylinositol 4,5-biphosphate manipulators. *Pflugers Arch* **457**, 77–89.

37 Lata S, Sharma BK & Raghava GP (2007) Analysis and prediction of antibacterial peptides. *BMC Bioinformatics* **8**, 263.

38 Matsuzaki K (2009) Control of cell selectivity of antimicrobial peptides. *Biochim Biophys Acta* **1788**, 1687–1692.

39 Gallo V, Dijk FN, Holloway JW, Ring SM, Koppelman GH, Postma DS, Strachan DP, Granell R, de Jongste JC, Jaddoe VW *et al.* (2017) TRPA1 gene polymorphisms and childhood asthma. *Pediatr Allergy Immunol* **28**, 191–198.

40 Akopian AN (2011) Regulation of nociceptive transmission at the periphery via TRPA1-TRPV1 interactions. *Curr Pharm Biotechnol* **12**, 89–94.

41 Rohacs T (2015) Phosphoinositide regulation of TRPV1 revisited. *Pflugers Arch* **467**, 1851–1869.

42 Chuang HH, Prescott ED, Kong H, Shields S, Jordt SE, Basbaum AI, Chao MV & Julius D (2001) Bradykinin and nerve growth factor release the capsaicin receptor from PtdIns(4,5)P2-mediated inhibition. *Nature* **411**, 957–962.

43 Dittert I, Benedikt J, Vyklicky L, Zimmermann K, Reeh PW & Vlachova V (2006) Improved superfusion technique for rapid cooling or heating of cultured cells under patch-clamp conditions. *J Neurosci Methods* **151**, 178–185.

44 Grethen A, Oluwole AO, Danielczak B, Vargas C & Keller S (2017) Thermodynamics of nanodisc formation mediated by styrene/maleic acid (2:1) copolymer. *Sci Rep* **7**, 11517.

45 Rouser G, Fkeischer S & Yamamoto A (1970) Two dimensional then layer chromatographic separation of polar lipids and determination of phospholipids by phosphorus analysis of spots. *Lipids* **5**, 494–496.

46 Micsonai A, Wien F, Kernya L, Lee YH, Goto Y, Refregiers M & Kardos J (2015) Accurate secondary structure prediction and fold recognition for circular dichroism spectroscopy. *Proc Natl Acad Sci USA* **112**, E3095–E3103.

47 Alves ID, Park CK & Hruby VJ (2005) Plasmon resonance methods in GPCR signaling and other membrane events. *Curr Protein Pept Sci* **6**, 293–312.

48 Harte E, Maalouli N, Shalabney A, Texier E, Berthelot K, Lecomte S & Alves ID (2014) Probing the kinetics of lipid membrane formation and the interaction of a nontoxic and a toxic amyloid with plasmon waveguide resonance. *Chem Commun* **50**, 4168–4171.

49 Alves ID & Lecomte S (2019) Study of G-protein coupled receptor signaling in membrane environment by plasmon waveguide resonance. *Acc Chem Res* **52**, 1059–1067.

50 Goormaghtigh E, Raussens V & Ruysschaert JM (1999) Attenuated total reflection infrared spectroscopy of proteins and lipids in biological membranes. *Biochim Biophys Acta* **1422**, 105–185.

51 Mendes P, Hoops S, Sahle S, Gauges R, Dada J & Kummer U (2009) Computational modeling of biochemical networks using COPASI. *Methods Mol Biol* **500**, 17–59.

52 Crooks GE, Hon G, Chandonia JM & Brenner SE (2004) WebLogo: a sequence logo generator. *Genome Res* **14**, 1188–1190.

Proximal C-Terminus Serves as a Signaling Hub for TRPA1 Channel Regulation via Its Interacting Molecules and Supramolecular Complexes

Lucie Zimova[1]*, Kristyna Barvikova[1], Lucie Macikova[1,2], Lenka Vyklicka[1], Viktor Sinica[1,3], Ivan Barvik[4] and Viktorie Vlachova[1]*

[1] Department of Cellular Neurophysiology, Institute of Physiology, The Czech Academy of Sciences, Prague, Czechia, [2] Department of Physiology, Faculty of Science, Charles University, Prague, Czechia, [3] Department of Physical and Macromolecular Chemistry, Faculty of Science, Charles University, Prague, Czechia, [4] Division of Biomolecular Physics, Faculty of Mathematics and Physics, Institute of Physics, Charles University, Prague, Czechia

Our understanding of the general principles of the polymodal regulation of transient receptor potential (TRP) ion channels has grown impressively in recent years as a result of intense efforts in protein structure determination by cryo-electron microscopy. In particular, the high-resolution structures of various TRP channels captured in different conformations, a number of them determined in a membrane mimetic environment, have yielded valuable insights into their architecture, gating properties and the sites of their interactions with annular and regulatory lipids. The correct repertoire of these channels is, however, organized by supramolecular complexes that involve the localization of signaling proteins to sites of action, ensuring the specificity and speed of signal transduction events. As such, TRP ankyrin 1 (TRPA1), a major player involved in various pain conditions, localizes into cholesterol-rich sensory membrane microdomains, physically interacts with calmodulin, associates with the scaffolding A-kinase anchoring protein (AKAP) and forms functional complexes with the related TRPV1 channel. This perspective will contextualize the recent biochemical and functional studies with emerging structural data with the aim of enabling a more thorough interpretation of the results, which may ultimately help to understand the roles of TRPA1 under various physiological and pathophysiological pain conditions. We demonstrate that an alteration to the putative lipid-binding site containing a residue polymorphism associated with human asthma affects the cold sensitivity of TRPA1. Moreover, we present evidence that TRPA1 can interact with AKAP to prime the channel for opening. The structural bases underlying these interactions remain unclear and are definitely worth the attention of future studies.

Keywords: TRPA1, TRP channel, calmodulin, A-kinase anchoring protein, transient receptor potential

INTRODUCTION

The Transient Receptor Potential (TRP) Ankyrin subtype 1 (TRPA1), originally called ANKTM1 (Story et al., 2003), is a cation channel expressed in a subset of dorsal root, trigeminal and visceral primary sensory neurons (Bautista et al., 2006; Kwan et al., 2006), but also in non-neuronal cells such as keratinocytes (Kwan et al., 2006), fibroblasts (Jaquemar et al., 1999), odontoblasts (El Karim et al., 2011), astroglia (Shigetomi et al., 2011), Schwann cells (De Logu et al., 2017), endothelial cells, and arterial vessels (Kwan et al., 2009). There, TRPA1 acts as a polymodal sensor of cell threats, being activated by a wide range of physical and chemical stimuli of extracellular or intracellular origin (for comprehensive reviews see (Zygmunt and Hogestatt, 2014; Chen and Hackos, 2015; Viana, 2016; Gouin et al., 2017; Koivisto et al., 2018; Wang et al., 2019) and references therein). Accumulating evidence links the physiological functions of TRPA1 to inflammation, temperature perception, mechanosensation, insulin secretion, itching, respiratory functions, regulation of the cardiovascular system, but also the homeostatic balance between the immune and nociceptive systems, as recently nicely reviewed by Talavera et al. (2019). Under certain pathological conditions such as tissue injury or inflammation, TRPA1 may undergo a wide range of posttranslational modifications that lead to various levels of functional modulation. Ca^{2+} influx through TRPA1 can release mediators such as calcitonin gene-related peptide, substance P, neurokinin A and bradykinin, which modulate the channel via G-protein-coupled receptor signaling cascades (Andrade et al., 2012; Petho and Reeh, 2012; Voolstra and Huber, 2014; Kadkova et al., 2017) and/or promote the recruitment of the channels to the cell surface (Schmidt et al., 2009; Takahashi and Ohta, 2017).

A large number (>150) of single-point mutations and chimeras of human TRPA1 have been functionally characterized in the literature (Meents et al., 2019), yet the published data do not enable us to fully understand the molecular details of the channel function, mostly because (1) the available structures of TRPA1 capture the channel in an intermediate or inactivated conformation (Paulsen et al., 2015; Suo et al., 2020) which does not allow to distinguish the functional states, (2) the structures lack information on a considerable (∼50%) part of the protein, (3) the impact of the interactions of TRPA1 with various important endogenous proteins and cellular signaling mechanisms has not yet been fully characterized (Zygmunt and Hogestatt, 2014; Gouin et al., 2017; Talavera et al., 2019), and (4) the extent to which TRPA1 can be regulated by its membrane environment is still only gradually being uncovered (Hirono et al., 2004; Akopian et al., 2007; Dai et al., 2007; Karashima et al., 2008; Witschas et al., 2015; Macikova et al., 2019; Startek et al., 2019). Obviously, a better understanding of all these issues is key for a precise description of the mechanisms of TRPA1 activation, and, perhaps more importantly, for rational screening of its novel modulators as potential therapeutic agents.

The thermosensitive properties of TRPA1 are even less understood. In mammals, TRPA1 is thought to function as a cold detector (Story et al., 2003; Viswanath et al., 2003; Bandell et al., 2004; Kwan et al., 2006; Karashima et al., 2009; Kremeyer et al., 2010), but it has been also found to play a crucial role in the detection of noxious heat (Hoffmann et al., 2013; Yarmolinsky et al., 2016; Vandewauw et al., 2018). *In vitro*, a direct cold activation of TRPA1 was demonstrated by several laboratories for mouse, rat and human orthologs (Story et al., 2003; Viswanath et al., 2003; Sawada et al., 2007; Karashima et al., 2009; del Camino et al., 2010; Moparthi et al., 2016). On the other hand, some other groups did not observe any cold activation (Jordt et al., 2004; Zurborg et al., 2007; Knowlton et al., 2010; Cordero-Morales et al., 2011; Chen et al., 2013). This is clearly not the whole story, and further intensive investigation is required to determine the specific role of mammalian TRPA1 as a temperature sensor (Sinica et al., 2019).

This article provides new evidence that the cold sensitivity of TRPA1 can be modulated by membrane phosphoinositides; specifically, by phosphatidylinositol-4,5-bisphosphate, PIP_2. Moreover, we demonstrate that AKAP, the scaffolding A-kinase anchoring protein that is necessary for the effective phosphorylation of TRPA1 by protein kinases A and C, potentiates the channel at negative membrane potentials, suggesting the existence of basal phosphorylation or a direct effect of AKAP on TRPA1. Although these primary results provide potentially important information indicating that the membrane proximal part of the C-terminus of TRPA1 may form a hot spot contributing to a highly effective regulation of TRPA1, additional structural/functional considerations are necessary to characterize the channel in its full physiological context.

MATERIALS AND METHODS

Cell Culture, Constructs, and Transfection

Human embryonic kidney 293T (HEK293T; ATCC, Manassas, VA, United States) cells were cultured and transfected with 400 ng of cDNA plasmid encoding wild-type or mutant human TRPA1 (pCMV6-XL4 vector, OriGene Technologies, Rockville, MD, United States) and 200 ng of GFP plasmid (TaKaRa, Shiga, Japan), and, for particular experiments, 300 ng of a plasmid of wild-type TRPA1 with 300 ng of plasmid Dr-VSP (in IRES2-EGFP vector, a gift from Yasushi Okamura, Addgene plasmid #80333) or 400 ng of the plasmid of wild-type TRPA1 with 200 ng of plasmid AKAP79 (pCMV6-XL4 vector, OriGene Technologies, Rockville, MD, United States), using the magnet-assisted transfection technique (IBA GmbH, Gottingen, Germany) as described previously (Zimova et al., 2018). The mutant H1018R was generated by PCR using a QuikChange II XL Site-Directed Mutagenesis Kit (Agilent Technologies, Santa Clara, CA, United States) and confirmed by DNA sequencing (Eurofins Genomics, Ebersberg, Germany).

Electrophysiology and Cold Stimulation

All electrophysiological recordings were carried out as described previously (Zimova et al., 2018). For the experiments described in **Figure 1**, the extracellular bath solution contained: 140 mM NaCl, 5 mM KCl, 2 mM $MgCl_2$, 5 mM EGTA, and 10 mM
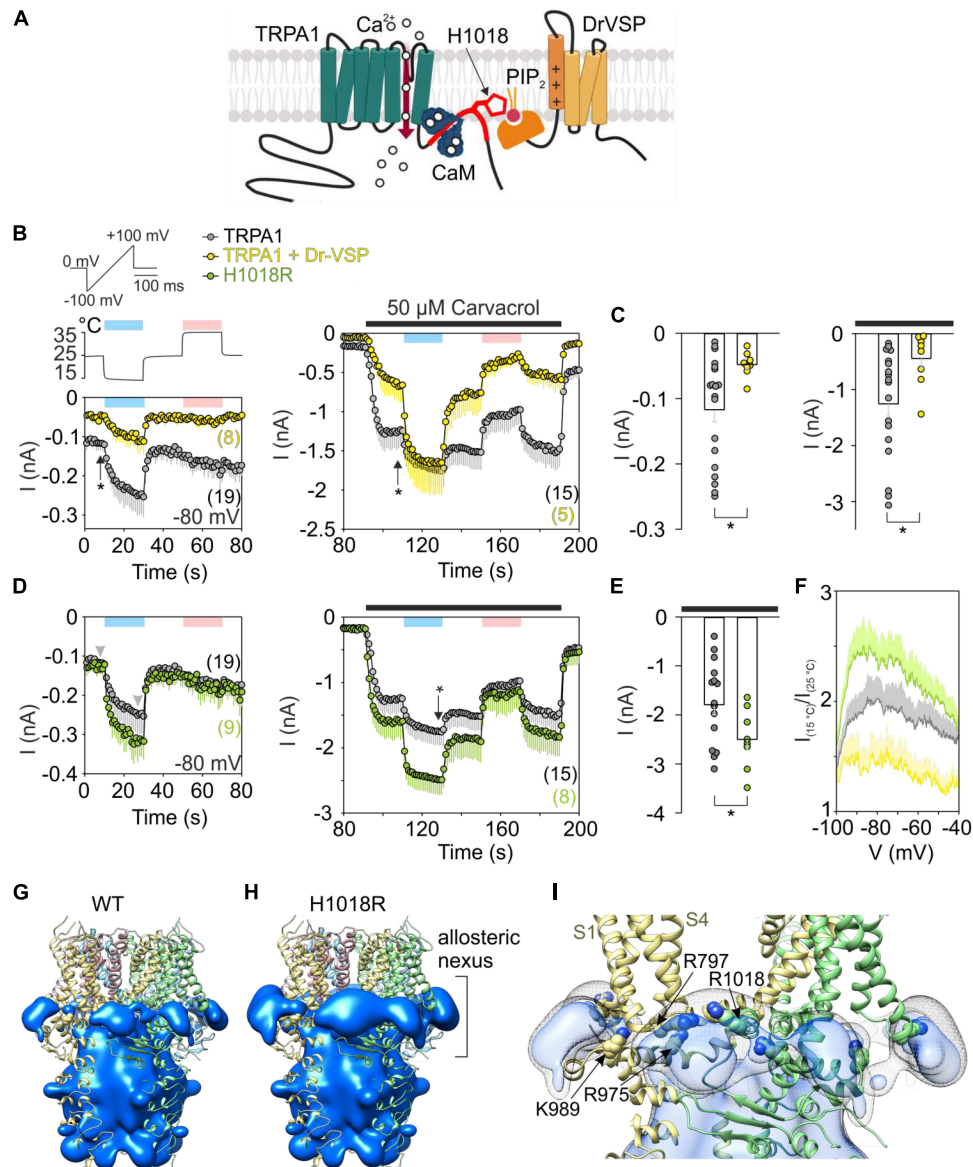
FIGURE 1 | Acute PIP$_2$ depletion has an opposite effect on cold-dependent gating of TRPA1 to missense histidine-to-arginine mutation at position 1018.
(A) Schematic diagram shows binding of Ca^{2+}-CaM (calmodulin) to C terminus of TRPA1 (Macikova et al., 2019). The binding domain for CaM partly overlaps with the proposed binding pocket for PIP$_2$ (in red) which includes H1018. Voltage-sensitive phosphatase (Dr-VSP) hydrolyses PIP$_2$ upon depolarization greater than +50 mV. **(B)** Time course of average whole-cell currents of human TRPA1 (TRPA1, gray circles with bars indicating mean values with – SEM) and TRPA1 co-expressed with Dr-VSP (yellow circles with bars indicating mean values with – SEM), measured at –80 mV. First, the cells were exposed to a 3 s depolarizing pulse to +80 mV to activate Dr-VSP. Then, the membrane potential was linearly ramped up each second from –100 mV to +100 mV (1 V.s^{-1}). The temperature was lowered first from room temperature 25°C to 15°C (blue bar) and then raised to 35°C (pink bar); the temperature trace is shown above the first record (left). Subsequently, 50 μM carvacrol (black bar) was applied together with temperature changes (right), n is indicated in brackets. **(C)** Comparison of current amplitudes at –80 mV at times marked in **(B)** with vertical arrows. Color coding as in **(B)**. Left: The basal current through TRPA1 is significantly smaller ($P = 0.028$) when it is co-expressed with Dr-VSP that causes acute PIP$_2$ depletion upon voltage stimulation. Right: Responses to carvacrol are also significantly smaller ($P = 0.032$). Data are shown as single points and as mean values – SEM. **(D)** Time course of average whole-cell currents of mutant H1018R of TRPA1 (green circles with bars indicating mean value – SEM) measured at –80 mV compared with wild-type hTRPA1 as in **(B)**. **(E)** The current responses of H1018R to simultaneous exposure to 50 μM carvacrol and cold (15°C) are significantly higher ($P = 0.043$) than the currents from wild-type hTRPA1. Data are shown as single points and as mean values – SEM at times marked in **(D)** with an arrow. Color coding as in **(B,D)**. **(F)** Voltage dependence of cold activation averaged at times indicated by gray arrowheads in **(D)**. The extent of cold potentiation of TRPA1 (gray line, mean + SEM), hTRPA1 co-expressed with Dr-VSP (yellow line, mean + SEM), and H1018R (green line, as mean + SEM) at negative membrane potentials. **(G)** Areas of positive electrostatic potential (blue surface) surrounding the ligand-free structure of TRPA1 [Protein Data Bank (PDB) ID: 6PQQ] and **(H)** its mutant H1018R. **(I)** A detailed view of the region around the allosteric nexus of TRPA1 shows substantially more positive values for H1018R (side chain shown) than for TRPA1 (depicted as light gray mesh encircling light blue surface). The allosteric nexus formed by the cytoplasmic region situated below the transmembrane core has been recently proposed to be an important determinant for phospholipid binding as well as for TRPA1 gating (Zhao et al., 2019; Suo et al., 2020).

HEPES, 10 mM glucose, pH 7.4 was adjusted with TMA-OH. The intracellular solution contained 140 mM KCl, 5 mM EGTA, 2 mM $MgCl_2$, and 10 mM HEPES, adjusted with KOH to pH 7.4. For the experiments shown in **Figure 2**, the extracellular bath solution contained: 140 mM NaCl, 4 mM KCl, 1 mM $MgCl_2$, 10 mM HEPES, 5 mM glucose, pH 7.4 adjusted with NaOH. The intracellular solution contained 125 mM Cs-glucono-δ-lactone, 15 mM CsCl, 5 mM EGTA, 0.5 mM $CaCl_2$, 2 mM MgATP, 0.3 NaGTP, and 10 mM HEPES, adjusted to pH 7.4 with CsOH. A system for the rapid cooling and heating of solutions superfusing isolated cells under patch-clamp conditions was used as described in Dittert et al. (2006). The temperature of the flowing solution was measured with a miniature thermocouple inserted into the common outlet capillary near to its orifice, which was placed less than 100 μm from the surface of the examined cell. Statistical significance was determined by Student's *t*-test or the analysis of variance, as appropriate; differences were considered significant at $P < 0.05$ where not stated otherwise. The data are presented as means ± (or +/−) SEM.

RESULTS AND DISCUSSION

Predicted Role of Phosphoinositides in the Regulation of Temperature–Dependent Gating of TRPA1

The transmembrane domain of TRPA1 is composed of the voltage sensor-like domain (VSLD) formed by a bundle of four antiparallel helices, S1–S4, and the pore domain (formed by S5, S6, and two pore helices) arranged in a domain-swap manner. The proximal C terminus contains a TRP-like domain that interacts with a pre-S1 helix. There are at least two sites with separate functions from which the activity of TRPA1 can be regulated by membrane phosphatidylinositol-4,5-bisphosphate (PIP_2) or other phosphoinositides: the first, formed by the intracellular part of VSLD and contributed to by K989 from the TRP-like domain (Samad et al., 2011; Witschas et al., 2015; Zimova et al., 2018), and the second localized between adjacent subunits (T1003–P1034), capable of directly affecting the gating of the channel through the S4-S5 linker and R975 from the TRP-like domain (Macikova et al., 2019). Mutation at the highly conserved phenylalanine F1020 located in the center of the latter interacting region produced channels with faster activation kinetics and with significantly suppressed responses at negative membrane potentials. The effectiveness of PIP_2 at inhibiting or promoting the activity of TRPA1 appears to substantially depend on the conformational states of the channel (Macikova et al., 2019). Importantly, two amino acids upstream of F1020, a missense mutation of a histidine residue (rs959976) was recently found to be associated with childhood asthma (Gallo et al., 2017). The histidine-to-arginine mutation (H1018R) increased the responses of recombinant channels to insoluble coal fly ash particles by 70%, suggesting an increased sensitivity to mechanical stimuli (Deering-Rice et al., 2015). We hypothesized that arginine at

position 1018 may alter the affinity of PIP_2 to TRPA1, and thereby also influence the activation of the channel by other stimuli, particularly by heat or cold temperatures. Several structures of thermosensitive TRP channels contain lipids in the regions essentially involved in agonist binding or pore gating (Cao et al., 2013; Singh et al., 2018, 2019), and it has been proposed that the association/dissociation of lipids may be one of the underlying mechanisms of temperature sensation (Cao et al., 2013). Also, recent molecular dynamics simulations performed with the structure of the TRPA1-related channel TRPV1 at different temperatures suggest that the lipid displacement from protein binding sites may contribute to temperature-evoked actuation (Melnick and Kaviany, 2018). Because human TRPA1 is considered to be a cold-sensitive channel (Moparthi et al., 2014), we tested whether the H1018R mutation may influence the cold sensitivity of human TRPA1.

Using depolarizing voltage ramps from –100 mV to +100 mV under whole-cell patch clamp conditions, we measured TRPA1-mediated responses from HEK293T cells transfected with wild-type human TRPA1 or wild-type human TRPA1 together with the voltage-dependent phosphatase cloned from *Danio rerio* (Dr-VSP) to selectively deplete PIP_2 (Hossain et al., 2008; Okamura et al., 2009; Zimova et al., 2018; **Figure 1A**). We applied 20 s steps from 25°C to 15°C and to 35°C first in control extracellular solution and then in 50 μM carvacrol, the non-electrophilic agonist of TRPA1. At positive membrane potentials the current responses were not significantly different, indicating comparable expression levels. The comparison at −80 mV indicates that an acute level of membrane PIP_2 regulates both the rate and extent of the response to individual stimuli (cold temperature or agonist) but does not affect the synergy between the stimuli (**Figures 1B,C**). Using the same voltage protocol, we measured currents from cells expressing the H1018R mutant (**Figure 1D**). Notably, the H1018R mutant exhibited significantly increased current responses at −80 mV upon the simultaneous application of agonist and cooling (**Figure 1E**). The voltage dependence of cold activation (**Figure 1F**) illustrates the opposite effects of the H1018R mutation and the acute PIP_2 depletion. To find where negatively charged PIP_2 will most likely be bound, we used the structure of human TRPA1 [Protein Data Bank (PDB) ID: 6PQQ; (Suo et al., 2020)]. By means of the "Mutate residue" plugin in VMD software (Humphrey et al., 1996), H1018 was mutated to R1018. The "PME Electrostatics" module of VMD was used to compute electrostatic maps, which were visualized with UCSF Chimera (Pettersen et al., 2004). As shown in **Figures 1G–I**, the H1018R mutation substantially extended the positive electrostatic potential surrounding the allosteric nexus formed by the cytoplasmic region situated just below the transmembrane core, indicating an increased probability of PIP_2 binding (see also the **Supplementary Material**).

These results further substantiate the previously proposed role of the proximal C-terminal linker in the PIP_2-mediated regulation of TRPA1, and also indicate that the cold sensitivity of the channel can be modulated by membrane lipids. Consistent with our results, the allosteric nexus containing this region has been recently proposed to be an important determinant for
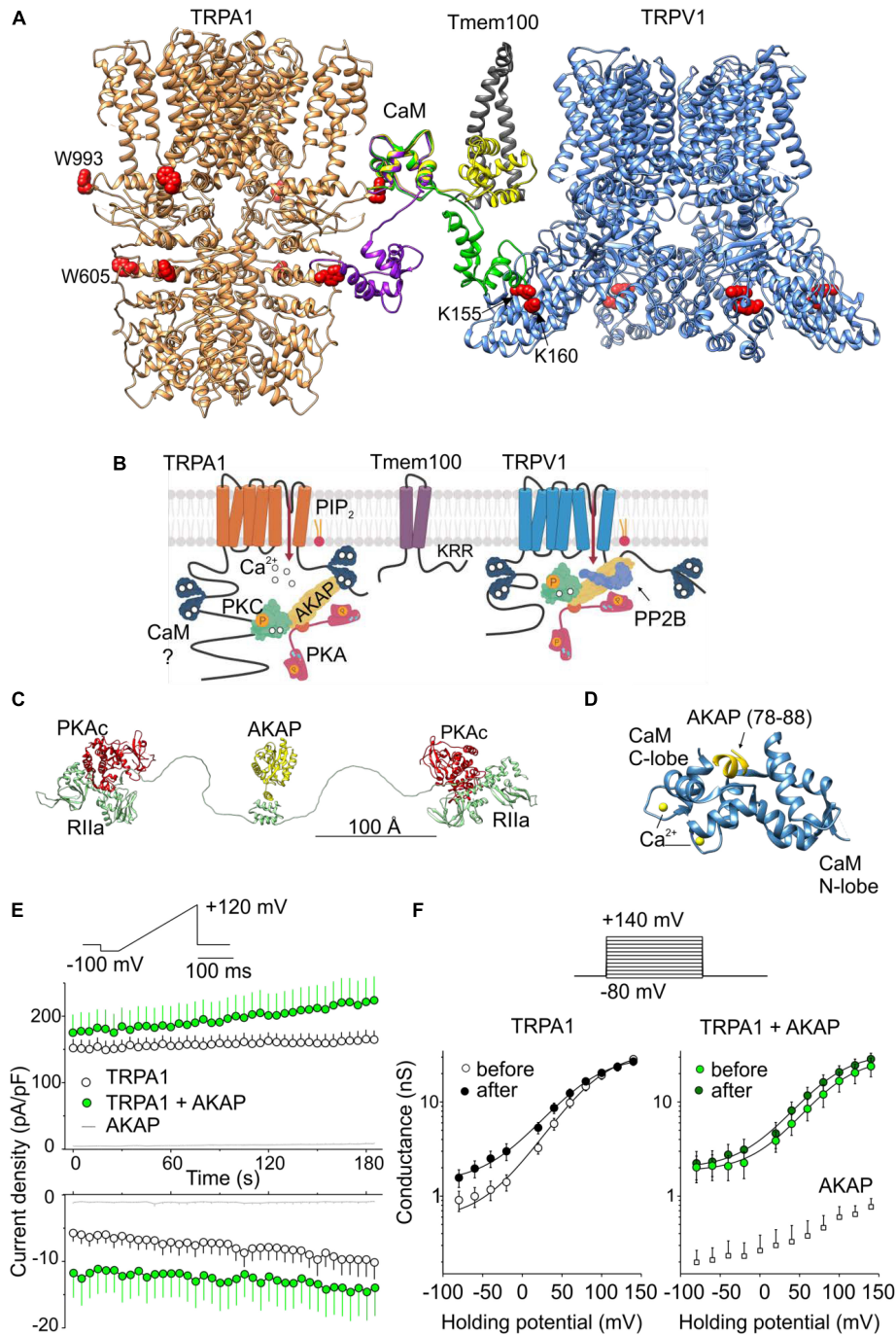
FIGURE 2 | Regulation of TRPA1 by phosphorylation and by predicted interactions with modulatory and scaffold proteins. **(A)** N- and C-lobes of Ca^{2+}/CaM (three conformers are shown in violet, green, and yellow) are capable of binding to TRPA1 but also serving as a linker binding either TRPA1 to the Tmem100 (gray ribbon) membrane protein or to the cytoplasmic binding site in the N-terminus of TRPV1. Tryptophans putatively involved in Ca^{2+}/CaM binding are shown as red side chains. **(B)** Permeating Ca^{2+} binds to calmodulin (forming a complex Ca^{2+}/CaM), phosphatidylinositol-4,5-bisphosphate (PIP$_2$) competes with Ca^{2+}/CaM for binding to TRPA1. A kinase anchoring protein AKAP79/150 (AKAP) binds to TRPA1 and functions as a signaling scaffold for protein kinase A (PKA) and C (PKC). The activation of PKA or PKC sensitizes TRPA1 by phosphorylation (P in orange circles). The interaction of TRPA1 with TRPV1 is regulated by the transmembrane adaptor protein Tmem100 via the amino acid KRR triplet on the C-terminus of Tmem100. AKAP also binds to TRPV1 and associates with protein phosphatase 2B (PP2B, calcineurin) to effectively dephosphorylate the channel. **(C)** Extended linear configuration (the end-to-end length ~385 Å) of pseudo-atomic model of pentameric protein assembly of AKAP (AKAP18γ, residues 88–317) connected to regulatory subunits (RIIα) with associated catalytic subunits (PKAc) of PKA [PDB ID: 3j4R; (Smith et al., 2013)]. **(D)** Published crystal structure of CaM (steel blue ribbon) in complex with AKAP79 peptide (yellow). Two EF hands of the C-lobe coordinate Ca^{2+} (yellow atoms). One of the two copies of the published structure is shown: PDB ID: 5NIN, chains **A** and **C**. **(E)** Average whole-cell current densities induced by depolarizing voltage measured from HEK293T cells expressing TRPA1 (white circles indicating mean ± SEM; n = 17), or TRPA1 together with

(Continued)

phospholipid binding as well as for TRPA1 gating (Zhao et al., 2019; Suo et al., 2020).

At present, however, it is not clear to what extent the results may reflect the situation *in vivo* and how the effects observed with the H1018R mutant may relate to human asthma. We have recently demonstrated that the cold sensitivity of human TRPA1 is similar in both HEK293T cells and also in F11 cells, which are a well characterized cellular model of peripheral sensory neurons (Sinica et al., 2019). Although the TRPA1-mediated cold responses do not differ between these two cellular models, PIP_2 signaling and H1018R expression could differ among various cell types.

Regulation of TRPA1 by Ca^{2+}-Calmodulin Complex

One of the most essential modulators of TRPA1 are calcium ions, which activate the channel at low concentrations and inactivate it at higher concentrations (Jordt et al., 2004; Nagata et al., 2005; Doerner et al., 2007; Zurborg et al., 2007; Cavanaugh et al., 2008; Wang et al., 2011). Mechanistically, Ca^{2+} ions permeating through the TRPA1 channel bind the Ca^{2+}-sensing protein calmodulin (CaM), which pre-associates with the membrane proximal C-terminal region of TRPA1 (L992-N1008) from where the Ca^{2+}-CaM enables the channel to distinctly respond to diverse Ca^{2+} signals (Hasan et al., 2017). It does so in a bimodal manner so that it potentiates TRPA1 at low concentrations of cytosolic Ca^{2+} and inactivates the channel at higher Ca^{2+} concentrations. The proposed Ca^{2+}-CaM-binding region at TRPA1 is integrated with a putative three-stranded β-sheet formed by two anti-parallel β-strands from the N-terminus and a contacting strand that follows the C-terminal TRP-like helix. The latter, peripherally exposed β-strand binds the carboxy-lobe (C-lobe) of calmodulin and even under resting concentrations of Ca^{2+} (∼100 nM) forms a tight complex with the channel (Hasan et al., 2017). As is seen from our structural comparisons shown in **Figures 1G–I** and from our previous results (Macikova et al., 2019), this region overlaps with the interaction site for membrane PIP_2 with which Ca^{2+}-CaM is likely to compete.

Whereas the C-lobe of CaM acts as an effector mediating Ca^{2+}-dependent gating and a tether anchoring CaM to the binding site at TRPA1, the N-lobe of CaM is only partly involved in binding and does not affect the channel gating (Hasan et al., 2017). What could the additional role of the N-lobe in TRPA1 regulation be? CaM is a well-studied ubiquitously expressed protein involved in the regulation of a large number

of membrane and cytoplasmic proteins (Ishida and Vogel, 2006) and its role as a Ca^{2+}-dependent modulator can be predicted with a relatively high degree of confidence (Yap et al., 2000; Mruk et al., 2014). Much less is known about its role as a Ca^{2+}-dependent protein linker and a regulator of scaffold proteins (Villalobo et al., 2018). Structural comparisons shown in **Figure 2A** indicate that the N-lobe of CaM may either bridge different domains of TRPA1 or link the channel with some different target protein(s). This is possible due to the fact that its two independently folded Ca^{2+}-binding lobes are able to interact differentially and, to some degree, separately. From the sequence analysis of human TRPA1 (Yap et al., 2000; Mruk et al., 2014), several putative CaM binding sites are predicted. Of these, the N-terminal regions K578-D606 and L488–S510, and the C-terminal region K988–K1009 have the highest score. Interestingly, the interaction of the N-lobe of CaM with the N-terminal region of TRPA1 may depend on the conformational state of the channel. Whereas the N-lobe of Ca^{2+}/CaM can interact with W605 in the TRPA1 structure 3J9P obtained in the presence of allyl isothiocyanate (Paulsen et al., 2015), this tryptophan is inaccessible in the recently published structures 6PQQ, 6PQP, and 6PQO, obtained, respectively, as an apo-structure and in the presence of the reversible and irreversible electrophilic agonists BITC and JT010 (Suo et al., 2020).

Regulation of TRPA1 by Protein-Protein Interactions

In a large subset of sensory neurons, TRPA1 physically and functionally interacts with the structurally related vanilloid receptor subtype 1 channel TRPV1 (Story et al., 2003; Akopian et al., 2007; Salas et al., 2009; Staruschenko et al., 2010; Akopian, 2011; Fischer et al., 2014; Patil et al., 2020; **Figure 2B**). These two channels may desensitize or sensitize each other via the elevation of intracellular calcium ions (Jordt et al., 2004; Akopian et al., 2007). In addition, a direct association of TRPA1 with TRPV1 strongly inhibits the responses of TRPA1 to electrophilic agonists, independently of Ca^{2+} (Staruschenko et al., 2010; Fischer et al., 2014). In peptidergic neurons, the interaction of these two channels is tightly regulated by the transmembrane adaptor protein Tmem100, which loosens their association and thereby releases TRPA1 from inhibition. Structurally, the regulation of this interaction depends on a KRR amino acid triplet on the C-terminus of Tmem100 (Weng et al., 2015). Importantly, the highly positively charged C-terminus of Tmem100 also contains a putative CaM binding site predicted

with high confidence (L99–L115). Thus, the N-lobe of CaM can bind to the N-terminus of TRPA1 but can also bind to Tmem100 or TRPV1.

In **Figure 2A**, we illustrate how CaM could in principle be capable of bridging two binding sites in the TRPA1 structure or serve as a linker binding TRPA1 to the Tmem100 membrane protein or to the cytoplasmic binding site in the N-terminus of TRPV1. We used the crystal structures TRPA1 (PDB ID: 3J9P), TRPV1 (3J5P), Tmem141 (2LOR), and CaM (1MUX - a set of 30 structures determined by NMR). The C-domains of several CaM conformers from the 1MUX set were placed close to W993 in TRPA1 (red spheres), which is likely to serve as a hydrophobic anchor in the experimentally confirmed L992–N1008 binding site of CaM in the proximal C-terminal region of TRPA1 (Hasan et al., 2017). The distance between W993 and W605 (in the second putative binding site for CaM in TRPA1) roughly corresponds to the distance of the N- and C-terminal subunits in the conformer of CaM (depicted as a violet ribbon). The green conformer of CaM indicates how it could potentially bridge known binding sites in TRPA1 and TRPV1 (Lau et al., 2012). Another structure of CaM (yellow) shows the N-terminal subunit returning to the membrane, where it could be anchored by Tmem100 disturbing the TRPA1-TRPV1 complex. Interestingly, recently, the N- (amino acids 220-260) and C- (684-720) terminal domains on TRPV1 responsible for TRPA1-TRPV1 complex formation were identified (Patil et al., 2020). These domains partially overlap with the previously identified binding sites for CaM/PIP2 (189-222/682-725) (Rosenbaum et al., 2004; Ufret-Vincenty et al., 2011). This provides further support for our hypothesis that CaM could serve as linker between TRPA1 and TRPV1.

Protein Kinase A Anchoring Protein 79/150 (AKAP) Interacts With TRPA1

It has been demonstrated that TRPA1 can be sensitized by protein kinase A (PKA), protein kinase C (PKC), cyclin-dependent kinase 5, and by early signaling events linked to Ca^{2+}-dependent phosphoinositide-specific phospholipase C (PLC) enzymes that hydrolyze PIP_2 in the inner membrane leaflet (Bandell et al., 2004; Bautista et al., 2006; Dai et al., 2007; Wang et al., 2008; Hynkova et al., 2016; Brackley et al., 2017; Meents et al., 2017; Hall et al., 2018; Sulak et al., 2018; **Figure 2B**). For effective phosphorylation by PKA and PKC, TRPA1 needs the presence of a scaffolding protein, AKAP (Brackley et al., 2017), that is also required for the PKA phosphorylation of TRPV1 (Zhang et al., 2008). AKAP directly interacts with TRPA1 (Zhang et al., 2008), but it also engages in multiple protein-protein interactions including Ca^{2+}-CaM (Faux and Scott, 1997; Patel et al., 2017). Given the recently proposed importance of the AKAP-PKA pathway in TRPA1-mediated mechanical allodynia and cold hyperalgesia (Brackley et al., 2017; Miyano et al., 2019), it would be particularly important to test the hypothesis that AKAP may serve as a molecular hub that contributes to the specificity and efficiency of the cellular signaling network regulating TRPA1 under various physiological or pathophysiological conditions (**Figures 2A–D**).

Although AKAP spatially constrains phosphorylation by PKA, the regulatory subunits of PKA are capable of providing an ~16 nanometer radius of motion to the associated catalytic subunits [(Smith et al., 2013) and **Figure 2C**] and, therefore, the pathways regulating TRPA1 and TRPV1 may together form a supramolecular signaling complex.

Previous co-immunoprecipitation studies confirmed the interaction of AKAP with TRPA1 in HEK293 cells (Zhang et al., 2008) and in cultured trigeminal neurons (Brackley et al., 2017). We asked whether the overexpression of AKAP in HEK293T cells may influence the functional response of TRPA1. We measured currents induced by repeated depolarizing voltage ramps or steps from cells expressing TRPA1 or TRPA1 together with AKAP (**Figures 2E,F**). In TRPA1-expressing cells, we observed gradual current increases at negative and at positive membrane potentials ($P < 0.001$ and $P = 0.005$, respectively; $n = 17$). In cells co-expressing TRPA1 and AKAP, significant basal currents were observed at negative potentials and they did not further increase upon repeated stimulation ($P = 0.111$; $n = 13$). The expression of AKAP did not affect endogenous currents from HEK293T cells. These data can be interpreted in at least three ways: (1) AKAP may recruit TRPA1 to the plasma membrane, (2) AKAP may increase the activity of TRPA1 by increasing basal phosphorylation, and (3) the interaction with AKAP induces a conformational change that primes the channel for activation. Future, more thorough structural and functional studies that resolve the underlying mechanism may help our understanding of TRPA1 regulation and could possibly identify new targets that activate or inhibit TRPA1 for therapeutic purposes. A future direction in the search for effective treatment of asthma or mechanical and cold hyperalgesia could be to focus on a pharmacology directed toward the interacting regions of the TRPA1 channel with phospholipids and with its partner proteins, or toward the interacting proteins themselves.

DATA AVAILABILITY STATEMENT

The **Supplementary Material** contains the Particle Mesh Ewald electrostatic potential maps for the wild-type human TRPA1 (PDB ID: 6PQQ) and the R1018 mutant, visualized in UCSF Chimera 1.13. Other raw data supporting the conclusions of this article will be made available by the authors, without undue reservation, to any qualified researcher.

AUTHOR CONTRIBUTIONS

VV and LZ conceptualized the study. VS, LZ, VV, KB, and IB contributed to formal analysis. VS, LM, LZ, KB, and IB investigated the study. VV, LZ, IB, and LV supervised the study. VV contributed to writing – original draft of manuscript preparation. VV, LZ, and LV contributed to writing, reviewing, and editing. All authors contributed to manuscript revision, read, and approved the submitted version.

FUNDING

SUPPLEMENTARY MATERIAL

The Supplementary Material for this article can be found online at: https://www.frontiersin.org/articles/10.3389/fphys.2020.00189/full#supplementary-material

REFERENCES

Akopian, A. N. (2011). Regulation of nociceptive transmission at the periphery via TRPA1-TRPV1 interactions. *Curr. Pharm. Biotechnol.* 12, 89–94. doi: 10.2174/138920111793937952

Akopian, A. N., Ruparel, N. B., Jeske, N. A., and Hargreaves, K. M. (2007). Transient receptor potential TRPA1 channel desensitization in sensory neurons is agonist dependent and regulated by TRPV1-directed internalization. *J. Physiol.* 583(Pt 1), 175–193. doi: 10.1113/jphysiol.2007.133231

Andrade, E. L., Meotti, F. C., and Calixto, J. B. (2012). TRPA1 antagonists as potential analgesic drugs. *Pharmacol. Ther.* 133, 189–204. doi: 10.1016/j.pharmthera.2011.10.008

Bandell, M., Story, G. M., Hwang, S. W., Viswanath, V., Eid, S. R., Petrus, M. J., et al. (2004). Noxious cold ion channel TRPA1 is activated by pungent compounds and bradykinin. *Neuron* 41, 849–857. doi: 10.1016/s0896-6273(04)00150-3

Bautista, D. M., Jordt, S. E., Nikai, T., Tsuruda, P. R., Read, A. J., Poblete, J., et al. (2006). TRPA1 mediates the inflammatory actions of environmental irritants and proalgesic agents. *Cell* 124, 1269–1282. doi: 10.1016/j.cell.2006.02.023

Brackley, A. D., Gomez, R., Guerrero, K. A., Akopian, A. N., Glucksman, M. J., Du, J., et al. (2017). A-Kinase anchoring protein 79/150 scaffolds transient receptor potential A 1 phosphorylation and sensitization by metabotropic glutamate receptor activation. *Sci. Rep.* 7:1842. doi: 10.1038/s41598-017-01999-4

Cao, E., Liao, M., Cheng, Y., and Julius, D. (2013). TRPV1 structures in distinct conformations reveal activation mechanisms. *Nature* 504, 113–118. doi: 10.1038/nature12823

Cavanaugh, E. J., Simkin, D., and Kim, D. (2008). Activation of transient receptor potential A1 channels by mustard oil, tetrahydrocannabinol and Ca(2+) reveals different functional channel states. *Neuroscience* 154, 1467–1476. doi: 10.1016/j.neuroscience.2008.04.048

Chen, J., and Hackos, D. H. (2015). TRPA1 as a drug target–promise and challenges. *Naunyn Schmiedeberg's Arch. Pharmacol.* 388, 451–463. doi: 10.1007/s00210-015-1088-3

Chen, J., Kang, D., Xu, J., Lake, M., Hogan, J. O., Sun, C., et al. (2013). Species differences and molecular determinant of TRPA1 cold sensitivity. *Nat. Commun.* 4:2501. doi: 10.1038/ncomms3501

Cordero-Morales, J. F., Gracheva, E. O., and Julius, D. (2011). Cytoplasmic ankyrin repeats of transient receptor potential A1 (TRPA1) dictate sensitivity to thermal and chemical stimuli. *Proc. Natl. Acad. Sci. USA.* 108, E1184–E1191. doi: 10.1073/pnas.1114124108

Dai, Y., Wang, S., Tominaga, M., Yamamoto, S., Fukuoka, T., Higashi, T., et al. (2007). Sensitization of TRPA1 by PAR2 contributes to the sensation of inflammatory pain. *J. Clin. Invest.* 117, 1979–1987. doi: 10.1172/jci30951

De Logu, F., Nassini, R., Materazzi, S., Carvalho Goncalves, M., Nosi, D., Rossi Degl'Innocenti, D., et al. (2017). Schwann cell TRPA1 mediates neuroinflammation that sustains macrophage-dependent neuropathic pain in mice. *Nat. Commun.* 8:1887. doi: 10.1038/s41467-017-01739-2

Deering-Rice, C. E., Shapiro, D., Romero, E. G., Stockmann, C., Bevans, T. S., Phan, Q. M., et al. (2015). Activation of transient receptor potential ankyrin-1 by insoluble particulate material and association with asthma. *Am. J. Respir. Cell Mol. Biol.* 53, 893–901. doi: 10.1165/rcmb.2015-0086OC

del Camino, D., Murphy, S., Heiry, M., Barrett, L. B., Earley, T. J., Cook, C. A., et al. (2010). TRPA1 contributes to cold hypersensitivity. *J. Neurosci.* 30, 15165–15174. doi: 10.1523/JNEUROSCI.2580-10.2010

Dittert, I., Benedikt, J., Vyklicky, L., Zimmermann, K., Reeh, P. W., and Vlachova, V. (2006). Improved superfusion technique for rapid cooling or heating of cultured cells under patch-clamp conditions. *J. Neurosci. Methods* 151, 178–185. doi: 10.1016/j.jneumeth.2005.07.005

Doerner, J. F., Gisselmann, G., Hatt, H., and Wetzel, C. H. (2007). Transient receptor potential channel A1 is directly gated by calcium ions. *J. Biol. Chem.* 282, 13180–13189. doi: 10.1074/jbc.m607849200

El Karim, I. A., Linden, G. J., Curtis, T. M., About, I., McGahon, M. K., Irwin, C. R., et al. (2011). Human dental pulp fibroblasts express the "cold-sensing" transient receptor potential channels TRPA1 and TRPM8. *J. Endod.* 37, 473–478. doi: 10.1016/j.joen.2010.12.017

Faux, M. C., and Scott, J. D. (1997). Regulation of the AKAP79-protein kinase C interaction by Ca2+/Calmodulin. *J. Biol. Chem.* 272, 17038–17044. doi: 10.1074/jbc.272.27.17038

Fischer, M. J., Balasuriya, D., Jeggle, P., Goetze, T. A., McNaughton, P. A., Reeh, P. W., et al. (2014). Direct evidence for functional TRPV1/TRPA1 heteromers. *Pflugers Arch.* 466, 2229–2241. doi: 10.1007/s00424-014-1497-z

Gallo, V., Dijk, F. N., Holloway, J. W., Ring, S. M., Koppelman, G. H., Postma, D. S., et al. (2017). TRPA1 gene polymorphisms and childhood asthma. *Pediatr. Allergy Immunol.* 28, 191–198. doi: 10.1111/pai.12673

Gouin, O., L'Herondelle, K., Lebonvallet, N., Le Gall-Ianotto, C., Sakka, M., Buhe, V., et al. (2017). TRPV1 and TRPA1 in cutaneous neurogenic and chronic inflammation: pro-inflammatory response induced by their activation and their sensitization. *Protein Cell* 8, 644–661. doi: 10.1007/s13238-017-0395-5

Hall, B. E., Prochazkova, M., Sapio, M. R., Minetos, P., Kurochkina, N., Binukumar, B. K., et al. (2018). Phosphorylation of the transient receptor potential ankyrin 1 by Cyclin-dependent Kinase 5 affects Chemo-nociception. *Sci. Rep.* 8:1177. doi: 10.1038/s41598-018-19532-6

Hasan, R., Leeson-Payne, A. T., Jaggar, J. H., and Zhang, X. (2017). Calmodulin is responsible for Ca2+-dependent regulation of TRPA1 Channels. *Sci. Rep.* 7:45098. doi: 10.1038/srep45098

Hirono, M., Denis, C. S., Richardson, G. P., and Gillespie, P. G. (2004). Hair cells require phosphatidylinositol 4,5-bisphosphate for mechanical transduction and adaptation. *Neuron* 44, 309–320. doi: 10.1016/j.neuron.2004.09.020

Hoffmann, T., Kistner, K., Miermeister, F., Winkelmann, R., Wittmann, J., Fischer, M. J., et al. (2013). TRPA1 and TRPV1 are differentially involved in heat nociception of mice. *Eur. J. f Pain* 17, 1472–1482. doi: 10.1002/j.1532-2149.2013.00331.x

Hossain, M. I., Iwasaki, H., Okochi, Y., Chahine, M., Higashijima, S., Nagayama, K., et al. (2008). Enzyme domain affects the movement of the voltage sensor in ascidian and zebrafish voltage-sensing phosphatases. *J. Biol. Chem.* 283, 18248–18259. doi: 10.1074/jbc.M706184200

Humphrey, W., Dalke, A., and Schulten, K. (1996). VMD: visual molecular dynamics. *J. Mol. Graph.* 14, 33–38. doi: 10.1016/0263-7855(96)00018-5

Hynkova, A., Marsakova, L., Vaskova, J., and Vlachova, V. (2016). N-terminal tetrapeptide T/SPLH motifs contribute to multimodal activation of human TRPA1 channel. *Sci. Rep.* 6:28700. doi: 10.1038/srep28700

Ishida, H., and Vogel, H. J. (2006). Protein-peptide interaction studies demonstrate the versatility of calmodulin target protein binding. *Protein Peptide Lett.* 13, 455–465. doi: 10.2174/092986606776819600

Jaquemar, D., Schenker, T., and Trueb, B. (1999). An ankyrin-like protein with transmembrane domains is specifically lost after oncogenic transformation of human fibroblasts. *J. Biol. Chem.* 274, 7325–7333. doi: 10.1074/jbc.274.11.7325

Jordt, S. E., Bautista, D. M., Chuang, H. H., McKemy, D. D., Zygmunt, P. M., Hogestatt, E. D., et al. (2004). Mustard oils and cannabinoids excite sensory nerve fibres through the TRP channel ANKTM1. *Nature* 427, 260–265. doi: 10.1038/nature02282

Kadkova, A., Synytsya, V., Krusek, J., Zimova, L., and Vlachova, V. (2017). Molecular basis of TRPA1 regulation in nociceptive neurons. A Review. *Physiol. Res.* 66, 425–439. doi: 10.33549/physiolres.933553

Karashima, Y., Prenen, J., Meseguer, V., Owsianik, G., Voets, T., and Nilius, B. (2008). Modulation of the transient receptor potential channel TRPA1 by phosphatidylinositol 4,5-biphosphate manipulators. *Pflugers Arch.* 457, 77–89. doi: 10.1007/s00424-008-0493-6

Karashima, Y., Talavera, K., Everaerts, W., Janssens, A., Kwan, K. Y., Vennekens, R., et al. (2009). TRPA1 acts as a cold sensor in vitro and in vivo.

Proc. Natl. Acad. Sci. U.S.A. 106, 1273–1278. doi: 10.1073/pnas.08084 87106

Knowlton, W. M., Bifolck-Fisher, A., Bautista, D. M., and McKemy, D. D. (2010). TRPM8, but not TRPA1, is required for neural and behavioral responses to acute noxious cold temperatures and cold-mimetics in vivo. *Pain* 150, 340–350. doi: 10.1016/j.pain.2010.05.021

Koivisto, A., Jalava, N., Bratty, R., and Pertovaara, A. (2018). TRPA1 Antagonists for Pain Relief. *Pharmaceuticals* 11:E117. doi: 10.3390/ph11040117

Kremeyer, B., Lopera, F., Cox, J. J., Momin, A., Rugiero, F., Marsh, S., et al. (2010). A gain-of-function mutation in TRPA1 causes familial episodic pain syndrome. *Neuron* 66, 671–680. doi: 10.1016/j.neuron.2010.04.030

Kwan, K. Y., Allchorne, A. J., Vollrath, M. A., Christensen, A. P., Zhang, D. S., Woolf, C. J., et al. (2006). TRPA1 contributes to cold, mechanical, and chemical nociception but is not essential for hair-cell transduction. *Neuron* 50, 277–289. doi: 10.1016/j.neuron.2006.03.042

Kwan, K. Y., Glazer, J. M., Corey, D. P., Rice, F. L., and Stucky, C. L. (2009). TRPA1 modulates mechanotransduction in cutaneous sensory neurons. *J. Neurosci.* 29, 4808–4819. doi: 10.1523/JNEUROSCI.5380-08.2009

Lau, S. Y., Procko, E., and Gaudet, R. (2012). Distinct properties of Ca2+-calmodulin binding to N- and C-terminal regulatory regions of the TRPV1 channel. *J. Gen. Physiol.* 140, 541–555. doi: 10.1085/jgp.201210810

Macikova, L., Sinica, V., Kadkova, A., Villette, S., Ciaccafava, A., Faherty, J., et al. (2019). Putative interaction site for membrane phospholipids controls activation of TRPA1 channel at physiological membrane potentials. *FEBS J.* 286, 3664–3683. doi: 10.1111/febs.14931

Meents, J. E., Ciotu, C. I., and Fischer, M. J. M. (2019). TRPA1: a molecular view. *J. Neurophysiol.* 121, 427–443. doi: 10.1152/jn.00524.2018

Meents, J. E., Fischer, M. J., and McNaughton, P. A. (2017). Sensitization of TRPA1 by Protein Kinase A. *PloS One* 12:e0170097. doi: 10.1371/journal.pone.0170097

Melnick, C., and Kaviany, M. (2018). Thermal actuation in TRPV1: role of embedded lipids and intracellular domains. *J. Theor. Biol.* 444, 38–49. doi: 10.1016/j.jtbi.2018.02.004

Miyano, K., Shiraishi, S., Minami, K., Sudo, Y., Suzuki, M., Yokoyama, T., et al. (2019). Carboplatin enhances the activity of human transient receptor potential ankyrin 1 through the Cyclic AMP-Protein Kinase A-A-Kinase Anchoring Protein (AKAP) Pathways. *Int. J. Mo. Sci.* 20:E3271. doi: 10.3390/ijms20133271

Moparthi, L., Kichko, T. I., Eberhardt, M., Hogestatt, E. D., Kjellbom, P., Johanson, U., et al. (2016). Human TRPA1 is a heat sensor displaying intrinsic U-shaped thermosensitivity. *Sci. Rep.* 6:28763. doi: 10.1038/srep28763

Moparthi, L., Survery, S., Kreir, M., Simonsen, C., Kjellbom, P., Hogestatt, E. D., et al. (2014). Human TRPA1 is intrinsically cold- and chemosensitive with and without its N-terminal ankyrin repeat domain. *Proc. Natl. Acad. Sci. U.S.A,*. 111, 16901–16906. doi: 10.1073/pnas.1412689111

Mruk, K., Farley, B. M., Ritacco, A. W., and Kobertz, W. R. (2014). Calmodulation meta-analysis: predicting calmodulin binding via canonical motif clustering. *J. Gen. Physiol.* 144, 105–114. doi: 10.1085/jgp.201311140

Nagata, K., Duggan, A., Kumar, G., and Garcia-Anoveros, J. (2005). Nociceptor and hair cell transducer properties of TRPA1, a channel for pain and hearing. *J. Neurosci.* 25, 4052–4061. doi: 10.1523/jneurosci.0013-05.2005

Okamura, Y., Murata, Y., and Iwasaki, H. (2009). Voltage-sensing phosphatase: actions and potentials. *J. Physiol.* 587, 513–520. doi: 10.1113/jphysiol.2008.163097

Patel, N., Stengel, F., Aebersold, R., and Gold, M. G. (2017). Molecular basis of AKAP79 regulation by calmodulin. *Nat. Commun.* 8:1681. doi: 10.1038/s41467-017-01715-w

Patil, M. J., Salas, M., Bialuhin, S., Boyd, J. T., Jeske, N. A., and Akopian, A. N. (2020). Sensitization of small-diameter sensory neurons is controlled by TRPV1 and TRPA1 association. *FASEB J.* 34, 287–302. doi: 10.1096/fj.201902026R

Paulsen, C. E., Armache, J. P., Gao, Y., Cheng, Y., and Julius, D. (2015). Structure of the TRPA1 ion channel suggests regulatory mechanisms. *Nature* 520, 511–517. doi: 10.1038/nature14367

Petho, G., and Reeh, P. W. (2012). Sensory and signaling mechanisms of bradykinin, eicosanoids, platelet-activating factor, and nitric oxide in peripheral nociceptors. *Physiol. Rev.* 92, 1699–1775. doi: 10.1152/physrev.00048.2010

Pettersen, E. F., Goddard, T. D., Huang, C. C., Couch, G. S., Greenblatt, D. M., Meng, E. C., et al. (2004). UCSF Chimera–a visualization system for exploratory research and analysis. *J. Comput. Chem.* 25, 1605–1612. doi: 10.1002/jcc.20084

Rosenbaum, T., Gordon-Shaag, A., Munari, M., and Gordon, S. E. (2004). Ca^{2+}/calmodulin modulates TRPV1 activation by capsaicin. *J. Gen. Physiol.* 123, 53–62. doi: 10.1085/jgp.200308906

Salas, M. M., Hargreaves, K. M., and Akopian, A. N. (2009). TRPA1-mediated responses in trigeminal sensory neurons: interaction between TRPA1 and TRPV1. *Eur. J. Neurosci.* 29, 1568–1578. doi: 10.1111/j.1460-9568.2009.06702.x

Samad, A., Sura, L., Benedikt, J., Ettrich, R., Minofar, B., Teisinger, J., et al. (2011). The C-terminal basic residues contribute to the chemical- and voltage-dependent activation of TRPA1. *Biochem. J.* 433, 197–204. doi: 10.1042/BJ20101256

Sawada, Y., Hosokawa, H., Hori, A., Matsumura, K., and Kobayashi, S. (2007). Cold sensitivity of recombinant TRPA1 channels. *Brain Res.* 1160, 39–46. doi: 10.1016/j.brainres.2007.05.047

Schmidt, M., Dubin, A. E., Petrus, M. J., Earley, T. J., and Patapoutian, A. (2009). Nociceptive signals induce trafficking of TRPA1 to the plasma membrane. *Neuron* 64, 498–509. doi: 10.1016/j.neuron.2009.09.030

Shigetomi, E., Tong, X., Kwan, K. Y., Corey, D. P., and Khakh, B. S. (2011). TRPA1 channels regulate astrocyte resting calcium and inhibitory synapse efficacy through GAT-3. *Nat. Neurosci.* 15, 70–80. doi: 10.1038/nn.3000

Singh, A. K., McGoldrick, L. L., Demirkhanyan, L., Leslie, M., Zakharian, E., and Sobolevsky, A. I. (2019). Structural basis of temperature sensation by the TRP channel TRPV3. *Nat. Struct. Mol. Biol.* 27, 221. doi: 10.1038/s41594-019-0318-7

Singh, A. K., McGoldrick, L. L., and Sobolevsky, A. I. (2018). Structure and gating mechanism of the transient receptor potential channel TRPV3. *Nat. Struct. Mol. Biol.* 25, 805–813. doi: 10.1038/s41594-018-0108-7

Sinica, V., Zimova, L., Barvikova, K., Macikova, L., Barvik, I., and Vlachova, V. (2019). Human and mouse TRPA1 are heat and cold sensors differentially tuned by voltage. *Cells* 9:E57. doi: 10.3390/cells9010057

Smith, F. D., Reichow, S. L., Esselltine, J. L., Shi, D., Langeberg, L. K., Scott, J. D., et al. (2013). Intrinsic disorder within an AKAP-protein kinase A complex guides local substrate phosphorylation. *eLife* 2:e01319. doi: 10.7554/eLife.01319

Startek, J. B., Boonen, B., Lopez-Requena, A., Talavera, A., Alpizar, Y. A., Ghosh, D., et al. (2019). Mouse TRPA1 function and membrane localization are modulated by direct interactions with cholesterol. *eLife* 8:e46084. doi: 10.7554/eLife.46084

Staruschenko, A., Jeske, N. A., and Akopian, A. N. (2010). Contribution of TRPV1-TRPA1 interaction to the single channel properties of the TRPA1 channel. *J. Biol. Chem.* 285, 15167–15177. doi: 10.1074/jbc.M110.106153

Story, G. M., Peier, A. M., Reeve, A. J., Eid, S. R., Mosbacher, J., Hricik, T. R., et al. (2003). ANKTM1, a TRP-like channel expressed in nociceptive neurons, is activated by cold temperatures. *Cell* 112, 819–829. doi: 10.1016/s0092-8674(03)00158-2

Sulak, M. A., Ghosh, M., Sinharoy, P., Andrei, S. R., and Damron, D. S. (2018). Modulation of TRPA1 channel activity by Cdk5 in sensory neurons. *Channels* 12, 65–75. doi: 10.1080/19336950.2018.1424282

Suo, Y., Wang, Z., Zubcevic, L., Hsu, A. L., He, Q., Borgnia, M. J., et al. (2020). Structural insights into Electrophile Irritant Sensing by the human TRPA1 channel. *Neuron* 105, 31009–31008. doi: 10.1016/j.neuron.2019.11.023

Takahashi, K., and Ohta, T. (2017). Membrane translocation of transient receptor potential ankyrin 1 induced by inflammatory cytokines in lung cancer cells. *Biochem. Biophys. Res. Commun.* 490, 587–593. doi: 10.1016/j.bbrc.2017.06.082

Talavera, K., Startek, J. B., Alvarez-Collazo, J., Boonen, B., Alpizar, Y. A., Sanchez, A., et al. (2019). Mammalian transient receptor potential TRPA1 channels: from structure to disease. *Physiol. Rev.* [Epub ahead of print].

Ufret-Vincenty, C. A., Klein, R. M., Hua, L., Angueyra, J., and Gordon, S. E. (2011). Localization of the PIP2 sensor of TRPV1 ion channels. *J. Biol. Chem.* 286, 9688–9698. doi: 10.1074/jbc.M110.192526

Vandewauw, I., De Clercq, K., Mulier, M., Held, K., Pinto, S., Van Ranst, N., et al. (2018). A TRP channel trio mediates acute noxious heat sensing. *Nature* 555, 662–666. doi: 10.1038/nature26137

Viana, F. (2016). TRPA1 channels: molecular sentinels of cellular stress and tissue damage. *J. Physiol.* 594, 4151–4169. doi: 10.1113/JP270935

Villalobo, A., Ishida, H., Vogel, H. J., and Berchtold, M. W. (2018). Calmodulin as a protein linker and a regulator of adaptor/scaffold proteins. *Biochim. Biophys. Acta Mol. Cell Res.* 1865, 507–521. doi: 10.1016/j.bbamcr.2017.12.004

Viswanath, V., Story, G. M., Peier, A. M., Petrus, M. J., Lee, V. M., Hwang, S. W., et al. (2003). Opposite thermosensor in fruitfly and mouse. *Nature* 423, 822–823. doi: 10.1038/423822a

Voolstra, O., and Huber, A. (2014). Post-translational modifications of TRP channels. *Cells* 3, 258–287. doi: 10.3390/cells3020258

Wang, S., Dai, Y., Fukuoka, T., Yamanaka, H., Kobayashi, K., Obata, K., et al. (2008). Phospholipase C and protein kinase A mediate bradykinin sensitization of TRPA1: a molecular mechanism of inflammatory pain. *Brain* 131(Pt 5), 1241–1251. doi: 10.1093/brain/awn060

Wang, Y. Y., Chang, R. B., Allgood, S. D., Silver, W. L., and Liman, E. R. (2011). A TRPA1-dependent mechanism for the pungent sensation of weak acids. *J. Gen. Physiol.* 137, 493–505. doi: 10.1085/jgp.201110615

Wang, Z., Ye, D., Ye, J., Wang, M., Liu, J., Jiang, H., et al. (2019). The TRPA1 channel in the cardiovascular system: promising features and challenges. *Front. Pharmacol.* 10:1253. doi: 10.3389/fphar.2019.01253

Weng, H. J., Patel, K. N., Jeske, N. A., Bierbower, S. M., Zou, W., Tiwari, V., et al. (2015). Tmem100 is a regulator of TRPA1-TRPV1 complex and contributes to persistent pain. *Neuron* 85, 833–846. doi: 10.1016/j.neuron.2014.12.065

Witschas, K., Jobin, M. L., Korkut, D. N., Vladan, M. M., Salgado, G., Lecomte, S., et al. (2015). Interaction of a peptide derived from C-terminus of human TRPA1 channel with model membranes mimicking the inner leaflet of the plasma membrane. *Biochim. Biophys. Acta* 1848, 1147–1156. doi: 10.1016/j.bbamem.2015.02.003

Yap, K. L., Kim, J., Truong, K., Sherman, M., Yuan, T., and Ikura, M. (2000). Calmodulin target database. *J. Struct. Funct. Genomics* 1, 8–14.

Yarmolinsky, D. A., Peng, Y., Pogorzala, L. A., Rutlin, M., Hoon, M. A., and Zuker, C. S. (2016). Coding and Plasticity in the Mammalian Thermosensory System. *Neuron* 92, 1079–1092. doi: 10.1016/j.neuron.2016.10.021

Zhang, X., Li, L., and McNaughton, P. A. (2008). Proinflammatory mediators modulate the heat-activated ion channel TRPV1 via the scaffolding protein AKAP79/150. *Neuron* 59, 450–461. doi: 10.1016/j.neuron.2008.05.015

Zhao, J., King Lin, J. V., Paulsen, C. E., Cheng, Y., and Julius, D. (2019). Mechanisms governing irritant-evoked activation and calcium modulation of TRPA1. *BioRxiv* [preprint]. doi: 10.1101/2019.12.26.888982

Zimova, L., Sinica, V., Kadkova, A., Vyklicka, L., Zima, V., Barvik, I., et al. (2018). Intracellular cavity of sensor domain controls allosteric gating of TRPA1 channel. *Sc.Signal.* 11:eaan8621. doi: 10.1126/scisignal.aan8621

Zurborg, S., Yurgionas, B., Jira, J. A., Caspani, O., and Heppenstall, P. A. (2007). Direct activation of the ion channel TRPA1 by Ca2+. *Nat. Neurosci.* 10, 277–279. doi: 10.1038/nn1843

Zygmunt, P. M., and Hogestatt, E. D. (2014). Trpa1. *Handb. Exp. Pharmacol.* 222, 583–630. doi: 10.1007/978-3-642-54215-_23

Human and Mouse TRPA1 Are Heat and Cold Sensors Differentially Tuned by Voltage

Viktor Sinica [1,2], Lucie Zimova [1,*] [iD], Kristyna Barvikova [1] [iD], Lucie Macikova [1] [iD], Ivan Barvik [3] and Viktorie Vlachova [1,*] [iD]

[1] Department of Cellular Neurophysiology, Institute of Physiology of the Czech Academy of Sciences, 142 20 Prague, Czech Republic; viktor.synytsya@fgu.cas.cz (V.S.); tynabarvikova@seznam.cz (K.B.); lucie.macikova@fgu.cas.cz (L.M.)

[2] Department of Physical and Macromolecular Chemistry, Faculty of Science, Charles University, 128 00 Prague, Czech Republic

[3] Division of Biomolecular Physics, Institute of Physics, Faculty of Mathematics and Physics, Charles University, 121 16 Prague, Czech Republic; ibarvik@karlov.mff.cuni.cz

* Correspondence: lucie.zimova@fgu.cas.cz (L.Z.); viktorie.vlachova@fgu.cas.cz (V.V.); Tel.: +420-296-442-759 (L.Z.); +420-296-442-711 (V.V.)

check for updates

Abstract: Transient receptor potential ankyrin 1 channel (TRPA1) serves as a key sensor for reactive electrophilic compounds across all species. Its sensitivity to temperature, however, differs among species, a variability that has been attributed to an evolutionary divergence. Mouse TRPA1 was implicated in noxious cold detection but was later also identified as one of the prime noxious heat sensors. Moreover, human TRPA1, originally considered to be temperature-insensitive, turned out to act as an intrinsic bidirectional thermosensor that is capable of sensing both cold and heat. Using electrophysiology and modeling, we compare the properties of human and mouse TRPA1, and we demonstrate that both orthologues are activated by heat, and their kinetically distinct components of voltage-dependent gating are differentially modulated by heat and cold. Furthermore, we show that both orthologues can be strongly activated by cold after the concurrent application of voltage and heat. We propose an allosteric mechanism that could account for the variability in TRPA1 temperature responsiveness.

Keywords: TRP channel; thermoTRP; noxious heat; noxious cold; transient receptor potential; ankyrin receptor subtype 1

1. Introduction

The transient receptor potential (TRP) channel subtype A1 (TRPA1) is a polymodal sensor that is implicated in thermal and chemical nociception. Across different species, this channel particularly serves as a key receptor for electrophilic irritant compounds, evoking defensive responses [1–3]. The temperature sensitivity of TRPA1, on the other hand, has been reported to be a less evolutionarily conserved activation mode or alternatively occurring at the expense of chemical sensitivity [2,4]. The physiological role of this channel as a heat sensor has likely changed during evolution, potentially altering the preferred temperature ranges among species [5,6] or enabling some of them to detect and transduce infrared signals [4]. In invertebrates and ancestral vertebrates, TRPA1 acts as a heat-sensing ion channel [4,7–12]. In mammals, TRPA1 has long been considered to function as a cold receptor [13–18]. More recently, however, it has been also found to mediate a crucial physiological role in the detection of noxious heat [19–21]. A direct cold activation of TRPA1 has been demonstrated in several laboratories for mouse, rat and human orthologues [13,14,17,22,23], but it has not been observed by some other

groups [4,24–27]. A substitution of a single specific amino acid residue (S250N) within the N-terminus of mouse TRPA1 results in a warm-sensitive channel [28], whereas human TRPA1 can become heat-activated when its N-terminal domain is transplanted from a rattlesnake orthologue [4]. Moreover, human TRPA1 reconstituted in an artificial membrane can act as an intrinsic bidirectional thermosensor that is capable of sensing both cold and heat [29], underscoring that the temperature-dependent behavior of the channel can be more complex than previously anticipated. A thorough perusal of all the available literature has indicated that there is still no common understanding of whether and, if so, under which conditions TRPA1 can directly act as a temperature sensor in mammals.

The sensitivity of TRPA1 to cold differs between primate and rodent species [26], and a single residue within the fifth transmembrane domain S5 has been proposed to underlie the observed differences. By using a chimeric domain swap analysis between rat and human TRPA1, the authors identified V875 in primates, corresponding to G878 in rodents, and demonstrated that the G878V mutation abolishes the cold activation of the rat and mouse TRPA1. Importantly, the same S5 region is involved in the sensitivity of TRPA1 to several nonelectrophilic agonists such as menthol, carvacrol, thymol, eudesmol, and protons, but also some pungent general anesthetics such as isoflurane, desflurane and propofol [30–33]. Moreover, mutations in S5 can strongly affect voltage-dependent characteristics of the channel [34] and the residues adjacent to V875 (S873 and T874) form, together with S6 (F944 and V948) and the first pore helix (F909), a binding pocket for the potent inhibitor A-967079 [31]. Most likely, the region around V875 is essentially involved in gating, and the sensitivity of TRPA1 to cold may thus depend on a proper allosteric coupling of a putative temperature-sensitive module to the gate domain.

The activation of certain temperature-sensitive TRP channels is associated with a temperature-induced a shift of their current–voltage relationships, and a simple two-state model has been proposed for a formal description of experimental measurements of channel activity [35]. Though this model seems to appropriately fit the voltage- and cold-dependent currents from mouse TRPA1 under some conditions [17], alternative modular allosteric models have been shown to be well-capable of capturing the characteristic the allosteric nature of thermo-TRP channel gating [36–40]. These models assume that the temperature and voltage sensors are separable parts of the protein that are allosterically coupled to the gate domain and to each other, and the transitions between the closed and open states are stimulus-independent. Particularly, the inverted coupling hypothesis was recently proposed by Jara-Oseguera and Islas [39], who demonstrated that the activation of cold-sensitive channels could be determined by the nature of the allosteric coupling between the heat-activated temperature sensor and the gate. We reasoned that TRPA1 is a prime candidate for testing such a predicted mechanism because some of the above studies have strongly suggested the modular nature of the temperature-dependent gating. Hence, we set out to compare the temperature- and voltage-dependent properties of human and mouse TRPA1 with the aim to decipher the fundamental differences between their mechanisms of gating.

2. Materials and Methods

2.1. Cell Culture, Constructs and Transfection

Human embryonic kidney 293T (HEK293T; ATCC, Manassas, VA, USA) cells were cultured in Opti-MEM I media (Invitrogen, Carlsbad, CA, USA) supplemented with 5% fetal bovine serum. The magnet-assisted transfection (IBA GmbH, Gottingen, Germany) technique was used to transiently co-transfect the cells in a 15.6 mm well on a 24-well plate coated with poly-L-lysine and collagen (Sigma-Aldrich, Prague, Czech Republic) with 200 ng of green fluorescent protein (GFP) plasmid (TaKaRa, Shiga, Japan) and with 400 ng of cDNA plasmid-encoding, wild-type or mutant human TRPA1 (pCMV6-XL4 vector, OriGene Technologies, Rockville, MD, USA) or mouse TRPA1 in pcDNA5/FRT vector, kindly provided by Dr. Ardem Patapoutian (Scripps Research Institute, La Jolla, CA, USA). The cells were used 24–48 h after transfection. At least three independent transfections were used

for each experimental group. The wild-type channel was regularly tested in the same batch as the mutants. The mutants were generated by PCR by using a QuikChange II XL Site-Directed Mutagenesis Kit (Agilent Technologies, Santa Clara, CA, USA), and they were confirmed by DNA sequencing (Eurofins Genomics, Ebersberg, Germany). F11 cells (The European Collection of Authenticated Cell Cultures, ECACC 08062601, Porton Down, UK) cultured in Dulbecco's Modified Eagle's Medium supplemented with 2 mM glutamine and 10% fetal bovine serum were passaged once a week by using Trypsin-EDTA (Invitrogen, CA, USA) and grown under 5% CO_2 at 37 °C. One-to-two days before transfection, cells were plated in 24-well plates (2×10^5 cells per well) in 0.5 ml of medium, and they became confluent on the day of transfection. The cells were transiently co-transfected with 400 ng of cDNA plasmid-encoding mouse (in the pcDNA5/FRT vector) or human (in the pCMV6-XL4 vector) TRPA1 and with 200 ng of the GFP plasmid (TaKaRa, Japan) with the use of Lipofectamine 2000 (Invitrogen, CA, USA) and then plated on poly-ʟ-lysine-coated glass coverslips.

2.2. Electrophysiology

Whole-cell membrane currents were filtered at 2 kHz by using the low-pass Bessel filter of the Axopatch 200B amplifier, and they were digitized (5–10 kHz) with a Digidata 1440 unit and the pCLAMP 10 software (Molecular Devices, San Jose, CA, USA). Patch electrodes were pulled from borosilicate glass and heat-polished to a final resistance of between 3 and 5 MΩ. Series resistance was compensated by at least 60%. The experiments were performed at room temperature (23–25 °C). Only one recording was performed on any one coverslip of cells to ensure that recordings were made from cells that had not been previously exposed to temperature or chemical stimuli. Extracellular bath solutions were Ca^{2+}-free and contained: 140 mM NaCl, 5 mM KCl, 2 mM $MgCl_2$, 5 mM EGTA (ethylene glycol-bis (β-aminoethyl ether)-*N*,*N*,*N'*,*N'*-tetraacetic acid), 10 mM 4-(2-Hydroxyethyl)piperazine-1-ethanesulfonic acid (HEPES), 10 mM glucose, and pH 7.4 was adjusted by tetramethylammonium hydroxide. The intracellular solution contained 140 mM KCl, 5 mM EGTA, 2 mM $MgCl_2$, 10 mM HEPES, adjusted with KOH to pH 7.4. For F11 cell recordings, the internal pipette solution contained 125 mM Cs-gluconate, 15 mM CsCl, 5 mM EGTA, 10 mM HEPES, 0.5 mM $CaCl_2$, 2 mM MgATP, 0.3 NaGTP, and 10 mM HEPES, adjusted to pH 7.4 with CsOH, 283 mOsm. All of the chemicals were purchased from Sigma-Aldrich (Prague, Czech Republic). The *I–V* relationships were recorded by using 400-ms steps ranging from −150 to +100 mV, followed by a 400-ms step to −150 mV (increment +25 mV) and a holding potential of 0 mV, or they were recorded by using 100-ms steps from −80 mV to +200 mV (increment +20 mV) and holding potential of −70 mV.

2.3. Temperature Stimulation

A system for the fast cooling and heating of solutions that superfuse isolated cells under patch-clamp conditions was used as described previously [41]. Briefly, experimental solutions are driven by gravity from 7 different barrels through automatically controlled valves to a manifold that consists of fused silica tubes (320 μm inner diameter) that are connected to a common outlet glass capillary through which the solutions are applied onto the cell surface. The upper part of the outlet capillary passes the solutions through a temperature exchanger driven by a miniature Peltier device that preconditions the temperature (precooling or preheating). The lower part of the capillary is wrapped with an insulated, densely-coiled copper wire (over a length of 5 mm, connected to a direct current source for resistive heating) that finally heats the passing solution to a chosen temperature. The Peltier device and the heating element are electrically connected to the headstage probe, which is fixed on to a micromanipulator for the positioning of the manifold. The temperature of the flowing solution is measured by a miniature thermocouple that is inserted into the common outlet capillary near to its orifice that is placed at a distance of less than 100 μm from the surface of the examined cell. The temperature is controlled either automatically or manually by voltage commands via the digital-to-analogue converter of a conventional data acquisition interface (Digidata 1440, Molecular

Devices). The system allows for the application of temperature changes within a range of 5–60 °C at maximum rates between −40 and ~110 °C/s.

2.4. Molecular Modelling

To elucidate the possible structural mechanism by which the substitutions at S804 (S804D, S804N, S804A) produce dramatic functional changes, we used the human TRPA1 structure with modeled S1–S2 and S2–S3 linkers, which is available in the Model Archive (www.modelarchive.org) under the accession code ma-auqu1 [42] and which is based on the structure with Protein Data Bank (PDB) ID: 3J9P, determined by cryo-electron microscopy [31]. The TRPA1 tetrameric structure was inserted into the patch of the 1-palmitoyl-2-oleoylphosphatidylcholine (POPC) bilayer and solvated in transferable intermolecular potential 3-point (TIP3P) [43] water molecules to ensure the presence of at least 10 Å of solvent on both sides of the membrane, and then the structure was neutralized in 0.5 M NaCl. This gave a periodic box size of $120 \times 120 \times 160$ Å for a simulated system consisting of ~205,000 atoms. All atom structure and topology files were generated by using VMD software [44]. Forces were computed by using the CHARMM27 force field for proteins, lipids, and ions [45–47]. All molecular dynamics (MD) simulations were produced with the aid of the software package NAMD2.13 [48] running on computers equipped with NVIDIA graphics processing units (Nvidia Corporation, Santa Clara, CA, USA). First, Langevin dynamics were used for temperature control, with the target temperature set to 285 K, the Langevin piston method was applied to reach an efficient pressure control with a target pressure of 1 atm [48]. The integration timestep was set to 2 fs. Simulated systems were energy-minimized, heated to 285 K, and production MD runs reached a length of 2000 ps. Data were recorded every 2 ps, and contacts of S804 (or S804D, S804N) with ambient polar residues within 12 Å were analyzed by using the CPPTRAJ module from Amber Tools suite [49].

To obtain a model of human TRPA1 with the C-terminal loop region (1007–1030), a homology model of the C-terminal loop region was created by using the Swiss-Model web server (https:/swissmodel. expasy.org/) and incorporated into the 3J9P structure. Then, we used the original electron density map of human TRPA1 with the Electron Microscopy Data Bank (EMDB) ID: 6267 [31] and applied the molecular dynamics flexible fitting (MDFF) method for combining high-resolution structures with cryo-electron microscopy (cryo-EM) maps, a method that creates atomic models that represent the conformational state captured by cryo-EM [50,51]. We followed standard procedure by using software packages, modules, and keywords described in detail in "MDFF Tutorial" (http://www.ks.uiuc.edu/Training/Tutorials/). MD trajectories were visualized with the aid of the VMD 1.9 software package [44]. Figures were produced with the software packages UCSF Chimera 1.13 [52] and CorelDraw X7 (Corel Corporation).

2.5. Statistical Analysis

The electrophysiological data were analyzed by using pCLAMP 10 (Molecular Devices), and the curve fitting of currents and statistical analyses were done in SigmaPlot 10 (Systat Software Inc.). Conductance–voltage (*G–V*) relationships were obtained from the steady-state whole cell currents measured at the end of voltage steps. Voltage-dependent gating parameters were estimated by fitting the conductance $G = I/(V - V_{rev})$ as a function of the test potential *V* to the Boltzmann equation:

$$G = [(G_{max} - G_{min})/(1 + \exp(-zF(V - V_{50})/RT))] + G_{min}, \tag{1}$$

where *z* is the apparent number of gating charges, V_{50} is the half-activation voltage, G_{min} and G_{max} are the minimum and maximum of the whole-cell conductance, V_{rev} is the reversal potential, and *F*, *R*, and *T* have their usual thermodynamic meanings. Activation time constants (τ_{fast} and τ_{slow}) were directly measured from outward currents by performing a double exponential Chebyshev fit to the rising phase of the activating currents. Fast and slow deactivation was characterized by a single or a double exponential fit to the current upon repolarization. The initial 1.3 ms interval was ignored. For comparisons between human TRPA1 (hTRPA1) and mouse TRPA1 (mTRPA1), we calculated the

average weighted time constants of the activation and deactivation process based on the amplitudes of the fast and slow components:

$$\tau_w = A_{fast}/(A_{fast} + A_{slow}) \times \tau_{fast} + A_{slow}/(A_{fast} + A_{slow}) \times \tau_{slow}, \tag{2}$$

Statistical significance was determined by Student's *t*-test or the analysis of variance, as appropriate; differences were considered significant at $p < 0.05$ where not stated otherwise. The data are presented as means ± (or +/−) SEM.

2.6. Kinetic Modeling and Simulations

The open probability versus voltage and temperature, P_o (*V*,*T*), landscapes were generated by using the analytic expression for the open probability (Equation (4) in [39]), written as a data transformation script in SigmaPlot 10 (Systat Software Inc., San Jose, CA, USA). The steady-state data were fit to an eight-state allosteric model that was written in COPASI 4.22 [53] by using the built-in genetic algorithm. The equilibrium constant of the temperature sensor $J(T)$ was set to the value published for TRPM8 [36,39]: $\Delta H^o = 91$ kcal mol^{-1} and $\Delta S^o = 0.317$ kcal mol^{-1} K^{-1}. The parameter ΔH^o was kept constant for all modeled situations. The parameters $K(0)$, z, L, E, D, $\Delta H^o{}_C$, and $\Delta S^o{}_C$ were estimated by fitting the average conductance to voltage (*G*/*V*) curves obtained for hTRPA1 at 25 and 12 °C. To qualitatively match the activation profile of a representative hTRPA1 recordings, two additional P_o (*V*,*T*) landscapes were calculated. The "green" and "red" P_o (*V*,*T*) landscapes (shown in the Results section below) were modeled to meet the assumptions coming from the activation profile of hTRPA1, normalized to G_{max}. $P_o = 0.15$ at −70 mV and 60 °C, $P_o = 0.005$ at −70 mV and 5 °C, $P_o = 0.21$ at +80 mV and 5 °C, and $P_o = 0.71$ at +80 mV and 60 °C (for green); $p = 0.91$ at −70 mV and 60 °C, $P_o = 0.998$ at −70 mV and 5 °C, $P_o = 0.23$ at +80 mV and 5 °C, and $P_o = 0.74$ at +80 mV and 60 °C (for red). To obtain the green P_o (*V*,*T*) landscape, all parameters from the blue $P(V,T)$ landscape were fixed except for the allosteric coupling factors E, D, $C(\Delta H^o{}_C, \Delta S^o{}_C)$ and equilibrium constant L. The parameters for the red landscape were obtained in two steps. In the first step, the parameters from the green P_o (*V*, *T*) landscape were fixed except for D, L, $\Delta H^o{}_C$ and $\Delta S^o{}_C$. The obtained values for D and L were used in the second step to find parameters: E, ΔS^o, $\Delta H^o{}_C$ and $\Delta S^o{}_C$. The resulting parameters were then used to simulate the time-dependent probability for each state of the model over the time interval of 10–50 s with a time step of 0.1 s. The exemplary data used for our kinetic simulations were obviously not sufficient to unambiguously constrain the large number of free model parameters. We performed a large number of different simulations with different initial sets of free parameters. In some cases, the fits successfully converged, but the obtained values were physically unrealistic. However, when the sort of constraints described above was applied, the fits converged to similar solutions when different initial parameter values were used for several repeated fittings.

3. Results

3.1. Temperature and Voltage Dependence of Human and Mouse TRPA1

Previous studies have shown that the cold sensitivity of mTRPA1 can be described by a two-state model in which temperature directly affects the equilibrium between the open and closed states of the channel, based on global changes in enthalpy and entropy during channel gating [17]. The authors demonstrated that upon cooling, the voltage dependence of mTRPA1 channel activation is shifted towards more negative voltages, similarly to the behavior of certain other temperature-activated TRP channels [35]. To compare the voltage-dependence and relaxation kinetics between hTRPA1 and mTRPA1, we measured whole-cell currents in response to a voltage step protocol akin to that used previously by [17], consisting of 400-ms steps ranging from −150 to +100 mV, followed by a 400-ms step to −150 mV (Figure 1A–D). The currents were measured at 12, 25, and 35 °C under Ca^{2+}-free conditions to prevent the Ca^{2+}-dependent potentiation and inactivation of TRPA1 [54]. We constructed the conductance-to-voltage (*G*/*V*) relationships and found that cold (12 °C) and heat (35 °C) increased

the conductance at negative membrane potentials in both channel orthologues (Figure 1B,D,E). An obvious difference was in a constitutive voltage independent conductance evident at 25 °C and negative membrane potentials in mTRPA1 (2.5 ± 0.7 nS at −150 mV; n = 23) but not in hTRPA1 (0.8 ± 0.1 nS; n = 7; p < 0.001). On the other hand, the maximum conductance at +100 mV measured in mTRPA1 at 25 °C (23.4 ± 10.9 nS) was not statistically different from that in hTRPA1 (23.5 ± 1.8 nS; p = 0.994), suggesting a shift in the basal gating equilibrium towards the open state at negative potentials rather than differences between the expression levels of the two channels. The half-maximum activation voltage (V_{50}) of hTRPA1 was shifted from 66.5 ± 6.7 mV at 25 °C to 53.4 ± 3.0 mV at 35 °C (p = 0.035). In contrast, the voltage activation curve was not shifted upon warming in mTRPA1 (V_{50} of 60.9 ± 6.4 mV at 25 °C and 62.8 ± 6.3 mV at 35 °C; n = 6; p = 0.732). In both channels, warming from 25 to 35 °C did not significantly alter the apparent gating charges (hTRPA1: 0.76 ± 0.03 e_0 and 0.85 ± 0.06 e_0; p = 0.256; paired *t*-test; n = 8; mTRPA1: 0.85 ± 0.05 e_0 and 0.82 ± 0.03 e_0; p = 0.523; paired *t*-test; n = 6). At 12 °C, the voltage-induced currents did not reach steady state at the end of the step pulse, and the G/V relationships were estimated from the exponential fit of the recorded activation curves (Figure 1A,C).

To compare the effects of temperature on the activation and deactivation kinetics, we determined the time constants by mono- or bi-exponential fits to the time course of the onset currents at +100 mV and the inward tail currents measured at −150 mV (Figure 1E,F). The activation phase of the outward currents mediated by mTRPA1 at 25 °C could be fitted by a monoexponential function with a time constant, τ_{on}, of 33.0 ± 2.7 ms (n = 10). In contrast, an adequate fit of the activation phase of the currents through hTRPA1 required at least two exponential functions with the average fast and slow components of 39.3 ± 3.3 ms (contributing by 80.6 ± 5.6%) and 155.4 ± 24.7 ms (n = 25), respectively. The temperature dependencies of the activation rates were compared by plotting the inverse of τ_{on} versus $1/T$ (Figure 1F). The relationship for mTRPA1 could be fitted well by linear regression with a resultant slope of 87.6 kJ mol^{-1}. Provided that the activation of mTRPA1 was limited by one main step, this value corresponded to Q_{10} = 3.3 within the 10–35 °C temperature range. In hTRPA1, the temperature dependencies of the fast and slow component of the activation process exhibited slopes of 95.1 kJ mol^{-1} (Q_{10} = 3.7) and 77.9 kJ mol^{-1} (Q_{10} = 2.9)

The time course of the inward tail currents at −150 mV (Figure 1F, right) was monoexponential in all cells expressing mTRPA1 (τ_{off} at 25 °C, 9.1 ± 0.6 ms; n = 10), which is in agreement with previously published results [17]. In a clear contrast, the hTRPA1 tail currents could be well-fitted only by two exponentials, τ_{fast} of 5.0 ± 0.4 ms (contributing by 70.4 ± 5.2%) and τ_{slow} of 28.4 ± 1.8 ms at 25 °C (n = 23). The initial rapid component of hTRPA1 deactivation was fast at 35 °C, which made the determination of τ_{fast} uncertain. To reliably extrapolate the temperature dependency of the deactivation rate for the human orthologue, we additionally measured the voltage-induced currents at 20 and 30 °C. From the Arrhenius plot of the deactivation rates, it was apparent that the deactivation process of mTRPA1 exhibited a slightly steeper temperature dependence (81.3 kJ mol^{-1}; Q_{10} = 3.1) than the fast component of the deactivation of hTRPA1 (67.2 kJ mol^{-1}; Q_{10} = 2.5). These results indicate that the voltage-dependent activation and deactivation processes of both orthologues exhibited only mild temperature dependencies over the temperature range of 12–35 °C. Compared to hTRPA1, the gating equilibrium of mTRPA1 was significantly shifted towards the open state.
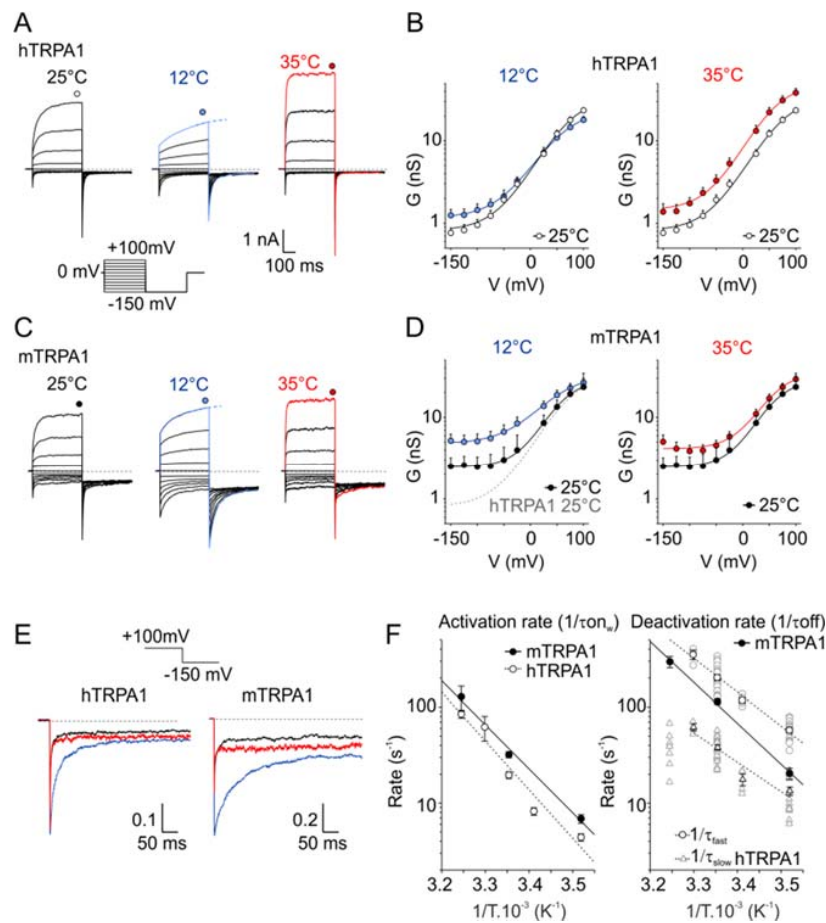
Figure 1. Effects of cooling and warming on the voltage-dependent gating kinetics of the human and mouse transient receptor potential (TRP) channel subtype A1 (TRPA1) orthologues. (**A**) Representative whole-cell currents in Ca^{2+}-free intracellular and extracellular solutions recorded from a human embryonic kidney (HEK) 293T cell line transiently expressing the wild-type human TRPA1 (hTRPA1) channel, measured by the indicated voltage-step protocol at different temperatures. The voltage-step protocol was previously used by [17]. Steady-state currents were measured at the end of the pulses, as indicated by colored symbols atop each record. At 12 °C, the steady-state currents were estimated from the exponential fit of the recorded activation curves, as indicated by dashed lines. (**B**) The average conductance of hTRPA1 was obtained from the voltage step protocols, as in (**A**). The data represent the means + SEM. ($n \geq 6$). The solid lines represent the best fit to a Boltzmann function, as described in Materials and Methods. (**C**) Representative whole-cell currents through wild-type mouse TRPA1 (mTRPA1), as in (**A**). (**D**) Average conductance of mTRPA1 obtained from voltage step protocols, as in (**C**). The data represent the means + SEM. ($n \geq 4$). The solid lines represent the best fit to a Boltzmann function, as described in Materials and methods. The fit of hTRPA1 at 25 °C is overlaid as a grey dashed line for comparison. Note the increased basal conductance of mTRPA1 at negative potentials. (**E**) Comparison of the deactivation kinetics of TRPA1 orthologues at different temperatures. Representative tail currents normalized to the maximum amplitude at +100 mV obtained as an indicated part of the voltage step protocols, as in (**A,C**). Color-coded as the rest of the figure: black for 25 °C, red for 35 °C, and blue 12 °C. While the mTRPA1 tail currents could be fitted by a monoexponential function, the hTRPA1 tail currents could be well-fitted only by two exponentials. (**F**) Arrhenius plots of the onset (left) and deactivation (right) time constants for hTRPA1 (open symbols) and mTRPA1 (close symbols). The time constants of the onset were determined by mono- (mTRPA1) or bi-exponential (hTRPA1, plotted as weighted mean) fits to the time course of the onset currents at +100 mV, as in (**A,C**). The time constants of the deactivation rate were determined by mono- (mTRPA1) or bi-exponential (hTRPA1, fast and slow components plotted separately as open circles and triangles) fits to the tail currents, as in (**E**).

3.2. Mutations hTRPA-V875G and mTRPA1-G878V in S5

Previous studies have identified G878 in mTRPA1 and V875 in hTRPA1 (Figure 2A) as residues underlying the species-specific differences in cold sensitivity [26]. We addressed the question of to what extent this residue could contribute to the temperature dependence of the voltage-induced gating. We measured the voltage-activated currents from hTRPA-V875G and mTRPA1-G878V at 12, 25, and 35 °C (Figure 2B–E and Figure S1) and compared the temperature dependencies of the deactivation rate by fitting the time course of the inward tail currents at −150 mV by mono- or bi-exponential functions (Figure 2F–I). Most interestingly, the temperature dependence of the fast component of the deactivation rate of hTRPA1-V875G became steeper, thus resembling that of mTRPA1 (83.6 kJ mol^{-1}; Figure 2G). The reverse mutation mTRPA1-G878V had an opposite effect: A decreased slope of the temperature dependence of the deactivation rate approached the less steep slope of the wild-type hTRPA1 (69.6 kJ mol^{-1}; Figure 2I). These results not only complement those obtained by Chen et al. [26] but also further emphasize the possible role of the residue V875/G878 in S5 in allosteric gating.

3.3. Functional Role of Non-Homologous Residues in the Vicinity of V875

Next, we wondered how the temperature signal might be conveyed to the gate and how the allosteric coupling or gating of primate and rodent orthologues is adjusted by the vicinity of V875/G878. By mapping all residues that are non-conserved between mouse and human TRPA1 onto the cryo-EM structure, we identified several sites in the inner part of the S1–S4 sensor and the S4–S5 linker located close to S5 (Figure S2). Accordingly, we constructed and functionally analyzed a set of reverse mutants of hTRPA1 (M801L, S804N, V806A, and I803Y/L867F) at 25, 12, and 35 °C. Among them, the single human to mouse mutation S804N was most affected, as it exhibited large basal currents, very slow activation and deactivation kinetics, and a strong voltage-independent component (Figure 3A–C and Figure S3). The half-maximum activation voltage, V_{50}, was drastically shifted to 21.6 ± 4.1 mV at 25 °C and to 29.5 ± 4.6 mV at 12 °C ($n = 7$; $p < 0.001$). The steady-state conductance measured at 35 °C almost overlapped with the G/V relationships measured at room temperature (Figure 3B). From the Arrhenius plot of the deactivation rates, it was apparent that the deactivation process of S804N exhibited a somewhat steeper temperature dependence (103.8 kJ mol^{-1}; $Q_{10} = 4.2$) compared to the wild-type channels (Figure 3C). To better understand the biophysical requirements at position 804, we explored small nonpolar and charged substitutions. The replacement of the serine with an alanine, S804A, rendered the channel nonfunctional (Figure 3D), whereas aspartate substitution resulted in a phenotype similar to S804N (Figure 3E) in that the activation of S804D by cold produced large and persisting currents at negative membrane potentials (see Figure S6 below).
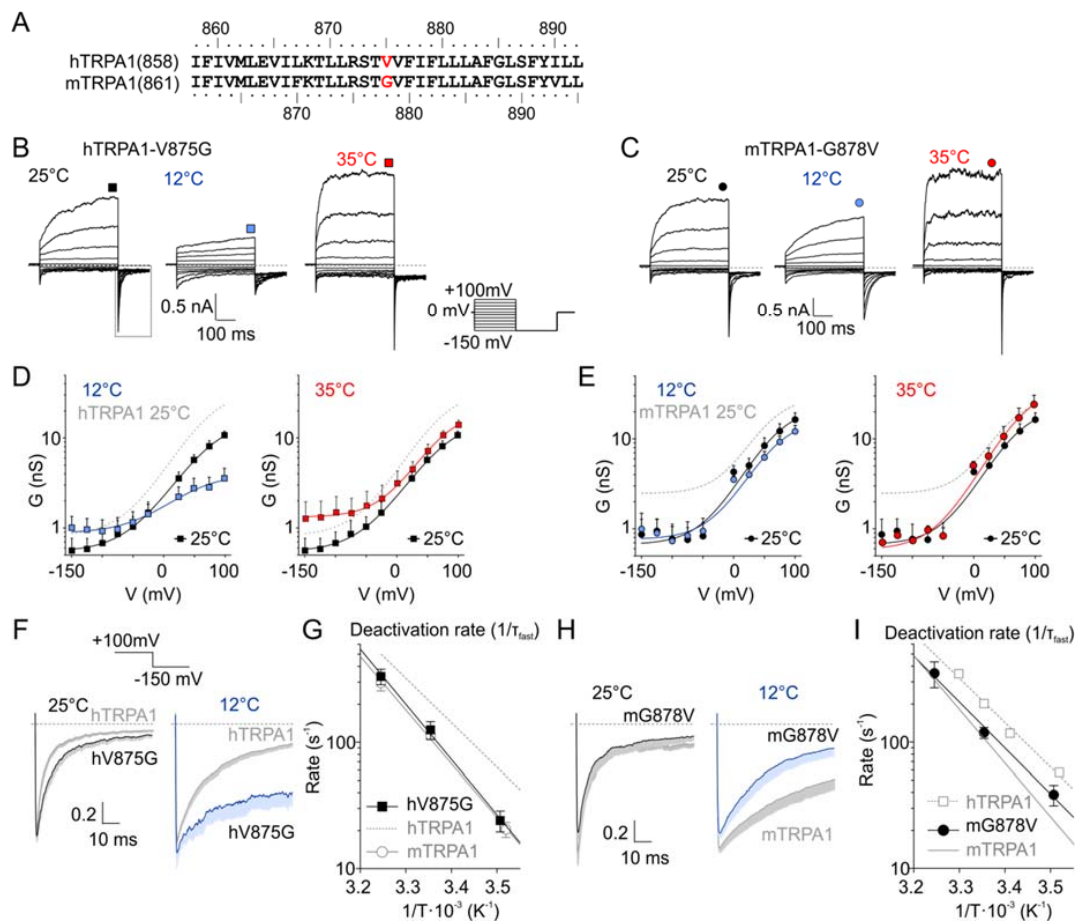
Figure 2. A single residue in S5 is involved in the species-specific differences in temperature sensitivity. (**A**) Sequence alignment of the fifth transmembrane domain (S5) of human and mouse TRPA1. The residues V875 (hTRPA1) and G878 (mTRPA1) underlying the species-specific differences in cold sensitivity are marked in red. (**B**) Representative whole-cell currents in Ca^{2+}-free intracellular and extracellular solutions recorded from a human embryonic kidney (HEK) 293T cell line transiently expressing the human-to-mouse mutation hTRPA1-V875G, measured by the indicated voltage-step protocol at different temperatures. Steady-state currents were measured at the end of the pulses, as indicated by colored symbols atop each record. Dashed lines indicate zero current. (**C**) Representative whole-cell currents of mouse-to-human mutation mTRPA1-G878V, as in (**B**). (**D**) Average conductance of hTRPA1-V875G obtained from voltage step protocols, as in (**B**). The data represent the means +SEM. (*n* = 7). The solid lines represent the best fit to a Boltzmann function, as described in Materials and Methods. The fit of hTRPA1 at 25 °C is included as grey dashed line for comparison. (**E**) Average conductance of mTRPA1-G878V obtained from voltage step protocols, as in (**C**). The data represent the means + SEM. (*n* = 4). The solid lines represent the best fit to a Boltzmann function, as described in Materials and methods. The fit of mTRPA1 at 25 °C is included as grey dashed line for comparison. (**F**) Deactivation kinetics of hTRPA1-V875G compared with hTRPA1 acquired at 25 °C (left) and 12 °C (right). Average tail currents normalized to the maximum amplitude at +100 mV, obtained as an indicated part of the voltage-induced currents, as in (**B**); dashed box. The average currents are shown with gray or blue bars that indicate means –SEM. (*n* = 5). (**G**) Arrhenius plots of fast deactivation time constants of hTRPA1-V875G (black squares). The linear regression (black line) is steeper than that of hTRPA1 (gray dashed line) and resembles that of mTRPA1 (gray open circles and gray line). Error bars are SEM. (*n* = 5). (**H**) Deactivation kinetics of mTRPA1-G878V mutant compared with mTRPA1 acquired at 25 °C (left) and 12 °C (right), as in (**C**). Error bars are SEM. (*n* = 4). (**I**) Arrhenius plots of fast deactivation time constants of mTRPA1-G878V (black circles). The linear regression (black line) is less steep than that of mTRPA1 (gray line), and its steepness resembles that of hTRPA1 (grey squares and gray dashed line). Error bars are SEM (*n* = 4).
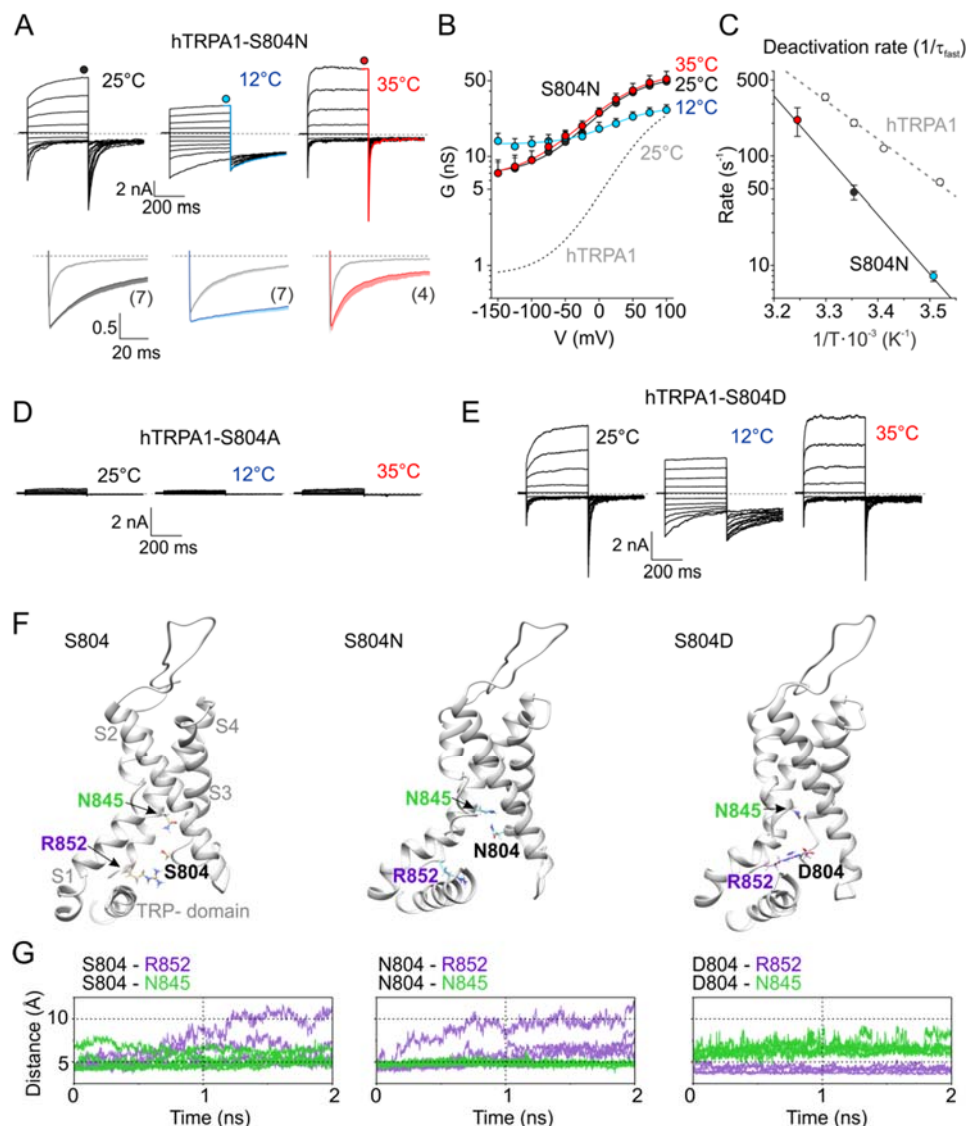
Figure 3. Functional screen for non-homologous residues in the vicinity of V875 identifies S804N as the most affected. (**A**) Representative whole-cell currents of mouse-to-human mutation mTRPA1-S804N obtained by voltage step protocol, as in Figure 1A. Below, the deactivation kinetics of S804N. Averaged tail currents normalized to the maximum amplitude at +100 mV (indicated by the circle above the record). The average currents are shown with color line and bars indicating means -SEM (number of cells indicated in parentheses). The gray lines with gray bars (-SEM) represent the averaged tail currents obtained from data for wild-type hTRPA1. Dashed lines indicate zero current. (**B**) Average conductance of hTRPA1-S804N obtained from voltage step protocols, as in (**A**). The data represent the means + SEM (*n* indicated in (**A**)). The solid lines represent the best fit to a Boltzmann function, as described in Materials and methods. The fit of hTRPA1 at 25 °C is included as grey dashed line for comparison. (**C**) Arrhenius plots of the fast deactivation time constants of hTRPA1-S804N (colored circles). The linear regression (black line) is steeper than hTRPA1 (gray dashed line). Error bars are ± SEM (*n* indicated in (**A**)). (**D,E**) Representative whole-cell currents of hTRPA1-S804A (**D**) or hTRPA1-S804D (**E**), obtained by voltage step protocol, as in (**A**). (**F**) Molecular dynamics (MD) simulation results obtained for wild-type TRPA1 (left), S804N (middle) and S804D (right). Snapshots from MD runs show the S1–S4 sensor domain and the TRP-like-box. (**G**) Time evolution of distances separating side chains at positions 804, 845 and 852 produced from MD simulations for all four subunits. Values lower than ~4 Å indicate the existence of inter-residue interactions (salt bridges and hydrogen bonds). Note that S804 alternates the interaction between R852 and N845. N804 prefers contact with N845, whereas D804 prefers contact with R852.

3.4. Molecular Modeling of the S804 Mutants

To explore the possible structural mechanism by which the substitutions at S804 produce such dramatic functional changes, we performed molecular simulations by using the structure of human TRPA1 (PDB code 3J9P) [31] completed with the S1–S2 and S2–S3 linkers [42,55]. The molecular dynamics (MD) run with the wild-type TRPA1 identified rather loose contacts between S804 and either R852 or N845 from S4 (Figure 3F,G). In contrast, the N804 side chain was involved in hydrogen bonding exclusively with N845, while the D804 side chain formed tight salt bridges with R852 in all monomers of the channel structure. The serine 804 was found to be a part of the lower cavity formed by the S1–S4 sensor domain, previously shown to be an important regulatory site of TRPA1, integrating the regions from the TRP-like domain, the S4–S5 linker, and S5 [42]. The results from our MD simulations thus reinforce the previous observations and highlight the key role of conserved polar residues comprising the putative lower crevice of the sensor domain in the integration of the activation signals and their transmission to the intracellular channel gate.

3.5. Modeling the Proximal C-Terminal Loop

V875 appears to be directly impacted by the proximal C-terminal loop (Y1006-Q1031) that follows the TRP-like helix and contains a short, predicted α-helix that is partly buried in the inner leaflet of the membrane (Figure S2). This loop is integrated with the pre-S1 region and, together with the S2–S3 linker, comprises an intracellular vestibule that forms a side 'fenestration' through which hydrophobic modulators and membrane phospholipids may affect channel gating [31]. Because the region Y1006-Q1031 is not well-resolved in the published cryo-EM structure [31], we used the molecular dynamics flexible fitting (MDFF) approach to refine fitting of the atomic structure to the density map and to gain an insight into the nature of the mechanical coupling within the channel. We found interactions between V875 and the subregion of the C-terminal loop L1019–F1022 with some variability in different TRPA1 monomers (Figure S4A,B). However, outside the area of the density with the predicted α-helix, the conformational promiscuity of the fitted protein chains was much more pronounced. This indicates rather loose contacts between this C-terminal segment and the remaining transmembrane core of TRPA1, which may be strengthened by the binding of various hydrophobic modulators.

To verify our structural model, we constructed and analyzed three reverse mutants based on the comparisons between rodent and primate TRPA1 sequences (Figure S2B): H1018R, ΔG1013 and G1027Q. The first residue was predicted to be located in close proximity to V875, whereas the latter two mutants seemed to have a good chance of reducing the conformational fluidity of the C-terminal region. We evaluated the temperature dependence of the steady-state conductance (Figure S4C–H) and of the faster, dominant component of the deactivation rate measured from the 'tail currents' following the repolarization from +200 to −70 mV (Figure S4I–K). The ΔG1013 and H1018R constructs had significantly ($p \leq 0.001$) faster deactivation kinetics in common at 13 °C ($58.3 \pm 3.2\,\text{s}^{-1}$ and $61.1 \pm 9.1\,\text{s}^{-1}$; $n = 4$ and 6) compared with wild-type hTRPA1 ($38.6 \pm 2.1\,\text{s}^{-1}$; $n = 20$). Within the 13–24 °C temperature range, the latter mutant exhibited slightly less steep temperature dependence ($61.1\,\text{kJ}\,\text{mol}^{-1}$) than hTRPA1 ($75.0\,\text{kJ}\,\text{mol}^{-1}$). G1027Q was not significantly different from wild-type hTRPA1, indicating that these residues are not key determinants of temperature sensitivity.

Previous studies have identified the C-terminal loop as a site for Ca^{2+}/calmodulin and phosphatidylinositol-4,5-bisphophate binding [54,56]. Mutations within this region affected TRPA1 responses induced by various stimuli including cinnamaldehyde, allyl isothiocyanate, voltage, Ca^{2+} and carvacrol. Thus, it seems most likely that the C-terminal loop serves as a universal regulatory domain that integrates signals from different parts of the protein, and its role in temperature sensitivity is not specific. This is further supported by the fact that introducing domain containing C-terminus of hTRPA1 did not affect cold activation of rodent TRPA1 [26].

3.6. Effects of Temperature on TRPA1 at a Constant Membrane Voltage

Our results indicate that hTRPA1 and mTRPA1 exhibit a dual warm and cold sensitivity that is apparent at negative membrane potentials (Figure 1B,D). This so-called U-shape thermosensitivity has been previously reported for purified hTRPA1 reconstituted into planar lipid bilayers [29], thus suggesting that the channel is inherently cold- and heat-sensitive. An allosteric eight-state model capable of replicating the U-shape thermosensitivity of thermal channels assumes that the channel possesses heat and voltage sensors allosterically coupled to the gate and to each other [39]. To explore the significance of the coupling energy between the voltage and temperature sensors, we measured currents at +80 mV by using increasing steps of temperature from 11 to ~50 °C in 3-second intervals (Figure 4A). Obviously, both TRPA1 orthologues exhibited U-shaped outward currents with a saddle point around the room temperature (Figure 4B). Though the hTRPA1-mediated currents were slightly shallower than those through mTRPA1, it was evident that the responses of the both channels were increased upon cooling and heating. Moreover, we reasoned that if the Arrhenius plot of the currents was extrapolated to even higher temperatures, TRPA1 could exhibit the properties of a heat-activated ion channel.
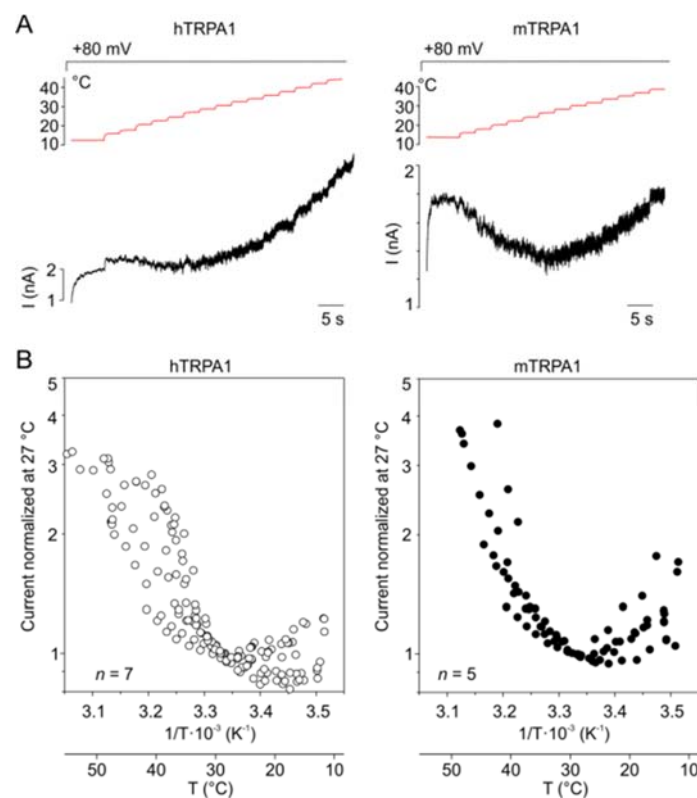
Figure 4. Both TRPA1 orthologues exhibited U-shaped outward currents. (**A**) Representative whole-cell currents of hTRPA1 (left) and mTRPA1 (right) elicited by the simultaneous activation of the voltage and temperature sensors at the holding potential of +80 mV and the temperature sensors by using increasing steps of temperature from ~11 to ~52 °C, as indicated above. (**B**) Arrhenius plots of currents normalized at 27 °C obtained from measurements, as in (**A**) for indicated (*n*) number of cells.

Therefore, we measured currents at −80 and +80 mV from hTRPA1 and mTRPA1 in a control bath solution by using temperature ramps from 25 to 60 °C that were applied at a maximum speed of about 35 °C/s in 1.5 s intervals (Figure 5A–C). Indeed, we observed specific heat-induced currents at negative and positive membrane potentials that were rapidly reversible and exhibited steep temperature dependence over the high temperature range of 53–59 °C for mTRPA1 and 55–57 °C for hTRPA1 (Figure S5). The heat-induced activation of mTRPA1 has been previously observed in sensory neurons

but not in non-neuronal cell lines, and it has thus been attributed to an indirect activation by some unknown mechanism [21]. Our data show that hTRPA1 and mTRPA1 can be directly, rapidly, and reversibly activated by noxious heat in non-neuronal cells, indicating that the both mammalian orthologues possess an intrinsic heat-sensing domain. The heat-induced currents measured at positive holding potentials were substantially greater than those at negative voltages, suggesting an allosteric mechanism of activation. Therefore, we next explored to what extent the allosteric coupling between the voltage- and heat-sensors may account for the observed variability in temperature responses.
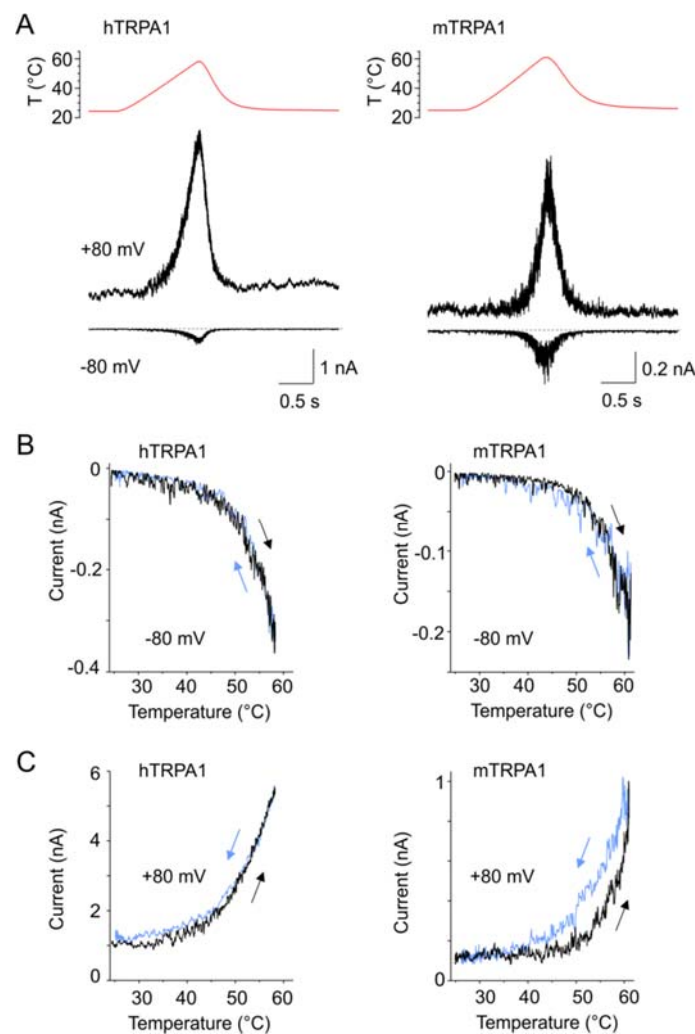
Figure 5. TRPA1 was directly and reversibly activated by heat at positive and negative membrane voltages. (**A**) Representative whole-cell currents of hTRPA1 (left) and mTRPA1 (right) activated by a temperature ramp (shown above the current traces) applied at a maximum speed of about 35 °C/s and at constant holding potentials +80 and −80 mV. (**B,C**) Currents measured at (**B**) −80 mV or (**C**) +80mV, as in (**A**), plotted as a function of temperature. The arrows indicate the direction of temperature increase (black) or decrease (blue). Note that the paths followed by activation and deactivation were almost identical, i.e., the activation–deactivation was accompanied by a low degree of hysteresis. Typical examples are shown for four (mTRPA1) and five (hTRPA1) similar recordings.

3.7. Interactions between Temperature- and Voltage-Sensor Modules

As evident from Figure 1A–F, the slower components of the activation and deactivation voltage-dependent characteristics of both TRPA1 orthologues could be substantially underestimated at cold temperatures over the time interval used for recording. To allow the channels to fully activate and relax back to equilibrium, we applied 10-s long depolarization pulses from −70 to +80 mV at a constant

cold temperature (~5–10 °C) and tested the effects of exposure to noxious (~60 °C) heat. When the temperature was stepped for ~5 s below 60 °C, the subsequent response to +80 mV did not significantly differ from the preceding one. However, if the heat step exceeded 60 °C, the subsequent response to +80 mV was much smaller, and the degree of reduction was strongly correlated to the maximum temperature applied (Figure 6A–D; Pearson correlation; $p = 0.0005$ and $p = 0.0003$ for hTRPA1 and mTRPA1; $n = 10$ and 19). Exposure to excessive heat thus seems to irreversibly impede either the activation of the voltage-sensor or its effective coupling to the gate.
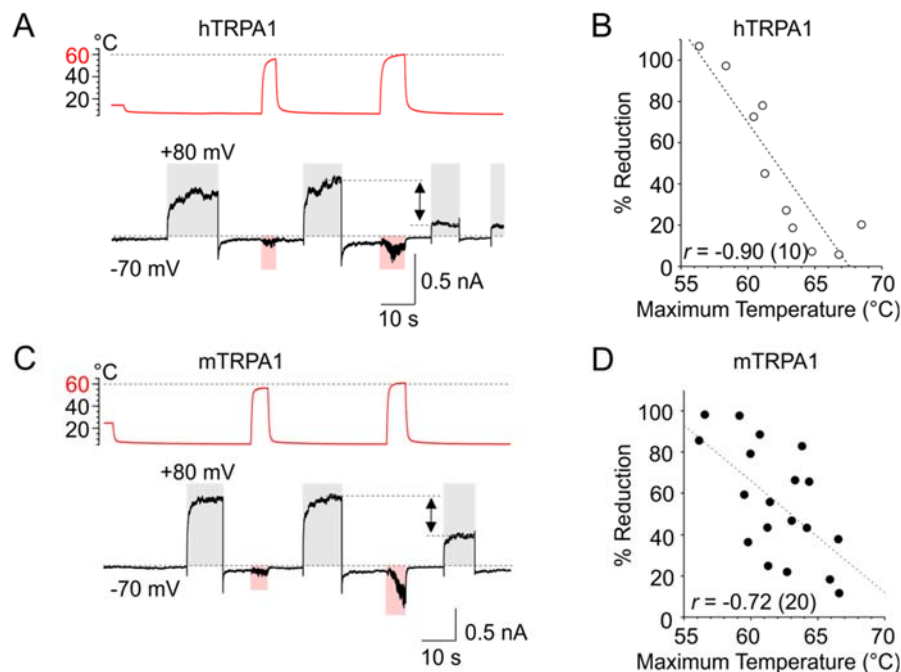
Figure 6. Temperatures above, but not below, 60 °C impede voltage-induced activation. (**A**) Representative whole-cell currents of hTRPA1 in response to temperature (shaded pink area) and voltage (shaded grey area) steps. The temperature trace is shown above the records. Repetitive depolarization from −70 to +80 mV elicited outward currents that were strongly reduced only if the heat step exceeded 60 °C. The time course of temperature changes (from 6 to 56 °C and then to 61 °C) is indicated above the record. The reduction is marked by arrow. (**B**) The degree of the reduction of voltage-induced currents was strongly correlated to the maximum temperature applied. (**C**) Representative whole-cell currents of mTRPA1 treated as in (**A**). (**D**) The current reduction of mTRPA1 was strongly correlated to the maximum temperature applied. The number of cells is indicated in brackets for each orthologue.

Most notably, when the channels were concurrently exposed to depolarization along with noxious heat above 60 °C, we observed strikingly large inward currents after cooling the cells to 5–8 °C and subsequent repolarization to −70 mV (Figure 7A–F). The cold-sensitized inward currents were produced independently of whether depolarization or heat was applied prior to the concurrent activation of both sensors (Figure 7E), but these currents were not seen after the heat- or voltage-sensors were individually activated/deactivated (Figure 7A,C,E,F). Similar cold-sensitized inward currents were observed in hTRPA1 and mTRPA1, as well as in the reverse mutants with slowed activation/deactivation kinetics (hTRPA1-S804D and mTRPA1-N807S; Figure S6).
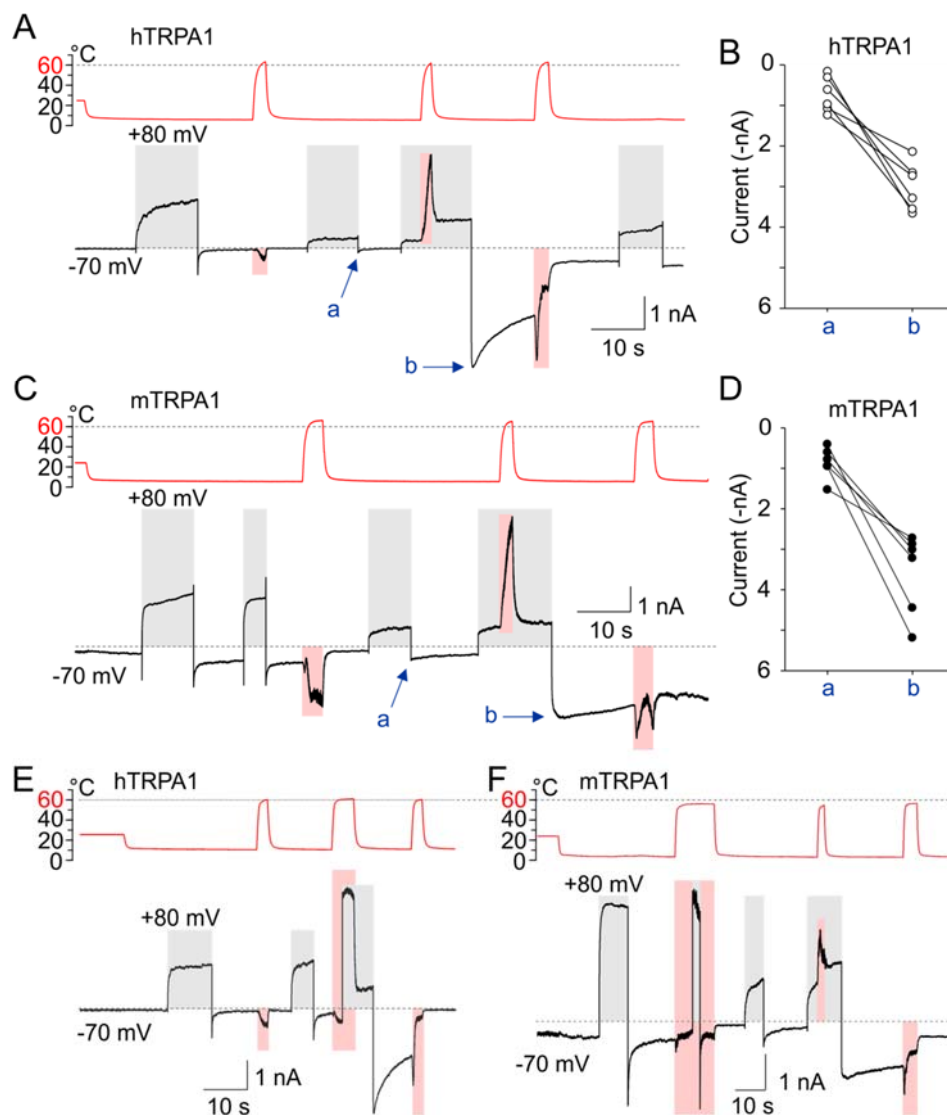
Figure 7. Concurrent activation of voltage- and heat-sensor renders the TRPA1 channel cold-sensitive. (**A**) Representative whole-cell currents of hTRPA1 in response to temperature (shaded pink area) and voltage (shaded grey area) steps. The temperature trace is shown above the records. The current-to-temperature relationship of the first heat response is shown in Figure S8A,B. Exposure to depolarization concurrently with excessive heat rendered the TRPA1 channels dramatically cold-activated (arrow b) once back at negative membrane potentials, as compared to inward current (arrow a) after exposure to only depolarization. (**B**) The increase in inward currents for individual cells expressing hTRPA1 (*n* = 6), measured at times indicated by arrows in (**A**). (**C**) Representative whole-cell currents of mTRPA1 treated like those in (**A**). (**D**) The increase in currents for six individual cells expressing mTRPA1 measured at times indicated by the arrows in (**C**). (**E**) Representative whole-cell currents of hTRPA1 treated similarly to those in (**A**). The cold-induced inward currents were produced independently of whether depolarization or heat was applied prior to the concurrent activation of both sensors. (**F**) Representative whole-cell currents of mTRPA1 treated similarly to those in (**A**). Note the difference in inward current after depolarization during noxious heat exposure or after noxious heat exposure during depolarization.

The inverted coupling hypothesis proposed by Jara-Oseguera and Islas [39] states that activation of thermosensitive TRP channels by cooling could be mediated by a heat-activated temperature sensor that is energetically unfavorably coupled to the pore gating. Similarly, voltage-gated channels can be activated either by depolarization or hyperpolarization, depending on whether their voltage sensors

are coupled favorably or unfavorably to the gate [57]. Our results indicated that noxious heat above 60 °C induces substantial structural rearrangements within the channel, leading to a strong inward rectification at cold temperatures. We therefore reasoned that the above hypothesis could be adopted to explain our observations, providing that either the heat- and/or voltage-sensors become unfavorably coupled to the gate as a consequence of the exposure to excessive heat.

3.8. Can the Temperature Sensitivity of TRPA1 Be Explained by Inverted Coupling Hypothesis?

We performed simulations by using the eight-state allosteric kinetic model that had previously been shown to be consistent with the gating of the TRPA1-related channels, TRPV1 and TRPM8 [36,39]. This model is based on the presumption that an independent voltage- and heat-sensors exist that are coupled to the channel gate and to each other (Figure 8A). At constant low temperatures and low voltages, the channel is confined to the equilibrium between closed and open states with an equilibrium constant L. The temperature dependence is characterized by the difference in enthalpy (ΔH^o) and entropy (ΔS^o) between the states. Temperature and voltage drive transitions between resting and activated states of the sensors with equilibrium constants $J(T)$ and $K(V)$, respectively. In turn, the temperature and voltage sensors are coupled to channel gating by allosteric coupling factors C and D, and the two sensors are coupled by the allosteric constant E. To involve the bidirectional thermosensitivity of the channels, the allosteric coupling factor C was assumed to be temperature-dependent: $C(T) = \exp[-(\Delta H^o{}_C - T\Delta S^o{}_C)/RT]$.

Using the parameters published for TRPM8 [39] as the initial values, we estimated $K(0)$, L, E, D, z, $\Delta H^o{}_C$ and $\Delta S^o{}_C$ by fitting the average G/V curves obtained for hTRPA1 at 25 and 12 °C (Figure 8B). These parameters were then refitted to qualitatively match the activation profile of a representative hTRPA1 recording, such as that shown in Figure 7A, normalized to G_{max}. We calculated the open probability (P_o) as a function of voltage and temperature and plotted the $P_o(V,T)$ landscapes (Figure 8C–E). We found that the model was capable of capturing all of the essential aspects of our experimental observations (Figure 8F):

1. Initially, voltage-dependent activation was only mildly temperature-dependent over the temperature range of 12–35 °C, and cold only weakly activated the channels at negative membrane potentials.
2. The channels were activated by high noxious temperatures, and the heat-induced responses were strongly outwardly rectifying (as shown in Figure 5).
3. Exposure to excessive heat (>60 °C) irreversibly reduced subsequent responses to depolarizing potentials. This could be achieved by a strong (72.5-fold) increase in the coupling factor E, a 1.4-fold increase in the relative magnitude of the enthalpy and entropy values of the allosteric factor C, $\Delta H^o{}_C/\Delta S^o{}_C$, a 10-fold decrease in the gating equilibrium L, and a 1.07-fold decrease in the coupling factor D (Figure 8D).
4. The channels became strongly inwardly rectifying after the concurrent activation of voltage and heat sensors and their subsequent deactivation. This could be simulated by an increase in L (271.9-fold) and E (5.27-fold), a decrease in the relative magnitude of the temperature sensor's enthalpy and entropy values ($\Delta H^o/\Delta S^o$, 2.1-fold), and the relative magnitude of the enthalpy and entropy values characterizing the allosteric factor C ($\Delta H^o{}_C/\Delta S^o{}_C$, 2.0-fold), and a large (32,733-fold) decrease in D (Figure 8E).
5. The responses activated during heating typically exhibited current transients, suggesting that the channels passed through several conformational states before they reached their steady-state (Figure 8F,G). This further supports the modular allosteric model (rather than the two-state model) as an appropriate approximation of TRPA1 activation.
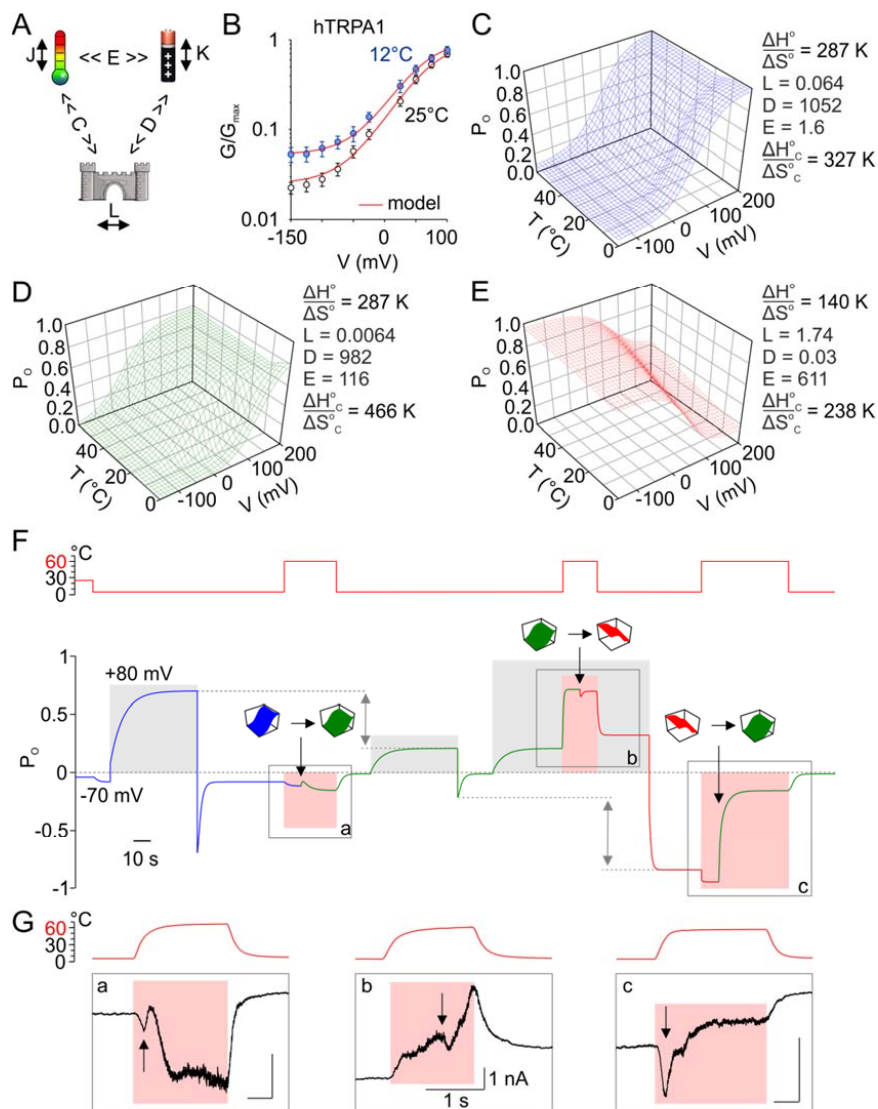
Figure 8. The eight-state allosteric model is adequate for explaining the variability in TRPA1 temperature responsiveness. (**A**) Allosteric model for temperature- and voltage-dependent activation of TRPA1. The transitions between open and closed states are given by the intrinsic equilibrium constant *L*. The transitions between resting and active conformations of temperature sensors and voltage sensors are given by equilibrium constants $J(T) = \exp[-(\Delta H - T\Delta S)/RT]$ and $K = K(0)\exp(zFV/RT)$, respectively. The coupling of the voltage sensor to the channel gate and to the temperature sensor is governed by the allosteric coupling constants *D* and *E*, which are assumed to be temperature-independent. The coupling of temperature sensor to the channel opening is assumed to be temperature-dependent by the term $C(T) = \exp[-(\Delta H^{o}_{C} - T\Delta S^{o}_{C})/RT]$. (**B**) Normalized conductance of hTRPA1 (same as in Figure 1B) at the indicated temperatures. Red lines are the global fit by using the model in (**A**). Parameters of the fit were used to plot open probability landscape in (**C**); for details, see Materials and Methods. (**C**) Open probability landscape obtained by calculating P_{o} as a function of temperature and voltage by using the parameters from fit in (**B**): $K(0) = 0.003$, $z = -0.74$, $\Delta H^{o}_{C} = 6.1$ kcal mol^{-1} and value $\Delta H = 91$ kcal mol^{-1} published for TRPM8 [39]. Note a mild U-shape thermosensitivity. (**D**) 'Irreversible switch-after-excessive heat' mechanism. Exposure to heat over 60 °C triggers the reduction of currents at +80 mV (as in Figure 6A,C). Open probability landscape was remodeled to qualitatively match the activation profile of hTRPA1, as shown in Figure 7A. The parameters $K(0)$, z and ΔH^{o} were preserved from blue P_{o} landscape in (**C**), $\Delta H^{o}_{C} = 1.4$ kcal mol^{-1}. (**E**) Concurrent activation of voltage- and heat-sensor rendered TRPA1 sensitized to cold. The open probability landscape obtained in (**D**) was

remodeled to approximate the experimentally observed data. The parameters $K(0)$, z and ΔH^o were preserved from blue P_o landscape in (**C**), $\Delta H^o_C = 4.3$ kcal mol^{-1}. (**F**) The model is capable of capturing all essential aspects of our observations. The time course of P_o modelled according to Figure 7A. The blue, green and red parts of the P_o trace were modelled by using the respective parameters from (**B,D,E**). The transitions between landscapes are indicated by black arrows and colored pictograms. The depolarizations to +80 mV are marked as shaded grey areas, and the applied temperature is shown above as red trace and shaded pink areas for 60 °C. Grey bidirectional arrows show the reduction of P_o (as in Figure 6A,C) after the first exposure to heat at −70 mV, and the increase in P_o (as in Figure 7A) after the second exposure to heat at +80 mV. Grey rectangles marked as a, b and c, correspond to panels in (**G**). (**G**) Representative whole-cell currents of mTRPA1 in response to noxious heat temperature. The situations correspond to those in (**F**), and the holding potential was −70 mV in a and c and +80 mV in b. Black arrows point to current transients that were captured also by our model in (**F**). The time course of temperature is indicated above the records. The bars indicate 1 s and 1 nA in panels a, b, and c.

3.9. Activation of TRPA1 in F11 Cells

To investigate whether TRPA1 can be activated by heat and cold under close-to-native conditions, we used F11 neuroblastoma cells derived from dorsal root ganglia neurons, which provide a well-characterized cellular model of peripheral sensory neurons [58]. We transfected the cells with mouse or human TRPA1 and measured currents at −70 mV by using a similar temperature and voltage protocol to that shown in Figure 7A. In addition, the TRPA1 inhibitor HC-030031 (50 μM) was used to assess the extent of specific contribution of TRPA1 to temperature-dependent currents. We observed very similar current characteristics to those seen in channels expressed in HEK293T cells. Though the application of heat above 60 °C was experimentally challenging and inevitably destroyed the seal in many cells (19 of 29), we succeeded in recording the typical responses to heat and voltage in eight neurons that expressed mTRPA1 and two neurons expressing hTRPA1 (Figure S7). In both TRPA1 orthologues, we observed a reduction in currents induced by depolarizing step to +80 mV only when the preceding heat step exceeded 60 °C. The responses activated during heating typically exhibited current transients, suggesting that the channels passed through several conformational states, as in HEK293T cells (see Figure 8G). When the neurons were depolarized and concurrently stimulated by noxious heat, inward currents arising from cooling the cell to 5–7 °C and repolarizing it to −70 mV were increased (Figure S7B) and slowed down (Figure S7A,C).

In a large subset of native dorsal root ganglia neurons, TRPA1 physically and functionally interacts with the structurally-related, heat-sensitive vanilloid receptor subtype 1 channel TRPV1 [59]. Our results indicate that TRPA1 may respond to heat in isolation from TRPV1, which adds further complexity to the mechanisms that contribute to noxious heat transduction in somatosensory neurons.

4. Discussion

The data presented in this study demonstrate that both human and mouse TRPA1 orthologues have an intrinsic propensity to respond to excessive heat and adopt conformations primed for cold activation at physiological membrane potentials. Most importantly, our results unveil a specific mode of TRPA1 activation that can be viewed as a 'heat-induced cold sensitivity.' This transition occurs after the channels are activated simultaneously by depolarizing voltage and high noxious heat and then are subsequently repolarized to the resting membrane potential at cold temperatures.

Our experimental observations indicate that excessive heat renders the channels less activated by voltage. As predicted from the eight-state allosteric model, heat above 60 °C may affect the gating equilibrium constant—the extent of allosteric coupling of the voltage- and heat-sensors to the gate domain and to each other. When the two stimuli, heat and voltage, were applied together, the channels became strongly sensitized to cold. Our simulations predict that the concurrent activation of the voltage- and heat-sensors can induce a conformational switch that leads to an increase in their energetic crosstalk, an increase in the gating equilibrium constant, and a drastic (~30,000-fold) decrease in the coupling of the voltage sensor to the channel gate.

Substantial differences in the pharmacological profiles between rodent and primate orthologues seriously hamper current screening and medicinal chemistry discovery efforts for targeting TRPA1 [60,61]. Moreover, the distinct temperature sensitivities of these channels raise important questions about the physiological relevance of all the findings obtained in rodent models. Our findings that both TRPA1 orthologues exhibit qualitatively similar temperature- and voltage-dependent characteristics suggest a conserved molecular logic for the gating of TRPA1 across different species and may reconcile the seemingly conflicting lines of evidence in published literature. At negative membrane potentials (−150 mV) and at 25 °C, the gating equilibrium of mTRPA1 is shifted toward the open state (11.4% of G_{max}) when compared with hTRPA1 (2.3%) (Figure 1B,D). From our predictions (using the parameters in Figure 8C while only changing *L*), this difference may lead to a 3–4-fold increase in responses induced by both heat (60 °C) and cold (5 °C) at −70 mV. Thus, the difference in the intrinsic gating equilibrium itself may account for the observed disparity between the two orthologues.

Moreover, hTRPA1 exhibits significantly faster deactivation kinetics that consist of two exponential components, one of these of a similar temperature dependence as mTRPA1 (Figure 1F). The slower voltage-dependent relaxation kinetics seen in mTRPA1 and in certain mutants of hTRPA1 (hTRPA1-S804D and S804N) allows these channels to dwell longer in the open state(s) at cold temperatures and, thus, produce significant and persistent currents at negative membrane potentials. This, together with the high sequence similarity (88.9% similarity and 79.8% identity), indicates that the difference between the two mammalian TRPA1 orthologues might lie not in their temperature- or voltage-sensing domains but rather in the mechanisms by which they are coupled to the channel gate and/or to each other. As TRPA1 acts as a heat-sensing ion channel in most species that were tested so far, the heat-sensitive domain could have been conserved during evolution while the evolutionary changes could serve to fine-tune its energetic coupling to the pore gate and/or the voltage-sensitive domain. From this point of view, it would be important to explore the temperature sensitivity of clones from various species under identical experimental conditions and, particularly, over as wide as possible a temperature range.

Since the first cloning and characterization in 2003 by Ardem Patapoutian's group [13], the mouse TRPA1 has been considered to be cold-activated. Fifteen years later, its role in heat (45 °C) detection was also convincingly shown, although it was assumed that the heat responsiveness depends on the cellular environment [21]. Our results do not contradict these observations and identify both the human and mouse TRPA1 as molecular detectors of noxious heat and noxious cold. The bidirectional thermosensitivity of hTRPA1 was previously reported in [29]. Interestingly, the authors also noticed that in the presence of nonelectrophilic agonist carvacrol, the channels respond to cold only when they are pre-exposed to a warm (~37 °C) temperature. We have shown that the cold sensitivity of hTRPA1 and mTRPA1 can be triggered after the co-application of noxious heat together with depolarizing voltage. Thus, various sources of energy, such as that derived from agonist binding or depolarization, could drive the channel opening by cooling. The fact that the cold-sensitized channels are typically inhibited by heat suggests that their temperature sensors might be activated by heating while being inversely coupled to the channel opening.

In human TRPA1, a 'gain-of-function' variant (rs398123010) associated with pathological cold pain has been identified [18]. In vitro, this missense variant, hTRPA1-N855S, induced a ~5-fold increase in inward currents upon activation by cold and was accompanied by a negative shift of the voltage dependence of channel activation compared with wild-type hTRPA1. This residue is located in the S4–S5 linker, which is a critical domain that impacts the TRP-like helix and the S5 region around V875. Apparently, mutations within the S4–S5 linker and the lower cavity of the sensor domain have dramatic effects on the gating equilibrium and/or the response to voltage [34]. Conformational changes in this allosteric nexus may propagate to the TRP-like domain, affect the process of α–π transition in S6 [62], and ultimately lead to a reduction or increase in free energy required to shift the channel gate from the closed to the open state. Interestingly, the superposition of the TRPA1 (closed) structure with the recently published open-state structure of TRPV3 obtained at 37 °C [63] has shown a very good

overlap within the S6 and the TRP-like domain. Thus, it is possible that the overall gating mechanism of thermosensitive TRP channels may be shared. During the review process, a structural study on TRPA1 was published identifying a direct interaction between N855 and the backbone carbonyl of C1024 from a short predicted C-terminal α-helix located at the cytosol-membrane interface near S1 and S4 of the sensor domain [64]. The findings support our previous predictions [56] and may partly explain our data presented in Figure S4.

Though more experimental support is required to unveil the exact molecular mechanism of the temperature-dependent activation of TRPA1, our data suggest the existence of a heat-sensitive domain in both human and mouse orthologues. The maximum slope of the temperature dependence of the responses induced by a heat-step protocol (Figure S8) was apparently higher than that obtained by heat ramps (Figure S5). Though the apparent Q_{10} reflects complex effects of temperature on channel gating kinetics and the applicability of such characteristics is limited [65,66], this observation is reminiscent to what has been recently described for the related channel TRPV3 [67]. If the rate of transition between the closed and open states of the channel is primarily driven by temperature, the direct measurement of the activation enthalpy would require a temperature stimulator that enabled the exchange of temperature at a very high speed (55 °C/ms). Most likely, the slower rate of the temperature exchange (~35 °C/s) compared to faster temperature steps (~110 °C/s) allowed the activated channels to transition to the state with a reduced energetics of gating. There is also no doubt that the speed of temperature exchange may be another source of variability among various reports (e.g., see [23]).

References

1. Kang, K.; Pulver, S.R.; Panzano, V.C.; Chang, E.C.; Griffith, L.C.; Theobald, D.L.; Garrity, P.A. Analysis of Drosophila TRPA1 reveals an ancient origin for human chemical nociception. *Nature* **2010**, *464*, 597–600. [CrossRef] [PubMed]

2. Arenas, O.M.; Zaharieva, E.E.; Para, A.; Vasquez-Doorman, C.; Petersen, C.P.; Gallio, M. Activation of planarian TRPA1 by reactive oxygen species reveals a conserved mechanism for animal nociception. *Nat. Neurosci.* **2017**, *20*, 1686–1693. [CrossRef] [PubMed]

3. Viana, F. TRPA1 channels: Molecular sentinels of cellular stress and tissue damage. *J. Physiol.* **2016**, *594*, 4151–4169. [CrossRef] [PubMed]

4. Cordero-Morales, J.F.; Gracheva, E.O.; Julius, D. Cytoplasmic ankyrin repeats of transient receptor potential A1 (TRPA1) dictate sensitivity to thermal and chemical stimuli. *Proc. Natl. Acad. Sci. USA* **2011**, *108*, E1184–E1191. [CrossRef]

5. Gracheva, E.O.; Bagriantsev, S.N. Evolutionary adaptation to thermosensation. *Curr. Opin. Neurobiol.* **2015**, *34*, 67–73. [CrossRef]

6. Saito, S.; Saito, C.T.; Nozawa, M.; Tominaga, M. Elucidating the functional evolution of heat sensors among Xenopus species adapted to different thermal niches by ancestral sequence reconstruction. *Mol. Ecol.* **2019**, *28*, 3561–3571. [CrossRef]

7. Gracheva, E.O.; Ingolia, N.T.; Kelly, Y.M.; Cordero-Morales, J.F.; Hollopeter, G.; Chesler, A.T.; Sanchez, E.E.; Perez, J.C.; Weissman, J.S.; Julius, D. Molecular basis of infrared detection by snakes. *Nature* **2010**, *464*, 1006–1011. [CrossRef]

8. Kohno, K.; Sokabe, T.; Tominaga, M.; Kadowaki, T. Honey bee thermal/chemical sensor, AmHsTRPA, reveals neofunctionalization and loss of transient receptor potential channel genes. *J. Neurosci.* **2010**, *30*, 12219–12229. [CrossRef]

9. Kang, K.; Panzano, V.C.; Chang, E.C.; Ni, L.; Dainis, A.M.; Jenkins, A.M.; Regna, K.; Muskavitch, M.A.; Garrity, P.A. Modulation of TRPA1 thermal sensitivity enables sensory discrimination in Drosophila. *Nature* **2011**, *481*, 76–80. [CrossRef]

10. Saito, S.; Nakatsuka, K.; Takahashi, K.; Fukuta, N.; Imagawa, T.; Ohta, T.; Tominaga, M. Analysis of transient receptor potential ankyrin 1 (TRPA1) in frogs and lizards illuminates both nociceptive heat and chemical sensitivities and coexpression with TRP vanilloid 1 (TRPV1) in ancestral vertebrates. *J. Biol. Chem.* **2012**, *287*, 30743–30754. [CrossRef]

11. Saito, S.; Banzawa, N.; Fukuta, N.; Saito, C.T.; Takahashi, K.; Imagawa, T.; Ohta, T.; Tominaga, M. Heat and noxious chemical sensor, chicken TRPA1, as a target of bird repellents and identification of its structural determinants by multispecies functional comparison. *Mol. Biol. Evol.* **2014**, *31*, 708–722. [CrossRef] [PubMed]

12. Saito, S.; Tominaga, M. Functional diversity and evolutionary dynamics of thermoTRP channels. *Cell Calcium* **2015**, *57*, 214–221. [CrossRef] [PubMed]

13. Story, G.M.; Peier, A.M.; Reeve, A.J.; Eid, S.R.; Mosbacher, J.; Hricik, T.R.; Earley, T.J.; Hergarden, A.C.; Andersson, D.A.; Hwang, S.W.; et al. ANKTM1, a TRP-like channel expressed in nociceptive neurons, is activated by cold temperatures. *Cell* **2003**, *112*, 819–829. [CrossRef]

14. Viswanath, V.; Story, G.M.; Peier, A.M.; Petrus, M.J.; Lee, V.M.; Hwang, S.W.; Patapoutian, A.; Jegla, T. Opposite thermosensor in fruitfly and mouse. *Nature* **2003**, *423*, 822–823. [CrossRef]

15. Bandell, M.; Story, G.M.; Hwang, S.W.; Viswanath, V.; Eid, S.R.; Petrus, M.J.; Earley, T.J.; Patapoutian, A. Noxious cold ion channel TRPA1 is activated by pungent compounds and bradykinin. *Neuron* **2004**, *41*, 849–857. [CrossRef]

16. Kwan, K.Y.; Allchorne, A.J.; Vollrath, M.A.; Christensen, A.P.; Zhang, D.S.; Woolf, C.J.; Corey, D.P. TRPA1 contributes to cold, mechanical, and chemical nociception but is not essential for hair-cell transduction. *Neuron* **2006**, *50*, 277–289. [CrossRef]

17. Karashima, Y.; Talavera, K.; Everaerts, W.; Janssens, A.; Kwan, K.Y.; Vennekens, R.; Nilius, B.; Voets, T. TRPA1 acts as a cold sensor in vitro and in vivo. *Proc. Natl. Acad. Sci. USA* **2009**, *106*, 1273–1278. [CrossRef]

18. Kremeyer, B.; Lopera, F.; Cox, J.J.; Momin, A.; Rugiero, F.; Marsh, S.; Woods, C.G.; Jones, N.G.; Paterson, K.J.; Fricker, F.R.; et al. A gain-of-function mutation in TRPA1 causes familial episodic pain syndrome. *Neuron* **2010**, *66*, 671–680. [CrossRef]

19. Hoffmann, T.; Kistner, K.; Miermeister, F.; Winkelmann, R.; Wittmann, J.; Fischer, M.J.; Weidner, C.; Reeh, P.W. TRPA1 and TRPV1 are differentially involved in heat nociception of mice. *Eur. J. Pain* **2013**, *17*, 1472–1482. [CrossRef]

20. Yarmolinsky, D.A.; Peng, Y.; Pogorzala, L.A.; Rutlin, M.; Hoon, M.A.; Zuker, C.S. Coding and Plasticity in the Mammalian Thermosensory System. *Neuron* **2016**, *92*, 1079–1092. [CrossRef]

21. Vandewauw, I.; De Clercq, K.; Mulier, M.; Held, K.; Pinto, S.; Van Ranst, N.; Segal, A.; Voet, T.; Vennekens, R.; Zimmermann, K.; et al. A TRP channel trio mediates acute noxious heat sensing. *Nature* **2018**, *555*, 662–666. [CrossRef] [PubMed]

22. Del Camino, D.; Murphy, S.; Heiry, M.; Barrett, L.B.; Earley, T.J.; Cook, C.A.; Petrus, M.J.; Zhao, M.; D'Amours, M.; Deering, N.; et al. TRPA1 contributes to cold hypersensitivity. *J. Neurosci.* **2010**, *30*, 15165–15174. [CrossRef] [PubMed]

23. Sawada, Y.; Hosokawa, H.; Hori, A.; Matsumura, K.; Kobayashi, S. Cold sensitivity of recombinant TRPA1 channels. *Brain Res.* **2007**, *1160*, 39–46. [CrossRef] [PubMed]

24. Jordt, S.E.; Bautista, D.M.; Chuang, H.H.; McKemy, D.D.; Zygmunt, P.M.; Hogestatt, E.D.; Meng, I.D.; Julius, D. Mustard oils and cannabinoids excite sensory nerve fibres through the TRP channel ANKTM1. *Nature* **2004**, *427*, 260–265. [CrossRef]

25. Zurborg, S.; Yurgionas, B.; Jira, J.A.; Caspani, O.; Heppenstall, P.A. Direct activation of the ion channel TRPA1 by Ca^{2+}. *Nat. Neurosci.* **2007**, *10*, 277–279. [CrossRef]

26. Chen, J.; Kang, D.; Xu, J.; Lake, M.; Hogan, J.O.; Sun, C.; Walter, K.; Yao, B.; Kim, D. Species differences and molecular determinant of TRPA1 cold sensitivity. *Nat. Commun.* **2013**, *4*, 2501. [CrossRef]

27. Knowlton, W.M.; Bifolck-Fisher, A.; Bautista, D.M.; McKemy, D.D. TRPM8, but not TRPA1, is required for neural and behavioral responses to acute noxious cold temperatures and cold-mimetics in vivo. *Pain* **2010**, *150*, 340–350. [CrossRef]

28. Jabba, S.; Goyal, R.; Sosa-Pagan, J.O.; Moldenhauer, H.; Wu, J.; Kalmeta, B.; Bandell, M.; Latorre, R.; Patapoutian, A.; Grandl, J. Directionality of temperature activation in mouse TRPA1 ion channel can be inverted by single-point mutations in ankyrin repeat six. *Neuron* **2014**, *82*, 1017–1031. [CrossRef]

29. Moparthi, L.; Kichko, T.I.; Eberhardt, M.; Hogestatt, E.D.; Kjellbom, P.; Johanson, U.; Reeh, P.W.; Leffler, A.; Filipovic, M.R.; Zygmunt, P.M. Human TRPA1 is a heat sensor displaying intrinsic U-shaped thermosensitivity. *Sci. Rep.* **2016**, *6*, 28763. [CrossRef]

30. Xiao, B.; Dubin, A.E.; Bursulaya, B.; Viswanath, V.; Jegla, T.J.; Patapoutian, A. Identification of transmembrane domain 5 as a critical molecular determinant of menthol sensitivity in mammalian TRPA1 channels. *J. Neurosci.* **2008**, *28*, 9640–9651. [CrossRef]

31. Paulsen, C.E.; Armache, J.P.; Gao, Y.; Cheng, Y.; Julius, D. Structure of the TRPA1 ion channel suggests regulatory mechanisms. *Nature* **2015**, *520*, 511–517. [CrossRef] [PubMed]

32. Meents, J.E.; Fischer, M.J.; McNaughton, P.A. Agonist-induced sensitisation of the irritant receptor ion channel TRPA1. *J. Physiol.* **2016**. [CrossRef] [PubMed]

33. De la Roche, J.; Eberhardt, M.J.; Klinger, A.B.; Stanslowsky, N.; Wegner, F.; Koppert, W.; Reeh, P.W.; Lampert, A.; Fischer, M.J.; Leffler, A. The molecular basis for species-specific activation of human TRPA1 protein by protons involves poorly conserved residues within transmembrane domains 5 and 6. *J. Biol. Chem.* **2013**, *288*, 20280–20292. [CrossRef] [PubMed]

34. Zima, V.; Witschas, K.; Hynkova, A.; Zimova, L.; Barvik, I.; Vlachova, V. Structural modeling and patch-clamp analysis of pain-related mutation TRPA1-N855S reveal inter-subunit salt bridges stabilizing the channel open state. *Neuropharmacology* **2015**, *93*, 294–307. [CrossRef] [PubMed]

35. Voets, T.; Droogmans, G.; Wissenbach, U.; Janssens, A.; Flockerzi, V.; Nilius, B. The principle of temperature-dependent gating in cold- and heat-sensitive TRP channels. *Nature* **2004**, *430*, 748–754. [CrossRef]

36. Brauchi, S.; Orio, P.; Latorre, R. Clues to understanding cold sensation: Thermodynamics and electrophysiological analysis of the cold receptor TRPM8. *Proc. Natl. Acad. Sci. USA* **2004**, *101*, 15494–15499. [CrossRef]

37. Matta, J.A.; Ahern, G.P. Voltage is a partial activator of rat thermosensitive TRP channels. *J. Physiol.* **2007**, *585*, 469–482. [CrossRef]

38. Yao, J.; Liu, B.; Qin, F. Kinetic and energetic analysis of thermally activated TRPV1 channels. *Biophys. J.* **2010**, *99*, 1743–1753. [CrossRef]

39. Jara-Oseguera, A.; Islas, L.D. The role of allosteric coupling on thermal activation of thermo-TRP channels. *Biophys. J.* **2013**, *104*, 2160–2169. [CrossRef]

40. Salazar, M.; Moldenhauer, H.; Baez-Nieto, D. Could an allosteric gating model explain the role of TRPA1 in cold hypersensitivity? *J. Neurosci.* **2011**, *31*, 5554–5556. [CrossRef]

41. Dittert, I.; Benedikt, J.; Vyklicky, L.; Zimmermann, K.; Reeh, P.W.; Vlachova, V. Improved superfusion technique for rapid cooling or heating of cultured cells under patch-clamp conditions. *J. Neurosci. Methods* **2006**, *151*, 178–185. [CrossRef] [PubMed]

42. Zimova, L.; Sinica, V.; Kadkova, A.; Vyklicka, L.; Zima, V.; Barvik, I.; Vlachova, V. Intracellular cavity of sensor domain controls allosteric gating of TRPA1 channel. *Sci. Signal.* **2018**, *11*. [CrossRef] [PubMed]

43. Jorgensen, W.L.; Chandrasekhar, J.; Madura, J.D.; Impey, R.W.; Klein, M.L. Comparison of Simple Potential Functions for Simulating Liquid Water. *J. Chem. Phys.* **1983**, *79*, 926–935. [CrossRef]

44. Humphrey, W.; Dalke, A.; Schulten, K. VMD: Visual molecular dynamics. *J. Mol. Graph.* **1996**, *14*, 33–38. [CrossRef]

45. Beglov, D.; Roux, B. Finite Representation of an Infinite Bulk System - Solvent Boundary Potential for Computer-Simulations. *J. Chem. Phys.* **1994**, *100*, 9050–9063. [CrossRef]

46. Schlenkrich, M.; Brickmann, J.; MacKerell, J.A.D.; Karplus, M. An Empirical Potential Energy Function for Phospholipids: Criteria for Parameter Optimization and Applications. In *Biological Membranes: A Molecular Perspective from Computation and Experiment*; Roux, K.M.M.A.B., Ed.; Birkhauser Boston: Boston, MA, USA, 1996; pp. 31–81.

47. MacKerell, A.D.; Bashford, D.; Bellott, M.; Dunbrack, R.L.; Evanseck, J.D.; Field, M.J.; Fischer, S.; Gao, J.; Guo, H.; Ha, S.; et al. All-atom empirical potential for molecular modeling and dynamics studies of proteins. *J. Phys. Chem. B* **1998**, *102*, 3586–3616. [CrossRef] [PubMed]

48. Phillips, J.C.; Braun, R.; Wang, W.; Gumbart, J.; Tajkhorshid, E.; Villa, E.; Chipot, C.; Skeel, R.D.; Kale, L.; Schulten, K. Scalable molecular dynamics with NAMD. *J. Comput. Chem.* **2005**, *26*, 1781–1802. [CrossRef]

49. Roe, D.R.; Cheatham, T.E. PTRAJ and CPPTRAJ: Software for Processing and Analysis of Molecular Dynamics Trajectory Data. *J. Chem. Theory Comput.* **2013**, *9*, 3084–3095. [CrossRef]

50. Trabuco, L.G.; Villa, E.; Mitra, K.; Frank, J.; Schulten, K. Flexible fitting of atomic structures into electron microscopy maps using molecular dynamics. *Structure* **2008**, *16*, 673–683. [CrossRef]

51. Trabuco, L.G.; Villa, E.; Schreiner, E.; Harrison, C.B.; Schulten, K. Molecular dynamics flexible fitting: A practical guide to combine cryo-electron microscopy and X-ray crystallography. *Methods* **2009**, *49*, 174–180. [CrossRef]

52. Pettersen, E.F.; Goddard, T.D.; Huang, C.C.; Couch, G.S.; Greenblatt, D.M.; Meng, E.C.; Ferrin, T.E. UCSF Chimera—A visualization system for exploratory research and analysis. *J. Comput. Chem.* **2004**, *25*, 1605–1612. [CrossRef] [PubMed]

53. Mendes, P.; Hoops, S.; Sahle, S.; Gauges, R.; Dada, J.; Kummer, U. Computational modeling of biochemical networks using COPASI. *Methods Mol. Biol.* **2009**, *500*, 17–59. [CrossRef] [PubMed]

54. Hasan, R.; Leeson-Payne, A.T.; Jaggar, J.H.; Zhang, X. Calmodulin is responsible for Ca2+-dependent regulation of TRPA1 Channels. *Sci. Rep.* **2017**, *7*, 45098. [CrossRef] [PubMed]

55. Marsakova, L.; Barvik, I.; Zima, V.; Zimova, L.; Vlachova, V. The First Extracellular Linker Is Important for Several Aspects of the Gating Mechanism of Human TRPA1 Channel. *Front. Mol. Neurosci.* **2017**, *10*, 16. [CrossRef] [PubMed]

56. Macikova, L.; Sinica, V.; Kadkova, A.; Villette, S.; Ciaccafava, A.; Faherty, J.; Lecomte, S.; Alves, I.D.; Vlachova, V. Putative interaction site for membrane phospholipids controls activation of TRPA1 channel at physiological membrane potentials. *FEBS J.* **2019**, *286*, 3664–3683. [CrossRef] [PubMed]

57. Rosenbaum, T.; Gordon, S.E. Quickening the pace: Looking into the heart of HCN channels. *Neuron* **2004**, *42*, 193–196. [CrossRef]

58. Yin, K.; Baillie, G.J.; Vetter, I. Neuronal cell lines as model dorsal root ganglion neurons: A transcriptomic comparison. *Mol. Pain* **2016**, *12*. [CrossRef]

59. Weng, H.J.; Patel, K.N.; Jeske, N.A.; Bierbower, S.M.; Zou, W.; Tiwari, V.; Zheng, Q.; Tang, Z.; Mo, G.C.; Wang, Y.; et al. Tmem100 Is a Regulator of TRPA1-TRPV1 Complex and Contributes to Persistent Pain. *Neuron* **2015**, *85*, 833–846. [CrossRef]

60. Bianchi, B.R.; Zhang, X.F.; Reilly, R.M.; Kym, P.R.; Yao, B.B.; Chen, J. Species comparison and pharmacological characterization of human, monkey, rat, and mouse TRPA1 channels. *J. Pharmacol. Exp. Ther.* **2012**, *341*, 360–368. [CrossRef]

61. Koivisto, A.; Jalava, N.; Bratty, R.; Pertovaara, A. TRPA1 Antagonists for Pain Relief. *Pharmaceuticals* **2018**, *11*, 117. [CrossRef]

62. Zubcevic, L.; Lee, S.Y. The role of pi-helices in TRP channel gating. *Curr. Opin. Struct. Biol.* **2019**, *58*, 314–323. [CrossRef] [PubMed]

63. Singh, A.K.; McGoldrick, L.L.; Demirkhanyan, L.; Leslie, M.; Zakharian, E.; Sobolevsky, A.I. Structural basis of temperature sensation by the TRP channel TRPV3. *Nat. Struct. Mol. Biol.* **2019**. [CrossRef] [PubMed]

64. Suo, Y.; Wang, Z.; Zubcevic, L.; Hsu, A.L.; He, Q.; Borgnia, M.J.; Ji, R.R.; Lee, S.Y. Structural insights into Electrophile Irritant Sensing by the human TRPA1 channel. *Neuron* **2020**, *105*. [CrossRef] [PubMed]

65. Liu, B.; Qin, F. Use Dependence of Heat Sensitivity of Vanilloid Receptor TRPV2. *Biophys. J.* **2016**, *110*, 1523–1537. [CrossRef] [PubMed]

66. Liu, B.; Qin, F. Single-residue molecular switch for high-temperature dependence of vanilloid receptor TRPV3. *Proc. Natl. Acad. Sci. USA* **2017**, *114*, 1589–1594. [CrossRef] [PubMed]

67. Macikova, L.; Vyklicka, L.; Barvik, I.; Sobolevsky, A.I.; Vlachova, V. Cytoplasmic Inter-Subunit Interface Controls Use-Dependence of Thermal Activation of TRPV3 Channel. *Int. J. Mol. Sci.* **2019**, *20*, 3990. [CrossRef]

NEUROPHYSIOLOGY

AQ1 # Odontoblast TRPC5 channels signal cold pain in teeth

Laura Bernal[1,2]*, Pamela Sotelo-Hitschfeld[1,3]*, Christine König[1], Viktor Sinica[1,4], Amanda Wyatt[5], Zoltan Winter[1†], Alexander Hein[6‡], Filip Touska[1,4], Susanne Reinhardt[7], Aaron Tragl[1], Ricardo Kusuda[1§], Philipp Wartenberg[5], Allen Sclaroff[8], John D. Pfeifer[9], Fabien Ectors[10], Andreas Dahl[7], Marc Freichel[11], Viktorie Vlachova[4], Sebastian Brauchi[3,12], Carolina Roza[2], Ulrich Boehm[5], David E. Clapham[6||¶], Jochen K. Lennerz[13¶], Katharina Zimmermann[1¶]

Teeth are composed of many tissues, covered by an inflexible and obdurate enamel. Unlike most other tissues, teeth become extremely cold sensitive when inflamed. The mechanisms of this cold sensation are not understood. Here, we clarify the molecular and cellular components of the dental cold sensing system and show that sensory transduction of cold stimuli in teeth requires odontoblasts. TRPC5 is a cold sensor in healthy teeth and, with TRPA1, is sufficient for cold sensing. The odontoblast appears as the direct site of TRPC5 cold transduction and provides a mechanism for prolonged cold sensing via TRPC5's relative sensitivity to intracellular calcium and lack of desensitization. Our data provide concrete functional evidence that equipping odontoblasts with the
AQ2 cold-sensor TRPC5 expands traditional odontoblast functions and renders it a novel integral cellular component of the dental cold sensing system.

INTRODUCTION

Insults to the tooth's dentin produces inflammation, most commonly during tooth decay. Dental caries is a chronic disease in which a bacterial biofilm on the tooth surface, in combination with fermentable carbohydrate substrates, causes demineralization and eventually tooth decay. Worldwide, 2.4 billion people have untreated caries in permanent teeth (1). Inflamed teeth are extremely cold sensitive, perceived as a short, sharp intense neuralgic pain (2). On the basis of the functional anatomy, in which ceramic-like enamel and dentin insulate nociceptive terminals from temperature changes (3), the tooth pulp's sensory plexus of Raschkow is widely accepted as mechano- and nociceptive. In Brännström's hydrodynamic or fluid movement theory, the transduction of thermal and other physical stimuli to activate dentinal nerve endings has been attributed to a fluid dynamic–induced mechanosensory process. In this theory, dentinal microcanals (tubules) act as a hydraulic link between the physical stimulus and the nerve terminals, which are sited at the pulp-dentin boundary (fig. S1) (4). Functional experimental evidence for this theory is lacking.

The lack of functional evidence for cold sensing in teeth is unexpected given the progress in our understanding of molecular cold-sensing molecules (5). Certain transient receptor potential (TRP) ion channel subtypes are strongly activated by cooling, acting as molecular sensors in the skin and mucous membranes where they depolarize nerve terminals to elicit action potentials (5). In the skin, TRPM8 and TRPA1 act synergistically and represent the key sensors of environmental cooling as well as painful cold (5, 6). TRPM8 and TRPA1 mRNA and protein are present in high density in the trigeminal ganglion (TG) and in the sensory axons of the tooth pulp (7–9). In addition, cultured human odontoblast-like cells (10) and cultured dental pulp fibroblasts (11) exhibit cold-induced increases in intracellular calcium in vitro, which is partly explained by their TRPA1 and TRPM8 channels. However, acutely isolated native human odontoblasts express TRPM8 but not TRPA1 (12), in contrast to these cells in more prolonged culture (10, 13). In rat odontoblasts in vitro, cold sensitivity is controversial (14, 15). The physiological significance of the observed cold transduction in odontoblast and fibroblasts is still unclear, because the specific contributions of TRPA1 and TRPM8 to cold-induced tooth pain in vivo were not observed (16) and electrophysiological models to directly examine the relevance of these channels in the tooth sensory system are missing. Thus, the cold transduction molecules and site of transduction in teeth remain unresolved.

We previously described that TRPC5 is cold sensitive in heterologous expression systems and its distribution in small- and medium-sized trigeminal and dorsal root ganglion neurons and the superficial laminae of the spinal dorsal horn is typical of sensors involved in temperature sensing and pain (17). Although TRPC5 is cold sensitive, no such function has yet been ascribed to TRPC5 in native cells. Here, we set out to understand the roles of TRPA1, TRPM8, and TRPC5 ion channels in cold sensing in teeth.

[1]Department of Anesthesiology, Erlangen University Hospital, Friedrich Alexander University of Erlangen-Nuremberg (FAU), Erlangen, Germany. [2]Departamento de Biología de Sistemas, Facultad de Medicina, Universidad de Alcalá, Alcalá de Henares, Madrid, Spain. [3]Institute of Physiology, Faculty of Medicine and Center for Interdisciplinary Studies on the Nervous System (CISNe), Universidad Austral de Chile, Valdivia, Chile. [4]Department of Cellular Neurophysiology, Institute of Physiology, Czech Academy of Sciences, Prague, Czech Republic. [5]Experimental Pharmacology, Center for Molecular Signaling (PZMS), Saarland University School of Medicine, Homburg, Germany. [6]HHMI, Cardiovascular Division, Boston Children's Hospital, and Department of Neurobiology, Harvard Medical School, Boston, MA, USA. [7]Center for Molecular and Cellular Bioengineering (CMCB), Technische Universität Dresden, Dresden, Germany. [8]Department of Otolaryngology, Washington University School of Medicine, St Louis, MO, USA. [9]Department of Pathology, Washington University School of Medicine, St Louis, MO, USA. [10]FARAH Mammalian Transgenics Platform, Liège University, Liège, Belgium. [11]Institute of Pharmacology, University of Heidelberg, Heidelberg, Germany. [12]Millennium Nucleus of Ion Channel-associated Diseases (MiNICAD), Santiago, Chile. [13]Center for Integrated Diagnostics, Department of Pathology, Massachusetts General Hospital/Harvard Medical School, Boston, MA, USA.
*These authors contributed equally to this work.
†Present address: Optical Imaging Centre Erlangen, Universität Erlangen-Nürnberg, Erlangen, Germany.
‡Present address: Department of Gynecology and Obstetrics, Erlangen University Hospital, Friedrich Alexander University of Erlangen-Nuremberg (FAU), Erlangen, Germany.
§On leave from: Departamento de Farmacologia, Faculdade de Medicina de Ribeirão Preto, Universidade de São Paulo, Ribeirão Preto, Brazil.
||Present address: Janelia Research Campus, Howard Hughes Medical Institute, Ashburn, VA, USA.
¶Corresponding author. Email: claphamd@hhmi.org (D.E.C.); jlennerz@partners.org (J.K.L.); katharina.zimmermann@fau.de (K.Z.)

MS no:	Emp name:	Date / Time:	PE's:	AA's:	Comments:	Art no:
RAabf5567/KP/NEUROPHYSIOLOGY, SIGNAL TRANSDUCTION	jroldan	2-26-2021 / 05:29				

Teaser: The odontoblast, with processes beyond the dentin-enamel boundary, is the initial site of TRPC5 cold transduction in teeth.

RESULTS

TRPC5 is required for inflammatory tooth pain

To evaluate cold transduction ion channels for inflammatory tooth pain, we first used an established dental pulp injury (DPI) model (*18*) in TRPC5, TRPA1, and TRPM8 null mice. A major sign of painful DPI in mice is a paradoxical increase in sucrose consumption (*18*). Administration of the anti-inflammatory analgesic indomethacin is sufficient to reverse the levels of sucrose consumption to that of uninjured controls (*18*). We found that DPI enhances the consumption of 5% room temperature sucrose water to ~3-fold above baseline (Fig. 1). In TRPA1$^{-/-}$ and TRPM8$^{-/-}$ mice, DPI induced a comparable increase in sucrose consumption. Notably, only in TRPC5$^{-/-}$ mice was sucrose consumption reversed to the level of the uninjured controls (Fig. 1), similar to the effect of indomethacin (*18*). These data indicate that cold-sensing TRPC5 is relevant and necessary for inflammatory tooth pain–associated behavior.

To enable functional examination of the entire tooth sensory system, we developed an intact mouse mandible-inferior alveolar nerve (jaw-nerve) preparation (Fig. 2). The ex vivo jaw-nerve preparation enables the recording of propagated action potentials from the inferior alveolar nerve to sensory stimuli in the mandibular incisor and molars, similar to recordings from nociceptors of the saphenous nerve with receptive fields in the skin (*6*). In contrast to the skin-nerve model in which recordings are made from finely split nerves (*19*), the inferior alveolar nerve in the jaw-nerve model is too short to enable these recordings. Therefore, we used a suction electrode to record voltage changes directly from the intact nerve end (Figs. 2 and 3A).

In this preparation, we focused on cold stimulation because it is adequate to produce tooth pain and activates the TRPC5 current in heterologous expression (*17*). When the intact jaw was exposed to cold, we observed large responses from ~10% of A- and C-fibers. Tooth cold receptor neurons fired 114 ± 15 action potentials per cold stimulus, with peak firing frequencies of 43 ± 5 per second. These values far exceed mouse skin nociceptor cold responses (16 ± 2 action potentials and firing frequencies of 3 ± 1 per second; Fig. 3, B and C). The threshold of the tooth pulp nociceptors was 19 ± 1°C, 2°C lower than the cold nociceptors in the skin (cutaneous nociceptor threshold = 21 ± 1°C; Fig. 3D). There were no notable differences in cold responses between A- and C-fibers in these specific parameters (fig. S2).
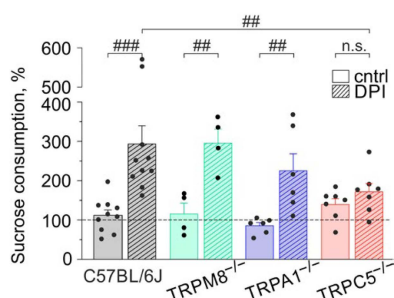
TRPC5 is a cold sensor in intact teeth

In the jaw-nerve preparation, the TRPC5 blockers HC-070 and ML204 effectively eliminated some tooth nociceptor's cold responses and, on average, reduced cold responses by 59 ± 13%. (Fig. 4, A and B). ML204, which also blocks TRPC4 and TRPC3 channels, had no effect in TRPC5$^{-/-}$ mice, suggesting that TRPC3 and TRPC4 were not involved as homomeric channels in cold responses. In addition, the TRPC5 agonist riluzole sensitized the cold response in TRPM8$^{-/-}$ jaws (fig. S3). In all fibers that remained unblocked by HC-070, the TRPA1 blocker HC-030031 abolished the remaining cold responses (97 ± 2%; Fig. 4, A and B). Furthermore, in the jaw-nerve preparations from TRPC5$^{-/-}$ mice, we found that the number of cold nociceptors was reduced by roughly half (Fig. 4C). We noted that although the remaining TRPC5$^{-/-}$ tooth nociceptors had unchanged response magnitudes, they had higher peak firing rates than any other strain (116 ± 34 action potentials, discharge rate of 66 ± 8 per second) and were activated at high threshold temperatures
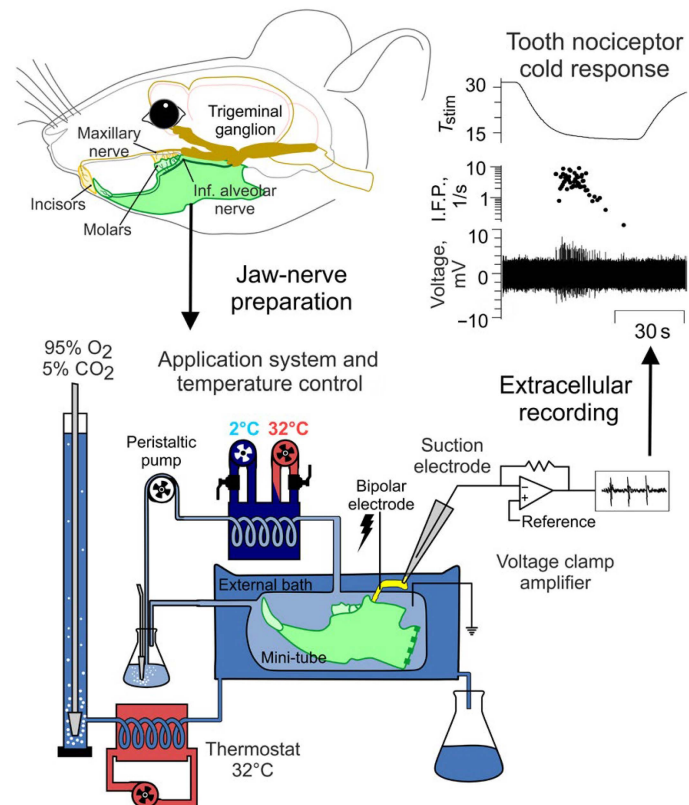

Fig. 2. Extracellular recordings from mouse tooth nociceptors in a novel jaw-nerve preparation. (**Top**) Illustration of mouse head with jaws and their innervation. The mandible-inferior alveolar nerve preparation is derived from the lower jaw and transferred to an organ bath consisting of an external solution and a mini-tube that is connected to a temperature-controlled application system. Connection of the application system's heating coil to a heating/cooling thermostat board permits rapid exchange of solution temperature in the mini-tube, where the preparation is exposed to chemical compounds and cold temperatures. Both the external and internal bath are supplied with oxygenized extracellular solution. Because of the short length of the inferior alveolar nerve, suction electrodes from glass capillaries are used and the amplifier is used in a single-ended configuration. The external bath is required to prevent cold block in the nerve when the teeth in the mini-tube are exposed to cold. Action potentials from the inferior alveolar nerve are recorded in gap-free mode with Spike 2 (Materials and Methods).

Fig. 1. TRPC5 is essential for inflammatory tooth pain. Percent change in sucrose consumption relative to baseline (dashed line) after DPI. DPI enhanced the consumption of 5% room temperature sucrose water to 293 ± 46% above baseline. Lack of TRPC5 ($P = 0.005$; 171 ± 21%), but not TRPM8 ($P = 0.9$; 299 ± 34%) or TRPA1 ($P = 0.1$; 225 ± 43%), reverts glucose consumption after DPI to baseline. The reduction in sucrose consumption in TRPC5$^{-/-}$ ($P = 0.5$), but not TRPA1$^{-/-}$ ($P = 0.006$) or TRPM8$^{-/-}$ (0.004), was not different from the respective controls without DPI. n.s., not significant.

MS no:	Emp name:	Date / Time:	PE's:	AA's:	Comments:	Art no:
RAabf5567/KP/NEUROPHYSIOLOGY, SIGNAL TRANSDUCTION	jroldan	2-26-2021 / 05:29				Fig 1,2

Teaser: The odontoblast, with processes beyond the dentin-enamel boundary, is the initial site of TRPC5 cold transduction in teeth.
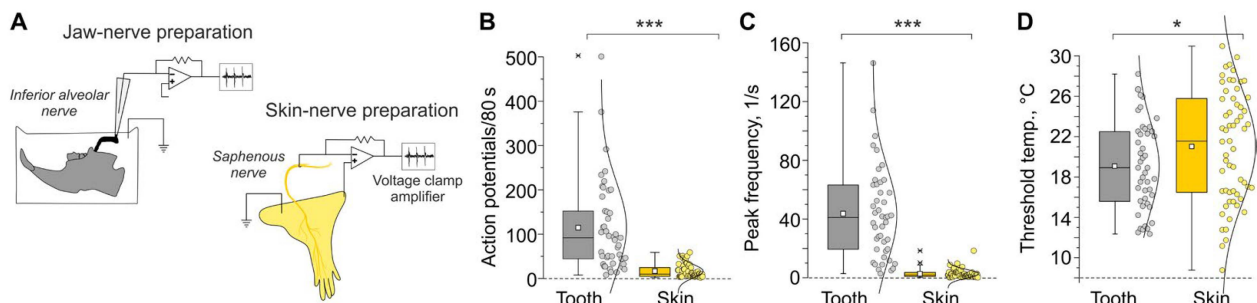
Fig. 3. Tooth nociceptor cold responses are much larger than skin cold nociceptor responses. (A) Schematic illustration of extracellular recordings from jaw-nerve as compared to skin-nerve preparations.**(B to D)** Comparison of the (B) cold response magnitude, (C) peak frequency, and (D) threshold temperature of C57BL/6J teeth ($n = 45$) and skin ($n = 59$) nociceptors. Statistical significance was identified by a two-sided Student's t test: $P = 2 \times 10^{-8}$, $P = 3 \times 10^{-11}$, and $P = 0.05$. Skin nociceptor cold responses are from (6, 50) and refer to the same background strain at equivalent stimulus conditions.

(22 ± 1°C; Fig. 4, E to G). Although in mouse skin most of the cold responses are TRPM8-mediated (6), the teeth cold responses appeared insensitive to pharmacological TRPM8 modulation (fig. S4).

The deficits in the prevalence of TRPC5$^{-/-}$ cold responses, combined with the high efficacy of HC-070 and HC-030031 blockers, suggest that TRPC5 and TRPA1 are essential for cold sensing in teeth. In jaw-nerve preparations derived from TRPC5/A1-DKO (double-knockout) mice, we found that the number of cold responses was reduced by one-third (to <3%; Fig. 4C). Moreover, these cold responses had reduced response magnitudes and action potential firing rates compared to normal tooth nociceptors (20 ± 9 action potentials, discharge rate of 9 ± 3 per second) and were activated at very low temperature thresholds (15 ± 1°C; Fig. 4, D to G). These small responses were insensitive to fast temperature drops (Fig. 4, D and H to J), and TRPM8 blockers or agonists had no effect (Fig. 4D).

We conclude that TRPC5 and TRPA1 are sufficient for cold transduction in healthy teeth. These findings raise the question of whether the specific anatomical context in teeth is required for TRPC5 cold sensitivity or if TRPC5 is also cold sensitive in the isolated cell bodies derived from the primary afferent terminals.

Dental primary afferent neurons (DPANs), the cell bodies of the sensory terminals in the maxillary plexus of Raschkow, are clustered in the cranial TG and were identified by retrograde labeling (7). Dissociated and in culture, they represent a model for the transduction processes in the tooth pulp's sensory nerves (fig. S5). We screened the red retro-labeled DPANs for cold-induced changes in [Ca^{2+}] and chemical responsiveness to the TRPM8 agonist menthol, the TRPA1 agonist carvacrol, the TRPC5 agonist riluzole, and the antagonist ML204. We identified ~17% of neurons as cold sensitive. Of these, 74% were sensitive to menthol and 57% to carvacrol, but only one neuron (<1%) was sensitized by the TRPC5 agonist riluzole (Fig. 5, A and B). Because menthol and carvacrol are not highly specific and can activate both TRPM8 and TRPA1, we also used DPANs derived from DKO strains, lacking TRPC5 and TRPM8 (TRPC5/M8-DKO) and TRPC5 and TRPA1 (TRPC5/A1-DKO). In DPANs derived from TRPC5/M8-DKO mice, we found that <5% of DPANs remained cold sensitive. These remaining DPANs were primarily sensitive to menthol and carvacrol, indicating activation of TRPA1 by cold. In DPANs derived from TRPC5/A1-DKO mice, 20% of cells were cold sensitive; of these, 75% were menthol sensitive and hence TRPM8 dependent (Fig. 5, A and C). These experiments imply that most of the DPANs use TRPM8 for cold responses, while few neurons rely on TRPA1 for independent cold responses. These

observations match previous observations from dorsal root ganglion neurons (20).

Similar to DPANs derived from TRPC5/M8-DKO mice, DPANs from TRPM8/A1-DKO mice had few cold-sensitive cells (~5%) and none of these cells were activated by carvacrol or menthol (Fig. 5A). The TRPC5 blocker ML204 reduced their remaining cold-induced activity by 90% (Fig. 5, C and D). ML204's blocking effect was also found in the background strain (23% reduction), but absent in TRPC5$^{-/-}$ DPANs, where virtually all cold-sensitive DPANs were sensitive to menthol (93%; Fig. 5, A and D). In examining the cold-activated [Ca^{2+}] kinetics, TRPM8/A1-DKO DPAN signals were smaller and rose more slowly compared with the fast-rising response of menthol-sensitive neurons (fig. S6). To test whether total activity (approximated by the slope of the cold-activated [Ca^{2+}] signals) of the TRPM8/A1-DKO DPANs and riluzole-induced sensitization of the cold response represented functional TRPC5, we compared it to the responses of *mTrpc5* in human embryonic kidney (HEK) 293T and found both response patterns to be similar and riluzole to largely increase TRPC5 cold responses (fig. S6). In summary, nerve (DPAN) cold responses are dominated by TRPM8 with smaller and slower contributions by TRPC5 and TRPA1 channels.

TRPC5 cold transduction originates in odontoblasts
Consistent with the small number of nerve cells with functional TRPC5, a transcriptomic analysis from acutely dissociated labeled DPANs in the background strain identified *Trpm8* and *Trpa1*, while *Trpc5* was below the detection threshold (Fig. 6A and table S1). However, we visualized and quantified TRPC5 protein by multiphoton microscopy in retrograde-labeled whole TGs of reporter mice expressing tau-GFP (green fluorescent protein) under the control of the TRPC5 promoter (21). We focused on areas from the mandibular and maxillary branches that have the largest density of DPANs (7) and identified 3.5% TRPC5$^+$ DPANs (Fig. 6B), similar to the 2.2 to 4.8% cold-sensitive, carvacrol- and menthol-insensitive DPANs in neuronal cultures from C57BL/6J or TRPM8/A1-DKO mice, respectively. In the cultured TRPC5$^+$ trigeminal neurons from the TRPC5 reporter mice, we identified the typical doubly rectifying current-voltage relationship characteristic of TRPC5 (Fig. 6C). The current was small (chloride was eliminated from the solution to remove contaminating currents) and only detected after activation with Englerin (Fig. 6C). This small current was not modified by cold, suggesting modification of the properties of the native TRPC5 current by Englerin binding or by other factors. These findings

MS no:	Emp name:	Date / Time:	PE's:	AA's:	Comments:	Art no:
RAabf5567/KP/NEUROPHYSIOLOGY, SIGNAL TRANSDUCTION	jroldan	2-26-2021 / 05:29				Fig 3

Teaser: The odontoblast, with processes beyond the dentin-enamel boundary, is the initial site of TRPC5 cold transduction in teeth.
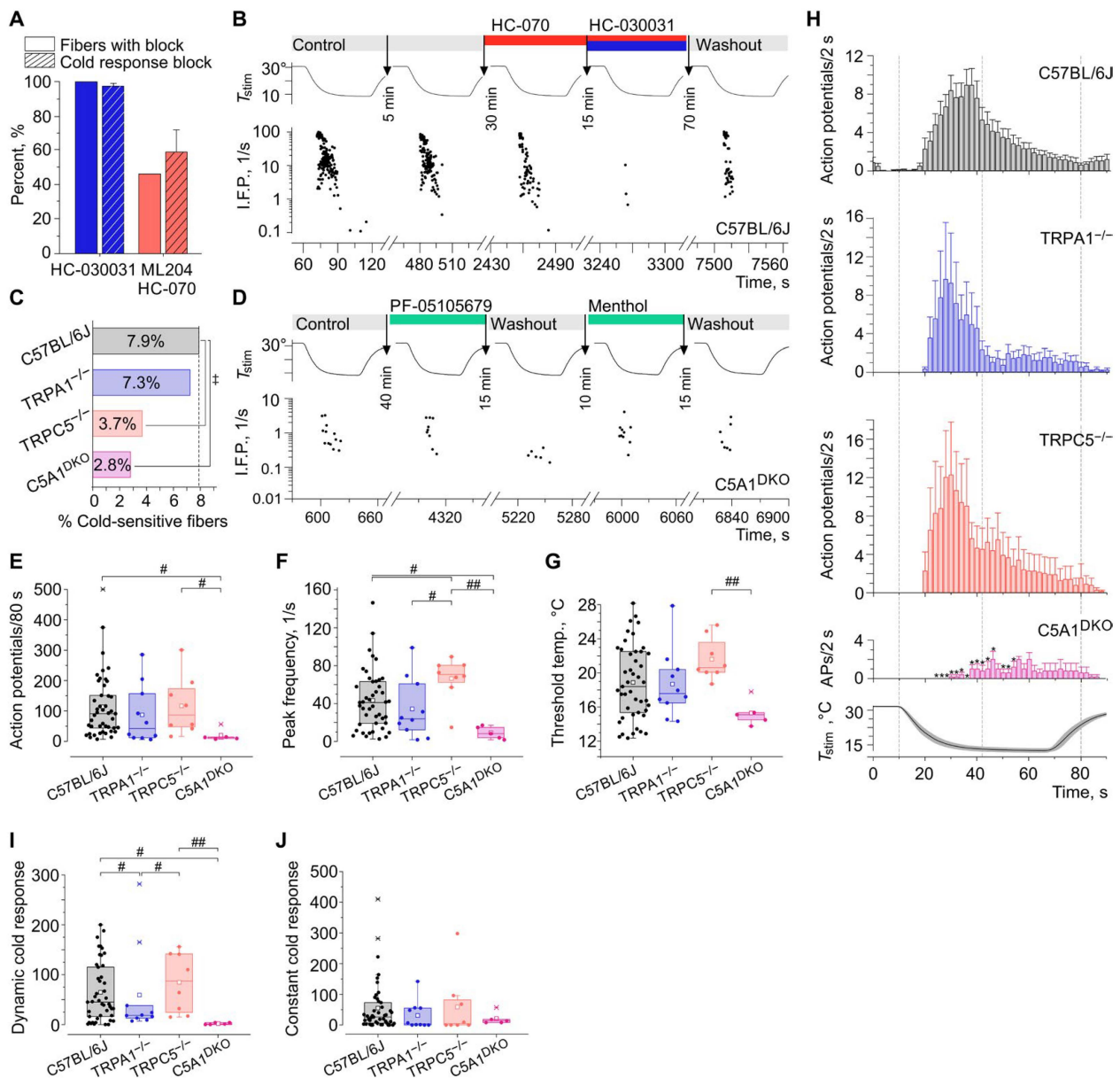
Fig. 4. TRPC5 and TRPA1 are sufficient as cold sensors in healthy teeth. (**A**) Percent cold-sensitive tooth nociceptors blocked by HC-030031 ($n = 9$ of 9 fibers) and ML204/HC-070 ($n = 6$ of 13 fibers) and respective fraction of block (means ± SEM). (**B**) C57BL/6J wt tooth nociceptor recording with temperature (top) and instantaneous frequency pattern (I.F.P.; bottom) blocked by HC-070 and HC-030031. Circles represent action potentials. (**C**) Tooth cold responses in TRPA1$^{-/-}$ ($n = 10$ of 138, $P = 1.0$), TRPC5$^{-/-}$ ($n = 8$ of 217, $P = 0.04$), and TRPC5/A1-DKO ($n = 5$ of 177, $P = 0.02$), chi-square tests versus C57BL/6J ($n = 45$ of 570). (**D**) Typical cold response of a TRPC5/A1-DKO tooth nociceptor with temperature (top) and instantaneous frequency pattern (I.F.P.; bottom). As in (B), circles represent action potentials, and horizontal bars and arrows indicate applications and respective time intervals. (**E** to **G**) Teeth nociceptor cold response characteristics according to genotype, (E) cold response magnitude [$P = 0.2$ between groups by one-way analysis of variance (ANOVA)], (F) peak firing frequency ($P = 0.01$), and (G) temperature threshold ($P = 0.06$). TRPC5/A1-DKO were statistically different from C57BL/6J wt ($P = 0.04$ and $P = 0.02$) and TRPC5$^{-/-}$ ($P = 0.05$, $P = 0.001$, and $P = 0.007$). TRPC5$^{-/-}$ were statistically different from TRPA1$^{-/-}$ ($P = 0.03$) and C57BL/6J ($P = 0.05$) in least significant difference post hoc tests. (**H** to **J**) Histograms in bins of 2 s (H) and respective box plots of (I) dynamic and (J) constant cold responses. Significant differences between groups by one-way ANOVA existed for dynamic (10 to 42 s of the histogram; $P = 0.01$) but not constant cold (44 to 80 s of the histogram; $P = 0.6$). TRPC5/A1-DKO ($n = 5$) and TRPA1$^{-/-}$ ($n = 10$) were different from C57BL/6J ($P = 0.02$ and $P = 0.03$, $n = 45$) and TRPC5$^{-/-}$ ($P = 0.01$ and 0.02, $n = 8$). Histograms present data as means ± SEM, and asterisks refer to two-sided Student's t test comparison of respective knockouts with the C57BL/6J background strain ($3 \times 10^{-6} < P < 0.002$). Lines represent medians, squares represent the mean, boxes represent the interquartile range (IQR), and whiskers represent 2.2-fold of IQR after exclusion of the >2.2 IQR outliers identified by crosses.

demonstrate that TRPC5 is present in sensory neurons, although with healthy teeth TRPC5 cold responses are apparently small and rare.

What then accounts for the large TRPC5-mediated cold responses we observed in intact teeth? When we examined TRPC5 in reporter mice molar teeth, we found TRPC5 in practically all predentinal odontoblasts in the root-adjacent tooth pulp. The processes of the TRPC5-positive odontoblasts in dentinal tubules contacted sensory axons at the pulp-dentin boundary and ascended in tight

MS no:	Emp name:	Date / Time:	PE's:	AA's:	Comments:	Art no:
RAabf5567/KP/NEUROPHYSIOLOGY, SIGNAL TRANSDUCTION	jroldan	2-26-2021 / 05:29				Fig 4

Teaser: The odontoblast, with processes beyond the dentin-enamel boundary, is the initial site of TRPC5 cold transduction in teeth.
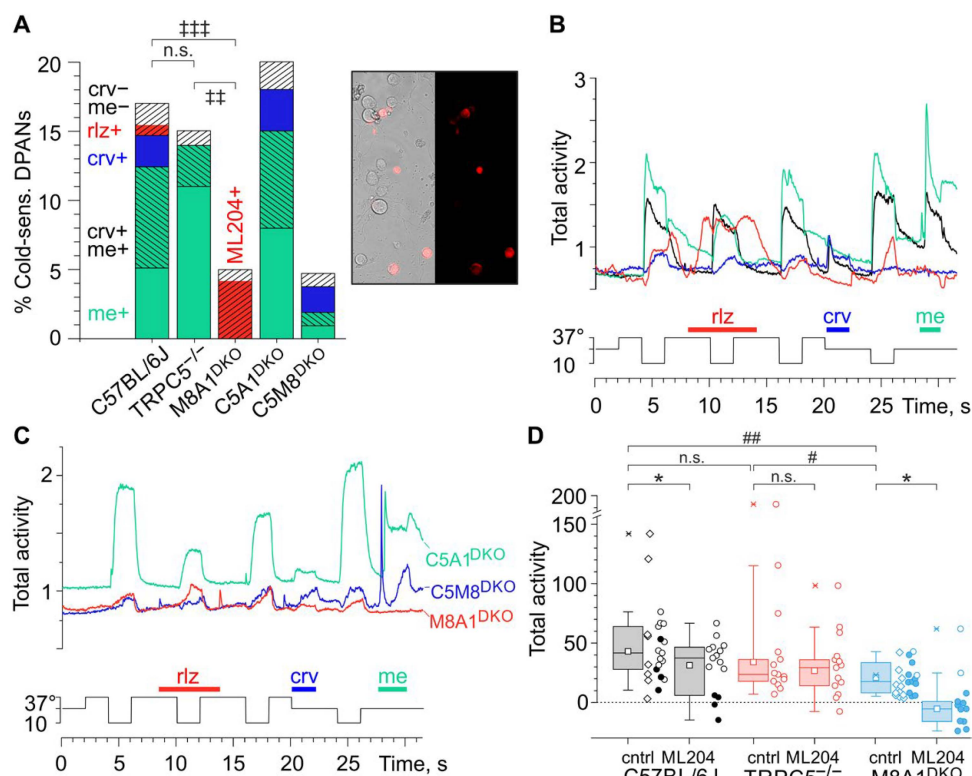
Fig. 5. Most cold-sensitive DPANs use TRPM8, but TRPA1 and TRPC5 are also functional cold transducers. (**A**) Characterization and quantification of cold-sensitive cultured DPANs (C57BL/6J: $n = 23$ of 136) based on Ca^{2+} transients measured with Fura-2 AM and sensitivity to TRP channel modulators menthol ($n = 7$), carvacrol ($n = 3$), both ($n = 10$, descending diagonal stripes), neither ($n = 4$, ascending diagonal stripes), and riluzole ($n = 1$). Cold-sensitive DPANs insensitive to menthol and carvacrol (ascending diagonal stripes) are unchanged in TRPC5$^{-/-}$ ($n = 1$ of 14 in 93) versus C57BL/6J (3 of 23 in 136; $P = 0.86$), but increased in TRPM8A1-DKO ($n = 23$ in 457; $P = 0.002$ and $P = 0.00003$). In TRPC5A1-DKO, cold-sensitive cells ($n = 20$ of 100) were mostly menthol sensitive ($n = 15$; crv+ $n = 10$; both, $n = 7$ and none, $n = 2$). TRPC5M8-DKO cold-sensitive cells ($n = 5$ of 103) were mostly sensitive to carvacrol ($n = 3$; me+ $n = 2$; both, $n = 1$ and none, $n = 1$). Inset: Photomicrograph of cultured mouse TG neurons with red DiI retro-labeled DPANs. (**B** and **C**) Ca^{2+} transient traces from (B) C57BL/6J representative of four types of cold-sensitive neurons and (C) TRPM8A1-DKO (red), TRPC5A1-DKO (green), and TRPC5M8-DKO (blue). Bottom: Temperature stimulator command. (**D**) TRPM8/A1-DKO cold responses ($n = 23$) were smaller than in C57BL/6J ($n = 23$; $P = 0.006$) and TRPC5$^{-/-}$ neurons ($n = 14$; $P = 0.01$). ML204 (circles = treated neurons) blocked most cold responses in TRPM8/A1-DKO ($\geq 50\%$ block = filled circles, $n = 12$; $P = 0.01$) and some in C57BL/6J neurons ($n = 15$; $P = 0.02$), but not in TRPC5$^{-/-}$ neurons ($n = 14$; $P = 0.2$).
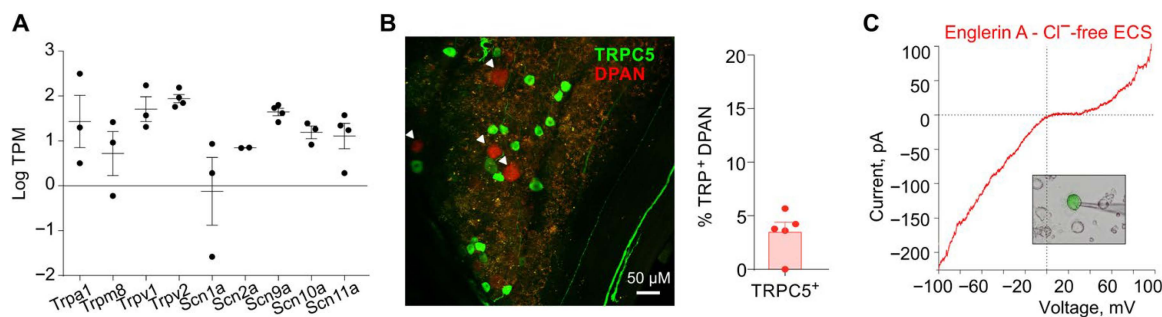

Fig. 6. Functional TRPC5 in trigeminal neurons. (**A**) Relative expression of TRP and nociceptor-specific subtypes of voltage-gated sodium channel genes in mouse DPANs given as transcripts per million (TPM). Data are presented as means ± SEM. Dots represent each replicate. Replicates with value 0 are not represented in the logarithmic scale. TRPC5 was not among the transcripts (see table S1). (**B**) Red DPANs (arrowheads) in TRPC5 reporter mouse ganglion (TG) multiphoton stacks of maxillo-mandibular regions. A total of 176 DPANs had 11 TRPC5$^+$ neurons (seven TGs, five mice). (**C**) Typical doubly rectifying current-voltage relation observed in a cultured TRPC5$^+$ neuron of a reporter mouse ($n = 13$). TRPC5 current is small and is only identified as Englerin-sensitized current subtracted from the baseline current in the absence of chloride in the solution.

association into the dentinal tubules. We did not identify TRPC5 in pulp fibroblasts or in sensory axons originating from the alveolar nerves and radiating through the root into the nerve plexus of Raschkow or in the inferior alveolar nerve (Fig. 7 and movies S1 and S2). Thus, TRPC5, in contrast to the ubiquity of TRPM8 and TRPA1 in

F7
AQ3

anatomical compartments of mouse and human teeth (fig. S7) (*7, 9–13, 22*), is largely restricted to the odontoblast cell layer.

Ideally, TRPC5 should also be recorded in response to cold in odontoblasts in the intact tooth system of live, unanesthetized mice, but this has not yet been technically possible. Isolated odontoblasts

MS no:		Emp name:	Date / Time:	PE's:	AA's:	Comments:	Art no:
RAabf5567/KP/NEUROPHYSIOLOGY, SIGNAL TRANSDUCTION		jroldan	2-26-2021 / 05:29				Fig 5,6

Teaser: The odontoblast, with processes beyond the dentin-enamel boundary, is the initial site of TRPC5 cold transduction in teeth.
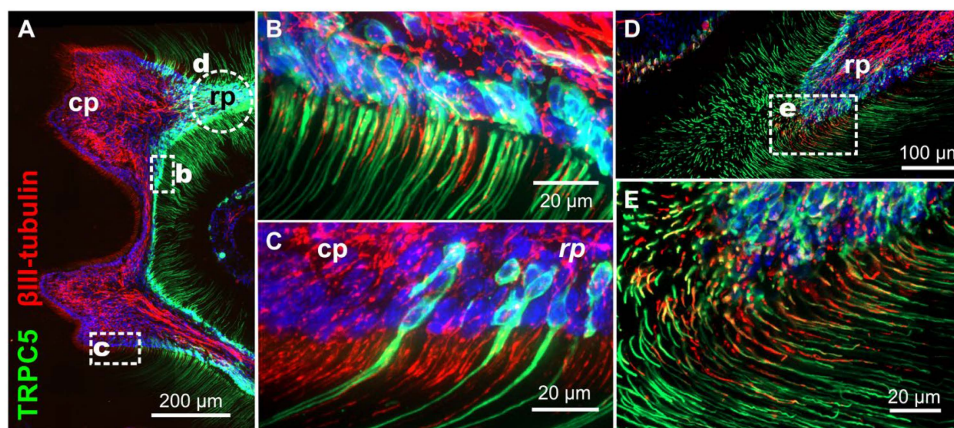
Fig. 7. TRPC5 cold sensing originates in odontoblasts. (**A**) TRPC5 reporter mouse molar tooth whole mount with densely packed TRPC5⁺ odontoblasts at the pulp-dentin boundary. (**B** and **C**) In tight association with sensory nerves. Green, TRPC5; red, βIII-tubulin; circle indicates area shown in (**D**) and (**E**) from a subsequent section. cp, coronal pulp; rp, radicular pulp. (E) Oblique section through the predentin radicular pulp to visualize the tight association of TRPC5⁺ odontoblast processes with their sensory nerves.

do not fulfill this need because gene expression may be altered during isolation and culture. In addition, the respective functional phenotype depends on the origin of the cells, methods used for the induction of odontoblastic differentiation (*12*), developmental stage, intradental location, and innervation of the odontoblasts (*23*). A recent study, based on TRP channel expression patterns, implied that rat odontoblasts do not acquire potential sensory function before they begin to form root dentin (*24*). With these caveats in mind, we propose that TRPC5 expression and cold sensing indicate an essential sensory receptor function for the odontoblasts in the transduction hierarchy from the enamel to the dentinal primary afferent nerves.

TRPC5 is increased in human teeth with pulpitis
A remaining question is whether TRPC5 is also a cold sensor in human teeth and expressed in human odontoblasts and how it is affected in caries and inflammatory conditions associated with injured or patent pulp. In healthy human teeth from adults, removed for orthodontic or cosmetic reasons, we identified TRPC5 in the odontoblastic layer. We found more TRPC5 than TRPM8 in sensory nerves at the pulp-dentin boundary and in dentinal tubules. The sensors (*25*) at the pulpo-dentinal border zone (type II/III) exhibited the largest proportion of TRPC5 colabeling. In addition, we found a proportion of dentinal (type IV) TRPC5⁺ fibers running within the dentinal tubules at the presumed site of sensory transduction (Fig. 8, A to E) (*26*).

Previous studies found that TRPM8 was decreased in axons of cold-hypersensitive human teeth (*22*). We thus directly compared TRPC5 with TRPM8 in inflamed human teeth with pulpitis (figs. S8 and S9) and found that TRPC5 sensory nerve expression markedly increased, while TRPM8 decreased. TRPC5 extended to the degenerating dentin and the entire tooth root, where we found a significantly higher percentage of TRPC5⁺ pulp and root fibers (Fig. 8, F to I, and fig. S9). We also observed TRPC5⁺ type IV fibers in the degenerating dentin (Fig. 8H). The higher percentage of TRPC5 in pulpitic teeth and the presence of dentinal fibers within the normal and degenerating dentinal tubules suggest that TRPC5 also acts as a cold sensor in human teeth.

DISCUSSION
Dentine sensitivity as a thermomechanical sensation
This study aimed to find the molecular cold-sensing mechanism in teeth. Using a novel jaw-nerve preparation that enabled us to record propagated electrical activity from intact teeth, we identified TRPC5 and TRPA1 as the molecular cold sensors and odontoblasts as the site of cold transduction. This experimental model allowed us to close an important gap in our understanding of tooth pain as it is the first model that allows the assessment of the tooth sensory system in its entire anatomical and, necessarily, physiological context in transgenic mice. This is critical because, unlike anywhere else in the body, the dental functional anatomy poses complex problems to sensing damaging physical stimuli. The odontoblast cellular layer's location in the outermost zone of the tooth pulp makes it a natural barrier between the mineralized hard tissues and the soft dental pulp. Each odontoblast has a process protruding in a dentinal tubule where it is immersed in dentinal fluid. Its cell body and process are surrounded by unmyelinated sensory nerves within the first 100 μm of the odontoblast-predentin border (fig. S1) (*26*). This unique hierarchical arrangement, from macroscale enamel via fluid-filled dentinal microtubules to molecular level ion channels, provides the structural basis for the encoding of thermal pain (*3*).

Previous theories of dentine sensitivity have interpreted tooth pain as the result of a thermomechanical sensory mechanism (*3, 26*). The nerve theory suggests that the unmyelinated nerve fibers at the interface between predentin and dentinal tubules are the source of dentine sensitivity (*25*). However, the temperature at the pulp-dentin interface is still within the normal range when action potential trains are measured in tooth nerves (*27*) and when patients perceive pain from tooth cooling (*28*). This apparent inconsistency is resolved in Brännström's hydrodynamic theory, in which odontoblasts, with their associated sensory nerves at the pulp-dentine boundary, are assumed to be mechanosensory units for pain-evoking thermally induced hydraulic forces in the tubules (*4, 26*). The tubule fluid has a greater coefficient of thermal expansion relative to the dentin matrix; thermal contraction and expansion of the dentinal fluid induces fluid movement (*29*). Flow-induced shearing was therefore considered as an adequate stimulus for molecular mechanoreceptors in the terminal

MS no:	Emp name:	Date / Time:	PE's:	AA's:	Comments:	Art no:
RAabf5567/KP/NEUROPHYSIOLOGY, SIGNAL TRANSDUCTION	jroldan	2-26-2021 / 05:29				Fig 7

Teaser: The odontoblast, with processes beyond the dentin-enamel boundary, is the initial site of TRPC5 cold transduction in teeth.
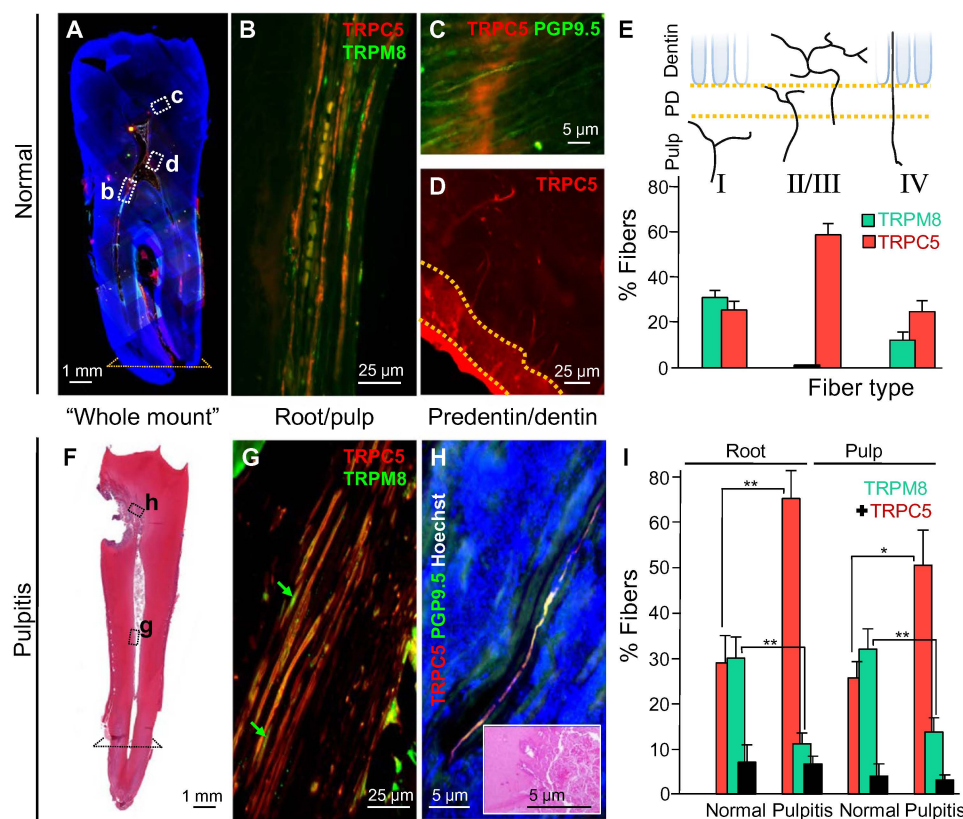
Fig. 8. TRPC5 is expressed in normal human teeth and increases with pulpitis. (**A**) Whole-mount panography of a human tooth; regions evaluated for TRPC5 expression are indicated; dotted line, level used in root measurement. (**B**) TRPC5$^+$ nerve fibers in the radicular pulp double labeled with TRPM8. (**C**) TRPC5$^+$ nerve fibers double labeled with PGP9.5 within the inner third of the dentinal tubules (type IV) ~40 μm above the odontoblast-predentinal border. (**D**) TRPC5$^+$ branched fibers (type II/III) in the predentin/dentin layer. (**E**) Quantification of TRPC5$^+$ and TRPM8$^+$ fiber types (four teeth). TRPC5/PGP9.5 and TRPM8/PGP9.5 for type I: 13/51 and 7/22; type II/III: 41/70 and 0/35; type IV: 26/105 and 6/49. (**F**) Hematoxylin and eosin (H&E)–stained human tooth whole mount with degenerated dentin (caries) and pulpitis. (**G**) Abundant TRPC5$^+$ and decreased TRPM8$^+$ (arrows) nerve fibers in the pulpitic tooth root. (**H**) TRPC5$^+$ nerve fibers (type IV) in degenerating dentin (inset, H&E). (**I**) Increased TRPC5$^+$ (190 of 660 versus 394 of 607 fibers; $P = 0.002$), decreased TRPM8$^+$ (197 of 660 versus 67 of 607; $P = 0.005$), and similar proportions of colabeled fibers (black) in normal versus pulpitic tooth roots [132 ± 78 ($n = 4$) versus 86 ± 21 ($n = 7$; $P = 0.2$)] and in the tooth pulp [TRPC5$^+$: 15 of 51 versus 81 of 161; $P = 0.01$; TRPM8$^+$: 622 of 161 versus 9 of 22; $P = 0.008$; colabeled fibers (black): 12 ± 3 ($n = 4$) versus 18 ± 8 ($n = 9$); $P = 0.3$]. Error bars, SEM.

nociceptor beads at the predentin-dentin interface. Although the rapid increase in cooling-induced outward-directed fluid flow observed in the dentinal tubules coincides with tooth pain and the intradental nerve discharge rate increases with increasing fluid flow (*27*, *29*), the theory is limited by lack of measurements and some inconsistencies. For example, etched dentinal tubules lead to dentine hypersensitivity but produce lower outward fluid flow in the tubules (*30*). Sealing the tubules then provides instant relief from cold hypersensitivity (*30*, *31*), but induces a larger cold-induced fluid flow (*30*). Humans with pulpal inflammation and painful cold hypersensitivity feel no pain from negative hydrostatic pressure on the tubules, despite the fact that it provokes equivalent outward fluid flow (*32*).

Last, some mechanical theories posit that the odontoblast processes are the initial mechanosensory nociceptors (*33*) based on the reasoning that odontoblast cells are more compliant relative to dentine and therefore would be expected to deform in registry with the tubules. The odontoblast transduction theory therefore hypothesizes that odontoblasts sense mechanical deformation and pass the signal to nearby nociceptors on nerve fibers through paracrine, electrical, or synaptic signaling (*3*, *33*). This transmission is implied by their

close relationship to the nerve fibers but has not been observed ex vivo or in vivo.

Are physical forces in dentinal tubules sufficient to activate TRP channels?

Could TRPC5 act as multimodal transducer and respond to changes in macroscopic physical forces in addition to temperature? Enamel not only conducts temperature changes but also may expand or contract when subjected to temperature changes (*3*, *29*). In primates, some of the odontoblast processes are "enamel spindles" (*26*) that span the boundary between enamel and dentin, where the two anisotropic materials may cause nonuniform temperature conduction. Property mismatch of bonded enamel and dentine leads to stress and flexure, even in the cause of a uniform change in temperature (*3*), causing friction and shear stress on the odontoblast processes.

TRPC5, like TRPA1 and TRPM8, channels are cold-activated in heterologous expression but, like all proteins, can potentially respond to primary physical forces. However, few TRP channels are subjected to these large forces in vivo (*34*) and only hTRPA1 has been shown to be gated by lipid-mediated forces, similar to Piezo

Teaser: The odontoblast, with processes beyond the dentin-enamel boundary, is the initial site of TRPC5 cold transduction in teeth.

channels (*35*). TRPC5 assembles with scaffolding proteins like EBP50 via cross-links between its VTTRL motif and the F-actin cytoskeleton, but deletion of TRPC5's C-terminal motif does not affect its membrane location or biophysical properties (*36*). Whether TRPC5 and TRPA1 are capable of recognizing shear stress in a compliant odontoblast or detect force changes of expanding and contracting enamel (*29*) is difficult to verify under physiologically relevant conditions. To date, all threshold mechanical forces found to open TRPC5 in cellular models [~2800 Pa; (*37*)] are many-fold larger than the forces in the dentinal tubules [~90 Pa provided from fitting predictions; (*3*, *34*)]. Proof of purely mechanically activated sensing because of temperature changes awaits the measurement of these forces at the site of the detector in vivo.

Odontoblasts are cold-transducing cells via TRPC5-mediated cold sensing

Here, we propose that the odontoblast processes—predominantly via TRPC5—are the initiating site of tooth cold transduction. The simplest interpretation of our data is that the observed restricted TRPC5 expression pattern, block of responses in genetically modified mice, and extracellularly recorded TRPC5 cold sensing indicate an essential sensory receptor function for the odontoblasts in tooth cold sensing.

More experiments are needed to clarify the functional relationship among odontoblasts, odontoblasts, and the tooth and between odontoblast processes and nerve endings. Some interesting observations may point the way. For example, the abovementioned enamel spindles cross the basement membrane of the enamel-dentine junction and may enable faster detection of temperature changes. For fast transmission, voltage-gated sodium currents in odontoblasts initiate rapid firing bursts similar to neurons (*38*). Axons produce bead-like swellings near odontoblasts with plasmalemmal appositions of 150 to 300 Å (*25*, *26*, *39*). Last, odontoblasts may couple to each other via gap junctions to act as a biological syncytium (*26*, *40*), and signal to axons via transmitters such as adenosine 5′-triphosphate (ATP), glutamate, or neuropeptides (*13*, *39*, *41*).

To summarize, our data clarify the molecular and cellular components of the dental cold sensing system and show that sensory transduction of cold stimuli in teeth requires odontoblasts. Thus, cultured neuron models alone are insufficient to capture the functional complexities of dental cold sensing. TRPC5 is a cold sensor in healthy teeth and, with TRPA1, is sufficient for cold sensing. Under human inflammatory conditions with injured or patent tooth pulp, TRPC5's expression increases in sensory axons. The odontoblast appears as the direct site of TRPC5 cold transduction and provides a mechanism for prolonged cold sensing via TRPC5's relative sensitivity to intracellular $[Ca^{2+}]$ and lack of desensitization (*42*). TRPM8, in contrast, is down-regulated in inflammation and, with its contrasting biophysical properties and its location in the coronal predentinal odontoblasts of the enamel (*8*), may trigger more transient cold responses or indicate a different function (e.g., as an osmosensor akin to reports of TRPM8 in the cornea) (*43*). In addition to being an odontoblast cold sensor, TRPC5 may signal prolonged pain and act as a sensor of oxidative stress during inflammation (*44*). In this respect, TRPC5 may be an effective target for the treatment of dentin hypersensitivity and inflammatory tooth pain. Oil of cloves' (*Syzygium aromaticum*) main ingredient, eugenol, has been used for centuries as an analgesic in dentistry (*45*) and inhibits TRPC5 currents (fig. S10).

In the evolutionary arms race between teeth and food, the odontoblast with its elongated process stretching beyond the dentin-enamel boundary (*26*) satisfies the need for a specialized nociceptor inside an obdurate shell (*46*). We propose that odontoblasts alert us to tooth damage by extracorporeal, lower temperature, objects.

MATERIALS AND METHODS AQ6
Animal models and behavior
Animals

The animal ethics committee and the local district government of Middle Franconia, Germany approved the protocol for in vivo surgical interventions in mouse teeth under protocol no. 55.2-2532.1-9/14. Generation of the new reporter strains was approved by the animal ethics committee and the local district government of Saarland, Germany under protocol no. 2.4.2.2-54/2015. We used adult male C57BL/6JCrl mice, congenic TRPA1$^{-/-}$ (*47*) congenic TRPM8$^{-/-}$ mice (*48*), and congenic TRPC5$^{-/-}$ mice (*49*). DKOs were generated from TRPA1$^{-/-}$ and TRPC5$^{-/-}$ mice, termed TRPC5/A1-DKO, from TRPM8$^{-/-}$ and TRPA1$^{-/-}$ mice, termed TRPM8/A1-DKO, and from TRPC5$^{-/-}$ and TRPM8$^{-/-}$ mice, termed TRPC5/M8-DKO. The TRPM8/A1-DKO mice were previously phenotyped for cold avoidance in the somatosensory system (*6*). Mice are specified in table S2. The animals were genotyped using the previously reported protocols (*49*–*51*). In addition, we generated reporter mouse lines to visualize TRPC5- and TRPA1-expressing cells by inserting an internal ribosome entry site (IRES) followed by a *Cre* recombinase complementary DNA (cDNA) downstream of the stop codon of the *Trpc5* (TRPC5-IC mice) (*21*) or the *Trpa1* gene, respectively (*52*). To generate the TRPA1 reporter mice, we produced an 8.7-kb targeting construct comprising a total of 5.2 kb of homologous sequence flanking an *IRES-Cre-PGK-Neomycin* cassette. The homologous stretches of DNA were generated by polymerase chain reaction (PCR), during which specific restriction sites were incorporated to enable assembly of the final construct by subsequent cloning steps. The *IRES-Cre-PGK-Neomycin* cassette is located 5 base pairs (bp) downstream of the stop codon, which is present in exon 27 of the *Trpa1* gene. After sequence verification, the targeting construct was electroporated into mouse embryonic stem cells. Correctly targeted stem cells were injected into blastocysts to generate the *Trpa1-IRES-Cre* (TRPA1-IC) knock-in mouse line. Flp recombinase deleter mice (*53*) were used to remove the neomycin resistance cassette. TRPC5-IC and TRPA1-IC mice were bred to *ROSA26*-floxed-stop tau GFP reporter mice (*54*) to label the TRPC5- or TRPA1-expressing cells with the microtubule-associated protein tau fused to GFP (tau GFP) (*52*). TRPC5-IC mice were genotyped using three primers (*trpc5F*: tggcaggacatccgctattc, *trpc5R*: gggtcacctctgagaacagg, and *trpc5neoremF*: ccgtctctggtgtagctgatg) that produce two bands, 364 and 500 bp from the *wild type* (*wt*) allele and *IRES-Cre* alleles, respectively. Three primers were also used for the TRPA1-IC mice and produced bands of 460 and 264 bp for the *wt* and *IRES-Cre* alleles, respectively (*trpa1F*: gcacagttacctggtgcagaac, *trpa1R*: gggtgaggttgcaggaactagg, and *trpa1neoremF*: tccgtaacctggatagtgaaacagg). Mice were housed in an open cage facility in a 12-hour light-dark cycle according to the European Parliament Council (directive 2007/526/EG). All experiments accorded with the guidelines and regulations of animal care of the European Parliament Council (directive 2010/63EU) and the International Association for the Study of Pain Guidelines for the Use of Animals in Research.

MS no:	Emp name:	Date / Time:	PE's:	AA's:	Comments:	Art no:
RAabf5567/KP/NEUROPHYSIOLOGY, SIGNAL TRANSDUCTION	jroldan	2-26-2021 / 05:29				

Teaser: The odontoblast, with processes beyond the dentin-enamel boundary, is the initial site of TRPC5 cold transduction in teeth.

Behavioral model of DPI and sucrose consumption

The experimental procedures were reproduced and then modified from Gibbs *et al.* (*18*). Female mice were used to be able to house them as adult mice in groups of four mice regardless of strain. Adaptation was performed in the home cage on two subsequent days where the mice were transferred to the experiment room at 8:00 a.m. and food and water were replaced by 5% sucrose until 5:00 p.m. Overnight, mice had free access to food and water. For the sucrose consumption measurement, the mice were weighed and then placed in individual cages without food and water for 7 hours. One hour before the measurement (3 hours before the beginning of the night phase), mice were transferred to the experimental room and water was replaced with individually prepared bottles filled with 5% freshly mixed sucrose solution (room temperature) and a charge-coupled device camera was centered on the bottle nipple of each cage. After 2 hours, the bottles were removed and weighed, and the animals transferred back to their group in the home cage. The amount of consumed glucose solution in 2 hours and the drinking attempts were analyzed from the video material to identify leaking bottles. Baseline sucrose consumption was assessed during two subsequent days. Animals needed to consume, on average, 0.4 ml to be included in the study. On the third day, animals were assigned to the control or DPI group. The DPI consisted of opening the pulp of the first and second maxillary molar with a dental burr during deep anesthesia (see DPAN surgery). The control animals were sham-treated by receiving anesthesia over a similar time, and the mouths were fixed open as during oral surgery in the DPI group. To reduce variability, all drilling was executed by the same experimenter. On the two subsequent days after the DPI or the sham operation, sucrose consumption was assessed after DPI and after sham treatment. The sucrose solution was prepared fresh every day, and the mice were weighed every day before the experiment. Raw data of sucrose consumption were subjected to an outlier analysis based on the interquartile range (IQR). The calculation of the quartiles and the statistical analysis was performed in SPSS 21 using weighted average quartiles (IBM), and the outliers were excluded on the basis of the 2.2-fold IQR rule (*55*).

Electrophysiology
Jaw-nerve preparation and extracellular recordings

This new technique was developed to record from mouse tooth nociceptors. Animals were euthanized and beheaded, and the skin of the head was removed. The head was placed in a petri dish filled with synthetic interstitial fluid (SIF) and kept on an ice bed. SIF contained 108 mM NaCl, 3.5 mM KCl, 0.7 mM $MgSO_4$, 26.2 mM $NaHCO_3$, 1.7 mM NaH_2PO_4, 1.5 mM $CaCl_2$, 9.6 mM sodium gluconate, 5.6 mM glucose, and 7.6 mM sucrose. Mandibles were removed and cleaned from muscle, and the gingiva, connective tissue, and the inferior alveolar nerve were exposed. The tooth pulp of incisor or molars was exposed to allow oxygen to diffuse, and part of the bone was removed to obtain an inferior alveolar nerve length of ~4 mm. The cleansed jaw-nerve preparations were kept refrigerated in oxygenated SIF until use. During the experiment, the jaw-nerve preparations were placed in a mini-tube and then in an organ bath chamber. The mini-tube was connected with the custom-built temperature control system, and the inferior alveolar nerve passed through a hole into the outer chamber. The jaw-nerve preparation was then continuously superfused with oxygenated SIF at a rate of 5 ml/min and maintained at 32°C by a thermostatic control system

(Lauda Eco Silver E4 and Lauda ECO RE415). Electrophysiological recordings were made with suction microelectrodes pulled from borosilicate glass filaments (Sutter P-1000 Micropipette Puller) from the proximal end of the inferior alveolar nerve as previously described (*56*). An Olympus SZX7 microscope, micromanipulator (Märzhäuser MM 33), and custom-modified differential amplifier (EXT-02F, NPI Electronic GmbH) were used. The signal was recorded at 20 kHz with a Micro1401 MKII from CED (Cambridge Electronic Design) and analyzed offline with the Spike2 software (CED). Single nerve fibers were detected by electrical pulses delivered to the nerve trunk with a concentric bipolar electrode (no. CBJPL75, FHC Inc.). Electrical pulses of variable duration and intensity were applied to determine the threshold, and suprathreshold stimuli were applied (20- to 200-µs pulse width, maximum amplitude of 4000 mV) to visualize all fibers, present in the recorded filament. A previously described, custom-built countercurrent heat-exchange system (*19*) was adapted to apply 60-s cold stimuli (from 32° to 6°C) exclusively to the jaw-nerve preparation in the tube to avoid cold-induced block of conduction. Because of the experimental arrangement, the temperature could only be recorded at the outlet of the mini tube, ~1 cm from the tooth. To obtain a better estimate of the temperature near the teeth, we made six temperature measurements between the two positions using two 0.05-mm-diameter ultrafast NiCr-Ni Type K thermoelements (#CHAL-002, Omega). We corrected the threshold temperatures of all cold responses individually with the adjusted temperature curve, taking into account the 4-s time difference and the −2.5°C offset. The difference amounted to ~6°C in threshold temperature. A cold response was defined as a discharge of more than two action potentials during the 60-s cooling periods before stimulation. At least two control stimuli were performed before any pharmacological treatment was applied. Only fibers with reproducible cold responses were included in the pharmacological assessment. The time interval between subsequent cold stimuli was 5 min, and two to four subsequent cold stimuli were applied to register the baseline cold responsiveness. Fibers were classified according to their conduction velocity (CV) into A-fibers (CV > 1 m/s) or C-fibers (CV < 1 m/s). The peak discharge instantaneous frequency value was calculated as the average of at least two subsequent largest instantaneous frequency values. The temperature threshold of activation was determined as the temperature of the first action potential during cooling, and the magnitude of the response refers to the number of action potentials per 80-s cold stimulus (thus including rewarming). All compounds are specified in table S3.

Patch clamp recordings from acutely dissociated TG neurons

Recordings were made from TRPC5 reporter mice 1 to 3 days after plating. Whole-cell currents were recorded at a sampling rate of 10 kHz and low pass–filtered (eight-pole Bessel) at 2 kHz using an Axopatch 200B amplifier, Digidata 1440A digitizer, and pCLAMP 10 software (Molecular Devices). The patch electrodes were pulled from borosilicate glass with resistances between 3 and 6 megohms. Series resistance was compensated by >40% in all recordings. The voltages were corrected for the respective liquid junction potential of the chloride-free ECS (+3.4 mV). Background chloride currents resulted in a negative shift of E_{rev}; therefore, chloride-free (Cl⁻-free) solutions were used. Cl⁻-free ECS contained 145 mM Na isethionate, 1 mM $Mg(OH)_2$, 2 mM $Ca(OH)_2$, 10 mM Hepes, 10 mM glucose, and 5 mM 4-aminopyridine (4-AP), pH 7.4 adjusted with D-gluconic acid and osmolarity of 320 mOsm. Tetrodotoxin (1 µM) and the

AQ7

MS no:	Emp name:	Date / Time:	PE's:	AA's:	Comments:	Art no:
RAabf5567/KP/NEUROPHYSIOLOGY, SIGNAL TRANSDUCTION	jroldan	2-26-2021 / 05:29				

Teaser: The odontoblast, with processes beyond the dentin-enamel boundary, is the initial site of TRPC5 cold transduction in teeth.

Na$_V$1.8 blocker PF-01247324 (1 μM) were added to the bath solution, prepared fresh from frozen stock on the day of experiment. The pipette solution contained 135 mM CsMES, 1 mM MgCl$_2$, 10 mM Hepes, 1 mM EGTA, 5 mM 4-AP, and 0.2 mM Na$_2$GTP, pH 7.4 adjusted with CsOH, osmolarity adjusted to 300 mOsm with glucose. The current-voltage relationships were recorded every 5 s using 500-ms linear voltage ramps from −100 to +100 mV (400 mV/s); holding potential was 0 mV. A combined automated fast solution changer with a double Peltier controller (CV Scientific) was used for drug application (Englerin A, 100 and 1000 nM). The Englerin-evoked currents were calculated by subtraction of currents recorded in the presence of Cl$^-$-free ECS from the currents obtained in the presence of Englerin A. Englerin A was made fresh from frozen stock at the day of the experiment. Only one recording was performed from each cell culture dish to ensure that recordings were made from cells not previously exposed to chemicals.

Patch clamp recordings from HM1 cells

HEK293T cells stably expressing human muscarinic M1 receptor were maintained in Dulbecco's modified Eagle's medium (DMEM)/F12 (1:1), supplemented with 10% fetal bovine serum (FBS) and penicillin/streptomycin (10,000 U ml^{-1}) in 5% CO$_2$. C-terminal–tagged mouse TRPC5–enhanced GFP (EGFP) was transiently transfected using Lipofectamine 2000 (Invitrogen). Cells were recorded 24 to 48 hours after transfection. Recordings were performed at defined temperatures in extracellular solution (ECS) containing 140 mM NaCl, 5 mM KCl, 2 mM CaCl$_2$, 1 mM MgCl$_2$, 10 mM Hepes, and 10 mM glucose (adjusted to pH 7.4 with NaOH). The pipette (intracellular) solution contained 120 mM Cs-MES, 10 mM Cs$_4$-BAPTA, 10 mM Hepes, 2 mM Mg-ATP, 0.4 mM Na$_2$-GTP, 0.47 mM MgCl$_2$, and 3.26 mM CaCl$_2$. Whole-cell recordings were acquired at 5 kHz and low pass–filtered (8-pole Bessel) at 2 kHz. Capacity current was reduced using amplifier circuitry; series resistance compensation was set to 60 to 80%. Pipettes were heat-polished to a final resistance of 1.3 to 1.8 megohms.

Dental primary afferent neurons
Retrograde labeling of mouse DPANs

As previously published (7), molars were drilled with a dental burr and the carbocyanine dye (NeuroTrace, Thermo Fisher Scientific) was applied into the molar cavities. The holes were sealed with light-curable cement using a halogen 470-nm light source (750 mW/cm^2; Translux CL). All mice were anesthetized using a mixture of ketamine (90 mg/kg; Ketavet, Pharmacia GmbH) and xylazine (6 mg/kg; Rompun 2%, Bayer Vital GmbH) with eye protection. To prevent tooth inflammation and inflammatory pain from the procedure, animals were subcutaneously treated once a day with enrofloxacin (7.5 mg/kg Baytril 5%, Bayer Vital GmbH) and carprofen (4 mg/kg Rimadyl, Pfizer GmbH).

Calcium imaging of DPANs

Recordings were made from acutely dissociated TG neurons after retrograde labeling. Dissociated neurons were loaded with Fura-2 AM (Invitrogen, 3 μM supplemented with 0.02% pluronic dissolved in ECS) for 30 min and then washed for 15 min in ECS containing 145 mM NaCl, 5 mM KCl, 1 mM MgCl$_2$, 1.3 mM CaCl$_2$, 10 mM Hepes, and 10 mM glucose at pH 7.4. Calcium imaging experiments were made with an Olympus IX83 inverted microscope equipped with an Olympus UApoN340 20× water immersion objective. Fura-2 AM–loaded cells were excited with a 300-W xenon lamp (Lambda DG-4, Sutter Instrument) at 340 and 380 nm, and the emission was examined at 510 nm.

An ORCA-Flash 4.0 LT digital camera (C11440, Hamamatsu Photonics) was used for image acquisition at a rate of 1 per second. Analysis was carried out with SlideBook 6 software (Intelligent Imaging Innovations). DiI-positive neurons were selected in the culture (excitation at 556 to 590 nm and examined at 602 to 664 nm). Cold stimulation of 10°C was realized with a combined automated fast solution changer with a double Peltier controller (CV Scientific). Menthol (500 μM), ML204 (100 μM), and KCl (145 mM) were applied during the measurement. Cold-induced activity of the fluorescence signal was computed as the area under the respective traces (120-s time frames). Cells were considered cold sensitive or sensitive to drugs (menthol, carvacrol, riluzole, ML204) when the averaged Ca^{2+} signal reached 2.5 × SD above the preceding baseline. All compounds are specified in table S3.

Multiphoton microscopy in retrograde-labeled mouse TG

Five days after surgery, mice were intracardially perfused with phosphate-buffered saline (PBS) and 4% PFA and the TGs were removed. TGs were left in PFA at 4°C for 6 hours. For staining with an anti-GFP antibody (table S4), the ganglia were pretreated with 100 μM digitonin according to a previously established protocol to preserve DiI from diffusion (57). The ganglia were mounted in agarose, and image stacks were acquired with a Zeiss LSM 880 NLO microscope equipped with a 680- to 1300-nm tunable and fixed 1040-nm two-photon laser (Newport Spectra-Physics) and a 20× W-Plan Apochromat objective lens. Fluorophores were excited at 1040 nm (DiI) and 920 nm (EGFPf or tau GFP), and fluorophore emissions were detected with nondescanned GaAsP detectors at 575 to 610 nm (DiI) and 500 to 550 nm (EGFPf or tau GFP). Fiji ImageJ was used to process the data, and the ImageJ Cell Counter plug-in was used to quantify cell numbers. For TGs, two different experimenters counted the cell bodies; the results represent their mean score.

RNA sequencing from DPANs

DPANs were selected from acutely dissociated TG cultures of C57BL/6JCrl mice, which were labeled as previously described with Neurotrace (7). After 3 days, the TGs were extracted, and cultures were obtained from dissociated neurons. Labeled cells were recognized and collected under an Olympus IX83 inverse microscope equipped with a vacuum-assisted single-cell collection device (Unipick, NeuroInDx). Four sets of red-labeled cells were selected, and 10 to 20 cells were pooled by transferring them to lysis buffer–containing tubes and stored on dry ice until subjecting them to transcriptomic analysis by the deep sequencing group at Technische Universität Dresden according to established protocols (58). Briefly, samples were amplified using single-cell exponential mRNA amplification service [SMARTer Ultra Low RNA Kit v2 (Clontech) or SMART-Seq2 (59)], further processed with a Nextera DNA library preparation kit (Illumina), and sequenced on Nextseq500 to depth between 15 and 20 million fragments per sample. The mapping was performed with Genomic Short-read Nucleotide Alignment Program (GSNAP, v 2017-08-15) (60) using the mm10 reference genome and Ensembl 87. The expression levels were calculated using featureCounts (v1.5.3) (61). To allow a comparison of the sets, data are represented as transcripts per kilobase million (TPM) and displayed on a logarithmic scale.

Cell culture
Mouse TG culture

Cultures were performed as previously described (7). Five days after surgery, mice were euthanized, and the TGs were removed. For

AQ8

AQ9

MS no:	Emp name:	Date / Time:	PE's:	AA's:	Comments:	Art no:
RAabf5567/KP/NEUROPHYSIOLOGY, SIGNAL TRANSDUCTION	jroldan	2-26-2021 / 05:29				

Teaser: The odontoblast, with processes beyond the dentin-enamel boundary, is the initial site of TRPC5 cold transduction in teeth.

each experiment, ganglia of two or three animals were combined, transferred in sterile DMEM (Thermo Fisher Scientific), and fragmented. For cell dissociation, TG fragments were incubated in a mix of protease (Sigma-Aldrich; 1:2000) and collagenase (Sigma-Aldrich; 1:1000) in DMEM at 37°C and 5% CO_2 for 45 min. The cell suspension was then washed in DMEM and TNB 100 medium (Biochrom GmbH), supplemented with TNB 100 lipid-protein complex (Biochrom GmbH), streptomycin/penicillin (100 µg/ml; Thermo Fisher Scientific), and 1 nM nerve growth factor-7S (Alomone Labs), and cell clusters were triturated. Twenty microliters of cell suspension was applied per poly-D-lysine–coated FluoroDish (World Precision Instruments) and incubated in 1-ml TNB medium for 15 to 18 hours at 37°C and 5% CO_2.

HEK293T cell culture and transfection procedure
Cells were transiently transfected with mouse *Trpc5* cDNA as previously described (*17, 42*), using Nanofectin (PAA Laboratories GmbH) according to the manufacturer's protocol. HEK293T cells were maintained in DMEM medium (Gibco Life Technologies) supplemented with 10% FBS, glucose (4.5 g/liter), and 1% penicillin/streptomycin. Cells plated on poly-D-lysine–coated coverslips were loaded with 3 µM Fura-2 AM (Invitrogen) supplemented with 0.02% pluronic acid (Invitrogen) for 30 min at 37°C and 5% CO_2 followed by a 15-min washout. Ratiometric calcium imaging of *mTRPC5* was performed 24 hours after transfection as described above.

Immunohistochemistry and histology
Immunohistochemistry in mouse molar tooth sections
Mice were intracardially perfused with PBS and 4% PFA, and the jaws were extracted and cleansed. For each genotype, tissues of two reporter mice were used. The jaws were left overnight in PFA at 4°C, then washed three times for 20 min in PBS at room temperature, and transferred to 20% EDTA for 24 hours at 37°C. We used S.C.E.M (Section Lab Co. Ltd.) and a small metal container immersed in hexane on dry ice at −77°C to embed the jaws. The frozen blocks were kept at −80°C and transferred to −20°C 6 hours before sectioning. The CryoJane Tape-Transfer System (CryoJane, Leica Microsystems, GmbH) was used to obtain serial sections of mouse molar teeth without distortion. Cryosectioning was performed (Leica CM3050) using adhesive tape applied to the frozen tissue block with a hand roller. The 16-µm-thick frozen sections were captured on tape, and the tape was rolled onto an adhesive glass slide (4× pretreated according to the manufacturer's instructions) and polymerized by ultraviolet-light irradiation into a plastic layer to anchor the frozen section to the glass slide. The tape was peeled off the section, and the section was subjected to immunohistochemical staining. The sections were blocked with 1% bovine serum albumin (BSA), 0.5% Triton X-100, and 5% goat serum in PBS at 4°C overnight, then incubated with antibodies diluted in 1% BSA and 0.5% Triton X-100 in PBS at 4°C overnight, and washed three times for 20 min in PBS. Subsequently, the sections were sealed with coverslips using a DAPI (4′,6-diamidino-2-phenylindole)–containing embedding medium. We visualized βIII-tubulin and amplified the GFP signal in reporter mice with antibodies listed in table S4. The sections were visualized using a Zeiss Spinning Disc Axio Observer Z1 microscope using a 25× or 63× objective lens with oil immersion. From selected areas, subsequent planes were acquired and the three-dimensional microscopy data were animated according to a previously published method (*62*).

Histology and microscopy of human tooth sections
Institutional approval was obtained for the use of human tissue samples (protocol 08-0209, Washington University, Department of Pathology).

Tissues and fixation. Extracted teeth were carefully stripped of periodontal, but not periapical, tissue and sectioned using a water-cooled diamond cutting wheel. For vertical sections, the plane was oriented toward the very tip of the root, slightly to the side of the apical foramen (typically offset 1 to 3 mm toward the crown). Split tooth segments were fixed for 2 days in phosphate-buffered 4% paraformaldehyde solution (pH 7.4). Decalcification protocols included demineralization for 1 to 3 weeks in a solution of 14% hypochloric acid and polyvinylpyrrolidone 2, two commercial solutions consisting of 10% formaldehyde, 8% formic acid, and 1% methanol (Decalcifier I, Surgipath Medical Industries) as well as HCl and EDTA in water (Decalcifier II, Surgipath Medical Industries), or methyl methacrylate embedding according to established protocols (*63*). All human samples were formalin-fixed and paraffin-embedded; hematoxylin and eosin (H&E) stains were performed using routine protocols.

Immunohistochemistry. For detection of TRPC5, TRPM8, and other neuronal markers, sections were incubated with combinations of the antibodies listed in table S4 and visualized with appropriate secondary antibodies conjugated to Alexa 350, 488, 555, or 594 (1:500) in combination with Hoechst 33258 staining (blue).

Microscopy. For fluorescence microscopy, sections were viewed and quantified using a Zeiss Axiovert 200 inverted fluorescence microscope and an Olympus AX70 epi-fluorescence microscope. For low power fluorescence of tissues larger than the 4× field, complete visualization was achieved by overlaying 150 to 450 manually acquired 20× to 40× images in the channels appropriate for the secondary antibodies (panography). H&E-stained slides were viewed with an Olympus BX51 light microscope and, for whole-mount views, scanned on a Scanscope XT microscope (Aperio). Quantification of nerve fibers and neurons followed established protocols (*64*). Briefly, nerve fiber quantification was performed in cross- and longitudinal sections obtained just superior to the apical foramen; image processing was performed using ImageJ (v. 1.37v http://rsb.info.nih.gov/ij/) and Photoshop CS3 (Adobe Systems).

Histopathology. Pulpitis was defined as previously described (*65*). Briefly, hyperemia and blood vessel dilatation were typically seen in combination with at least focal disruption of the odontoblastic layer. Abundant serous exudate (as a result of increased vascular permeability), early neutrophils, or partial pulp necrosis were not a requirement for diagnosis of pulpitis, but frequently present. Teeth with previous endodontic treatment and extensive pulp necrosis extending to the apex were excluded from analysis.

Statistical analysis
We used a two-sided Student's *t* test, as indicated, for the comparison of dependent samples. Group comparisons were performed using one-way analysis of variance (ANOVA) followed by the least significant difference (LSD) test for extracellular electrophysiology data and behavioral data and a Tukey test for calcium imaging analysis. Chi-square tests were used to compare observed frequencies of the different genotypes with the background strain. In the figures, significant differences are indicated with one symbol for $P < 0.05$, two for $P < 0.01$, and three for $P < 0.001$. We used asterisks (*) for the *t* test, hashtags (#) for one-sided ANOVA followed by the LSD

MS no:	Emp name:	Date / Time:	PE's:	AA's:	Comments:	Art no:
RAabf5567/KP/NEUROPHYSIOLOGY, SIGNAL TRANSDUCTION	jroldan	2-26-2021 / 05:29				

Teaser: The odontoblast, with processes beyond the dentin-enamel boundary, is the initial site of TRPC5 cold transduction in teeth.

or Tukey post hoc tests, and double daggers (‡) for the chi-square test. Raw data were analyzed for outliers using the 2.2-fold IQR (*55*) from weighted average quartiles calculated in SPSS 21, and then box plot graphs were computed in Origin 2017.

SUPPLEMENTARY MATERIALS

Supplementary material for this article is available at http://advances.sciencemag.org/cgi/content/full/7/13/eabf5567/DC1

View/request a protocol for this paper from *Bio-protocol*.

AQ10 **REFERENCES AND NOTES**

1. N. J. Kassebaum, E. Bernabé, M. Dahiya, B. Bhandari, C. J. L. Murray, W. Marcenes, Global burden of untreated caries: A systematic review and metaregression. *J. Dent. Res.* **94**, 650–658 (2015).
2. R. A. Alghaithy, A. J. E. Qualtrough, Pulp sensibility and vitality tests for diagnosing pulpal health in permanent teeth: A critical review. *Int. Endod. J.* **50**, 135–142 (2017).
3. M. Lin, G. M. Genin, F. Xu, T. Lu, Thermal pain in teeth: Electrophysiology governed by thermomechanics. *Appl. Mech. Rev.* **66**, 0308011–3080114 (2014).
4. M. Brännström, G. Johnson, Movements of the dentine and pulp liquids on application of thermal stimuli. An in vitro study. *Acta Odontol. Scand.* **28**, 59–70 (1970).
5. J. Vriens, B. Nilius, T. Voets, Peripheral thermosensation in mammals. *Nat. Rev. Neurosci.* **15**, 573–589 (2014).
6. Z. Winter, P. Gruschwitz, S. Eger, F. Touska, K. Zimmermann, Cold temperature encoding by cutaneous TRPA1 and TRPM8-carrying fibers in the mouse. *Front. Mol. Neurosci.* **10**, 209 (2017).
7. A. Kadala, P. Sotelo-Hitschfeld, Z. Ahmad, P. Tripal, B. Schmid, A. Mueller, L. Bernal, Z. Winter, S. Brauchi, U. Lohbauer, K. Messlinger, J. K. Lennerz, K. Zimmermann, Fluorescent labeling and 2-photon imaging of mouse tooth pulp nociceptors. *J. Dent. Res.* **97**, 460–466 (2018).
8. Y. S. Kim, T. H. Kim, D. D. McKemy, Y. C. Bae, Expression of vesicular glutamate transporters in transient receptor potential melastatin 8 (TRPM8)-positive dental afferents in the mouse. *Neuroscience* **303**, 378–388 (2015).
9. Y. S. Kim, H. K. Jung, T. K. Kwon, C. S. Kim, J. H. Cho, D. K. Ahn, Y. C. Bae, Expression of transient receptor potential ankyrin 1 in human dental pulp. *J. Endod.* **38**, 1087–1092 (2012).
10. I. A. El Karim, G. J. Linden, T. M. Curtis, I. About, M. K. McGahon, C. R. Irwin, F. T. Lundy, Human odontoblasts express functional thermo-sensitive TRP channels: Implications for dentin sensitivity. *Pain* **152**, 2211–2223 (2011).
11. I. A. El Karim, G. J. Linden, T. M. Curtis, I. About, M. K. McGahon, C. R. Irwin, S. A. Killough, F. T. Lundy, Human dental pulp fibroblasts express the "cold-sensing" transient receptor potential channels TRPA1 and TRPM8. *J. Endod.* **37**, 473–478 (2011).
12. K. Tazawa, H. Ikeda, N. Kawashima, T. Okiji, Transient receptor potential melastatin (TRPM) 8 is expressed in freshly isolated native human odontoblasts. *Arch. Oral Biol.* **75**, 55–61 (2017).
13. O. Egbuniwe, S. Grover, A. K. Duggal, A. Mavroudis, M. Yazdi, T. Renton, L. Di Silvio, A. D. Grant, TRPA1 and TRPV4 activation in human odontoblasts stimulates ATP release. *J. Dent. Res.* **93**, 911–917 (2014).
14. K. Y. Yeon, G. Chung, M. S. Shin, S. J. Jung, J. S. Kim, S. B. Oh, Adult rat odontoblasts lack noxious thermal sensitivity. *J. Dent. Res.* **88**, 328–332 (2009).
15. M. Tsumura, U. Sobhan, M. Sato, M. Shimada, A. Nishiyama, A. Kawaguchi, M. Soya, H. Kuroda, M. Tazaki, Y. Shibukawa, Functional expression of TRPM8 and TRPA1 channels in rat odontoblasts. *PLOS ONE* **8**, e82233 (2013).
16. B. Michot, C. S. Lee, J. L. Gibbs, TRPM8 and TRPA1 do not contribute to dental pulp sensitivity to cold. *Sci. Rep.* **8**, 13198 (2018).
17. K. Zimmermann, J. K. Lennerz, A. Hein, A. S. Link, J. S. Kaczmarek, M. Delling, S. Uysal, J. D. Pfeifer, A. Riccio, D. E. Clapham, Transient receptor potential cation channel, subfamily C, member 5 (TRPC5) is a cold-transducer in the peripheral nervous system. *Proc. Natl. Acad. Sci. U.S.A.* **108**, 18114–18119 (2011).
18. J. L. Gibbs, R. Urban, A. I. Basbaum, Paradoxical surrogate markers of dental injury-induced pain in the mouse. *Pain* **154**, 1358–1367 (2013).
19. K. Zimmermann, A. Hein, U. Hager, J. S. Kaczmarek, B. P. Turnquist, D. E. Clapham, P. W. Reeh, Phenotyping sensory nerve endings in vitro in the mouse. *Nat. Protoc.* **4**, 174–196 (2009).
20. T. Memon, K. Chase, L. S. Leavitt, B. M. Olivera, R. W. Teichert, TRPA1 expression levels and excitability brake by K_V channels influence cold sensitivity of TRPA1-expressing neurons. *Neuroscience* **353**, 76–86 (2017).
21. Y. Schwarz, K. Oleinikov, B. Schindeldecker, A. Wyatt, P. Weißgerber, V. Flockerzi, U. Boehm, M. Freichel, D. Bruns, TRPC channels regulate Ca^{2+}-signaling and short-term plasticity of fast glutamatergic synapses. *PLOS Biol.* **17**, e3000445 (2019).
22. L. T. Alvarado, G. M. Perry, K. M. Hargreaves, M. A. Henry, TRPM8 Axonal expression is decreased in painful human teeth with irreversible pulpitis and cold hyperalgesia. *J. Endod.* **33**, 1167–1171 (2007).
23. M. R. Byers, R. E. Westenbroek, Odontoblasts in developing, mature and ageing rat teeth have multiple phenotypes that variably express all nine voltage-gated sodium channels. *Arch. Oral Biol.* **56**, 1199–1220 (2011).
24. A. Tanaka, Y. Shibukawa, M. Yamamoto, S. Abe, H. Yamamoto, S. Shintani, Developmental studies on the acquisition of perception conducting pathways via TRP channels in rat molar odontoblasts using immunohistochemistry and RT-qPCR. *Anat. Sci. Int.* **95**, 251–257 (2020).
25. T. Gunji, Morphological research on the sensitivity of dentin. *Arch. Histol. Jpn.* **45**, 45–67 (1982).
26. C. F. Cox, K. Suzuki, H. Yamaguchi, J. D. Ruby, S. Suzuki, N. Akimoto, N. Maeda, Y. Momoi, Sensory mechanisms in dentine: A literature review of light microscopy (LM), transmission microscopy (TEM), scanning microscopy (SEM) & electro physiological (EP) tooth sensitivity: Is the ciliary organelle on the odontoblast the elusive primary nociceptor? *Dent. Oral Craniofacial Res.* **4**, 1–14 (2017).
27. N. Vongsavan, B. Matthews, The relationship between the discharge of intradental nerves and the rate of fluid flow through dentine in the cat. *Arch. Oral Biol.* **52**, 640–647 (2007).
28. H. O. Trowbridge, M. Franks, E. Korostoff, R. Emling, Sensory response to thermal stimulation in human teeth. *J. Endod.* **6**, 405–412 (1980).
29. P. Linsuwanont, J. E. Palamara, H. H. Messer, An investigation of thermal stimulation in intact teeth. *Arch. Oral Biol.* **52**, 218–227 (2007).
30. W. Chidchuangchai, N. Vongsavan, B. Matthews, Sensory transduction mechanisms responsible for pain caused by cold stimulation of dentine in man. *Arch. Oral Biol.* **52**, 154–160 (2007).
31. K. B. Muzzin, R. Johnson, Effects of potassium oxalate on dentin hypersensitivity in vivo. *J. Periodontol.* **60**, 151–158 (1989).
32. O. Ajcharanukul, W. Chidchuangchai, P. Charoenlarp, N. Vongsavan, B. Matthews, Sensory transduction in human teeth with inflamed pulps. *J. Dent. Res.* **90**, 678–682 (2011).
33. H. Magloire, M. L. Couble, B. Thivichon-Prince, J. C. Maurin, F. Bleicher, Odontoblast: A mechano-sensory cell. *J. Exp. Zool. B Mol. Dev. Evol.* **312B**, 416–424 (2009).
34. Y. A. Nikolaev, C. D. Cox, P. Ridone, P. R. Rohde, J. F. Cordero-Morales, V. Vasquez, D. R. Laver, B. Martinac, Mammalian TRP ion channels are insensitive to membrane stretch. *J. Cell Sci.* **132**, jcs238360 (2019).
35. L. Moparthi, P. M. Zygmunt, Human TRPA1 is an inherently mechanosensitive bilayer-gated ion channel. *Cell Calcium* **91**, 102255 (2020).
36. A. G. Obukhov, M. C. Nowycky, TRPC5 activation kinetics are modulated by the scaffolding protein ezrin/radixin/moesin-binding phosphoprotein-50 (EBP50). *J. Cell. Physiol.* **201**, 227–235 (2004).
37. A. Gomis, S. Soriano, C. Belmonte, F. Viana, Hypoosmotic- and pressure-induced membrane stretch activate TRPC5 channels. *J. Physiol.* **586**, 5633–5649 (2008).
38. B. Allard, H. Magloire, M. L. Couble, J. C. Maurin, F. Bleicher, Voltage-gated sodium channels confer excitability to human odontoblasts: Possible role in tooth pain transmission. *J. Biol. Chem.* **281**, 29002–29010 (2006).
39. M. R. Byers, Dental sensory receptors. *Int. Rev. Neurobiol.* **25**, 39–94 (1984).
40. H. Ikeda, H. Suda, Odontoblastic syncytium through electrical coupling in the human dental pulp. *J. Dent. Res.* **92**, 371–375 (2013).
41. Y. S. Cho, C. H. Ryu, J. H. Won, H. Vang, S. B. Oh, J. Y. Ro, Y. C. Bae, Rat odontoblasts may use glutamate to signal dentin injury. *Neuroscience* **335**, 54–63 (2016).
42. N. T. Blair, J. S. Kaczmarek, D. E. Clapham, Intracellular calcium strongly potentiates agonist-activated TRPC5 channels. *J. Gen. Physiol.* **133**, 525–546 (2009).
43. P. R. Lee, J. Y. Lee, H. B. Kim, J. H. Lee, S. B. Oh, TRPM8 mediates hyperosmotic stimuli-induced nociception in dental afferents. *J. Dent. Res.* **99**, 107–114 (2019).
44. S. Yamamoto, N. Takahashi, Y. Mori, Chemical physiology of oxidative stress-activated TRPM2 and TRPC5 channels. *Prog. Biophys. Mol. Biol.* **103**, 18–27 (2010).
45. E. K. Curtis, In pursuit of palliation: Oil of cloves in the art of dentistry. *Bull. Hist. Dent.* **38**, 9–14 (1990).
46. P. W. Lucas, S. M. Philip, D. Al-Qeoud, N. Al-Draihim, S. Saji, A. van Casteren, Structure and scale of the mechanics of mammalian dental enamel viewed from an evolutionary perspective. *Evol. Dev.* **18**, 54–61 (2016).
47. K. Y. Kwan, A. J. Allchorne, M. A. Vollrath, A. P. Christensen, D. S. Zhang, C. J. Woolf, D. P. Corey, TRPA1 contributes to cold, mechanical, and chemical Nociception but is not essential for hair-cell transduction. *Neuron* **50**, 277–289 (2006).
48. A. Dhaka, A. N. Murray, J. Mathur, T. J. Earley, M. J. Petrus, A. Patapoutian, TRPM8 is required for cold sensation in mice. *Neuron* **54**, 371–378 (2007).
49. T. Xue, M. T. H. Do, A. Riccio, Z. Jiang, J. Hsieh, H. C. Wang, S. L. Merbs, D. S. Welsbie, T. Yoshioka, P. Weissgerber, S. Stolz, V. Flockerzi, M. Freichel, M. I. Simon, D. E. Clapham, K.-W. Yau, Melanopsin signalling in mammalian iris and retina. *Nature* **479**, 67–73 (2011).
50. I. Vetter, A. Hein, S. Sattler, S. Hessler, F. Touska, E. Bressan, A. Parra, U. Hager, A. Leffler, S. Boukalova, M. Nissen, R. J. Lewis, C. Belmonte, C. Alzheimer, T. Huth, V. Vlachova,

MS no:	Emp name:	Date / Time:	PE's:	AA's:	Comments:	Art no:
RAabf5567/KP/NEUROPHYSIOLOGY, SIGNAL TRANSDUCTION	jroldan	2-26-2021 / 05:29				

Teaser: The odontoblast, with processes beyond the dentin-enamel boundary, is the initial site of TRPC5 cold transduction in teeth.

P. W. Reeh, K. Zimmermann, Amplified cold transduction in native nociceptors by M-channel inhibition. *J. Neurosci.* **33**, 16627–16641 (2013).

51. I. Vetter, F. Touska, A. Hess, R. Hinsbey, S. Sattler, A. Lampert, A. Sergejeva, A. Sharov, L. S. Collins, M. Eberhardt, M. Engel, P. J. Cabot, J. N. Wood, V. Vlachova, P. W. Reeh, R. J. Lewis, K. Zimmermann, Ciguatoxins activate specific cold pain pathways to elicit burning pain from cooling. *EMBO J.* **31**, 3795–3808 (2012).

52. A. Wyatt, P. Wartenberg, M. Candlish, G. Krasteva-Christ, V. Flockerzi, U. Boehm, Genetic strategies to analyze primary TRP channel-expressing cells in mice. *Cell Calcium* **67**, 91–104 (2017).

53. C. I. Rodriguez, F. Buchholz, J. Galloway, R. Sequerra, J. Kasper, R. Ayala, A. F. Stewart, S. M. Dymecki, High-efficiency deleter mice show that FLPe is an alternative to Cre-*loxP*. *Nat. Genet.* **25**, 139–140 (2000).

54. S. Wen, I. N. Götze, O. Mai, C. Schauer, T. Leinders-Zufall, U. Boehm, Genetic identification of GnRH receptor neurons: A new model for studying neural circuits underlying reproductive physiology in the mouse brain. *Endocrinology* **152**, 1515–1526 (2011).

55. D. C. Hoaglin, B. Iglewicz, Fine-tuning some resistant rules for outlier labeling. *J. Am. Stat. Assoc.* **82**, 1147–1149 (1987).

56. C. Roza, J. A. Lopez-Garcia, Retigabine, the specific KCNQ channel opener, blocks ectopic discharges in axotomized sensory fibres. *Pain* **138**, 537–545 (2008).

57. Y. Matsubayashi, L. Iwai, H. Kawasaki, Fluorescent double-labeling with carbocyanine neuronal tracing and immunohistochemistry using a cholesterol-specific detergent digitonin. *J. Neurosci. Methods* **174**, 71–81 (2008).

58. K. N. Natarajan, Z. Miao, M. Jiang, X. Huang, H. Zhou, J. Xie, C. Wang, S. Qin, Z. Zhao, L. Wu, N. Yang, B. Li, Y. Hou, S. Liu, S. A. Teichmann, Comparative analysis of sequencing technologies for single-cell transcriptomics. *Genome Biol.* **20**, 70 (2019).

59. S. Picelli, A. K. Björklund, O. R. Faridani, S. Sagasser, G. Winberg, R. Sandberg, Smart-seq2 for sensitive full-length transcriptome profiling in single cells. *Nat. Methods* **10**, 1096–1098 (2013).

60. T. D. Wu, S. Nacu, Fast and SNP-tolerant detection of complex variants and splicing in short reads. *Bioinformatics* **26**, 873–881 (2010).

61. Y. Liao, G. K. Smyth, W. Shi, featureCounts: An efficient general purpose program for assigning sequence reads to genomic features. *Bioinformatics* **30**, 923–930 (2014).

62. B. Schmid, P. Tripal, T. Fraass, C. Kersten, B. Ruder, A. Gruneboom, J. Huisken, R. Palmisano, 3Dscript: Animating 3D/4D microscopy data using a natural-language-based syntax. *Nat. Methods* **16**, 278–280 (2019).

63. M. P. Whyte, W. H. McAlister, D. V. Novack, K. L. Clements, P. L. Schoenecker, D. Wenkert, Bisphosphonate-induced osteopetrosis: Novel bone modeling defects, metaphyseal osteopenia, and osteosclerosis fractures after drug exposure ceases. *J. Bone Miner. Res.* **23**, 1698–1707 (2008).

64. J. K. Lennerz, V. Ruhle, E. P. Ceppa, W. L. Neuhuber, N. W. Bunnett, E. F. Grady, K. Messlinger, Calcitonin receptor-like receptor (CLR), receptor activity-modifying protein 1 (RAMP1), and calcitonin gene-related peptide (CGRP) immunoreactivity in the rat trigeminovascular system: Differences between peripheral and central CGRP receptor distribution. *J. Comp. Neurol.* **507**, 1277–1299 (2008).

65. R. A. Colby, *Color Atlas of Oral Pathology; Histology and Embryology, Developmental Disturbances, Diseases of the Teeth and Supporting Structures, Diseases of the Oral Mucosa and Jaws, Neoplasms* (Lippincott Williams & Wilkins, 1961).

66. N. N. Shuhaibar, A. R. Hand, M. Terasaki, Odontoblast processes of the mouse incisor are plates oriented in the direction of growth. *Anat. Rec. (Hoboken)*, 1–8 (2020).

AQ11

Citation: L. Bernal, P. Sotelo-Hitschfeld, C. König, V. Sinica, A. Wyatt, Z. Winter, A. Hein, F. Touska, S. Reinhardt, A. Tragl, R. Kusuda, P. Wartenberg, A. Sclaroff, J. D. Pfeifer, F. Ectors, A. Dahl, M. Freichel, V. Vlachova, S. Brauchi, C. Roza, U. Boehm, D. E. Clapham, J. K. Lennerz, K. Zimmermann, Odontoblast TRPC5 channels signal cold pain in teeth. *Sci. Adv.* **7**, eabf5567 (2021).

MS no:	Emp name:	Date / Time:	PE's:	AA's:	Comments:	Art no:
RAabf5567/KP/NEUROPHYSIOLOGY, SIGNAL TRANSDUCTION	jroldan	2-26-2021 / 05:29				

Teaser: The odontoblast, with processes beyond the dentin-enamel boundary, is the initial site of TRPC5 cold transduction in teeth.